Universitat Autònoma de Barcelona

γ-ray emission from regions of star formation: Theory and observations with the MAGIC Telescope

Ph.D. Dissertation

Eva Domingo Santamaría

March 2006

supervised by

Juan Cortina Blanco & Diego F. Torres

Universitat Autònoma de Barcelona
Departament de Física

Institut de Física d'Altes Energies (IFAE)

Edifici C-n, Campus UAB,
E-08193 Bellaterra (Barcelona)

A todos ellos,
por la fuerza que me han dado.

Agradecimientos

Quisiera comenzar agradeciendo a todos aquellos que en su día me dieron la oportunidad de pasar 6 años de mi vida en el mundo de la investigación, empezando por Enrique Fernández por acogerme en el IFAE, y terminando por Manel Martínez, quien me abrió una puerta al fascinante mundo de MAGIC y la astrofísica de altas energías.

Una vez ahí las vivencias, las personas, los momentos, las dificultades, los nervios, las ilusiones, han sido muchas y muy variadas. Pero sin duda, si pienso en esta tesis, son dos las personas a quienes más debo mi agradecimiento: mis directores, Juan Cortina y Diego Torres. Es mucho lo que he aprendido con y gracias a ellos, Juan, enseñándome los entresijos del telescopio y del análisis de los datos, y Diego ayudándome a atreverme con la teoría y los modelos y a disfrutar con la física de los poderosos objetos que MAGIC observa. Ambos cercanos, ambos implicados, mucho más no se puede pedir. Cada cual con su opinión (no siempre la misma) pero siempre manteniendo esa combinación de profesionalidad, respeto, cercanía y confianza, que sé tan difícil de lograr (y más entre 3 personas), y que sin duda ha sido la base de que haya sido capaz de hacer y poner por escrito todo este trabajo. Y sí, es cierto, me siento afortunada, para mi han sido la combinación perfecta. Gracias a los dos por vuestra confianza, vuestra paciencia y vuestro esfuerzo, que sé que no ha sido poco, espero trasmitiros lo mucho que lo aprecio.

La verdad es que trabajar en la colaboración MAGIC ha sido un gran placer, ya no sólo porque me ha permitido empezar a imaginar un poco mejor todo esa enormidad que nos rodea, sino que también (y sobretodo) por el genial ambiente humano que tantos han logrado crear siempre. Están los magicians del IFAE. Primero con quienes empecé tirando cables ahi arriba en La Palma y de quien he acabado aprendiendo tanto porque siempre han estado ahí, para echar una mano: Oscar, que se fue a Paris pero sigue estando siempre cerca; Pepe, con quien he tenido el placer de trabajar codo a codo y desesperarnos y emocionarnos juntos; Javi, que siempre tuvo un minuto y una sonrisa amable; y Markus, siempre dispuesto a ayudar. Y no me quiero olvidar de Xavi, y nuestras bombillas disipadoras de calor, ni de Jose, que siempre tuvo una solución para todo y que me enseñó de cables y de charlas tranquis. Luego están los que llegaron más tarde y que espero que no nos maldigan mucho por lo que les hayamos dejado: Ester y Núria, mis compañeras de despacho en alguna de mis mudanzas, gracias por las ayudas en todos los sentidos, Roger y nuestro cooling y sus fabulosos scripts, Alex y su genial ironía, Manel y Diego, y Javi (gracias por las discusiones) y Emma (gracias por la luna). Pero el mundo magician sigue fuera de las paredes del IFAE. En especial quiero agradecer las charlas, los emails, las discusiones, los ratos, las ayudas, los viajes a Wolfgang, Abelardo, Pratik, Florian, Ciro, Nadia, Nepomuk, Antonio, Arnau, Dorota, Fabrizio, Raquel, Andreu, Daniela, Villi, Toni, el otro Daniel... y a tantos otros...

Pero el día a día no ha sido sólo MAGIC, puesto que el IFAE es grande y muchos han sido los que han alimentado las ganas de estar allí. Primero mi Laieta, que estuvo el

primer año que llegué, se fue al CERN, le dio tiempo a volver, y sigue como siempre, aún más cercana. Luego Ana y nuestras escasas pero valiosas charlas. Y Carlos y su dulzura. Sigrid y sus sonrisas. Y Ester, que nos mantiene activos. Y Jose, Gabriel, Natalia, Magali, Alex y Mireia, y Olga y Xavi desde los USA.

Antes de salir del mundo de la investigación, que tantas horas me ha retenido, quiero acordarme de Magda, mi gran amiga mexicana, con quien tan buenos momentos he pasado y con quien charlar, de física y no física, siempre ha sido un placer y un aprendizaje.

Y, bueno, aún quedan por ahí mi pandilla de físicos (y no físicos) que al final han acabado rondado casi todos siempre por la uni. Felisa, que tanto me conoce y siempre tanto me da, a menudo sin darse cuenta. Marieta, que no podría no cuidarnos a todos. Juanma, siempre atento y dispuesto a dar un abrazo a la hora que sea. Y Ro, que no nos falten sus sueños y sus locuras. Y el bueno de Ángel, y la silenciosa Marcel·la. Gracias por todos los buenos ratos y vuestro respaldo. Y prepararos, que ya vuelvo a por mi vida social.

Luego están y han estado, a quienes veo menos, por pura distancia (calculada desde mi asiento en el despacho del fondo del pasillo del IFAE). Jose Luis y lo mucho compartido y conservado, mi Evita y su cariño, Mateo y sus rizos amables, Ramon y sus inquietudes, Paquita y su manera de cuidarme, Zaida y sus emails dando ánimos cuando más falta hacen, Sergio y el gran aprecio que hay, Montse y su ternura, Josep y su locura, Yanina y nuestra amistad y ese viaje, Susana y los buenos reencuentros, y Raquel y Diego que siempre me esperan en mi Salou, con el mar.

No me quiero dejar esta vez a mi familia, tíos y tías, primos y primas, más o menos cercanos, que no han parado de interesarse por lo que hacía, de asaltarme alguna vez con preguntas que jamás me había planteado, y que ahora 'amenazan' con venir, desde donde haga falta, a apoyarme en la recta final.

Y para acabar, los míos. Mi hermano, aunque ausente siempre presente. Mi hermanita, ya ALBA con todas las letras bien puestas, por su cariño, su apoyo, nuestras charlas y su esfuerzo por seguir fortaleciendo día a día nuestra relación que tanto bien me hace. Y mis padres, que siempre están ahí, dándome fuerzas y apoyo, aunque yo a veces no me deje. Gracias por cuidarme, por quererme y demostrármelo, y por haber confiado siempre en mí.

A todos, gracias por lo aprendido y compartido, y por aguantar de cerca mis nervios e inestabilidades y, de lejos, mis largas ausencias.

Contents

List of Figures

List of Tables

Chapter 1

Introduction: Astrophysics with γ-rays

This Thesis deals with some unresolved questions in the γ-ray band of the electromagnetic spectrum. Being the latter the most energetic end of the radiation emitted by any astrophysical source, we are confronted with issues involving the acceleration, production, interactions, and decays of highly relativistic particles. Photons, the carriers of the information that we process from the astrophysical environments, are then inextricably related not only with the parent population of particles that generated them through interactions, but also with the environment within which these interactions proceed. γ-ray astronomy, then, is the most adequate vehicle to study non-thermal processes in the universe, from the neighborhood of active nuclei at all scales to diffuse emissions in extended scenarios, such as galaxies and supernova remnants.

Systems that are able to produce energetic γ-rays are in general also producing photons at lower frequencies. Note that the converse is not true; e.g., thermal radiation can be emitted in narrow bands. This fact makes of γ-ray astronomy essentially a multi-frequency enterprize where most advanced models need to give account of observations from radio to TeV γ-rays. This kind of multi-frequency modeling and the required checks with observations, particularly for the case of regions of star formation within our Galaxy and beyond, constitutes the purpose of this study. In fact, not only photon astronomy is involved. When non-thermal sources are powerful enough to produce significant fluxes of γ-rays through interactions among hadrons (cosmic rays, nuclei), neutrinos are expected to be emitted at a similar flux level. Neutrino and γ-ray astronomy are indeed converging in what refers to the achieved sensitivity and angular resolution of their equipments and it is intrinsic to current high energy astrophysics that one will learn and feedback from the other. Moreover, both γ-rays and neutrinos freely propagate in space, without deflecting in the interstellar and intergalactic magnetic fields, and thus trace back to their original source. This is in fact the major advantage of neutrino and γ-ray astronomy in front of cosmic ray astronomy. Charged cosmic rays are indeed much more abundant but only those with the highest energy arrive to the Earth without being substantially deflected, and even in that cases, it is hardly possible to correlate the observed flux of particles with a concrete region in the sky. All in all, having yet not sufficiently large collection areas in the existing neutrino detectors so as to compensate the extremely low cross-sections with which neutrinos interact with matter, γ-ray astronomy is presently the only viable technique to deeply study high energy phenomena in selected astrophysical objects, i.e.,

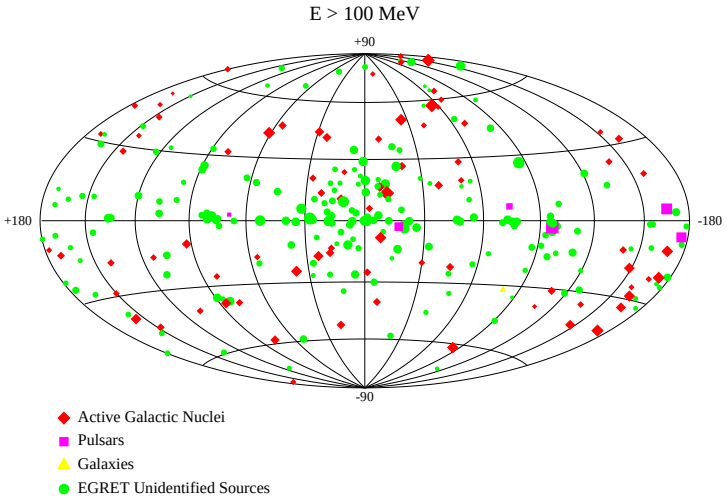

Figure 1.1: The EGRET point-like sources γ-ray sky. About 170 significant signals are still unidentified sources.

controlling directionality.

Before embarking in the description of the particular issues that will be treated along this Thesis, next Sections present a brief account of the main historical milestones of instrumental γ-ray astronomy. The evolution of the field through the last twenty years, as well as the prospects for future achievements during the following ten, is volcanic. High-energy astrophysics, currently fully immersed into the larger framework provided by astroparticle physics, is an observationally-driven science.

1.1 The experimental status at GeV energies

The first firm detection of cosmic high-energy γ-rays was achieved using the Orbiting Solar Observatory (OSO-3, whose last transmission occurred on November 1969), when it was discovered that the plane of the Galaxy was a source of photons with energy above 70 MeV. Higher spatial resolution studies made with the SAS-2 satellite, launched in 1972, revealed an individual source of γ-rays in the Vela pulsar, and confirmed the high-energy emission from the Crab Nebula. Finally, the long life of ESA's COS-B satellite (1975-1982) produced a major breakthrough: for the first time a significant number of sources were seen which could not be identified with objects known at other wavelengths (e.g., Bignami & Hermsen 1983). The difficult problem of understanding γ-ray sources, and particularly those that are unidentified, would last and worsen since. The successor of COS-B was the Compton Gamma-ray Satellite, which carried a set of powerful γ-ray instruments covering the energy band from photons with tens of MeV to GeV. Figure 1.1 shows the last Energetic γ-ray Telescope (EGRET) all-sky map and the sources reported in its final catalog (e.g., Hartman et al. 1999). The Third EGRET Catalog contains 271 detections with high significance, including 5 pulsars, 1 solar flare, about 70 plausible blazar identifications, 1 radio galaxy (Cen A), 1 normal galaxy (LMC), and around 170 yet unidentified sources ($\sim 2/3$ of all detections), marked as green dots in the Figure.

A forthcoming European mission is entirely dedicated to high-energy astrophysics. AGILE (acronym for Astro-rivelatore Gamma a Immagini LEggero), whose expected

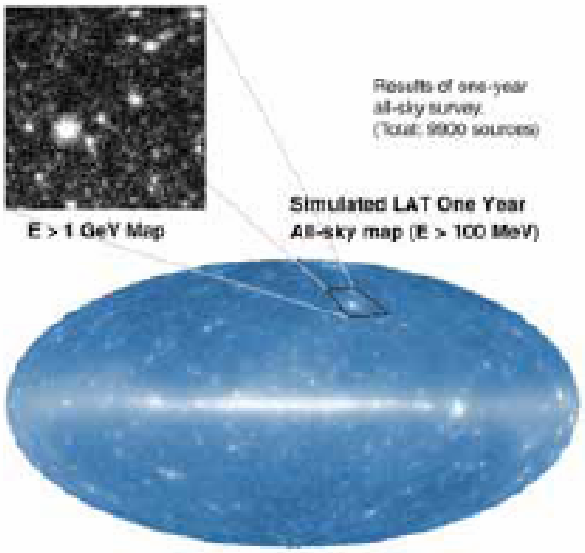

Figure 1.2: Simulated predictions of the one-year all-sky survey of the LAT experiment.

launch date is within the next two years, has three instruments, which will cover the energy range from tens of KeV to 50 GeV, being the first satellite that will produce simultaneous detections in the X-ray and γ-ray band. AGILE point source sensitivity is comparable to that of EGRET for on-axis sources and substantially better for off-axis sources, but will have a much larger field of view coverage at energies above 30 MeV ($\sim$ 1/5 of the entire sky), to improve background subtraction.

GLAST is a DOE/NASA mission to be launched in September 2007. It will explore the energy range from 30 MeV to 100 GeV with 10% energy resolution between 100 MeV and 10 GeV. The LAT (acronym for Large Area Telescope, the main instruments onboard GLAST) has a field of view about twice as wide (more than 2.5 steradians), and sensitivity at least about 50 times as large, as that of EGRET at 100 MeV, a comparison that improves at higher energies. GLAST will be able to locate sources to positional accuracies from 30 arc seconds to 5 arc minutes, given a much better point spread function, what would allow better searches of counterparts at other frequencies. Figure 1.2 is the simulated GLAST sky after 1 year of survey: several thousand sources are expected to be detected with unprecedented resolution. The LAT instrument onboard GLAST is such that just after 1 day of observations it will detect the weakest of the EGRET sources with 5 σ confidence level. And after 1 week of observations, GLAST will have reached the same sensitivity and coverage than the whole decade of earlier EGRET operations. With a nominal lifetime of five years, and an expected of ten, GLAST will change the perspective of astrophysics in the GeV energy domain in the early 21st century.

1.2 The experimental status at TeV energies

One of the last challenges of γ-ray astronomy is the distribution of the sources of GeV and TeV photons. Contrary to the lowest energy γ-ray band, photons in this band can be detected using ground-based detectors. To date, almost all the observational results

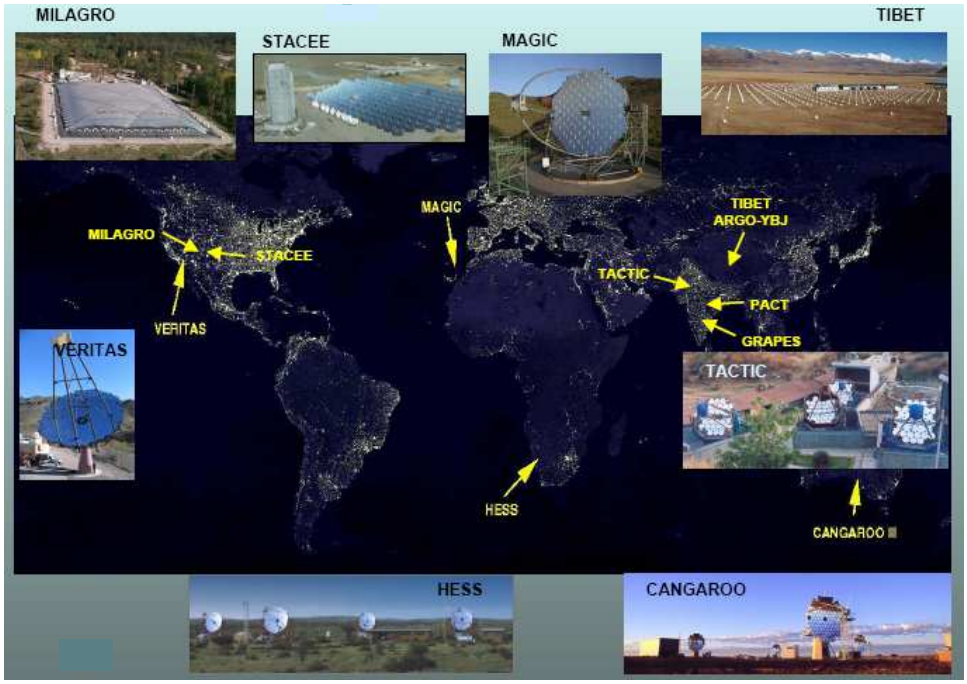

Figure 1.3: Current ground-based experiments operating in the high energy γ-ray domain.

in the energy interval from 100 GeV to 100 TeV have come from observations using the so-called Imaging Atmospheric Cherenkov Technique (IACT). Although considerable effort has been applied to the development of alternative techniques (solar arrays like STACEE (Hanna et al. 2002), air-shower particle detectors like MILAGRO (Atkins et al. 2000), etc.), they are not yet competitive.

The window of ground-based γ-ray astronomy was opened in 1989 by the observation of a strong signal from the first TeV γ-ray source, the Crab Nebula, by the Whipple collaboration. The instrument used was the 10 m diameter Whipple Imaging Atmospheric Cherenkov telescope on Mount Hopkins in Arizona. The breakthrough in the technique was achieved by means of the image parameterization suggested by Hillas (Hillas 1985) allowing separation between the rare γ-ray showers and the background from showers induced by charged cosmic rays, which is orders of magnitude more intense. Since then, increasing progress has been made. The old generation of IACTs operating in the 1990s, Whipple, the HEGRA array and CAT, had an energy threshold of several hundreds GeV to several TeV. The turn of the century has brought a new generation of telescopes and arrays of telescopes which are equipped with larger dishes that bring the energy threshold down to $\sim$100 GeV.

The first such instrument was the HESS array (Hinton 2004) of four 12 m diameter telescopes in Namibia. HESS started operation in 2003 and has an energy threshold of about 200 GeV with an unprecedented 5σ flux sensitivity around 0.5% crab for a 50 hour observation. Its angular resolution, around 0.07°, and wide field of view turn it into an excellent instrument for sky scans.

The 17 m diameter single MAGIC Telescope (Albert et al. 2005a) was commissioned one year later in La Palma, Spain. MAGIC is the lowest energy threshold IACT in the world. It combines a huge ultralight reflector with a large number of technical innovations. The camera has a total field of view of about 3.5°. The design of the telescope was

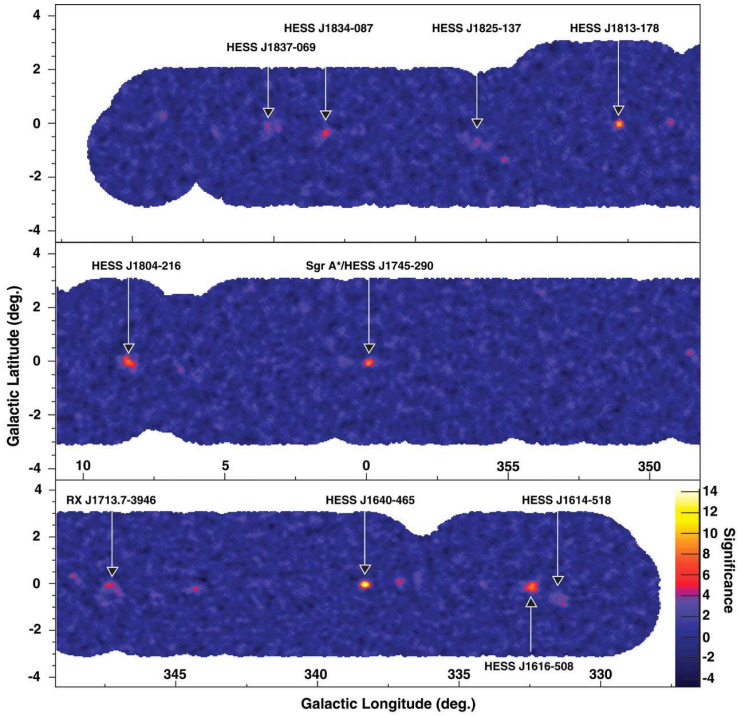

Figure 1.4: Significance map of the H.E.S.S. 2004 Galactic plane scan. 8 high significant sources have been detected. From Aharonian et al. (2005e).

optimized for fast repositioning with an eye to perform follow-ups of the prompt emission of Gamma-Ray Bursts (GRBs).

Two more telescope systems are well on their way. The VERITAS array (Holder et al. 2005) in Kitt Peak, US, and an upgrade of the existing CANGAROO array (Kawachi et al. 2001) in Australia. Both HESS and MAGIC have recently announced plans for an extension. HESS is to build a gigantic 28 m diameter single telescope at the center of the existing array and MAGIC is already installing a second 17 m telescope to be operated in coincidence with the first one. It will be commissioned in 2007. Figure 1.3 depicts the main ground-based γ-ray experiments nowadays operating world-wide.

After the Crab Nebula was established as the standard candle at very high energies (VHE) by Whipple, several years elapsed until the discovery of a second source. Mrk 421, an Active Galactic Nucleus (AGN) was claimed in 1994 again by the Whipple collaboration, that subsequently discovered a second AGN also of the BL Lac type, Mrk 501. The progress was slow during the 1990s. By 2003 the number of confirmed VHE sources had crept up to 12. Thanks to the new generation of IACTs the GeV-TeV astronomy has gone through a phase transition during the last two years. The number of sources has almost tripled.

HESS has performed a 112 hour scan (Aharonian et al. 2005e) of the galactic plane in the range of galactic longitude [-30, 30] and $\pm 3^\circ$ latitude. Eight new sources were detected above 6σ (see Figure 1.4) and seven tentative ones above 4σ have been recently released. Four of the eight high significance sources are potentially associated with supernova remnants (SNRs) and two with EGRET sources. In three cases they could be associated with pulsar wind nebulae (PWN). In one case the source has no counterpart at other wavelengths. Along with two other unidentified sources in this energy band, this suggests

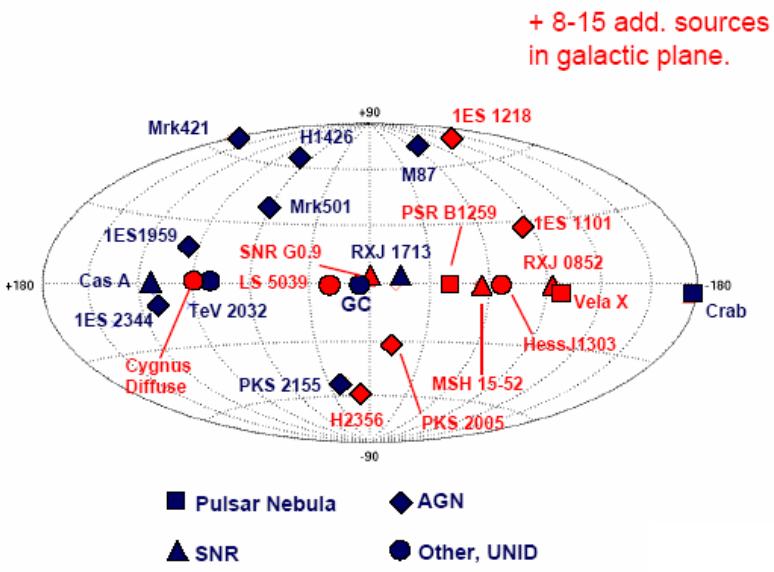

Figure 1.5: The Very High Energy γ-ray sky in 2005. Not shown are 8 more sources discovered by HESS in a survey of the galactic plane. Red symbols indicate the most recent detections, brought during 2004 and 2005 by the last generation of IACTs: HESS and MAGIC. From Ong (2005).

the possibility of a new class of 'dark' particle accelerators in our galaxy. Two of the objects in the scan have been recently confirmed by MAGIC (Albert et al. 2005b).

Figure 1.5 shows how the number of detected sources in the TeV energy domain has increased in the last two years as soon as the last generation of ground-based Čerenkov telescopes have started operating. The most recent catalogue of sources claims 32 sources, including 6 unidentified objects. There are now two consolidated populations of galactic VHE emitters (PWN and SNRs). The VHE catalogue lists six PWN, six SNRs, one binary pulsar, one microquasar, a region of diffuse emission and eleven AGNs. In the last months MAGIC and HESS have detected several new AGNs with redshifts up to 0.19, at distances almost a factor 10 larger than the two first ones detected at TeV energies.

1.3 This thesis

Is the aim of this Thesis to focus on one of the multiple astrophysical targets of γ-ray astronomy: the sites of star formation. These extremely active regions are prone of some of the most violent astrophysics phenomena, and thus have been proposed as one of the possible sites for the production of the high energy cosmic rays. However, not many detailed models nor deep high-energy γ-ray observations have yet been devoted to these interesting regions. Is in the better understanding of these regions that this study intends to contribute.

The work herein presented is divided in three parts. In the first one, a theoretical and phenomenological approach to both galactic and extragalactic star forming regions is sketched: Chapter 2 investigates the plausibility for the powerful starburst galaxies and ultra-luminous infrared galaxies to appear as a new population of γ-ray sources; Chapter

3 presents a detailed modeling of the γ-ray emission from the two best candidates from the known extragalactic sites of star formation, looking at them from a multi-wavelength approach; and finally, Chapter 4 proposes that galactic stellar OB associations are possibly detectable TeV γ-ray sources by the current Čerenkov telescopes, without having strong emission at lower γ-ray energies. The second part of the Thesis starts in Chapter 5, summarizing the fundamentals of the Čerenkov technique for γ-ray astronomy and the main characteristics of the MAGIC Telescope; and ends with a description of the analysis applied for the reduction of MAGIC data in Chapter 6. To conclude, the third part reviews the results of the analysis of the first MAGIC observations of star forming regions. Chapter 7 provides the reference analysis of the Crab Nebula data, Chapter 8 presents the upper limits imposed from MAGIC observations to the γ-ray flux of the ultra-luminous infrared galaxy Arp 220, and Chapter 9 reports on the results of the MAGIC observations of the unidentified TeV J2032+4130 source detected by the HEGRA array in the Cygnus region. Finally, Chapter 10 gives some final concluding remarks.

This thesis represents the author's effort to understand a little more about high energy astrophysics in regions of star formation. This effort was threefold. On one hand, technical: participating in the tasks and developments to bring a new Imaging Air Čerenkov Telescope (MAGIC) to work. On the other, theoretical: in order to study what γ-ray output to expect from these regions based on the most detailed possible theoretical models. And finally, observational: in order to begin the long and yet unfinished path to thoroughly test the former predictions. It is here hoped that some of these lines of research will be inspire new developments.

Part I

Theory and phenomenology of regions of star formation

Chapter 2

Extragalactic sites of star formation: Phenomenology

Regions prone to have a strong process of star formation are good candidates to be intense γ-ray emitters. Out from the Milky Way, the more powerful sites of star formation are very active galaxies such as starbursts (SGs) and Luminous or Ultra-Luminous Infrared Galaxies (LIRGs or ULIRGs). This Chapter analyzes the plausibility for these extragalactic sites of star formation to appear as a new population of γ-ray sources for the new generation of γ-ray experiments, both ground and space-based. This Chapter is partially based on the paper by Torres, Reimer, Domingo-Santamaría & Digel (2004).

2.1 Diffuse γ-ray emission from galaxies

The diffuse γ-ray emission observed from a galaxy basically consists of three components: the emission from the galactic interstellar medium (ISM) itself, the radiation coming from the extragalactic background, and the contribution of unresolved and faint point-like sources, which may belong to the same galaxy or be beyond it but in the same line-of-sight by chance. The galactic diffuse emission generated in interactions with the ISM has a wide energy distribution and normally dominates the other components. γ-rays are produced in energetic interactions of particles with the interstellar gas and the radiation fields present in the galaxy. The diffuse high energy γ-ray emission mainly comes from the interaction of high energy cosmic ray nucleons with gas nuclei, via neutral pion production. Contributions from energetic cosmic ray electrons interacting with the existing photon field via inverse Compton scattering and with the matter field of the galaxy via relativistic bremsstrahlung are generally more important below 70 MeV. Since these processes dominate in different parts of the spectrum, information about the overall spectrum of the cosmic ray population can be extracted. If γ-rays absorption in the galaxy is neglected, the diffuse γ-ray flux can be estimated as the line-of-sight integral over the emissivity of the ISM. The latter is essentially the product of the cosmic ray spectrum, the density of the gas or radiation field in the galaxy, and the corresponding cross section for a given process. Therefore, γ-ray measurements together with estimations of the gas content and photon field densities provide a tool to determine the cosmic rays spectrum.

The interstellar hydrogen distribution (in its molecular form, H_2, atomic, or ionized, HI or HII) is basically derived from radio surveys. It can be traced from the emission lines of molecules that get radiatively or collisionally excited, by means of corresponding

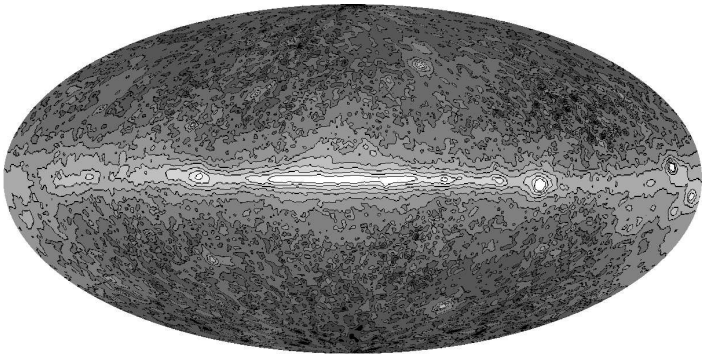

Figure 2.1: Intensity of γ-rays ($>$ 100 MeV) observed by EGRET. The broad, intense band near the equator is interstellar diffuse emission from the Milky Way. The intensity scale ranges from 1×10^{-5} cm^{-2} s^{-1} sr^{-1} to 5×10^{-4} cm^{-2} s^{-1} sr^{-1} in ten logarithmic steps. The data is slightly smoothed by convolution with a gaussian of FWHM 1.5°.

calibrations or conversion factors. CO molecules are generally the primary tracers of molecular hydrogen. CO is a polar molecule with strong dipole rotational emission at millimeter-wavelengths. H_2, though much more abundant than CO, has only a weak quadrupole signature. Generally, the conversion factor between the CO luminosity and molecular mass is estimated and constrained from measurements in our own Galaxy. Masses of individual Galactic molecular clouds can be independently determined from cloud dynamics and then be related to the cloud CO luminosity (Solomon et al. 1987; Young & Scoville 1991). Alternatively, assuming the spectrum of cosmic rays of the Galaxy and a given γ-ray flux, it is possible to obtain a calibration for the CO luminosity to estimate the conversion factor (e.g., Bloemen et al. 1986). The atomic neutral hydrogen content can be estimated trough the intensity of 21-cm emission line. HCN, CS and HCO^+ are the most frequently observed interstellar molecules after CO. Due to their higher dipole moment ($\mu_0 \sim 2.0$ – 3.0 debyes), they require about two orders of magnitude higher gas densities for collisional excitation than CO ($\mu_0 \sim 0.1$ debyes). HCN is one of the most abundant high dipole moment molecules and traces molecular gas at densities $n(H_2) \gtrsim 3 \times 10^4$ cm^{-3}, compared to densities of about $\gtrsim 500$ cm^{-3} traced by CO. Because of this fact, dense regions associated with star formation sites are usually better traced at the higher HCN frequencies.

2.1.1 Diffuse γ-ray emission from the Galaxy

Studies of the Galactic diffuse γ-ray emission provide privileged insights into the generation processes of γ-rays in galactic environments. The diffuse γ-ray continuum emission is in fact the dominant feature of the γ-ray sky of the Milky Way (see the EGRET γ-ray map above 100 MeV presented in Figure 2.1), approximately amounting 90% of the high energy γ-ray luminosity ($\sim 1.3 \times 10^6$ L$_\odot$, Strong, Moskalenko, & Reimer 2000). This emission, in the range of 50 KeV to 50 GeV, was systematically studied by all hard X-ray/γ-ray satellites, from SAS-2 and COS-B in the 70's and early 80's, to OSSE, COMPTEL and EGRET experiments onboard of the Compton Gamma-Ray Observatory (CGRO),

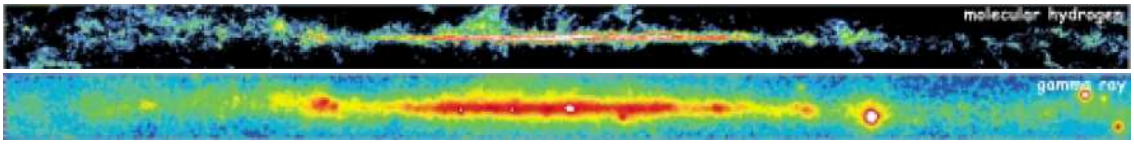

Figure 2.2: The Milky Way in molecular material and γ-rays. An obvious correlation favors the idea of a diffuse generation of high energy radiation.

launched in 1990, as well as, more recently, by INTEGRAL. Hunter et al. (1997) present a review of CGRO observations. Figure 2.2 shows a comparison between the maps of the Milky Way in molecular material and γ-rays. An obvious correlation favors the idea of a diffuse generation of high energy radiation.

First detailed analysis of the diffuse emission from the Galactic plane, assuming a cosmic ray spectrum as in the solar vicinity, revealed an excess of the measured EGRET spectrum, with respect to the expected flux, above 1 GeV (see Figure 2.3). The so-called "GeV excess" has led to an attempt of optimizing γ-ray emission models. One of the discussed options to explain the discrepancy is that the local cosmic ray particle spectra may not be representative of the Galactic average. Spatial inhomogeneity of sources and propagation effects can change the spectrum of the accelerated particles. A harder Galactic nucleon spectrum has been suggested as a possible solution (Mori 1997), requiring a proton power-law index of about 2.4 – 2.5. Also flatter electron spectrum has been proposed, being the γ-ray excess explained in this case in terms of inverse Compton emission. Very recently, Kamae et al. (2005) have presented a calculation of the neutral pion production cross section from pp interactions, including diffractive pp collisions and scaling violation effects as well as the non-diffractive contribution (see Appendix B for more details).[1] The diffractive process makes the γ-ray spectrum harder than the incident proton spectrum by ~ 0.05 in power-law index, and the scaling violation produces 30 – 80% more neutral pions than the scaling model for proton energies above 100 GeV. A combination of both improvements in the pp cross section description can explain part of the GeV excess with the local cosmic proton spectrum (slope ~ 2.7), but just about a half of the excess flux. The detection of diffuse γ-ray emission from other galaxies but ours could be a good opportunity to obtain new hints about this problem: If the origin of the Galactic GeV bump is intrinsic to an exclusive characteristic of the Milky Way, the excess is not expected to appear in the γ-ray spectrum of other galaxies. But, should spectral resolution and sensitivity be large enough as for such a similar excess to be observed elsewhere, it would provide an indication of a more universal origin. Current models describing diffuse γ-ray emission would need reformulation, perhaps in a fundamental way.

2.1.2 Detection (and non-detection) of other local group galaxies

To date, the Large Magellanic Cloud (LMC) is the only external galaxy that has been detected in the light of its diffuse γ-ray emission (Sreekumar et al. 1992). This fact is explained by the isotropic flux dilution by distance. At 1 Mpc, for example, the flux of the Milky Way would approximately be 2.5 $\times 10^{-8}$ photons cm^{-2} s^{-1} above 100 MeV, well below the sensitivity achieved up to now by the γ-ray missions in the relevant energy

[1] See Appendix B, Section B.2.1 for definitions too.

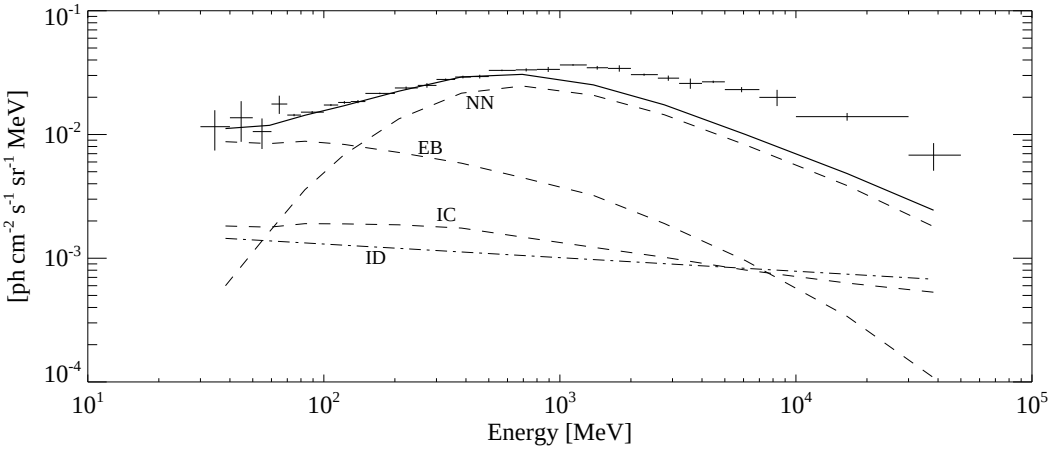

Figure 2.3: Spectrum of the inner Milky Way ($|l| < 60°$, $|b| < 10°$) with calculated components from bremsstrahlung (EB), inverse Compton (IC), neutral pion decay (NN), and extragalactic isotropic emission (ID).

domain. Although normal or even galaxies with fairly intense star formation such as the LMC are quite numerous, their distances ought to make them very faint γ-ray sources.

The LMC was detected by EGRET with a flux of $(1.9\pm0.4) \times 10^{-7}$ photons cm^{-2} s^{-1} above 100 MeV (see Figure 2.4). Interestingly, as can be noticed in Figure 2.4, the distribution of the diffuse γ-ray emission from the LMC is consistent with the infrared IRAS map profile, being the more intense γ-ray emission region in spatial coincidence with the position of 30 Doradus, a particular region of the LMC with large molecular clouds and extensive ongoing star formation. This correspondence is indeed the reason why the EGRET team claimed the detection of the LMC. This result had been predicted by Fichtel et al. (1991) as the output of pion decay resulting from the interaction between cosmic ray protons and interstellar gas, assuming galactic dynamic balance between the expansive pressures of the cosmic rays, magnetic fields and kinematic motions, and the gravitational attraction of matter.

It is instructive to show how to obtain the predicted flux. One can consider that the electron spectrum is a power-law $N(E)dE = KE^{-\gamma}dE$, with $N(E)$ being the number of electrons per unit energy per unit volume, and K the spectrum normalization. The intensity of the synchrotron radiation in the presence of random magnetic fields is

$$I_\nu = 1.35\times10^{-22} a(\gamma) L\, K\, B^{(\gamma+1)/2} \times \left(\frac{6.26\times10^{18}}{\nu}\right)^{(\gamma-1)/2} \text{erg cm}^{-2}\ \text{s}^{-1}\ \text{sr}^{-1}\ \text{Hz}^{-1}, \quad (2.1)$$

(Ginzburg & Syrovatskii 1964) where ν is the observing radio frequency in Hz, $a(\gamma)$ is a numerical coefficient of order 0.1, L is the length over which the electrons and magnetic fields are present and B is the magnetic field strength. The normalization of the spectrum is assumed proportional to B^2 both in the LMC and our Galaxy, and the shape of the spectrum in the LMC is assumed the same as that in the Milky Way. Then, if K_0 and B_0 are the corresponding values of these parameters in our Galaxy, and $w(x)K_0$ is the value in the LMC, $B = w(x)^{1/2}B_0$. Using this expression in Equation (2.1) the scaling can be determined as

$$w(x) = \left(\frac{2.40 I_\nu}{a(\gamma) L_{21} K_0}\right)^{4/\gamma+5} B_0^{-2(\gamma+1)/(\gamma+5)} \left(\frac{\nu}{6.26\times10^{18}}\right)^{2(\gamma+1)/(\gamma+5)}, \quad (2.2)$$

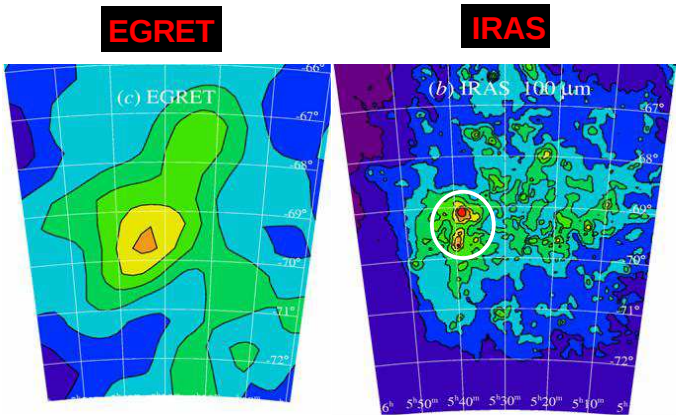

Figure 2.4: LMC as seen by EGRET (γ-rays) and IRAS (infrared). White circle indicates the position of 30 Doradus, a large molecular cloud and intense star formation region. By courtesy of Seth Digel.

where $L_{21} = L/(3.09 \times 10^{21}\mathrm{cm})$ is the distance in kpc. Assuming best guesses for all parameters involved (see, for instance, the Appendix of Fichtel et al. 1991), the electron normalization can be determined. The additional assumption that the electron-to-proton ratio is the same in the LMC as in the Galaxy yields the proton spectrum. An estimation of the matter column density then allows the γ-ray flux to be computed as:

$$F(E > 100\mathrm{MeV}) \simeq \int d\Omega \left[2 \times 10^{-25} \times \frac{w(x)}{4\pi} \times \int dl (n_a + n_m) \right] \frac{1}{4\pi d^2} \quad \text{photons s}^{-1}\ \text{cm}^{-2}, \quad (2.3)$$

with $d\Omega$ being the solid angle subtended by the emitting region, $j_\gamma = 2 \times 10^{-25} \times w(x)/4\pi$ photons s^{-1} sr^{-1} H-atom^{-1} being the γ-ray production, and $\int dl(n_a+n_m)$, with n_a and n_m the atomic and molecular density, respectively, being the column density. Note that the prediction allows different emission level contours to be plotted, depending on the position in the galaxy. However, in order to make a direct comparison with EGRET or any other experiment, the predicted γ-ray intensity has to be compared with the corresponding point-spread function. Although the predicted intensity based on the dynamic balance is in good agreement with the EGRET result, it is also in agreement with the cosmic ray density being the same throughout the galaxy, as if, for instance, the cosmic ray density were universal in origin (as proposed, for instance, by Brecher and Burbidge 1972).

The Small Magellanic Cloud (SMC) was also observed by EGRET, but no detection was found. An upper limit of 0.5×10^{-7} photons cm^{-2} s^{-1} was set for the γ-ray emission above 100 MeV (Sreekumar et al. 1993). If the cosmic ray density in the SMC were as high as it is in our Galaxy, the flux in γ-rays would be $\sim 2.4 \times 10^{-7}$ photons cm^{-2} s^{-1}, a level incompatible with the experimental result. It was then the non-detection of the SMC what defined that the distribution of cosmic rays is galactic in origin, local to accelerators, and not universal.

Very recently, Pavlidou and Fields (2001) presented an observability study for several of the local group galaxies, assuming that the γ-ray flux above 100 MeV is represented

by

$$F(E > 100\mathrm{MeV}) = 2.3 \times 10^{-8} f_G \left(\frac{\Sigma}{10^4 \mathrm{M}_\odot \mathrm{kpc}^{-2}} \right) \mathrm{photons\,cm^{-2}\,s^{-1}}, \qquad (2.4)$$

with f_g being the ratio between the supernova rates of the galaxy G and the Milky Way, and Σ being the gas mass-to-distance squared ratio. This amounts to the assumption that supernova remnants alone are the source of cosmic rays, and that once produced, their propagation is described by a leaky box model, with the additional supposition of an equal time/length of escape to that of our Galaxy. This approach is far simpler than that followed by Fichtel, Sreekumar and coworkers when analyzing the LMC and SMC cases, and probably not quite correct, especially for those galaxies which are different from ours, like the SMC. [2] For example, the Andromeda galaxy M31, a case studied previously by Özel and Berkhuijsen (1987), would present a flux of 1×10^{-8} photons cm^{-2} s^{-1}, consistent with the observational upper limit set by Blom et al. (1999) using more recent EGRET data. This flux could be detected by GLAST in the first 2 years of its all-sky survey with 14σ significance. If such is the case, it will be possible to study the correlation between regions of higher column density and higher γ-ray emission. It could even be possible to observe effects of the magnetic torus (e.g., Beck et al. 1996) and the star forming ring (e.g., Pagani et al. 1999), a morphological feature analogous to the Milky Way's H_2 ring extending in radius from 4 to 8 kpc (e.g., Bronfman et al. 1988), which has been detected in γ-ray surveys (Stecker et al. 1975). Other results for Local Group Galaxies show that, unless the assumptions are severely misrepresenting the physics, only M33 might have some chance of being detected by future instruments (Digel et al. 2000).

2.2 Galaxies with higher star formation rate

Galaxies where star formation is a powerful active process may be able to compensate the dilution effect that their diffuse γ-ray flux suffers because of their relatively larger distance to Earth. The large masses of dense interstellar gas and the enhanced densities of supernova remnants and massive young stars expected to be present in such galaxies suggest them to emit γ-ray luminosities orders of magnitude greater than normal galaxies. Such environments will typically emit large amount of infrared (IR) radiation, because abundant dust molecules absorb the UV photons emitted by the numerous young massive stars and remit them as IR radiation. Therefore, the infrared luminosity, L_{IR}, of a galaxy can (but not always) be an indication of star formation taking place in it.

Luminous infrared galaxies (LIRGs) have been identified as a class, generally selected for emitting more energy in the IR band ($\sim 50 - 500$ μm) than in all other wavelengths combined. The most luminous galaxies in the IR band constitute by themselves a subclass of the more powerful galaxies ever known. LIRGs are defined as galaxies with IR luminosities larger than $10^{11} L_\odot$. Those with $L_{\mathrm{IR}} > 10^{12} L_\odot$ are called ultraluminous infrared galaxies (ULIRGs). See Sanders & Mirabel (1996) for an extensive review about these objects. LIRGs are the dominant population of extragalactic objects in the local universe ($z < 0.3$) at bolometric luminosities above $L > 10^{11}$ $\mathrm{L}_\odot$, ULIRGs are in fact the

[2] Using the same approach, Pavlidou and Fields (2002) have presented a computation of the contribution to the γ-ray background produced by cosmic-ray interactions with diffuse gas of normal galaxies. They found that a multi-component fit (e.g., blazars + normal galaxies) of the extragalactic γ-ray background emission is better than the one obtained with unresolved active nuclei alone.

most luminous local objects. Our current understanding of LIRGs and ULIRGs suggests that they are recent galaxy mergers in which much of the gas of the colliding objects, particularly that located at distances less than $\sim$ 5 kpc from each of the pre-merger nuclei, has fallen into a common center (typically less than 1 kpc in extent), triggering a huge starburst (e.g., Sanders et al. 1988, Melnick & Mirabel 1990). The size of the inner regions of ULIRGs, where most of the gas is found, can be even as small as a few hundreds parsecs; there, an extreme molecular environment is found. This large nuclear concentration of molecular gas has been detected in the millimeter lines of CO by many groups, and estimates of molecular mass and density have been made. Not surprisingly, these estimates were found to be orders of magnitude larger than the corresponding values found in our Galaxy. However, using Milky Way molecular clouds to calibrate the conversion factor between CO luminosity and gas mass soon led to the paradox that most, if not all, of the dynamical mass of ULIRGs was gas (e.g., for Arp 220, see Scoville et al. 1991). In some extreme cases, the derived gas mass exceeded the dynamical mass estimation, which unambiguously showed caveats in the assumptions. Downes et al. (1993) showed that in the central regions of ULIRGs, much of the CO luminosity comes from an intercloud medium that fills the whole volume, rather than from clouds bound by self gravity. Hence, the CO luminosity of ULIRGs traces the geometric mean of the gas and the dynamical mass, rather than just the gas. The Milky Way conversion factor, being relevant for an ensemble of giant molecular clouds (GMCs) in an ordinary spiral galaxy, seems to overestimate the gas mass of ULIRGs. Solomon et al. (1997), Downes & Solomon (1998), Bryant & Scoville (1999), and Yao et al. (2003) have argued for that and conversion factors between gas mass and CO luminosities $\sim$ 3–5 times smaller than that of the Milky Way were proposed for ULIRGs. However, even with such corrections, the amount of molecular gas in ULIRGs is very large, typically reaching 10^{10} $M_{\odot}$.

A high level of IR emission does not univocally imply the presence of high star formation in a galaxy. The IR luminosity can be simply generated through the dust remission of the UV photon field emitted by an enshrouded active galactic nuclei (AGN). In some cases, as in Arp 299, a hidden AGN was observed, but it cannot account for the whole FIR luminosity (Della Cecca et al. 2002). Supporting the idea that IR luminosities in LIRGs are mainly due to starburst regions rather than to enshrouded AGNs it is the fact that LIRGs not only possess a large amount of molecular gas, but a large fraction of it is at high density (e.g., Gao & Solomon 2003a, 2003b). This makes them prone to star formation, and thus to have significant CR enhancements. In addition, there is evidence for the existence of extreme starbursts regions within LIRGs (see, e.g., Downes & Solomon 1998). These, larger than GMCs but with densities found only in small cloud cores, appear to be the most outstanding star-forming regions in the local universe (each representing about 1000 times as many OB stars as 30 Doradus). They are well traced by HCN emission, i.e., they represent a substantial fraction of the whole HCN emission observed for the whole galaxy (Downes & Solomon 1998, Solomon et al. 1992). The CR enhancement factor in these small but massive regions can well exceed the average value for the galaxy.

However, to date no LIRGs or ULIRGs, nor any other starburst galaxy has been detected in γ-rays by EGRET, upper limits were imposed for M82, $F(E > 100\mathrm{MeV}) < 4.4 \times 10^{-8}$ photons cm^{-2} s^{-1}, and NGC 253, $F(E > 100\mathrm{MeV}) < 3.4 \times 10^{-8}$ photons cm^{-2} s^{-1} (Blom et al. 1999), the two nearest starbursts. Similar constraints were found for many LIRGs by means of a search in existing EGRET data for the fluxes of likely γ-ray–bright LIRGs (Torres et. al. 2004, Cillis et al. 2005). The limits imposed in the

Table 2.1: EGRET upper limits (in units of 10^{-8} photons cm^{-2} s^{-1}) on nearby LIRGs that might be detected by next generation telescopes. D_L, the luminosity distance, the FIR luminosity, and the minimum value of cosmic ray enhancement that is needed for the galaxy to appear as a GLAST γ-ray source (see below) is given.

Name	D_L [Mpc]	$\log(L_{\rm FIR}/{\rm L}_\odot)$	$\log(M({\rm H}_2)/{\rm M}_\odot)$	$\langle k \rangle$	$F^{\rm EGRET}_{>100\,{\rm MeV}}$
NGC3079	15	10.52	9.56	62	<4.4
NGC1068	15	10.74	9.46	78	<3.6
NGC2146	20	10.78	9.43	149	<9.7
NGC4038/9	22	10.65	9.07	412	<3.7
NGC520	29	10.58	9.47	285	<4.6
IC694	41	11.41	9.59	432	<2.2
Zw049.057	52	10.95	9.67	578	<6.9
NGC1614	64	11.25	9.78	680	<5.0
NGC7469	65	11.26	9.89	544	<3.2
NGC828	72	11.03	10.09	421	<6.1
Arp220	72	11.91	10.43	193	<6.1
VV114	80	11.35	10.03	597	<3.9
Arp193	94	11.34	10.22	532	<5.2
NGC6240	98	11.52	10.03	896	<6.4
Mrk273	152	11.85	10.33	1081	<2.3
IRAS17208−0014	173	12.13	10.67	640	<7.5
VIIZw31	217	11.66	10.70	940	<3.2

work by Torres, Reimer, Domingo-Santamaría, and Digel (2004) are presented in Table 2.1. These upper limits are barely above the theoretical predictions of models for the diffuse γ-ray emission of some of these galaxies; models constructed with different levels of detail (see Torres 2004b for a review and the next Chapter for particular examples).

2.2.1 Plausibility estimation

Neglecting possible CR density gradients within the interstellar medium of the galaxy, the hadronically-generated γ-ray number luminosity (photons per unit of time) is given by:

$$I_\gamma(E_\gamma) = \int n(r) q_\gamma(E_\gamma) dV = \frac{M}{m_p} q_\gamma \,, \tag{2.5}$$

where r represents the position within the interaction region V, M is the mass of gas, m_p is the proton mass, n is the number density, and q_γ is the γ-ray emissivity (photons per unit of time per atom). The γ-ray flux is then:

$$F(>100\,{\rm MeV}) = \frac{I_\gamma(>100\,{\rm MeV})}{4\pi {D_L}^2} \,, \tag{2.6}$$

where D_L is the luminosity distance in a Friedman universe.[3] In an appropriate scaling, the γ-ray flux can be estimated from:

$$F(>100\ \mathrm{MeV}) \sim 2.4\times10^{-9}\left(\frac{M}{10^9\mathrm{M}_\odot}\right)\left(\frac{D_L}{\mathrm{Mpc}}\right)^{-2} k \quad \text{photons cm}^{-2}\text{s}^{-1}\,. \tag{2.8}$$

The previous estimation introduces k as the enhancement factor of γ-ray emissivity in the galaxy under study compared to the local value near the Earth. If the slope of the CR spectrum at the galaxy does not differ much from that existing near the Earth, k can be at the same time an estimator of the enhancement of CR energy density: $k \equiv q_\gamma/q_{\gamma,\oplus} \sim \omega/\omega_\oplus$, with $q_{\gamma,\oplus} = 2.4\times10^{-25}$ photons s^{-1} H-atom^{-1} being the γ-ray emissivity of the interestellar medium at the Earth neighbourhood, and $\omega_\oplus$ being the CR energy density near Earth. The numerical factor of Equation (2.8) already takes into account the γ-ray emissivity from electron bremsstrahlung (see, e.g., Pavlidou & Fields 2001 and references therein)[4]. Note that $F(>100$ MeV$) \sim 2.4\times10^{-9}$ photons cm^{-2}s^{-1} is approximately the GLAST satellite sensitivity after 1 yr of all-sky survey. Therefore, from Equation (2.8), having an estimation of the mass gas content of the galaxy through the measured CO luminosity, the minimum average value of k for which the γ-ray flux above 100 MeV will be at least 2.4 $\times10^{-9}$ photons cm^{-2} s^{-1} can be computed:

$$\langle k\rangle_{min} = \left(\frac{M_{H_2}}{10^9\mathrm{M}_\odot}\right)^{-1}\left(\frac{D_L}{\mathrm{Mpc}}\right)^{2}\,. \tag{2.9}$$

This approach represents a first step in order to establish the plausibility of the future detection of a given LIRG or SG in the γ-ray band.

A similar estimation can be made for the TeV flux expected from these objects. Völk et al. (1996) found:

$$F(>1\ \mathrm{TeV}) \sim 1.7\times10^{-13}\left(\frac{E}{\mathrm{TeV}}\right)^{-1.1}\left(\frac{M}{10^9\mathrm{M}_\odot}\right)\left(\frac{D_L}{\mathrm{Mpc}}\right)^{-2} k \quad \text{photons cm}^{-2}\text{s}^{-1}\,, \tag{2.10}$$

where a power law slope of 2.1 is assumed for the CR spectrum. For comparison, it is useful to keep in mind that an integrated flux above 1 TeV of about 1×10^{-13} photons cm^{-2} s^{-1} is the expected 5σ flux sensitivity for a 50 hr observation at small zenith angle

[3]The luminosity distance describes the distance at which an astronomical body would lie based on its observed luminosity. If a source of luminosity L emits into a non-expanding universe, the integral of the photon flux over a sphere of given radius will be equal to the source luminosity. In an expanding space-time, the photon wavelength is redshifted, diluting the energy over the sphere by a factor of $(1+z)$, where z is the redshift. Another factor $(1+z)$ is introduced as the emission rate of the photons from the source is time dilated with respect to an observer due to the Doppler effect. Therefore, the observed luminosity is attenuated by two factors: relativistic redshift and the Doppler shift of emission, each of them contributing a $(1+z)$ attenuation. The luminosity distance can be expressed in terms of the Hubble parameter, H_0, the deceleration parameter, q_0, and the redshift:

$$D_L = \frac{c}{H_0 q_0^2}\left[1 - q_0 + q_0 z + (q_0-1)\sqrt{2q_0 z + 1}\right]. \tag{2.7}$$

[4]Note that γ-rays can also be produced by inverse Compton interactions with the strong FIR field of the galaxy. However, this contribution has been disgarded in favor of the hadronic channel (between accelerated protons and diffuse material of density n), which is a well justified approach above 100 MeV (see below). Additional hadronic production of high energy γ-rays with matter in the winds of stars (see Chapter 4) is also disregarded. In any case, both these effects would improve the possibility for the galaxies to be detected.

of the new ground-based imaging atmospheric Čerenkov telescopes (IACTs). Then, those galaxies that might appear in the new GeV catalogs might also constitute new targets for the ground-based telescopes at higher energies, provided their proton spectrum are sufficiently hard.[5]

Once produced, photons can be assumed to escape the FIR-dominant field of the galaxy, as can be seen in detail using the $\gamma\gamma$ and γp pair-production cross sections (see Appendix C or Cox 1999, p.213ff, and next Chapter for a detailed proof) and typical LIRG parameters, e.g., the < 1 kpc-radius of the central starburst where the γ-ray emission proceeds. In addition, the small redshifts ($z < 0.05$) for the LIRGs considered here make negligible the values of opacities due to processes with photons of the CMB and IR-background (see, e.g., Stecker 1971, p.200ff), so that once they escape the galaxy they may reach Earth unscathed.

2.2.2 The HCN and the Pico Dos Dias surveys: looking for candidates

Gao & Solomon (2003a, 2003b) presented an HCN survey: a systematic observation of 53 IR-bright galaxies (essentially, all galaxies with strong CO and IR emission were chosen), including 20 LIRGs with $L_{\rm IR} > 10^{11}{\rm L}_\odot$, 7 with $L_{\rm IR} > 10^{12}{\rm L}_\odot$, and more than a dozen of the nearest normal spiral galaxies. The survey also includes a literature compilation of data for another dozen IR-bright objects. It is the largest and most sensitive HCN survey (and thus of dense interstellar mass) of galaxies to date. Table 1 in Gao and Solomon (2003b) lists all galaxies, providing, among other information, their luminosity distances[6] and the measured IR, CO and HCN luminosities.

The standard CO-to-H_2 conversion factor (e.g., Solomon and Barrett 1991) has been used to derive the molecular gas mass in galaxies from the observed CO luminosity:

$$M(H_2) = 4.78 \left(\frac{L_{CO}}{\rm K\ km\ s^{-1}\ pc^2} \right) \ M_\odot \, . \tag{2.11}$$

From Equation (2.9), having the estimated mass and taking those luminosities distances provided in the HCN survey, the minimum average value of the enhancement to provide a flux above GLAST sensitivity, has been computed. Results are plotted in Figure 2.5 left panel, together with the luminosity distance distribution of the galaxies (shown in the inset). See also Table 2.1.

Naively, the smaller the value of $\langle k \rangle$, the greater the possibility for these galaxies to appear as γ-ray sources. All but three objects in the HCN survey require a value $\langle k \rangle < 10^3$ to be above the GLAST satellite sensitivity. A typical case for a plausible new GLAST source would be a LIRG with $L_{\rm IR} \sim 10^{11}{\rm L}_\odot$, $D_L \sim 10 - 100$ Mpc, $M({\rm H}_2) \sim 10^{10}{\rm M}_\odot$, and an enhancement of the order of 100. This enhancement is an average value over the innermost central starburst region, where most of the CO and HCN luminosity is observed (see, e.g., Taniguchi & Ohyama 1998, Gao & Solomon 2003a, 2003b), i.e., it considers that all molecular mass in that region is illuminated by the enhanced CR spectrum. It is reasonable to expect local variations from the average k, particularly if extreme starbursts

[5] In addition, the signal-to-noise ratio in neutrino telescopes (neutrinos will be unavoidably produced in hadronic interactions leading to charged pions, as discussed in Appendix C) can be approximately computed starting from the γ-ray flux (see, e.g., Anchordoqui et al. 2003b). LIRGs could be new candidate sources for ICECUBE if they are detectable sources of TeV photons.

[6] Gao and Solomon assumed a Hubble parameter of H_0=75 km s^{-1} Mpc^{-1} for the luminosity distances estimation (see footnote 3). However, since galaxies under study have low enough redshifts, changes in the cosmological model do not introduce significant differences.

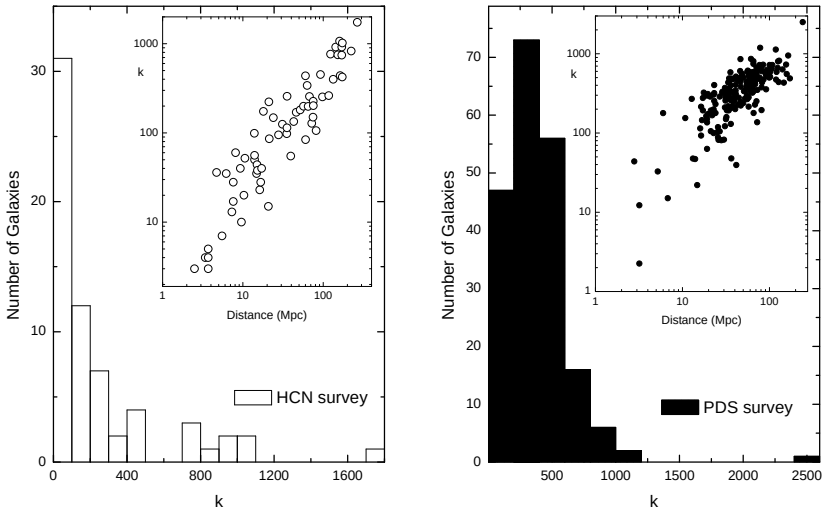

Figure 2.5: Distribution of luminosity distances (insets) and minimum average CR enhancements needed for galaxies in the HCN (left) and Pico Dos Dias (right) surveys to appear as γ-ray sources for GLAST and the new ground based Čerenkov telescopes.

regions are separate from the core, but yet it is a useful criterion for an observability study (Völk et al. 1996).

It is worth mentioning that the correlation between the molecular gas mass content and the CO luminosity have been proven to be good over a wide range of bolometric luminosities. However, as already mentioned at the beginning of this Chapter, several authors presented the case for a reduction in the CO-to-H_2 conversion factor when applied to powerful starburst regions, particularly those with $L_{\rm FIR} > 10^{12}{\rm L}_\odot$, i.e. ULIRGs. Downes & Solomon (1998) derived gas masses from a model of radiative transfer, finding gas masses a factor of $\sim 3-5$ lower than previous estimates got from CO luminosities. Solomon et al. (1997) (see also Bryant & Scoville 1999) concurred, but showed that even after reducing the conversion factor by such amount, the best estimations for molecular masses in LIRGs are about $(1.0 \pm 0.3) \times 10^{10}$ $M_\odot$, still in agreement with the standard conversion factor estimations. Thus, as suggested by Gao and Solomon 2003a, all estimations of mass using the standard conversion factors is retained (note that most LIRGs in the sample have $L_{\rm FIR} < 10^{12}{\rm L}_\odot$ anyway, and that an uncertainty of a factor of a few in $\langle k \rangle$ would not affect the plausibility for detection in most cases). Additionally, the HCN survey gives only H_2 molecular mass; contributions to the full content of interstellar matter other than H_2, e.g., He, are not considered.

In order to enlarge the sample of candidate galaxies, the more extensive Pico dos Dias Survey (PDS, Coziol et al. 1998) has also been considered. It consists of relatively nearby luminous galaxies, selected in the FIR. PDS galaxies form a complete sample limited in flux in the FIR at 2×10^{-10} erg cm^{-2} s^{-1}. They have a mean IR luminosity $\log({\rm L_{IR}/L_\odot}) = 10.3 \pm 0.5$, which is lower than the HCN survey one, and redshifts smaller than 0.1. The FIR luminosity of each PDS galaxy is given by Coziol et al. (1998) in their table 2. Unfortunately, PDS does not provide the CO luminosity of the galaxies and in fact, no CO or other line measurements are currently available for most of them. Thus, in order to get a first insight on the plausibility of PDS galaxies to appear as γ-ray sources for GLAST, a serie of correlations need to be applied. Gao and Solomon (2003a)

confirmed the strong correlation that exists between HCN and IR luminosities (which was already proposed by Solomon et al. 1992), making it is tight throughout three orders of magnitude (see figure 4 from Gao and Solomon 2003a). The following correlation was found:

$$\log L_{\rm IR} = 0.97 \log L_{\rm HCN} + 3.1\,. \tag{2.12}$$

At the same time, Gao and Solomon (2003b) also showed the existence of a strong correlation between CO and HCN luminosities, indicating that the more molecular gas-rich galaxies tend to have larger amount of dense molecular gas as well (see Gao and Solomon 2003b figure 3). The correlation, however, is much better for normal galaxies than for LIRGs and ULIRGs. For normal spiral galaxies it is a tight linear relationship, which indeed is the underlying reason that the FIR-CO correlation is also linear for normal galaxies and CO is reasonably good at predicting their star formation rate (SFR). Almost all LIRGs and ULIRGs lie above the normal galaxies correlation line, indicating an excess in the HCN emission compared to the CO emission for those stronger starbursting galaxies. The fit to all HCN survey galaxies gives the following relation:

$$\log L_{\rm HCN} = 1.38 \log L_{\rm CO} - 4.79\,. \tag{2.13}$$

Then, for PDS galaxies, using the $L_{\rm CO}$ deduced from the $L_{\rm HCN}$, that in turn is obtained from the measured $L_{\rm FIR}$[7], the total amount of molecular gas is estimated through the standard conversion (Equation 2.11). Finally, the minimum average CR enhancement required for the PDS galaxies to be detectable by GLAST is computed from Equation (2.9), having estimated the luminosity distances of the galaxies from Coziol et al. (1998) redshift values and assuming H_0=75 km s^{-1} Mpc^{-1} and $q_o \sim 0.5$ (see footnote 3). In the left panel of Figure 2.5, the distribution of enhancements required for GLAST detection is shown for all the PDS galaxies; in the inset, their luminosity distances are also shown. 153 out of 203 PDS galaxies (75%) need an average enhancement $\langle k \rangle < 500$ to appear as γ-ray sources in the next generation of catalogs.

2.2.3 Requirements for detection

Required minimum enhancement distributions of Figure 2.5 appear to be different for HCN and for PDS galaxies. The reason is that the PDS galaxies are in general less IR-luminous than the former ones, contain less molecular mass and thus require larger enhancement factors to be detectable by GLAST (typically a factor of 3–5 larger than a typical case in the HCN survey).

[7]It is important to notice that Coziol et al. (1998, table 2) give the FIR luminosity calculated as (Sanders and Mirabel 1996):

$$\begin{aligned} \log L_{\rm FIR} &= \log F_{\rm FIR} + 2\log\left[z(z+1)\right] + 57.28, \qquad \text{with} \\ F_{\rm FIR}(40-500\mu m) &= 1.26\times10^{-11}(2.58 f_{60} + f_{100})\ \ [\text{ergs}^{-1}\text{cm}^{-2}]\,, \end{aligned} \tag{2.14}$$

where f_i are the IRAS flux densities in Jy measured at 60 and 100 μm. In contrary, all the correlations derived in the HCN survey entertain the IR luminosity, not the FIR luminosity. Then, while analyzing the PDS sample, one needs to recompute –starting from the IRAS Catalog– the IR luminosities of all PDS starbursts using the following expression (Sanders and Mirabel 1996):

$$\begin{aligned} \log L_{\rm IR} &= 4\pi D_L^2 F_{\rm IR}\ \ [L_\odot], \qquad \text{with} \\ F_{\rm IR}(8-1000\mu m) &= 1.8\times10^{-11}(13.48 f_{12} + 5.16 f_{25} + 2.58 f_{60} + f_{100})\ \ [\text{ergs}^{-1}\text{cm}^{-2}]\,. \end{aligned} \tag{2.15}$$

However, having reasonable values of the minimum $\langle k \rangle$ required (e.g., lower than 1000 for HCN survey galaxies or lower than 500 for the less powerful PDS galaxies) is not a sufficient condition to claim the plausibility of a galaxy to be detected: it is needed that the galactic environment is active enough as to provide the minimum computed $< k >$ value. A first indication of the average value of the CR enhancement in a given galaxy can be indirectly estimated from the star formation rate (SFR), quantity that can be directly related to observations. More star formation implies a higher supernova explosion rate, and as this happens, there are more cosmic ray acceleration sites and thus an enhanced cosmic ray density. Therefore, a reasonable first assumption is (e.g., Drury et al. 1994, Aharonian & Atoyan 1996, Torres et al. 2003, etc.):

$$< k > \equiv \frac{q_\gamma}{q_{\gamma,\oplus}} \sim \frac{\omega_{CR}}{\omega_{CR,\oplus}} \sim \frac{SNrate}{SNrate_{\rm MW}} \sim \frac{SFR}{SFR_{\rm MW}} \,. \tag{2.16}$$

The SFR is highly correlated to the quantity of dense molecular gas present in the galaxy, as can be seen in Gao and Solomon (2003b) figure 6,

$$SFR = 1.8 \left(\frac{M_{dense}}{10^8 M_\odot} \right) \left(\frac{10}{\alpha_{\rm HCN}} \right) \ {\rm M_\odot yr^{-1}} \,. \tag{2.17}$$

The dense mass is traced by the HCN emission and it is found to be proportional to the HCN luminosity (Gao and Solomon 2003a):

$$M_{dense} = \alpha_{\rm HCN} L_{\rm HCN} \sim 10 \left(\frac{L_{\rm HCN}}{\rm K\ km\ s^{-1}\ pc^2} \right) \ {\rm M_\odot} \,. \tag{2.18}$$

Therefore:

$$SFR = 18 \left(\frac{L_{\rm HCN}}{10^8\ {\rm K\ km\ s^{-1}\ pc^2}} \right) \ {\rm M_\odot yr^{-1}} \,. \tag{2.19}$$

The Milky Way star formation rate (quoted as $SFR_{\rm MW}$) can be also estimated from Equation (2.19), being the HCN luminosity $L_{\rm HCN}(MW) \sim 0.04 \times 10^8\ {\rm K\ km\ s^{-1}\ pc^2}$ (e.g., Solomon et al. 1992, Wild & Eckart 2000). Then, a plausible value of the CR enhancement (obtained as the ratio between the SFR of the galaxy and that of our Milky Way) can be computed for each HCN galaxy. Figure 2.6 shows these values versus the needed k in order to make the galaxy detectable by GLAST. Only galaxies appearing above or around the line of unit slope can be considered prime candidates for detection. While a galaxy with high $L_{\rm HCN}/L_{\rm CO}$ ratio (i.e., with a high mass fraction of dense gas) will be a LIRG (or a ULIRG), the converse is not always true (Gao & Solomon 2003a). There are gas-rich galaxies which are LIRGs only because of the huge amount of molecular gas they possess, not because they have most of it at high density (and thus are undergoing a particularly strong starburst phenomenon). In some of these cases, while the value of enhancement needed for detection might only be of a few hundreds, the plausible value of k is much lower, since no strong star formation is ongoing.[8] In the context of γ-ray observability, GLAST will detect those galaxies that, being close enough, not only shine in the FIR but that do so *because* of their active strong star formation processes. In conclusion, the expectation of LIRGs to shine at γ-rays is not automatically granted. It is not only the

[8]For example, in the HCN survey, there are a group of 7 LIRGs (out of 31) that are gas-rich (CO-luminous) but have normal star formation efficiency $L_{\rm IR}/L_{CO}$ (i.e., $L_{HCN}/L_{CO} < 0.06$). Some examples are NGC 1144, Mrk 1027, NGC 6701, and Arp 55. They are using the huge molecular mass they have in creating stars at a normal SFR.

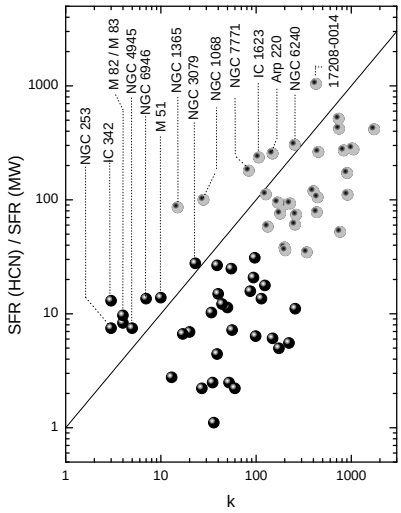

Figure 2.6: Plausible values of enhancements for the HCN galaxies obtained as the ratio between the SFR of each galaxy and that of the Milky Way versus the needed one for them to be detectable by GLAST. LIRGs (less luminous galaxies) are shown as white points (black) points. See text for discussion.

amount of gas (actually, the amount of gas divided by the distance square to its location) what yields to detectability at high energies, but rather it is the amount of gas that is found at high density, and thus that it is prone to form stars and be subject to significant enhancements of cosmic rays.

Quantitatively, only 5% of the PDS galaxies have star formation rates larger than 100 $M_\odot$ yr^{-1} (just 10 galaxies out of 203), the largest being 255 $M_\odot$ yr^{-1}. This has to be compared with 20% of the HCN galaxies having the same characteristics, with the largest star formation rate being 660 $M_\odot$ yr^{-1}. In any case, since there are good candidates for detection in both surveys it is suggested that both the HCN and PDS samples are taken into account when planning population analyses with the next generation of catalogs of point-like γ-ray sources. Note that only non-variable γ-ray sources can be ascribed to LIRGs. Variability indices (Torres et al. 2001, Nolan et al. 2003) can then play a role in the acceptance or rejection of possible counterparts of LIRGs.

2.3 Concluding remarks

This Chapter has shown that the class of starburst and luminous infrared galaxies are to appear in the GLAST survey. Given these estimations, perhaps some of them will also appear as TeV γ-ray sources provided enough observation time is granted in the current generation of ground based telescopes. Further insight into the expected high energy γ-ray emission from these objects can only be obtained with more detailed and particularized theoretical studies, what is presented next.

Chapter 3

Extragalactic sites of star formation: Modeling

Detailed theoretical models of the nearest starburst galaxy, NGC 253, and the nearest ULIRG, Arp 220, are discussed here. Supporting material is given in three Appendices, which comment on the numerical procedure implemented, the physics it contains, and details on the neutral pion emissivity computation. Although some of these Appendices have been referred before, heavy use of them is made here. This Chapter is partially based on the papers by Domingo-Santamaría & Torres (2005a) and Torres & Domingo-Santamaría (2005).

3.1 Emission model of the nearest starburst galaxy

NGC 253 is one of the candidates pointed out in the plausibility study of the previous Chapter, and it is one of the best studied galaxies due to its closeness and power. The aim here is to see whether a model based on observations at all wavelengths and first principles would predict that the central region of NGC 253 produces a sufficiently high γ-ray flux so as to be detected by current experiments.

3.1.1 CANGAROO GeV-TeV observations of NGC 253

Recently, the CANGAROO collaboration reported the detection of NGC 253 at TeV γ-ray energies (at 11σ confidence level), observed during a period of two years in 2000 and 2001 by about 150 hours (Itoh et al. 2002, 2003). Their measured differential flux was fitted by Itoh et al. (2003) with two functions:

$$\frac{dF}{dE} = (2.85 \pm 0.71) \times 10^{-12} \left(\frac{E}{1\mathrm{TeV}}\right)^{(-3.85\pm0.46)} \ \mathrm{cm}^{-2}\mathrm{s}^{-1}\mathrm{TeV}^{-1}\,, \qquad (3.1)$$

and

$$\frac{dF}{dE} = a e^{\sqrt{E_0}/b} \left(\frac{E}{E_0}\right)^{-1.5} e^{-\sqrt{E}/b} \ \mathrm{cm}^{-2}\mathrm{s}^{-1}\mathrm{TeV}^{-1}\,, \qquad (3.2)$$

with $a = 6 \times 10^{-5}$ cm^{-2}s^{-1}TeV^{-1}, $E_0 = 0.0002$ TeV, and $b = 0.25 \pm 0.01$ $\sqrt{\mathrm{TeV}}$. Both parameterizations are sensible reproductions of the observational data, although the former is clearly preferred for simplicity upon the light of an equally good fit. The flux uncertainty is the square root of the quadratic sum of the statistical and systematic

errors. Note that the slope of the power law spectrum is very uncertain, but steep. Indeed, an extrapolation of this power-law spectrum to lower energies greatly deviates from the measured upper limits in the GeV regime. The CANGAROO collaboration suggested a turn-over below the TeV region and proposed the second spectral form shown above. They have also claimed that the emission at the highest energies is inconsistent with it being produced in a point like source, and proposed an inverse Compton origin in a kpc-scale γ-ray halo of the NGC 253 galaxy.

The HESS array has also observed NGC 253 (see below). In several other observations of sources that have previously been targets for CANGAROO, the HESS collaboration have presented results in clear contradiction with the former CANGAROO reports. This is most notably the case for SN 1006 (Aharonian et al. 2005a), PSR B1706-44 (Aharonian et al. 2005b), and to some extent also for the supernova remnant RX J1713-3857 (Aharonian et al. 2004a), and the Galactic Center (Aharonian et al. 2004b). This may suggest some kind of systematic difference in the treatment of both sets of observational data. Such systematic effect should explain why CANGAROO spectra are steeper and their measured fluxes are one order of magnitude higher than the upper limits or measurements obtained by HESS. The CANGAROO collaboration is now calibrating their stereo system, and plan to re-observe these problematic cases within a year or so (R. Enomoto 2005, private communication).

In what follows, the aim is producing a detailed multiwavelength theoretical model for the central region of NGC 253, irrespective of CANGAROO measurements (i.e., without trying to reproduce their spectrum, but predicting fluxes based on a set of well-founded assumptions).[1] The central region of the galaxy would look like a point like source for the field of view and angular resolution of imaging Cerenkov telescopes. Then, this Chapter explores if one would rather expect a HESS non-confirmation of CANGAROO results regarding both the flux and the extension.

3.1.2 Phenomenology of the central region of NGC 253

A wealth of new multiwavelength data was obtained for NGC 253 during the last decade, after the previous modeling by Paglione et al. 1996, which did not include photons energies above 100 GeV (see below). It is located at a distance of ~ 2.5 Mpc (Turner and Ho 1985, Maurbersger et al. 1996) and is a nearly edge-on (inclination 78^o, Pence 1981) barred Sc galaxy. The continuum spectrum of NGC 253 peaks in the FIR at about 100 μm with a luminosity of 4×10^{10} $L_\odot$ (Telesco & Harper 1980, Rice et al. 1988, Melo et al. 2002). The FIR luminosity is at least a factor of 2 larger than that of our own Galaxy (Cox & Mezger 1989, Dudley & Wynn-Williams 1999), and it mainly comes from the central nucleus, about half of it according to the Melo et al. (2002) 1 arcmin resolution ISOPHOT observations. IR emission can be understood as cold ($T \sim 50K$) dust reprocessing of stellar photon fields.

When observed at 1 pc resolution, at least 64 individual compact radio sources have been detected within the central 200 pc of the galaxy (Ulvestad & Antonucci 1997), and roughly 15 of them are within the central arcsec of the strongest radio source, considered to be either a buried active nucleus or a very compact SNR. Of the strongest 17 sources, about one half have flat spectra and half have steep spectra. This indicates that perhaps half of the individual radio sources are dominated by thermal emission from H II regions, and half are optically thin synchrotron sources, presumably SNRs. There is no compelling

[1] This approach has been supported by recent additional HESS observations, which are discussed below.

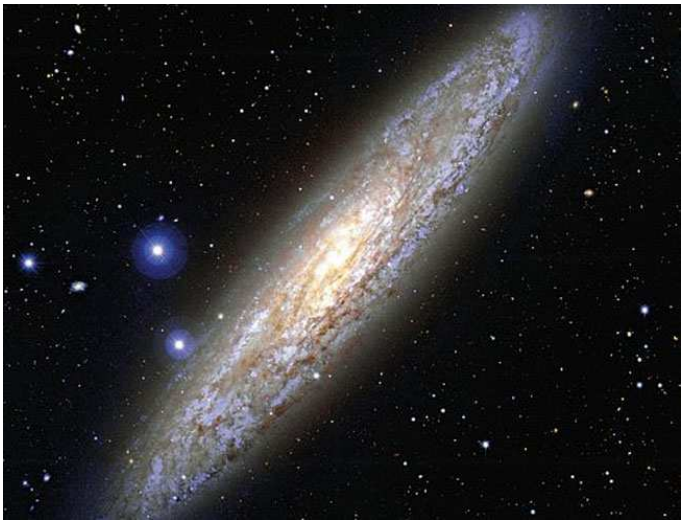

Figure 3.1: An optical image of NGC 253. The high value of inclination, and the grand-design type of this galaxy makes of it one of the most spectacular objects in the sky.

evidence of any sort of variability in any of the compact sources over an 8-yr time baseline. The most powerful flat-spectrum central radio source is clearly resolved in the study of Ulvestad and Antonucci (1997) and appears to be larger than the R136 cluster located in 30 Doradus, containing about 10^5 $M_\odot$ in stars and 600 $M_\odot$ in ionized gas. The age was estimated to be less than 4×10^6 yr. The region surrounding the central 200 pc has also been observed with subarcsec resolution and 22 additional radio sources stronger than 0.4 mJy were detected within 2kpc of the galaxy nucleus (Ulvestad 2000). The region outside the central starburst may account for about 20% of the star formation of NGC 253, is subject to a supernova explosion rate well below 0.1 yr^{-1}, and has an average gas density in the range 20–200 cm^{-3}, much less than in the most active nuclear region of NGC 253 (Ulvestad 2000).

Carilli (1996) presented low frequency radio continuum observations of the nucleus at high spatial resolution. Free-free absorption was claimed as the mechanism producing a flattening of the synchrotron curve at low energies, with a turnover frequency located between $10^{8.5}$ and 10^9 Hz. The emission measure needed for this turnover to happen is at least 10^5 pc cm^{-6} for temperatures on the order of 10^4 K. Tingay (2004) observed NGC 253 using the Australian Long Baseline Array and provided fits with free-free absorption models for the radio spectrum of six sources. He concluded that the free-free opacity in the central region has to be in the range of 1 to 4 at 1.4 GHz, implying emission measures of a few times 10^6 pc cm^{-6} in this particular direction, again for temperatures of the order of 10^4 K.

As shown by infrared, millimeter, and centimeter observations, the 200 pc central region dominates the current star formation in NGC 253, and is considered as the starburst central nucleus (e.g., Ulvestad and Antonucci 1997, Ulvestad 2000). Centimeter imaging of this inner starburst and the limits on variability of radio sources indicate a supernova rate less than 0.3 yr^{-1} (Ulvestad & Antonucci 1997), which is consistent with results ranging from 0.1 to 0.3 yr^{-1} inferred from models of the infrared emission of the entire galaxy (Rieke et al. 1980; Rieke, Lebofsky & Walker 1988, Forbes et al. 1993). Van Buren

and Greenhouse (1994) developed a direct relationship between the FIR luminosity and the rate of supernova explosions, starting from Chevalier's (1982) model for radio emission from supernovae blast waves expanding into the ejecta of their precursor stars. The result is $\mathcal{R} = 2.3 \times 10^{-12} L_{\rm FIR}/L_\odot$ yr^{-1}, which is in agreement with the previous estimates within uncertainties. The star formation rate at the central region has been computed from IR observations, resulting in 3.5 M$_\odot$ yr^{-1}, and it represents about 70% of the total star formation rate measured for NGC 253 (Melo et al. 2002). When compared with Local Group Galaxies, the supernova rate in NGC 253 is one order of magnitude larger than that of M31, the largest of the Local Group (Pavlidou and Fields 2001).

Paglione et al. (2004) obtained high resolution (5".2 × 5".2) interferometry of the CO line $J = 1 \rightarrow 0$ in order to study the structure and kinematics of the molecular gas in the central nucleus. This study enhances that of Sorai et al. (2000), which obtained compatible results, although done with less angular resolution. The general morphology of the CO map is consistent with other high resolution studies. It shows an extended ridge of emission aligned with an infrared-bright bar and a central group of bright clouds aligned with the major axis of the galaxy, orbiting the radio nucleus in a possible ring. The central clouds move around the radio nucleus as a solid body, similar to the distribution of the radio sources, central HCN clouds, and central near-infrared emission (Paglione et al. 1995, 1997; Ulvestad & Antonucci 1997). Much of the molecular gas in NGC 253 appears to be highly excited (Wild et al. 1992; Mao et al. 2000; Ward et al. 2003). Observations of $J = 4 \rightarrow 3$ and $J = 6 \rightarrow 5$ transitions of CO, as well as HCN lines, suggest the existence of localized spots with values of densities in excess of 10^4 cm^{-3} (Israel & Baas 2002, Paglione, Jackson, & Ishizuki 1997, Paglione, Tosaki & Jackson 1995, Harris et al. 1991). Bradford et al. (2003) report CO $J = 7 \rightarrow 6$ observations and also find that the bulk of molecular gas in the central 180 pc of the galaxy is highly excited and at a temperature of about 120 K. They conclude that the best mechanism for heating the gas is cosmic ray bombardment over the gas residing in clouds, with density about 4.5 $\times 10^4$ cm^{-3}.

Current estimates of the gas mass in the central 20" – 50" (< 600 pc) region range from 2.5 $\times 10^7$ M$_\odot$ (Harrison, Henkel & Russell 1999) to 4.8 $\times 10^8$ M$_\odot$ (Houghton et al. 1997); see Bradford et al. (2003), Sorai et al. 2000, and Engelbracht et al. (1998) for discussions. For example, using the standard CO to gas mass conversion, the central molecular mass was estimated as 1.8 $\times 10^8$ M$_\odot$ (Mauersberger et al. 1996). It would be factor of ~ 3 lower if such is the correction to the conversion factor in starburst regions, which are better described as a filled intercloud medium, as in the case of ULIRGs, instead of a collection of separate large molecular clouds; see Solomon et al. (1997), Downes & Solomon (1998), and Bryant & Scoville (1999) for discussions. Thus, in agreement with the mentioned measurements, it is assumed that within the central 200 pc, a disk of 70 pc height has $\sim 2 \times 10^7$ M$_\odot$ uniformly distributed, with a density of ~ 600 cm^{-3}. Additional target gas mass with an average density of $\sim$50 cm^{-3} is assumed to populate the central kpc outside the innermost region, but subject to a smaller supernova explosion rate ~ 0.01 yr^{-1}, 10% of that found in the most powerful nucleus (Ulvestad 2000).

The central region of this starburst is packed with massive stars. Watson et al. (1996) discovered four young globular clusters near the center of NGC 253; they alone can account for a mass well in excess of 1.5×10^6M$_\odot$ (see also Keto et al. 1999). Assuming that the star formation rate has been continuous in the central region for the past 10^9 yrs and a Salpeter IMF for 0.08–100 M$_\odot$, Watson et al. (1996) find that the bolometric luminosity of NGC 253 is consistent with 1.5 $\times 10^8$M$_\odot$ of young stars. Physical, morphological, and

kinematic evidence for the existence of a galactic superwind has been found for NGC 253 (e.g., McCarthy et al. 1987, Heckman et al. 1990, Strickland et al. 2000, 2002, Pietsch et al. 2001, Forbes et al. 2000, Weaver et al. 2002, Sugai, Davies & Ward 2003). This superwind creates a cavity of hot ($\sim 10^8$ K) gas, with longer cooling times than the typical expansion timescales. As the cavity expands, a strong shock front is formed on the contact surface with the cool interstellar medium. Shock interactions with low and high density clouds can produce X-ray continuum and optical line emission, respectively, both of which have been directly observed (McCarthy et al. 1987). The shock velocity can reach thousands of km s^{-1}. This wind has been proposed as the convector of particles that have been already accelerated in individual SNRs, to the larger superwind region, where Fermi processes could upgrade their energy up to that detected in ultra high energy cosmic rays (Anchordoqui et al. 1999, Anchordoqui et al. 2003, Torres & Anchordoqui 2004).

3.1.3 Diffuse modeling

The approach to compute the steady multiwavelength emission from NGC 253 follows that implemented in the numerical package $\mathcal{Q}$-DIFFUSE, which has been used here with some further improvements. Its flow is described in detail in Appendix A, and the physics it contains is described in Appendix B and C. The steady state particle distribution is computed within $\mathcal{Q}$-DIFFUSE as the result of an injection distribution being subject to losses and secondary production in the interstellar medium. In general, the injection distribution may be defined to a lesser degree of uncertainty when compared with the steady state one, since the former can be directly linked to observations, e.g., to the supernova explosion rate.

The injection proton emissivity, following Bell (1978), is assumed to be a power law in proton kinetic energies with index p

$$Q_{\rm inj}(E_{\rm p,\,kin}) = K \left(\frac{E_{\rm p,\,kin}}{\rm GeV} \right)^{-p} , \tag{3.3}$$

where K is a normalization constant and units are such that $[Q]$= GeV^{-1} cm^{-3} s^{-1}. This expression is strictly valid at high energies (say, for kinetic energies above a few GeV). At lower energies the distribution of cosmic rays is flatter, e.g., it would be given by equation (6) of Bell (1978), correspondingly normalized. Neglecting this difference at low energy does not produce any important change in the computation of secondaries, and especially on γ-rays at the energies of interest.

The normalization is obtained from the total power transferred by supernovae into CRs kinetic energy within a given volume:

$$\int_{E^{\rm kin}_{\rm p,\,min}}^{E^{\rm kin}_{\rm p,\,max}} Q_{\rm inj}(E^{\rm kin}_{\rm p}) E^{\rm kin}_{\rm p} dE^{\rm kin}_{\rm p} = -K \frac{(E^{\rm kin}_{\rm p,\,min})^{-p+2}}{-p+2} \equiv \frac{\sum_i \eta_i \mathcal{P} \mathcal{R}_i}{V} , \tag{3.4}$$

where it was assumed that $p \neq 2$ and used the fact that $E_{\rm p,\,kin\,min} \ll E_{\rm p,\,kin,max}$ in the second equality. $\mathcal{R}_i$ ($\sum_i \mathcal{R}_i = \mathcal{R}$) is defined as the rate of supernova explosions in the star forming region being considered, V being its volume, and η_i the transfered fraction of the supernova explosion power ($\mathcal{P} \sim 10^{51}$ erg) into CRs. The summation over i takes into account that not all supernovae will transfer the same amount of power into CRs (alternatively, that not all supernovae will release the same power). The rate of power

transfer is assumed to be in the range $0.05 \lesssim \eta_i \lesssim 0.15$, the average value for η being $\sim$ 10%. Note that $E^{\rm kin}_{\rm p,\,min}$ is also fixed by requiring that the minimum kinetic proton energy with which a CR escapes from a shock front is larger than $2m_p v_s^2$ (Bell 1978). For shock velocities of the order of 10^{3-4} km s^{-1}, this is in the range of a few MeV. A value of 10 MeV is taken to fix numerical constants. These assumptions imply that the injection is fixed as:

$$Q_{\rm inj}(E_p) = \left[\frac{\mathcal{P}\times\sum_i \eta_i \mathcal{R}_i \times V^{-1}}{\rm GeV\,s^{-1}\,cm^{-3}}\right][p-2]\left[\frac{E_{\rm p,\,kin,\,min}}{\rm GeV}\right]^{p-2}\left[\frac{E_p - m_p}{\rm GeV}\right]^{-p}. \tag{3.5}$$

The general diffusion-loss equation is given by (see, e.g., Longair 1994, p.279; Ginzburg & Syrovatskii 1964, p.296):

$$-D\bigtriangledown^2 N(E) + \frac{N(E)}{\tau(E)} - \frac{d}{dE}\left[b(E)N(E)\right] - Q(E) = -\frac{\partial N(E)}{\partial t}\,. \tag{3.6}$$

In this equation, D is the scalar diffusion coefficient, $Q(E)$ represents the source term appropriate to the production of particles with energy E, $\tau(E)$ stands for the confinement timescale, $N(E)$ is the distribution of particles with energies in the range E and $E + dE$ per unit volume, and $b(E) = -(dE/dt)$ is the rate of loss of energy (see Table A.1 for units). The functions $b(E)$, $\tau(E)$, and $Q(E)$ depend on the kind of particles (i.e., electrons/positrons and protons are subject to different kind of losses and are also produced differently), but the form of the equation will be the same for all. In the steady state, $\partial N(E)/\partial t = 0$, and, under the assumption of a homogeneous distribution of sources, the spatial dependence is considered to be irrelevant, so that $D\bigtriangledown^2 N(E) = 0$. Equation (4.5.3) can be solved, as can be proven by direct differentiation, by using the following Green function:

$$G(E,E') = \frac{1}{b(E)}\exp\left(-\int_E^{E'} dy \frac{1}{\tau(y)b(y)}\right)\,, \tag{3.7}$$

such that for any given source function, or emissivity, $Q(E)$, the solution is:

$$N(E) = \int_E^{E_{\rm max}} dE' Q(E') G(E,E')\,. \tag{3.8}$$

Note that the integral in E' is made on the primary energies which, after losses, produce secondaries with energy E. In general, however, $G(E,E')$ has not a close analytical expression, and neither does $N(E)$. Numerical integration techniques are then needed to compute Equation (3.8). Note that if $Q(E)$ is a power law, $N(E)$ scales linearly with its normalization. However, there is no immediate scaling property with the density of the interstellar medium, which enters differently into the several expressions of losses that conform $b(E)$.

The confinement timescale will be determined by several contributions. One on hand, the characteristic escape time in the homogeneous diffusion model (Berezinskii et al. 1990, p. 50-52 and 78) is $\tau_D = R^2/(2D(E)) = \tau_0/(\beta(E/{\rm GeV})^\mu)$, where β is the velocity of the particle in units of c, R is the spatial extent of the region from where particles diffuse away, and $D(E)$ is the energy-dependent diffusion coefficient, whose dependence is assumed $\propto E^\mu$, with $\mu \sim 0.5$.[2] τ_0 is the characteristic diffusive escape time at ~ 1

[2]The use of a homogeneous model is an assumption, but is justified in the compactness of the innermost starburst region. It is basically assumed that there is a homogeneous distribution of supernovae in the central hundreds of pc, which is supported observationally (Ulvestad and Antonucci 1997).

GeV. It is not known for NGC253, one can only assume its value and compare it with the one for other galaxies (e.g. our own Galaxy, or M33, Duric et al. 1995); the value chosen also parallels the one obtained in an earlier study of NGC 253 or on M82 (Paglione et al. 1996, Blom et al. 1999). The sensitivity of the model to τ_0 is analyzed below. On the other, the total escape timescale will also take into account that particles can be carried away by the collective effect of stellar winds and supernovae. The convective timescale, τ_c, is $\sim R/V$, where V is the collective wind velocity. For a wind velocity of 300 km/s and a radius of about the size of the innermost starburst (see below), this timescale is less than a million years (3×10^5 yr). The outflow velocity is not very well known; however, minimum reasonable values between 300 and 600 km s^{-1} have been claimed, and could even reach values on the order of thousands of km s^{-1} (Strickland et al. 2002). Pion losses (which are catastrophic, since the inelasticity of the collision is about 50%) produce a loss timescale $\tau_{\rm pp}^{-1} = (dE/dt)^{\rm pion}/E$ (see, e.g., Mannheim & Schlickeiser 1994), which is similar in magnitude to the convective timescale and dominates with it the shaping of the proton spectrum. Thus, in general, for energies higher than the pion production threshold, $\tau^{-1}(E) = \tau_D^{-1} + {\tau_c}^{-1} + \tau_{\rm pp}^{-1}$.

For electrons, the total rate of energy loss considered is given by the sum of that involving ionization, inverse Compton scattering, bremsstrahlung, synchrotron radiation and adiabatic losses, as is also discussed in Appendix C. Full Klein-Nishina cross section is used while computing photon emission, and either Thomson or extreme Klein-Nishina approximations, as needed, are used while computing losses. This approach proves to be accurate, while significantly reduces the computational time. For the production of secondary electrons, $\mathcal{Q}$-DIFFUSE computes knock-on electrons and charged pion processes producing both electrons and positrons (see also Appendix C for a review of the related formulae). In the case of γ-ray photons, bremsstrahlung, inverse Compton and neutral pion decay processes are computed. For the latter, a dedicated appendix (Appendix B) provides a more detailed discussion of the different approaches to compute the neutral pion-induced γ-ray emissivity. For radio photons, the synchrotron emission by the steady distribution of electrons is computed. Free-free emission and absorption from electrons of the hot plasma present in the medium is also considered in order to reproduce the radio data at low frequencies. The FIR emission is modelled with a dust emissivity law given by $\nu^\sigma B(\epsilon, T)$, where $\sigma = 1.5$ and B is the Planck function. The computed FIR photon density is used as a target for inverse Compton process as well as to give account of losses in the γ-ray scape. The latter basically comes from the opacity to $\gamma\gamma$ pair production with the photon field of the galaxy nucleus. The fact that the dust within the starburst reprocesses the UV star radiation to the less energetic infrared photons implies that the opacity to $\gamma\gamma$ process is significant only at the highest energies. The opacity to pair production from the interaction of a γ-ray photon in the presence of a nucleus of charge Z is considered too. Further details and relevant formulae is given in Appendix C.

3.1.3.1 Comparison with previous models

When compared with the previous study of high energy emission from NGC 253 by Paglione et al. (1996), several methodological and modeling differences need to be mentioned. The distance, size, gas mass, density, and supernova explosion rate of the central region that they assume are different from those quoted in Table 1. Based on earlier data (e.g., Canzian et al. 1988), the former authors modelled a starburst region at 3.4 Mpc (a factor of 1.36 farther than the one currently adopted), with a 325 pc radius

(about 3 times larger than the one adopted here). This region is larger than implied by current knowledge of the central starburst, where the supernova explosion rate Paglione et al. used is actually found and the cosmic ray density is maximally enhanced. The average density assumed by Paglione et al., 300 cm^{-3}, gives a target mass $\sim 2 \times 10^8$ $M_\odot$, which is at the upper end of all current claims for the central nucleus or was already found excessive. The target mass of the innermost region differs from ours by a factor of about 6, ours being smaller. The fraction of the supernova explosion energy converted into cosmic rays (20% for Paglione et al., a factor of 2 larger than ours) also seems excessive as regards the current measurements of SNR at the highest energies. A surrounding disk with a smaller supernova rate is also considered, following the discovery of several SNRs in that region (Ulvestad 2000), especially to test its influence in the total γ-ray output. Finally, the Paglione et al. (1996) study did not produce results above 200 GeV. [3]

The $\mathcal{Q}$-DIFFUSE set uses different parameterizations for pion cross sections as compared with those used by Marscher and Brown (1978), whose code was the basis of the Paglione et al. study. Our computation of neutral pion decay γ-rays is discussed in Appendix B. In addition, $\mathcal{Q}$-DIFFUSE uses the full inverse Compton Klein-Nishina cross section, computes secondaries (e.g., knock-on electrons) without resorting to parameterizations that are valid only for Earth-like cosmic ray (CR) intensities, fixes the photon target for Compton scattering starting from modeling the observations in the FIR, and considers opacities to γ-ray scape.

3.1.4 Results

3.1.4.1 Summary of model parameters

A summary of the parameters used for, and obtained from, the modeling are given in Table 3.1. There, the mark `OM` refers to *Obtained from modeling* and `ST` or *see text* refers to parameters discussed in more detail in the previous Section on phenomenology, where references are also given. These parameters values or ranges of values are fixed by observations. Finally, the mark `A` refers to *assumed parameters*, in general within a range. Variations to the values given in Table 3.1 are discussed below.

3.1.4.2 Steady proton and electron population

The numerical solution of the diffusion-loss equation for protons and electrons, each subject to the losses described in Appendix B, is shown in Figure 3.2. A residence timescale of 10 Myr has been adopted, as has a density of ~ 600 cm^{-3}. In the case of electrons, the magnetic field with which synchrotron losses are computed in Figure 3.2 is 300 μG. The latter is fixed below, requiring that the steady electron population produces a flux level of radio emission matching observations. An injection electron spectrum is considered –in addition to the secondaries– in generating the steady electron distribution. The primary electron spectrum is assumed as that of the protons times a scaling factor; the inverse of the ratio between the number of protons and electrons, N_p/N_e (e.g., Bell 1978). This ratio is about 100 for the Galaxy, but could be smaller in star forming

[3] To further ease the comparison, some typos in the Paglione et al. (1996) paper are noted: The factor $b(E)$ should be elevated to minus one in their Eq. (4), as well as the term τ_c in their Eq. (3). The y-axis of their Fig. 1 is not the emissivity, but the emissivity divided by the density; units need to be modified accordingly , see e.g. Abraham et al. (1966). E_p in their Eq. (7) and x-axis of Fig. 2 and 3 is the kinetic energy, but the generic E in Eq. (1) is the total energy. The y-axis of Fig. 2 is in units of cm^{-3} GeV^{-1}.

Table 3.1: Measured, assumed, and derived values for different physical quantities at the innermost starburst region of NGC 253 (IS), a cylindrical disk with height 70 pc, and its surrounding disk (SD).

Physical parameters	Symbol	Value	Unit	Notes
Distance	D	2.5	Mpc	ST
Inclination	i	78	degrees	ST
IR Lum. of the innermost starburst (IS)	$L_{\rm IR}$	2×10^{10}	$L_\odot$	ST
Radius of the IS	–	100	pc	ST
Radius surrounding disk (SD)	–	1000	pc	ST
Uniform density of the IS	$n_{\rm IS}$	~ 600	cm^{-3}	ST
Uniform density of the SD	$n_{\rm SD}$	~ 50	cm^{-3}	ST
Gas mass of the IS	$M_{\rm IS}$	$\sim 3 \times 10^7$	$M_\odot$	ST
Gas mass of the SD	$M_{\rm SD}$	$\sim 2.5 \times 10^8$	$M_\odot$	ST
Supernova explosion rate of the IS	$\mathcal{R}$	~ 0.08	SN yr^{-1}	ST
Supernova explosion rate of the SD	–	~ 0.01	SN yr^{-1}	ST
Typical supernova explosion energy	–	10^{51}	erg	ST
SN energy transferred to cosmic rays	η	~ 10	%	ST
Dust emissivity index	σ	1.5	–	OM
Dust temperature	$T_{\rm dust}$	50	K	OM
Emission measure	EM	5×10^5	pc cm^{-6}	OM
Ionized gas temperature	T	10^4	K	OM
Magnetic field of the IS	B	300	μG	OM
Slope of primary injection spectrum	p	2.2–2.3	–	A
Maximum energy considered for primaries	–	100	TeV	A
Diffusion coefficient slope	μ	0.5	–	A
Proton to electron primary ratio	N_p/N_e	50	–	A
Diffusive timescale	τ_0	1–10	Myr	A

regions, where there are multiple acceleration sites. For instance, Völk et al. (1989) obtained $N_p/N_e \sim 30$ for M82. $N_p/N_e = 50$ is assumed for the central disk of NGC 253. From about $E_e - m_e \sim 10^{-1}$ to 10 GeV, the secondary population of electrons dominates, in any case. This is shown in Figure 3.4. It is in this region of energies where most of the synchrotron radio emission is generated, and thus the ability of producing a high energy model compatible with radio observations is a cross check for the primary proton distribution.

Figure 3.3 shows the ratio of the steady proton population in the SD to that in the IS. Because the SD is subject to a smaller supernova explosion rate, it has an smaller number of protons in its steady distribution, at all energies, of the order of 1% of that of the IS. Then, it will play a subdominant role in the generation of γ-ray emission, as shown below. In the right panel of Figure 3.3, and for further discussion in the following Sections, the ratio between the steady proton distribution in the IS, when the gas density is artificially enhanced and diminished by a factor of 2 from the assumed value of 600 cm^{-3} are presented.

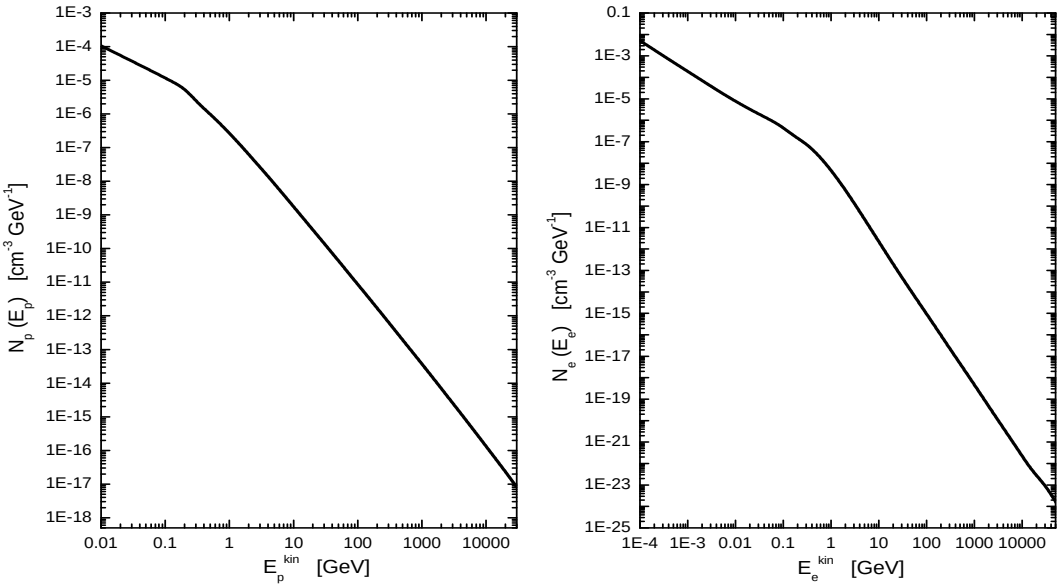

Figure 3.2: Steady proton (left panel) and electron (right panel) distributions in the innermost region of NGC 253.

3.1.4.3 IR and radio emission

The continuum emission from NGC 253, at wavelengths between $\sim$ 1 cm and $\sim$ 10 microns, was measured by several authors, e.g., see Figure 3.5 and Section 3.1.2. These observations did not in general distinguish, due to angular resolution, only the emission coming from the innermost starburst region. Instead, they also contain a contribution coming from photons produced in the surrounding disk and farther away from the nucleus. The IR continuum emission is mainly produced thermally, by dust, and thus it could be modelled with a spectrum having a dilute blackbody (graybody) emissivity law, which is proportional to $\nu^{\sigma} B(\epsilon, T)$, where B is the Planck function. Figure 3.5 shows the result of this modeling and its agreement with observational data when the dust emissivity index $\sigma = 1.5$ and the dust temperature $T_{\rm dust} = 50K$. Different total luminosities, the normalization of the dust emission (see the appendix of Torres 2004 for details), are shown in the Figure to give an idea of the contribution of the innermost region with respect to that of the rest of the galaxy. According to Melo et al. (2002), about half of the total IR luminosity is produced in the IS, what is consistent with the data points being intermediate between the curves with $L_{\rm IR}$ equal to 2×10^{10} and 4×10^{10} $L_{\odot}$, since the latter were obtained with beamsizes of about 20–50 arcsec ($\sim$ 240–600 pc at the NGC 253 distance).

The influence of the magnetic field upon the steady state electron distribution is twofold. On one hand, the greater the field, the larger the synchrotron losses –what is particularly visible at high energies, where synchrotron losses play a relevant role. On the other, the larger the field the smaller the steady distribution. These effects evidently compete between each other in determining the final radio flux. The magnetic field is required to be such that the radio emission generated by the steady electron distribution is in agreement with the observational radio data. This is achieved by iterating the feedback between the choice of magnetic field, the determination of the steady distribution, and

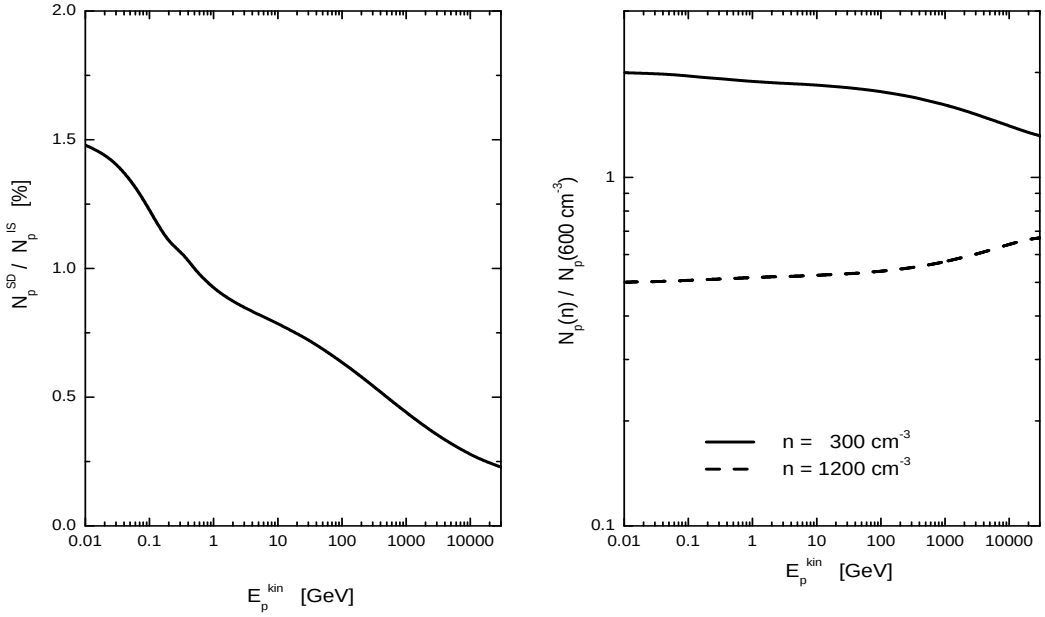

Figure 3.3: Left: Ratio of the steady proton population in the surrounding disk to that in the innermost starburst region. Right: Ratio between the steady proton distribution in the IS, when the gas density is artificially enhanced and diminished by a factor of 2.

the computation of radio flux, additionally taking into account free-free emission and absorption processes. Whereas free-free emission is subdominant when compared with the synchrotron flux density, free-free absorption plays a key role at low frequencies, determining the opacity. A reasonable agreement with all observational data is found for a magnetic field in the innermost region of 300 μG, an ionized gas temperature of about 10^4 K, and an emission measure of 5×10^5 pc cm^{-6}, the latter two are in separate agreement with the free-free modeling of the opacity of particular radio sources, as discussed in Section 3.1.2. The value of magnetic field found for the IS is very similar to that of the disk of Arp 220 (Torres 2004) and compatible with measurements in molecular clouds (Crutcher 1988, 1994, 1999). It is also close to the (270 μG) value proposed by Weaver et al. (2002) using the equipartition argument.

3.1.4.4 γ-ray emission

In the left panel of Figure 3.6, bremsstrahlung, inverse Compton, and pion decay γ-ray fluxes of the IS are shown together with the total contribution of the SD and the total differential flux of the whole system. These results are obtained with the model just shown to be in agreement with radio and IR observations. As mentioned before, the contribution of the SD, even when having a factor of ~ 8 more mass than the IS, is subdominant. The reason for this needs to be found in that this region is much less active (Ulvestad 2000).

Our predictions, while complying with EGRET upper limits, are barely below them. If this model is correct, NGC 253 is bound to be a bright γ-ray source for GLAST. The integral fluxes are shown in the right panel of Figure 3.6. Our model complies again with the integral EGRET upper limit for photons above 100 MeV, and predicts that, given enough observation time, NGC 253 is also to appear as a point-like source in an instrument like HESS, whose first measurements are discussed below. Note, however, that

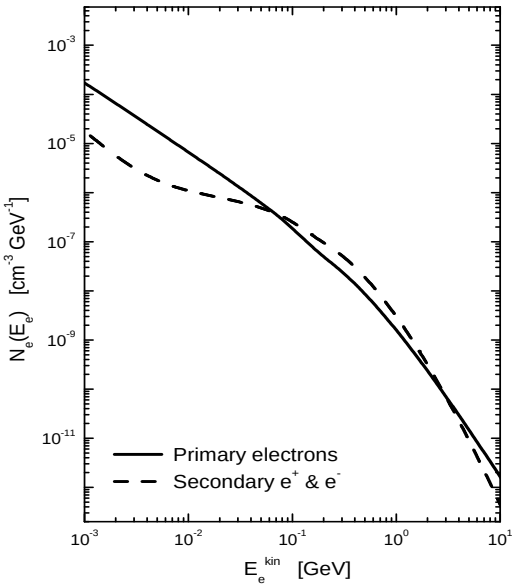

Figure 3.4: Steady population of primary-only and secondary-only electrons. Only the region of the secondary dominance of the distribution is shown.

quite a long exposure may be needed to detect the galaxy, and also, that these fluxes are only a few percent of those reported by the CANGAROO collaboration.

An additional source of TeV photons not considered here is the hadronic production in the winds of massive stars (Romero & Torres 2003). However, a strong star forming region such as the nucleus of NGC 253 is bound to possess much more free gas than that contained within the winds of massive stars, which albeit numerous, have mass loss rates typically in the range of 10^{-6}–10^{-7} $M_\odot$.[4]

3.1.4.5 Opacities to γ-ray escape

In the left panel of Figure 3.7, the different contributions to the opacity are shown. The equation of radiation transport appropriate for a disk is used to compute the predicted γ-ray flux taking into account all absorption processes (see Appendix C.4 for details). The right panel of Figure 3.7 shows the effect of the opacity on the integral γ-ray fluxes, only evident above 3 TeV.

3.1.4.6 Exploring the parameter space and degeneracies

As it is summarized in Table 3.1, most of the model parameters are well fixed from observations. There are, however, a couple of assumptions which may produce slight degeneracies, while not being well bounded from experiments. Consider for instance the proton injection slope p and the diffusive scale τ_0. For the former, $p = 2.3$ is

[4]In Romero & Torres (2003), higher mass loss rates up to 10^{-5} $M_\odot$, i.e., grammages between 50 and 150 g cm^{-2} were allowed. These values, although have been found in perhaps one or two Galactic early O stars, are uncommon. Since the size of the base of the wind for each star, the grammage, and the ambient enhancement of cosmic rays were independently allowed to take values within their assumed ranges in the Monte Carlo simulation of Romero & Torres (2003), the stars with the most favorable parameters would dominate the sum, overestimating the relative importance of their fluxes.

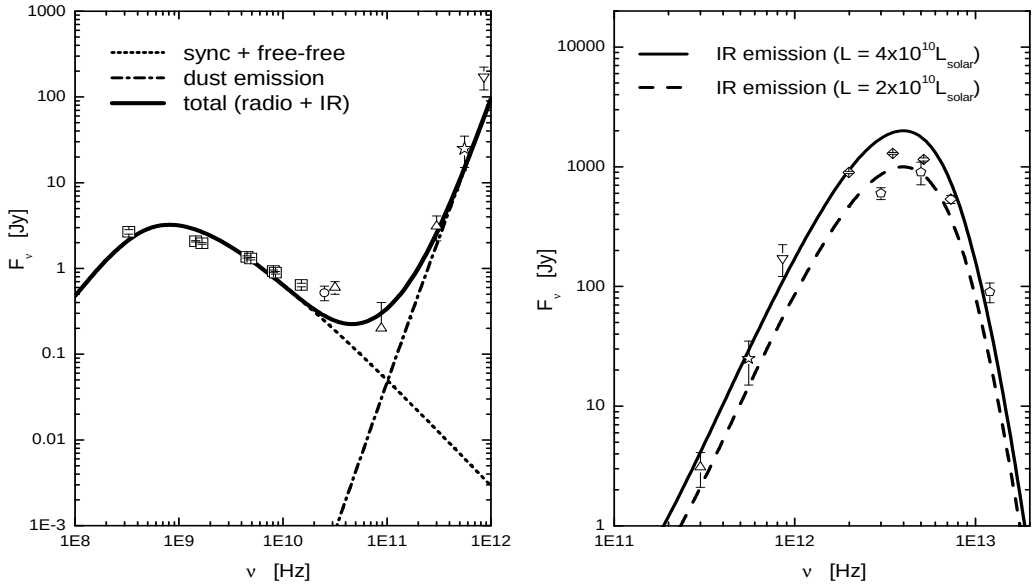

Figure 3.5: Left: IR flux from NGC 253 assuming a dilute blackbody with temperature $T_{\rm dust} = 50$ K and different total luminosities. Right: Multifrequency spectrum of NGC 253 from radio to IR, with the result of this modeling. The experimental data points correspond to: pentagons, Melo et al. (2002); diamonds, Telesco et al. (1980); down-facing triangles, Rieke et al. (1973); stars, Hildebrand et al. (1977); up-facing triangles, Elias et al. (1978); circles, Ott et al. (2005); squares, Carilli (1996).

assumed, which agrees with the recent results from HESS regarding γ-ray observations at TeV energies of supernova remnants and unidentified extended sources. However, it would certainly be within what one would expect from proton acceleration in supernova remnants, and also within experimental uncertainty, if a better description for the average proton injection slope in NGC 253 is 2.2 instead of 2.3. Table 3.2 shows the influence of this kind of choice on the final results. A harder slope slightly increases the integral flux. Similarly, the diffusive timescale is not well-determined, and it may be arguable perhaps within one order of magnitude. Table 3.2 also shows the influence of this choice. Ultimately, high energy γ-ray observations (from GeV to TeV) are the ones to impose constraints on these values. In any case, pp interaction and convection timescales are much shorter (< 1 Myr), thus dominating the form of $N(E)$. To show this in greater detail, the result for the proton distribution when different convective and the pp timescales are taken into account as compared with the solution when $\tau(E) = \tau_D$, i.e., diffusion only is shown in Fig. 3.8. Clearly, convection plus pp timescales dominates the spectrum.

Regarding degeneracies, both the proton slope and the confinement timescales, however, cannot be much different from what was assumed. If the former were to differ significantly, it would be impossible to reproduce the radio data, which is the result of the synchrotron emission of the secondary electrons. Changes in the number of protons in the IS would imply a change in the magnetic field to reproduce radio observations, which clearly cannot be pushed much either.

In a less impacting way, varying the value of N_p/N_e can also vary the results. This variation would be slight because of the influence of the more numerous secondary electrons in the energetic region of interest for radio emission. On the same track, varying the

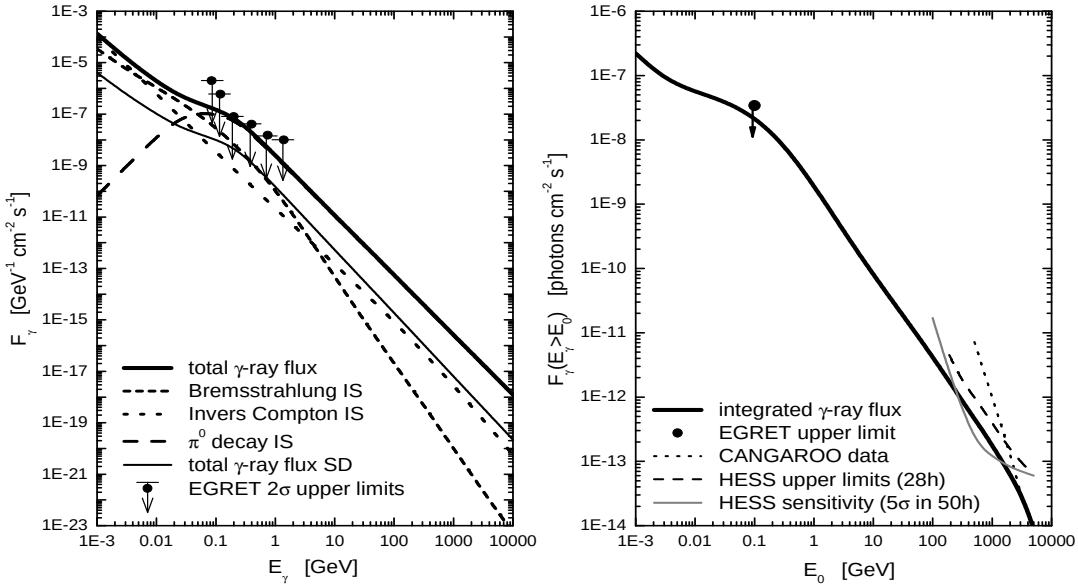

Figure 3.6: Left: Differential γ-ray fluxes from the central region of NGC 253. Total contribution of the surrounding disk is separately shown, as are the EGRET upper limits. In the case of the IS, the contributions of bremsstrahlung, inverse Compton, and neutral pion decay to the γ-ray flux are also shown. Right: Integral γ-ray fluxes. The EGRET upper limit (for energies above 100 MeV), the CANGAROO integral flux as estimated from their fit, and the HESS sensitivity (5σ detection in 50 hours) are given. Absorption effects are already taken into account. Also shown is the recently released HESS upper limit curve on NGC 253.

diffusion coefficient μ does not cause substantial changes. Finally, if the maximum proton energy were to differ from the value of 100 TeV that has been assumed, the end of the spectrum would accordingly shift slightly, but this is not expected to happen in a significant way (it is now observationally know that supernova remnants are sources of ~ 10 TeV photons).

Even within an artificially enlarged uncertainty of the gas density, the results will not be modified much; if for any reason the average particle density were to be a factor of 2 smaller or larger, the γ-ray integral flux variations would be within 4% for energies above 100 MeV, and within 25% for energies above 200 GeV. Table 3.3 shows these results by presenting the integral fluxes above a given threshold if the assumed density of 600 cm^{-3} is doubled or halved. As can be seen in the right panel of Fig. 3.3, if the density is larger (smaller) by a factor ~ 2, the resulting steady proton distribution from the same proton injection population is smaller (bigger) by a similar factor over a wide range of proton energies. As γ-ray emissivities are proportional to both the medium density and the number of steady protons, the variations in γ-ray fluxes are compensated for quite well.

3.1.4.7 Energetics and cosmic ray enhancement

The left panel of Figure 3.9 presents the energy density contained in the steady proton population above a certain energy, i.e., based on Figure 3.2, the curve shows the integral

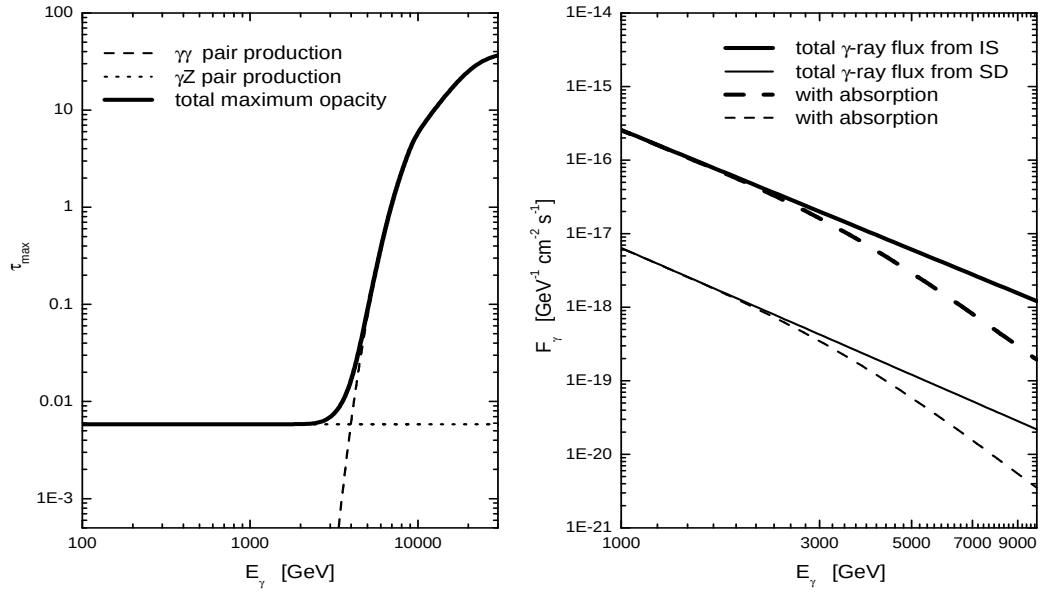

Figure 3.7: Left: Opacities to γ-ray scape as a function of energy. The highest energy is dominated by $\gamma\gamma$ processes, whereas γZ dominates the opacity at low energies. Significant $\tau_{\rm max}$ are only encountered above 1 TeV. Right: Detail of the modification of the γ-ray spectrum introduced by the opacity to γ-ray escape.

$\int_E N_p(E_p)\, E_p\, dE_p$. The total energy density contained by the steady population of cosmic rays above 1 GeV is about 10^{-3} of the power emitted by all supernova explosions in the last 5 million years. The energy density contained in the steady electron population is orders of magnitude less important.

The cosmic ray enhancement is a useful parameter in estimations of γ-ray luminosities in different scenarios. It is defined as the increase in the cosmic ray energy density with respect to the local value, $\omega_{\rm CR,\oplus}(E) = \int_E N_{p\oplus}(E_p) E_p dE_p$, where $N_{p\oplus}$ is the local cosmic ray distribution obtained from the measured local cosmic ray flux. The enhancement factor ς is then a function of energy given by $\varsigma(E) = (\int_E N_p(E_p)\, E_p\, dE_p)/\omega_{\rm CR,\odot}(E)$. Values of enhancement for NGC 253 were proposed $\varsigma < 3000$ for energies above 1 GeV (e.g., Suchkov et al. 1993), what can actually be verified in this model. The right panel of Figure 3.9 presents the enhancement factor as a function of proton energy. The larger

Table 3.2: Exploring the parameter space for p and τ_0. The results of the adopted model are given in the first column. These results already take the opacity to photon escape into account.

$F(E > E_0)$	$p = 2.3$	$p = 2.3$	$p = 2.2$	$p = 2.2$
E_0 [GeV]	$\tau_0 = 10$ Myr	$\tau_0 = 1$ Myr	$\tau_0 = 10$ Myr	$\tau_0 = 1$ Myr
0.1	2.32E-8	2.21E-8	2.95E-8	2.75E-8
200	1.60E-12	4.76E-13	4.04E-12	1.15E-12
600	3.61E-13	8.98E-14	1.00E-12	2.40E-13
1000	1.78E-13	4.10E-14	5.16E-13	1.14E-13
2000	6.29E-14	1.31E-14	1.92E-13	3.87E-14

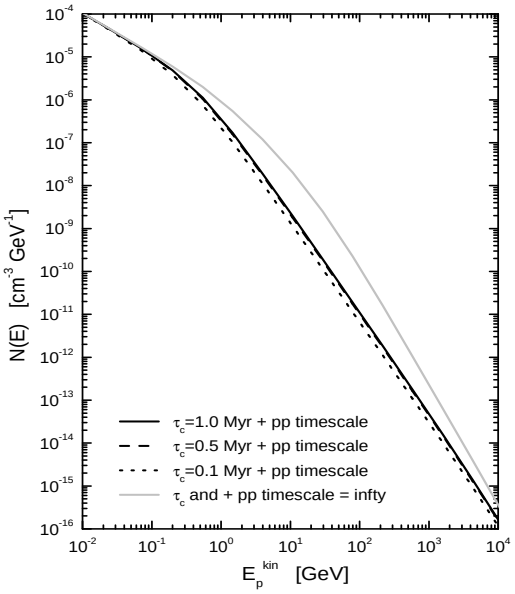

Figure 3.8: Proton distribution when different convective and the pp timescales are taken into account as compared with a (arbitrary) solution when $\tau(E) = \tau_D$, i.e., diffusion only. Clearly, convection plus pp timescales dominates the spectrum.

Table 3.3: The effect of the medium gas density on the γ-ray integral fluxes. Results provided are in units of photons cm^{-2} s^{-1}, and already take the opacity to photon escape into account.

$F(E > E_0)$	n=300 cm^{-3}	n=600 cm^{-3}	n=1200 cm^{-3}
$E_0 = 100$ Mev	2.22E-8	2.32E-8	2.37E-8
$E_0 = 200$ Gev	1.20E-12	1.60E-12	1.95E-12
$E_0 = 600$ Gev	2.60E-13	3.61E-13	4.52E-13
$E_0 = 1$ Tev	1.26E-13	1.78E-13	2.26E-13
$E_0 = 2$ Tev	4.36E-14	6.29E-14	8.09E-14

the energy, the larger the enhancement, due to the steep decline ($\propto E^{-2.75}$) of the local cosmic ray spectrum.

3.1.5 HESS observations of NGC 253

The HESS array has just released (Aharonian et al. 2005c) their results for NGC 253. These are based on data taken during the construction of the array. The total observation time was 28 hs, with a mean zenith angle of about 14 degrees. Only events where at least two telescopes were triggered were used, to enable stereoscopic reconstruction. The energy threshold for this dataset was 190 GeV. The angular distribution of γ-ray photons and significance are shown in Figures 3.10 and 3.11 using the two standard HESS method of analysis. Upper limits from H.E.S.S. on the integral flux of γ-rays from NGC 253 (99 % confidence level) are shown, together with the obtained predictions, in the right panel of Figure 3.6, and zoomed in the region above 100 GeV in Figure 3.12. As an example, above 300 GeV, the upper limit is 1.9×10^{-12} photons cm^{-2} s^{-1}. It can be seen that the

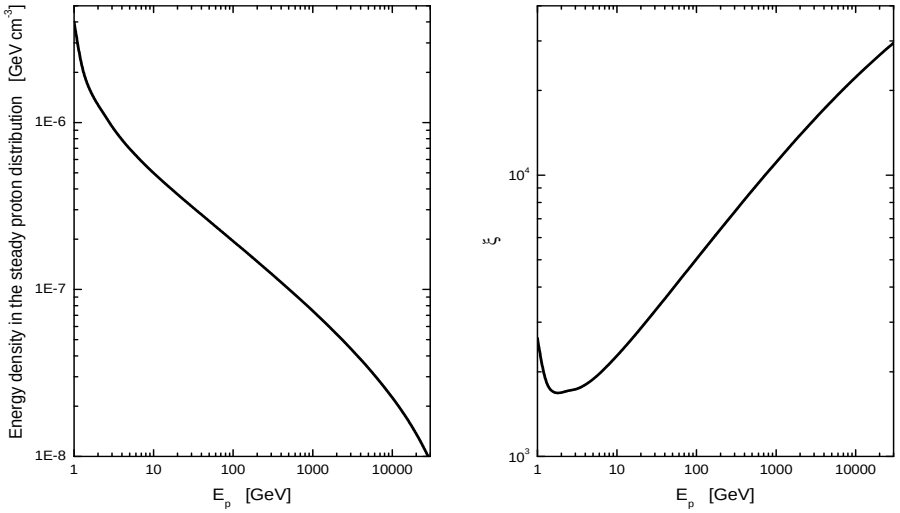

Figure 3.9: Left: Energy density contained in the steady population of protons above the energy given by the x-axis. Right: Cosmic ray enhancement factor obtained from the steady spectrum distribution in the innermost starburst nucleus of NGC 253.

predictions are below these upper limits at all energies but still above HESS sensitivity for reasonable observation times. It is herein proposed that a further observation of NGC 253 by HESS could lead to its detection.

3.1.6 Summary of NGC 253 modeling

A multifrequency model of the central region of NGC 253 has been presented. Following recent observations, an innermost starburst with a radius of 100 pc and a supernova explosion rate of 0.08 yr^{-1}, and a surrounding disk up to a 1 kpc in radius with an explosion rate about tenfold smaller has been modelled. As a result of this modeling, a magnetic field of 300 μG for the innermost region is consistent with high resolution radio observations, with the radiation at 1 GHz being significantly produced by secondary electrons of cosmic ray interactions. The magnetic field found for the innermost part of NGC 253 is typical of dense molecular clouds in our Galaxy, and is close to the (270 μG) value proposed by Weaver et al. (2002) using the equipartition argument. Free-free emission and absorption has been considered, as has opacities to the γ-ray escape. The hard X-ray emission from IC and bremsstrahlung processes produced in this model is below observational constraints, e.g., by OSSE, in agreement with previous estimations of bremsstrahlung diffuse emission (Bhattacharya et al. 1994). This is consistent with measurements in the center of the Galaxy, where INTEGRAL have shown that hard X-ray emission is not diffusively, but produced by point like sources (Lebrun et al. 2004).

The flux predicted is based on a set of a few well founded assumptions, mainly a) that supernova remnants accelerate most of the cosmic rays in the central region of NGC 253, and b) that they interact with the present gas, whose amount has been measured using a variety of techniques. The low opacity to γ-ray escape secure that basically all γ-rays produced in the direction towards Earth reach us. Observational constraints establishes the values of the supernova explosion rate and gas content. The ease of all the assumptions made in the model, its concurrence with all observational

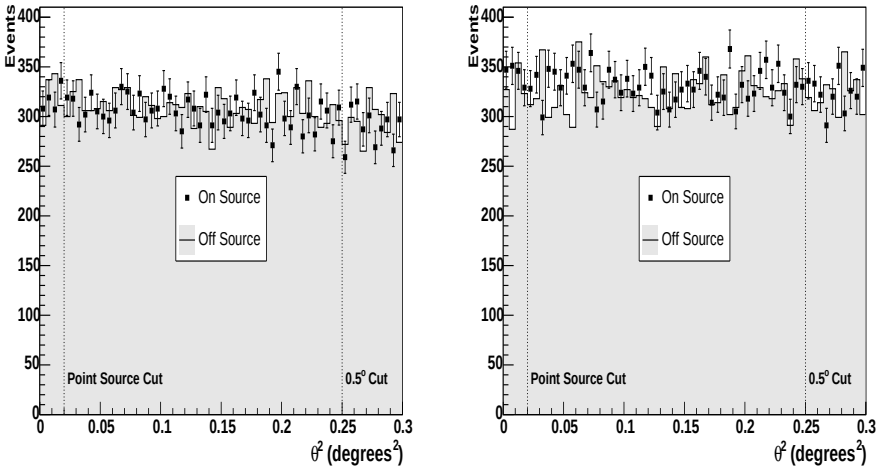

Figure 3.10: Top left: Angular distribution of γ-like images relative to the centre of NGC 253 (On) and relative to the background control region (Off) for HESS Analysis method 1. Events are plotted versus the squared angular distance to give equal solid angle in each bin. Background curves (histograms) are determined relative to points 1 degree away from the source position. Top right: idem but using HESS Analysis method 2 (for description of these two methods see Aharonian et al. (2005c). Courtesy of the HESS collaboration.

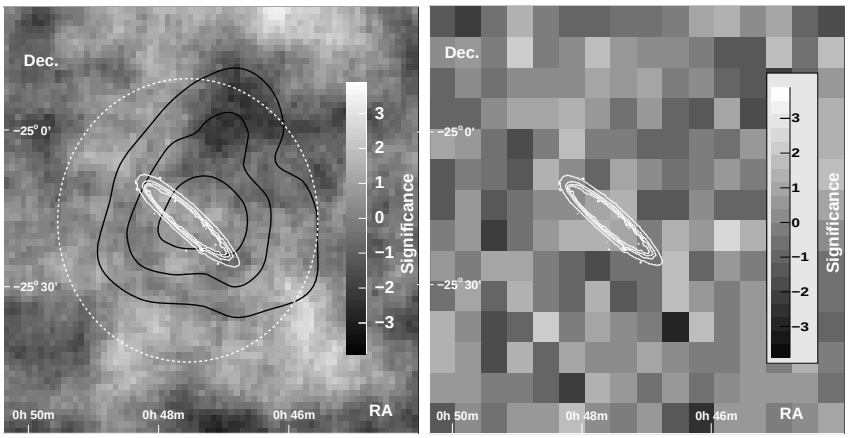

Figure 3.11: Left: γ-ray point source significance map (grey-scale) derived from two telescope HESS data taken in August and September 2004, using Analysis 1. The white contours show the optical emission from the galaxy (in a linear scale) using data from the STScI Digitized Sky Survey. Black contours are confidence levels (at 40%, 65% and 80%) for TeV γ-ray emission reported by CANGAROO collaboration. The dashed white line shows the angular cut used to derive extended source flux limits. Right: Significance map derived from the same dataset using Analysis 2. In contrast to the left panel the statistical significance in each bin is independent. The bin size is matched to the angular resolution of the instrument for these data. Courtesy of the HESS collaboration.

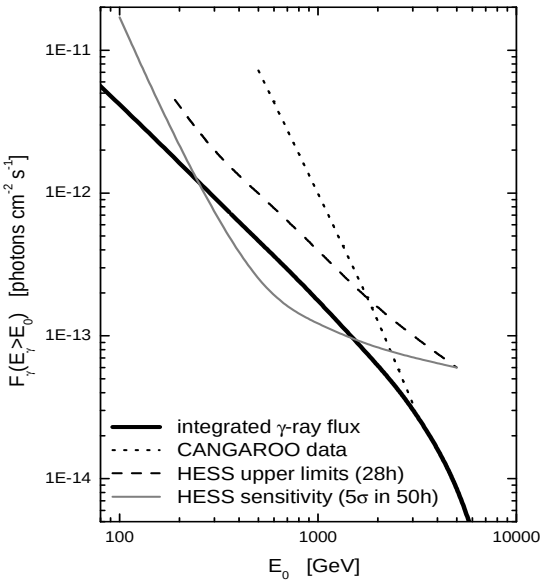

Figure 3.12: Integral γ-ray fluxes produced in this model zoomed in the region above 100 GeV. The CANGAROO integral flux as estimated from their fit, and the HESS sensitivity (5σ detection in 50 hours) are given, together with HESS upper limits. Absorption effects are already taken into account.

constraints, and the unavoidability of the processes analyzed, lead us to conclude that 1) GLAST will detect NGC 253, being the predicted luminosity (2.3×10^{-8} photons cm^{-2} s^{-1} above 100 MeV) well above its 1 yr all sky survey sensitivity (GLAST Science Requirements Doc. 2003); 2) that the predicted TeV fluxes are about one order of magnitude smaller than what was claimed by CANGAROO, and thus, that perhaps in this case, a similar problem to that found in other sources affected their data taking or analysis, and 3) that HESS could detect the galaxy as a point like source provided it is observed long enough ($\gtrsim$ 50 hours, for a detection between 300 and 1000 GeV.) [5] This model predicts a steady γ-ray source, so that a posteriori variability estimators (e.g., Torres et al. 2001) can be checked for consistency.

3.2 Comments on an emission model of the nearest ULIRG

Torres (2004) developed a complete multiwavelength model of Arp 220, as the first application of the numerical code $\mathcal{Q}$-DIFFUSE. At that moment, Blattnig et al. (2000) parameterization of the Stephens and Badhwar's (1981) pp interaction cross section was incorporated into the code to compute the γ-ray production through neutral pion decay. However, as shown (see Appendix B), extrapolating such parameterization to high energies overestimates γ-ray fluxes. In this Section, a recalculation of the γ-ray spectra expected from Arp 220 which is devoid of these problems is presented.

[5] HESS site latitude provides that NGC 253 can be observed very close to the zenith (the minimum zenith angle for NGC 253 from HESS site is 2 degrees). As a consequence, HESS observations of NGC 253 can be done with the minimum energy threshold of the experiment. The MAGIC Telescope, although being at a northern hemisphere site, is also able to observe NGC 253 at a larger zenith angle, about 53 degrees.

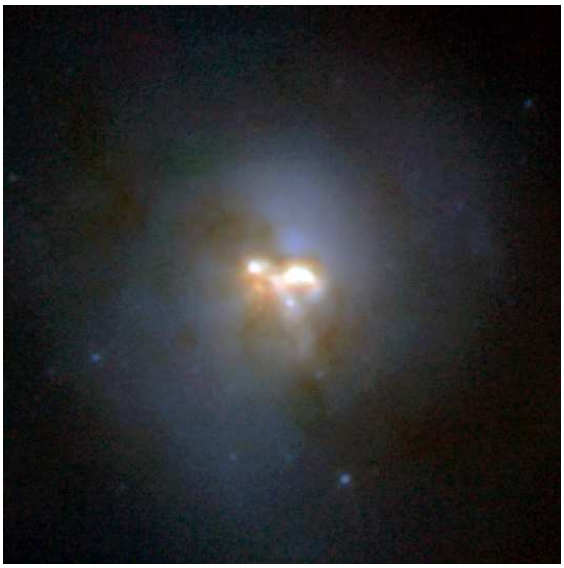

Figure 3.13: A near-infrared image of the peculiar galaxy Arp 220 from the Hubble Space Telescope. More luminous than 100 Milky Ways and radiating most of its energy in the infrared, Arp 220 is a ULIRG. It is likely the result of a collision of 2 spiral galaxies.

Table 3.4: Some properties of Arp 220's extreme starbursts.

Property	West	East
Geometry	sphere	sphere
Radius [pc]	68	110
Average gas density (H_2) [cm^{-3}]	1.8×10^4	8.0×10^3
Luminosity (FIR) [$L_\odot$]	0.3×10^{12}	0.2×10^{12}

3.2.1 Some words on phenomenology of Arp 220

Arp 220's center has two radio-continuum and two IR sources, separated by ~ 1 arcsec (e.g., Scoville et al. 1997, Downes et al. 1998, Soifer et al. 1999, Wiedner et al. 2002). The two radio sources are extended and nonthermal (e.g., Sopp & Alexander 1991; Condon et al. 1991; Baan & Haschick 1995), and likely produced by supernovae in the most active star-forming regions. CO line, cm, mm-, and sub-mm continuum (e.g., Downes & Solomon 1998) as well as recent HCN line observations (e.g., Gao & Solomon 2004a,b) are all consistent with these two sources being sites of extreme star formation and having very high molecular densities. Arp 220 is also an OH megamaser galaxy, as first discover by Baan et al. (1982). The 1.6 GHz continuum emission of Arp 220 has a double component structure too, with the two components being separated by about 1 arcsec and located at the same positions as the 1.4 GHz, the 4.8 GHz, and the 1.3 mm emission (see, e.g., Rovilos et al. 2002, 2003). In the eastern nucleus, the position of the maser coincide with that of the continuum. In the western one, the OH maser emission arises from regions north and south from the continuum (Rovilos et al. 2002, 2003).

Different characteristics of the two extreme starbursts and the molecular disk, some of which are used as input in Torres (2004) modeling, are given in tables 3.4 and 3.5, as derived by Downes and Solomon (1998). Torres' (2004) model adopted Downes and

Table 3.5: Some properties of Arp 220's disk.

Property	Value
Geometry	cylinder
Thickness [pc]	90
Outer radius [pc]	480
Inclination from face-on	40^o
Average gas density within the outer radius (H_2) [cm^{-3}]	1.2×10^3
Luminosity (FIR) [$L_\odot$]	0.7×10^{12}

Table 3.6: Parameters for radio modeling.

Component	Magnetic Field	Critical Frequency
western starburst	6.5 mG	0.38 GHz
eastern starburst	4.5 mG	2.86 GHz
disk	280 μG	0.07 GHz

Solomon's (1998) value of Arp 220 luminosity distance: 72.3 Mpc. For further details and discussion on other authors treatment of the object see Torres (2004). The model assumed the geometry of the central region of Arp 220 as sketched in Figure 3.14, not to scale. The CO disk is inclined 40° from face-on, Arp 220-west (one of the extreme starbursts) is assumed spherical, with a radius of 68 pc. Similarly, Arp 220-east has a radius of 110 pc. The disk thickness is 90 pc. The rotational curve of the CO disk indicates a dynamical mass of at least 12×10^9 $M_\odot$ interior to the outer disk radius, of 480 pc, which corresponds to the central bulge mass of a large spiral like the Milky Way. The gas mass in each of the two extreme starburst nuclei is at least 6×10^8 $M_\odot$. Their individual FIR luminosities are $\sim 3 \times 10^{11}$ $L_\odot$. About half of the Arp 220 FIR luminosity comes from the molecular disk. The masses of the two extreme starbursts are negligible in comparison with the mass that controls the motion of the molecular disk. The gas density quoted in tables 3.4 and 3.5 corresponds only to estimates of molecular hydrogen, thus the total density ought to be larger, perhaps especially in the disk. Therefore, from the point of view of target mass, estimates in Torres' (2004) model and in this Section (for instance, neutral pion decay γ-rays) could be regarded as a conservative estimation. Values of the magnetic fields in the different regions of Arp 220 needed to reproduce the observed radio and infrared spectrum are summarized in Table 3.6.

3.2.2 High energy γ-ray fluxes and observability

At the time Torres 2004 multiwavelength model for Arp220 was made, it was unclear whether the Blattnig et al. (2000) parameterization, which actually produces the right total cross section at all energies, would also produce the correct differential cross section above 100 GeV. This parameterization was then incorporated into the $\mathcal{Q}$-DIFFUSE code to compute the neutral pion γ-ray production. As discussed in Appendix B, this yield to overestimate of fluxes above 100 GeV, where Blattnig et al. parameterization should not be used. New estimates of the neutral pion decay contribution to the γ-ray flux expected from Arp 220 have been calculated using more reliable approaches to the cross section

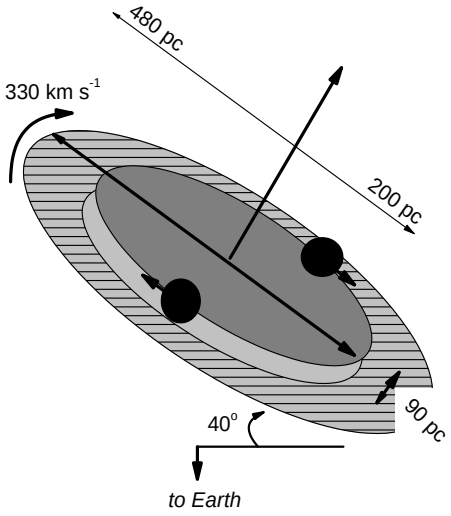

Figure 3.14: Geometry and different components in the model of Arp 220. Two central spherical *nuclei* are extreme regions of star formation, and co-rotate with the molecular disk.

at high energies, and are shown in Figure 3.15 (see Appendix B for a discussion on the parameterizations used). This comparison uses the same galactic model as Torres 2004 in every other respect (e.g., an injection proton distribution following a power law in proton kinetic energies with slope index 2.2), but just different differential cross sections.

Although the prediction of a possible detection of Arp 220 by the GLAST satellite is supported (all parameterizations provide the same result at energies lower than few hundred GeV), its detection in the IACTs regime now looks much more difficult. The total predicted fluxes in γ-rays above 300 GeV and 1 TeV are $\sim 3 \times 10^{-13}$ photons cm^{-2} s^{-1} and $\sim 8 \times 10^{-14}$ photons cm^{-2} s^{-1}, respectively. It can be seen in Figure 3.15 that Arp 220 is barely below the HESS sensitivity curve (which has however to observe Arp 220 at large zenith angle because of its location) and also below MAGIC capabilities unless very deep observations are performed.

3.3 Concluding remarks

The HESS colaboration, due to the location of its array in the southern hemisphere, will continue to add observation time towards NGC 253. Soon, the model for this galaxy presented in this Chapter will be directly tested. Should NGC 253 still elude detection, what is not expected provided enough observation time, feedback onto some of the fundamental assumption of the model will proceed. On the contrary, if a detection confirming this model is reported, confidence in that the basic aspects of diffuse emission of γ-rays in starburst are understood will be built up. Arp 220 has been observed by MAGIC, although with much more less integration time than needed for detection. These observations are reported in Chapter 8.

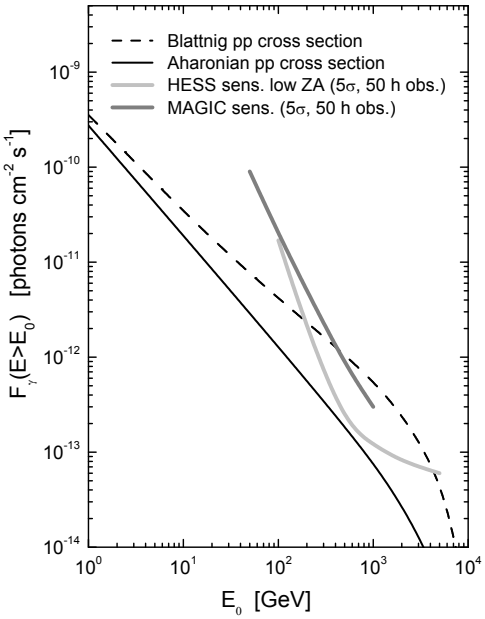

Figure 3.15: Total integral flux predictions for Arp 220. The dashed line shows the results obtained with the $\mathcal{Q}$-DIFFUSE numerical package using Blattnig et al. (2000) parameterization of the pp cross section; the solid line shows the fluxes obtained with the same model but using other cross sections (Aharonian & Atoyan, or Kamae et al.). The HESS and MAGIC telescopes sensitivities, 50 hours of observation time for a 5σ detection, for low zenith angles (although note that this is shown here just for quick comparison, since HESS can only observed Arp 220 above $\sim 50^{\circ}$), are also shown to remark the differences in predictions for observability that the use of one or other cross section can induce. Absorption effects are already taken into account in both cases.

Chapter 4

Galactic sites of star formation: OB associations

It is here proposed that the interaction between relativistic protons resulting from Fermi first order acceleration in the superbubble of a stellar OB association or in other nearby accelerator and ions residing in single stellar winds of massive stars could lead to TeV sources without strong counterparts at lower energies. The expected γ-ray emission from these regions, considering in an approximate way the effect of cosmic ray modulation, is computed here. Secondary particle production is calculated, and the loss equation is solved. Examples where configurations may produce sources for the GLAST satellite, and the MAGIC, HESS, and VERITAS telescopes in non-uniform ways, i.e., with or without the corresponding counterparts, are shown. This Chapter is partially based on the papers by Torres, Domingo-Santamaría & Romero 2004 and Domingo-Santamaría & Torres 2005b.

4.1 Introduction

Early-type stellar associations have long been proposed as cosmic ray acceleration sites (Cesarsky & Montmerle 1983, Manchanda et al. 1996, Bozhokin & Bykov 1994, Parizot et al. 2004, also Dorman 1999, Romero et al. 1999). For instance, it is expected that collective effects of strong stellar winds and supernova explosions at the core of the associations will produce a large-scale shock (the supperbubble region) which will accelerate particles up to energies of hundreds of TeV (e.g., Bykov & Fleishman 1992a,b; Bykov 2001). Such relativistic particles, if colliding with a dense medium, may produce significant γ-ray emission, mainly through hadronic interactions.

O, B and WR stars, lose a significant fraction of their mass in their winds. Indeed, the ultimate result of a stellar wind with a high mass-loss rate is to give back gas mass to the interstellar medium (ISM). A distinction is made between the mass that is still contained in single or collective winds of massive stars (in movement) and the mass that is free in the ISM (at rest). If star formation is on-going, the latter would greatly dominate, since only a fraction of the total gas mass contained in the association is transferred into stars. However, when the star formation is coeval and is currently ended, and particularly if one or several supernova explosions have pushed away the free gas mass of the region, or when the stars under consideration are located in the outskirts of a larger association, the mass contained in the innermost regions of the winds can exceed that contained in a

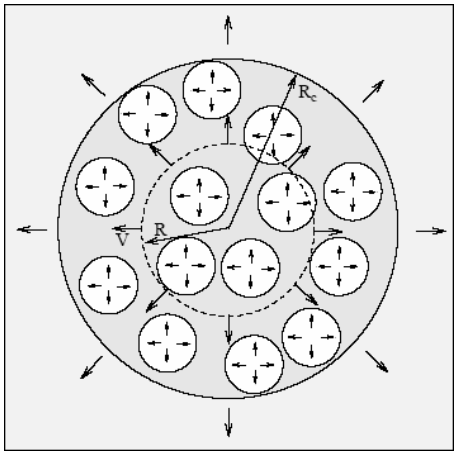

Figure 4.1: Schematic diagram showing the wind-wind interaction that takes place in a dense stellar cluster or sub-cluster. The stars are assumed to be uniformly distributed within the outer radius of the cluster. The material ejected from the R_c stars goes through stellar wind shocks (drawn as circles) and then participates in an outward flow [with mean velocity $V(R)$ and density $n(R)$] which eventually leaves the cluster and interacts with the surrounding interstellar matter. After Canto et al. (2000).

similarly sized area of the ISM. When computing hadronic γ-ray luminosities, the mass in winds cannot be considered negligible in these situations.

Consequently, the winds of a group of massive stars, particularly if located close to a cosmic ray acceleration region, may act as an appropriate cosmic ray target (e.g., Romero & Torres 2003). Because of the wind modulation of the incoming cosmic ray flux, discussed in more detail below, only high energy particles will be able to penetrate into the wind. Thus, only high energy photons might be generated copiously enough to be detected. The proposed scenario may then predict new potential sources for the new generation of ground-based Čerenkov telescopes, which would at the beginning be unidentified due of their lack of a lower energy counterpart.[1] In view of the several unidentified sources already detected by HESS in the hundred of GeV – TeV energy regime (Aharonian et al. 2005e), the aim of this Chapter is to evaluate this possibility.

4.2 The gas within a collective wind

The model of Cantó et al. (2000) is adopted (see also Chevalier & Clegg 1985, Ozernoy et al. 1997, Stevens & Hartwell 2003) to describe the wind of a cluster (or a sub-cluster) of stars. This is a hydrodynamical model that does not consider the effects of magnetic fields; see next section for further discussion on the expected (low) values of the magnetic field in the collective wind region.

Imagine that there are N stars in close proximity, uniformly distributed within a radius R_c, with a number density

$$n = \frac{3N}{4\pi R_c^3}\,. \tag{4.1}$$

[1]For an alternative scenario for producing sources in the GeV-TeV regime in non-uniform ways see Bosch-Ramon et al. (2005).

See Figure 4.1 for an schematic drawing of the configuration. Each star has its own mass-loss rate ($\dot{M}_i$) and (terminal) wind velocity (V_i), and average values can be defined as

$$\dot{M}_w = \frac{1}{N}\sum_i^N \dot{M}_i\,, \tag{4.2}$$

$$V_w = \left(\frac{\sum_i^N \dot{M}_i {V_i}^2}{N\,\dot{M}_w}\right)^{1/2}\,. \tag{4.3}$$

All stellar winds are assumed to mix with the surrounding ISM and with each other, filling the intra-cluster volume with a hot, shocked, collective stellar wind. A stationary flow in which mass and energy provided by stellar winds escape through the outer boundary of the cluster is established. For an arbitrary distance R from the center of the cluster, mass and energy conservation imply that

$$\frac{4\pi}{3}R^3 n\dot{M}_w = 4\pi R^2\rho V\,, \tag{4.4}$$

$$\frac{4\pi}{3}R^3 n\dot{M}_w\left(\frac{1}{2}{V_w}^2\right) = 4\pi R^2\rho V\left(\frac{1}{2}V^2+h\right)\,, \tag{4.5}$$

where ρ and V are the mean density and velocity of the cluster wind flow at position R and h is its specific enthalpy (sum of internal energy plus the pressure times the volume),

$$h = \frac{\gamma}{\gamma-1}\frac{P}{\rho}\,, \tag{4.6}$$

with P being the mean pressure of the wind and γ being the adiabatic index (hereafter $\gamma = 5/3$ to fix numerical values). From the mass conservation equation one obtains

$$\rho V = \frac{n\dot{M}_w}{3}R\,, \tag{4.7}$$

whereas the ratio of the two conservation equations imply

$$\frac{1}{2}V^2 + h = \frac{1}{2}{V_w}^2\,. \tag{4.8}$$

The equation of motion of the flow is

$$\rho V\frac{dV}{dR} = -\frac{dP}{dR} - n\dot{M}_w V\,, \tag{4.9}$$

which, introducing the adiabatic sound speed c,

$$c^2 = \gamma\frac{P}{\rho}\,, \tag{4.10}$$

can be written as

$$\rho V\frac{dV}{dR} = -\frac{1}{\gamma}\frac{d(\rho c^2)}{dR} - n\dot{M}_w V\,. \tag{4.11}$$

From the definition of enthalpy and Equation (4.8), the adiabatic sound speed can be expressed as

$$c^2 = \frac{\gamma-1}{2}({V_w}^2 - V^2)\,. \tag{4.12}$$

Using Equation (4.7), its derivative $d\rho$ and Equation (4.12) in (4.11) one obtains

$$\frac{dR}{R} = \frac{dV}{V}\left[\frac{(\gamma-1){V_w}^2 - (\gamma+1)V^2}{(\gamma-1){V_w}^2 + (5\gamma+1)V^2}\right], \tag{4.13}$$

which can be integrated and expressed in more convenient dimensionless variables ($v \equiv V/V_w$ and $r \equiv R/R_c$) as follows

$$v\left[1 + \frac{5\gamma+1}{\gamma-1}v^2\right]^{-(3\gamma+1)/(5\gamma+1)} = Ar\,, \tag{4.14}$$

with A an integration constant.

When $R > R_c$, i.e., outside the cluster, by definition n is equal to 0, and the mass conservation equation is

$$\dot{M}_{\rm assoc} \equiv \frac{4\pi}{3}{R_c}^3 n\dot{M}_w = 4\pi R^2\rho V\,, \tag{4.15}$$

where the middle equality gives account of the contribution of all stars in the association, and $\dot{M}_{\rm assoc} = \sum_i \dot{M}_i$ is the mass-loss rate at the outer boundary R_c. Substituting Equation (4.12) and (4.15) into the $n = 0$ realization of Equation (4.11) one obtains

$$-\frac{dR}{R} = \frac{dV}{V}\left[\frac{(\gamma-1){V_w}^2 - (\gamma+1)V^2}{2(\gamma-1)(V_w^2 - V^2)}\right], \tag{4.16}$$

and integrating, the velocity in this outside region is implicitly defined from

$$v(1-v^2)^{1/(\gamma-1)} = Br^{-2}, \tag{4.17}$$

with B an integration constant. Having constants A and B in Equations (4.14) and (4.17), see below, the velocity at any distance from the association center can be determined by numerically solving its implicit definitions, and hence the density is also determined, through Equation (4.7) or (4.15).

From Equation (4.17), two asymptotic branches can be found. When $r \to \infty$, either $v \to 0$ (asymptotically subsonic flow) or $v \to 1$ (asymptotically supersonic flow) are possible solutions. The former one (subsonic) produces the following limits for the density, the sound speed and the pressure

$$\rho_\infty = \frac{\dot{M}_{\rm assoc}}{4\pi B{R_c}^2 V_w}\,, \tag{4.18}$$

$$c_\infty^2 = \frac{\gamma-1}{2}{V_w}^2\,, \tag{4.19}$$

$$P_\infty = \frac{\gamma-1}{2\gamma}\frac{\dot{M}_{\rm assoc}V_w}{4\pi B{R_c}^2}\,. \tag{4.20}$$

From (4.20), if P_∞ is the ISM pressure far from the association, the constant B can be obtained as

$$B = \frac{\gamma-1}{2\gamma}\frac{\dot{M}_{\rm assoc}V_w}{4\pi P_\infty {R_c}^2}\,. \tag{4.21}$$

The velocity of the flow at the outer radius $r = 1$ follows from Equation (4.17)

$$v_{r=1}(1-{v_{r=1}}^2)^{1/(\gamma-1)} = B\,, \tag{4.22}$$

and continuity implies that

$$v_{r=1}\left[1+\frac{5\gamma+1}{\gamma-1}{v_{r=1}}^2\right]^{-(3\gamma+1)/(5\gamma+1)} = A\,. \tag{4.23}$$

Equation (4.14) implicitly contains the dependence of v with r in the inner region of the collective wind. Its left hand side is an ever increasing function. Thus, for the equality to be fulfilled for all values of radius ($0< r <1$), the right hand side of the equation must reach its maximum value at r=1. Deriving the right hand side of Eq. (4.14), one can find the velocity that makes it maximum

$$v_{\max} = \left(\frac{\gamma-1}{\gamma+1}\right)^{1/2}\,. \tag{4.24}$$

Since v grows in the inner region, the maximum velocity is reached at $r = 1$, and from Equation (4.22),

$$B = \left(\frac{\gamma-1}{\gamma+1}\right)^{1/2}\left(\frac{2}{\gamma+1}\right)^{1/(\gamma-1)}\,. \tag{4.25}$$

Continuity (Equation 4.23) implies that the value of A is

$$A = \left(\frac{\gamma-1}{\gamma+1}\right)^{1/2}\left(\frac{\gamma+1}{6\gamma+2}\right)^{(3\gamma+1)/(5\gamma+1)}\,. \tag{4.26}$$

With the former value of B, and from Equation (4.21), if

$$P_\infty < \frac{1}{\gamma}\left(\frac{\gamma-1}{\gamma+1}\right)^{1/2}\left(\frac{\gamma+1}{2}\right)^{\gamma/(\gamma-1)}\frac{\dot{M}_{\rm assoc}V_w}{4\pi R_c^2}\,, \tag{4.27}$$

the subsonic solution is not attainable (continuity of the velocity flow is impossible) and the supersonic branch is the only physically viable. In this regime, the flow leaves the boundary of the cluster R_c at the local sound speed $v_{\max}$ (equal to 1/2 for $\gamma = 5/3$) and is accelerated until $v = 1$ for $r \to \infty$.

Figure 4.2 shows four examples of the supersonic flow (velocity and particle density) for a group of stars generating different values of $\dot{M}_{\rm assoc}$, V_w, and R_c, as given in Table 4.2. The total mass contained up to 10 R_c is also included in that Table. A typical configuration of a group of tens of stars (see next Section) may generate a wind in expansion with a velocity of the order of 1000 km s^{-1} and a mass between tenths and a few solar masses within a few pc (tens of R_c). Hadronic processes with this matter are discussed below.

4.3 Mass loss rates and terminal velocities of individual stars

To estimate how many stars, and of what kind, are needed to obtain certain averages for the association parameters, the theoretical wind model C of Leitherer, Robert & Drissen (1992) is adopted. This model, referred to as Model THEOR in Leitherer et al. (1999), is the standard model used in the synthesis program STARBURST99 to compute spectrophotometric and statistics of starburst regions.[2] Characteristic mass-loss rates

[2]http://www.stsci.edu/science/starburst99

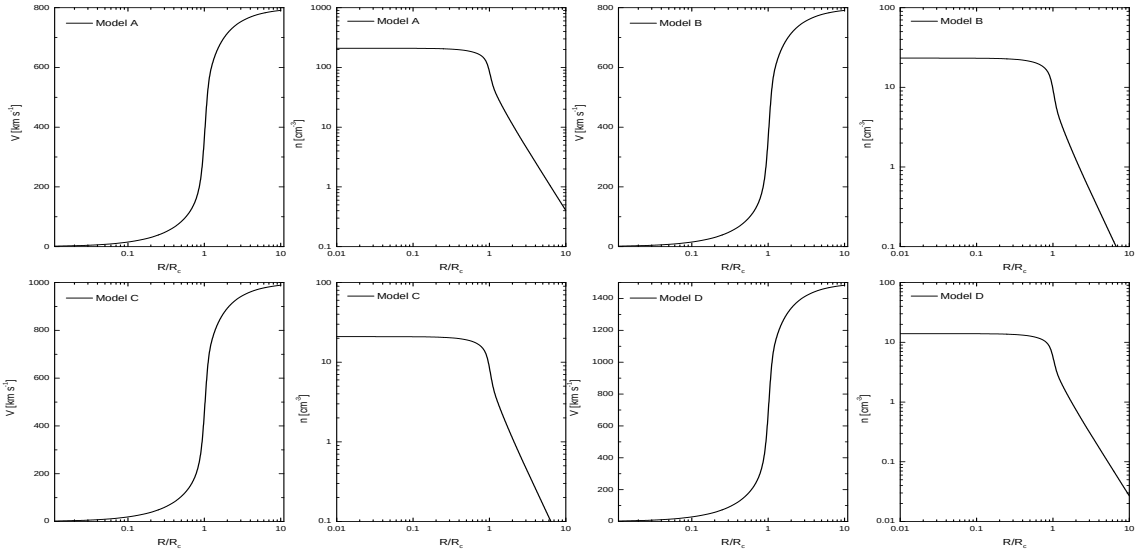

Figure 4.2: Examples of configurations of collective stellar winds. Main parameters are as in Table 1.

Table 4.1: Examples of configurations of collective stellar winds. The mass is that contained within 10 R_c. n_0 is the central density.

Model	$\dot{M}_{\rm assoc}$ [$M_\odot$ yr^{-1}]	V_w [km s^{-1}]	R_c pc	n_0 cm^{-3}	Wind mass [$M_\odot$]
A	10^{-4}	800	0.1	210.0	0.13
B	10^{-4}	800	0.3	23.3	0.39
C	5×10^{-5}	1000	0.2	20.9	0.11
D	2×10^{-4}	1500	0.4	13.9	0.56
E	2×10^{-4}	2500	0.2	33.5	0.17

and terminal velocities are uncertain (typically about $\sim 30\%$). Varying the mass-loss rate and terminal velocity to those corresponding to other models will have an impact in any γ-ray luminosity computation. Alternative parameterizations to the ones below for $\dot{M}_\star$ and V_∞ can be found, for instance, in the work by Vink. et al. (2000).

For WR stars[3], mass-loss rates are based on observations by van der Hucht et al. (1986) and Prinja et al. (1990). Average terminal velocities have been taken from Prinja (1990). For O and B stars, the parameterizations of $\dot{M}$ ($M_\odot$ yr^{-1}) and V_∞ (km s^{-1}) in terms of stellar parameters (Leitehrer et al. 1992, 1999) are used, also part of Model THEOR. A multidimensional fit to $\dot{M}$ ($M_\odot$ yr^{-1}) and V_∞ (km s^{-1}) as a function of stellar

[3]The first evolutionary phase of a WR star is the nitrogen-line stage (WNL), which begins when CNO processed material is exposed at the stellar surface. The second stage is the WNE, during which no surface hydrogen is detectable. After the helium envelope is shed, the WC stage occurs, in which strong carbon lines can be seen, and finally, WO stars are formed, with high surface oxygen abundances. Further sub-classifications are made according to line strength ratios (e.g., Smith & Maeder 1991).

Table 4.2: Wind model parameters of WR, O and B stars.

Stellar type	$\log[\dot{M}]$ $M_\odot$ yr^{-1}	V_∞ [km s^{-1}]
WNL	-4.2	1650
WNE	-4.5	1900
WC6-9	-4.4	1800
WC4-5	-4.7	2800
WO	-5.0	3500
O3	-5.2	3190
O4	-5.4	2950
O4.5	-5.5	2900
O5	-5.6	2875
O5.5	-5.7	1960
O6	-5.8	2570
O6.5	-5.9	2455
O7	-6.0	2295
O7.5	-6.2	1975
O8	-6.3	1755
O8.5	-6.5	1970
O9	-6.7	1500
O9.5	-6.8	1500
B0	-7.0	1000
B0.5	-7.2	500
B1	-7.7	500
B1.5	-8.2	500
B2	-8.6	500
B3	-9.5	500
B5	-10.0	500
B7	-10.9	500
B8	-11.4	500
B9	-12.0	500

luminosity L, mass M, effective temperature $T_{\rm eff}$, and metallicity Z, gives

$$\begin{aligned}\log \dot{M}(\mathrm{M}_\odot\,\mathrm{yr}^{-1}) &= -24.06 + 2.45\log[L(\mathrm{L}_\odot)] \\ &\quad -1.10\log[M(\mathrm{M}_\odot)] + 1.31\log[T_{\rm eff}(K)] \\ &\quad +0.80\log[Z(Z_\odot)], \end{aligned} \tag{4.28}$$

$$\begin{aligned}\log V_\infty(\mathrm{km\,s}^{-1}) &= 1.23 - 0.30\log[L(\mathrm{L}_\odot)] + 0.55\log[M(\mathrm{M}_\odot)] \\ &\quad +0.64\log[T_{\rm eff}(K)] + 0.13\log[Z(Z_\odot)]. \end{aligned} \tag{4.29}$$

In order to obtain the mass-loss rates and terminal velocities, a calibration between the spectral sub-types of the O and B stars and their stellar parameters is needed. For early B and O stars the work by Vacca et al. (1996) is adopted, see their Tables 5-7. Columns 2 and 3 of Table 4.3 show the stellar wind parameters resulting from the previous calibration.

Since in general, many of the stars in a young association will be of luminosity class V, only results for this class are given, although combining this Section with the work by Vacca et al. (1996), values for other classes could be obtained as needed. The values of masses are taken from those derived using evolutionary codes, since as discussed by Vacca et al. (1996), the cause of the mass discrepancy between results from the former codes and spectroscopic analysis seems to be that the models used in the spectroscopic studies do not properly take into account the effects of the wind extension, mass outflow and velocity fields, and are thus less reliable. For B stars of late type, the calibration by Vacca et al. (1996) is completed with that of Humphreys & Mc Elroy (1984), see their Table 2, and Schmidt-Kaler (1982), which give the bolometric corrections, (BC), and effective temperatures. The total luminosity is then computed using the equation

$$\log(L/L_{\odot}) = -0.4(M_v + BC - M_{\mathrm{bol}\,\odot}), \tag{4.30}$$

where $M_{\mathrm{bol}\,\odot} = 4.75$ mag (Vacca et al. 1996). The masses and visual magnitudes M_v of B stars are obtained following the method described in Appendix A of Knödlseder (2000). The radius of each of the stars can be obtained by the usual relationship $R_{\star}^2 = L/(4\pi\sigma T_{\mathrm{eff}}^4)$, where $\sigma = 5.67 \times 10^{-5}$ erg s^{-1} cm^{-2} K^{-4}.

This mass-loss parameterization may yield to an under-estimation for certain stars, and an over-estimation of the terminal velocities, for example in the case of HD 93129A (Benaglia & Koribalski 2004). It is to be remarked that almost 400 Galactic O stars have been compiled in the new 'Galactic O Star Catalogue' (GOS) by Maíz-Apellániz & Walborn (2002), but there are only about a dozen stars known with spectral types O3.5 or earlier, thus limiting the statistical knowledge for comparison. However, this parameterization is sufficient to show that a group of several tens of early stars can reach a $\dot{M}_{\mathrm{assoc}} \sim \mathcal{O}(10^{-5} - 10^{-4})$ M$_{\odot}$ yr^{-1}.

4.4 Modulation and counterparts

As it happens in the solar system for cosmic rays with less energy than $\sim$ 100 MeV, not all cosmic rays will be able to enter the collective wind of several massive stars. The difference between an *inactive target*, as that provided by matter in the ISM, and an *active or expanding target*, as that provided by matter in a single or a collective stellar wind, is given by modulation effects. Although wind modulation has only been studied in detail for the case of the relatively weak solar wind (e.g. Parker 1958, Jokipii & Parker 1970, Kóta & Jokipii 1983, Jokipii et al. 1993), and a proper treatment would have to include a number of different effects like diffusion, convection, particle drifts, energy change, and terminal shock barriers, a first approach to determine whether particles can pervade the wind is to compute the ratio between the diffusion and convection timescales

$$\epsilon = \frac{t_d}{t_c} = \frac{(3R^2/D)}{(3R/V(R))}. \tag{4.31}$$

Here D is the diffusion coefficient, R is the position in the wind, and V is the wind velocity. Only particles for which $\epsilon < 1$ will be able to overcome convection and enter into the wind region to produce γ-rays through hadronic interactions with matter residing there. A similar approach has also been followed by White (1985) when computing the synchrotron emission generated by relativistic particles accelerated in shocks within the wind. In order to obtain an analytic expression for ϵ for a particular star it is considered

that the diffusion coefficient within the (single) wind is given by (White 1985, Völk and Forman 1982)

$$D \sim \frac{1}{3}\lambda_r c, \tag{4.32}$$

where λ_r is the mean-free-path for diffusion in the radial direction (towards the star). The use of the Bohm parameterization seems justified, contrary to the solar heliosphere, since in the innermost region of a single stellar wind there are many disturbances (relativistic particles, acoustic waves, radiatively driven waves, etc.). In the case of a collective wind, the collision of individual winds of the particular stars forming the association also produce many disturbances. A change in the diffusion coefficient (say a flatter dependence on the energy E) will affect the value of the minimum particle energy that protons need to enter into the interacting region (see below). Unless changes in $E_{\rm min}$ are extreme, the results are not significantly affected.

The mean-free-path for scattering parallel to the magnetic field direction is considered to be $\lambda_\parallel \sim 10 r_g = 10E/eB$, where r_g is the particle gyro-radius and E its energy. In the perpendicular direction λ is shorter, $\lambda_\perp \sim r_g$. The mean-free-path in the radial direction is then given by $\lambda_r = {\lambda_\perp}^2 \sin^2\theta + {\lambda_\parallel}^2 \cos^2\theta = r_g(10\cos^2\theta + \sin^2\theta)$, where $\cos^{-2}\theta = 1 + (B_\phi/B_r)^2$. Here, the geometry of the magnetic field for a single star is represented by the magnetic rotator theory (Weber and Davis 1967; see also White 1985; Lamers and Cassinelli 1999, Ch. 9)

$$\frac{B_\phi}{B_r} = \frac{V_\star}{V_\infty}\left(1 + \frac{R}{R_\star}\right) \tag{4.33}$$

and

$$B_r = B_\star \left(\frac{R_\star}{R}\right)^2, \tag{4.34}$$

where $V_\star$ is the rotational velocity at the surface of the star, and $B_\star$ the surface magnetic field. Near the star the magnetic field is approximately radial, while it becomes tangential far from the star, where λ_r is dominated by diffusion perpendicular to the field lines. This approximation leads —when the distance to the star is large compared with that in which the terminal velocity is reached, what happens at a few stellar radii— to values of magnetic field and diffusion coefficient normally encountered in the ISM.

Using all previous formulae,

$$E^{\rm min}(r) \sim \frac{3eB_\star V_\infty (r - R_\star)}{c}\left(\frac{R_\star}{r}\right)^2 \frac{\left(1 + \left(\frac{V_\star}{V_\infty}\left(1 + \frac{r}{R_\star}\right)\right)^2\right)^{3/2}}{10 + \left(\frac{V_\star}{V_\infty}\left(1 + \frac{r}{R_\star}\right)\right)^2}. \tag{4.35}$$

Equation (4.35) defines a minimum energy below which the particles are convected away from the wind. $E^{\rm min}(r)$ is an increasing function of r, the limiting value of the previous expression being

$$E^{\rm min}(r \gg R_\star) \sim \frac{3eB_\star V_\infty R_\star}{c}\left(\frac{V_\star}{V_\infty}\right) \sim 4.3\left(\frac{B_\star}{10{\rm G}}\right)\left(\frac{V_\star}{0.1V_\infty}\right)\left(\frac{R_\star}{12{\rm R}_\odot}\right){\rm TeV}\,. \tag{4.36}$$

Therefore, particles that are not convected away in the outer regions are able to diffuse up to the base of the wind. Note that $E^{\rm min}(r \gg R_\star)$ is a linear function of all $R_\star$, $B_\star$ and $V_\star$, which is typically assumed as $V_\star \sim 0.1V_\infty$ (e.g., Lamers and Cassinelli 1999). There

is a large uncertainty in these parameters, about one order of magnitude. The values of the magnetic field on the surface of O and B stars is under debate. Despite deep searches, only 5 stars were found to be magnetic, with sizeable magnetic fields in the range of $B_\star \sim 100$ G (e.g., Henrichs et al. 2004 and references therein). Typical surface magnetic fields of OB stars are then presumably smaller.

In the kind of collective wind analyzed, a first estimation of the order of magnitude of the energy scale $E^{\min}$ can be obtained considering that the collective wind behaves as that of a single star having a radius equal to R_c. The mass-loss rate is equal to that of the whole association, i.e., $\dot{M}_{\rm assoc}$. The wind velocity at R_c, $V_\star$ is given by Equation (4.24). The order of magnitude of the *surface* magnetic field (i.e., the field at $R = R_c$) is assumed as the value corresponding to the normal decay of a single star field located within R_c, for which a sensitive assumption can be obtained using Equations (4.33) and (4.34), $\mathcal{O}(10^{-6})$ G. This results, for the whole association, in

$$[E^{\min}(r \gg R_\star)]^{\rm assoc} \sim 0.8 \left(\frac{B(R_c)}{1\mu{\rm G}}\right)\left(\frac{R_c}{0.1{\rm pc}}\right) {\rm TeV}. \tag{4.37}$$

The value of the magnetic field is close to that typical of the ISM, and should be consider as an average (this kind of magnetic fields magnitude was also used in modeling the unidentified HEGRA source in Cygnus, see below and Aharonian et al. 2005d). In particular, if a given star is close to R_c its contribution to the overall magnetic field near its position will be larger, but at the same time, its contribution to the opposite region (distant from it 2 R_c) will be negligible. In what follows, hadronic processes up to 10 – 20 R_c are considered, so that a value of the magnetic field typical of ISM values is expected. Two realizations of $[E^{\min}(r \gg R_\star)]^{\rm assoc}$ are considered to give sufficient latitude so to encompass the uncertainties, 100 GeV and 1 TeV.

4.5 Secondaries from a cosmic ray spectrum with a low energy cutoff

4.5.1 The normalization of the cosmic ray spectrum

For normalization purposes, the expression of the energy density that is contained in cosmic rays, $\omega_{\rm CR} = \int_E N(E)\, E\, dE$ is used to compare with the energy contained in cosmic rays in the Earth neighborhood, $\omega_{{\rm CR},\oplus}(E) = \int_E N_\oplus(E)\, E\, dE$, where $N_\oplus$ is the local cosmic ray distribution obtained from the measured cosmic ray flux. The Earth-like spectrum is $J_\oplus(E) = 2.2(E/{\rm GeV})^{-2.75}{\rm cm}^{-2}{\rm s}^{-1}{\rm sr}^{-1}{\rm GeV}^{-1}$ (e.g. Aharonian et al. 2001, Dermer 1986), so that $\omega_{{\rm CR},\oplus}(E > 1{\rm GeV}) \sim 1.5\,{\rm eVcm}^{-3}$. This implicitly defines –as discussed before– an enhancement factor, ς, as a function of energy

$$\varsigma(E) = \frac{\int_E N(E)\, E\, dE}{\omega_{{\rm CR},\oplus}(E)}. \tag{4.38}$$

$N(E)$ is assumed as a power law of the form $N(E) = K_p E^{-\alpha}$. Values of enhancement $\gg$ 100 at all energies are typical of star forming environments (see, e.g., Bykov & Fleishman 1992a,b; Bykov 2001; Suchkov et al. 1993, Völk et al. 1996, Torres et al. 2003, Torres 2004; Domingo-Santamaría & Torres 2005a) and they would ultimately depend on the spectral slope of the cosmic ray spectrum and on the power of the accelerator. For a fixed slope, harder than that found in the Earth environment, the larger the energy the larger

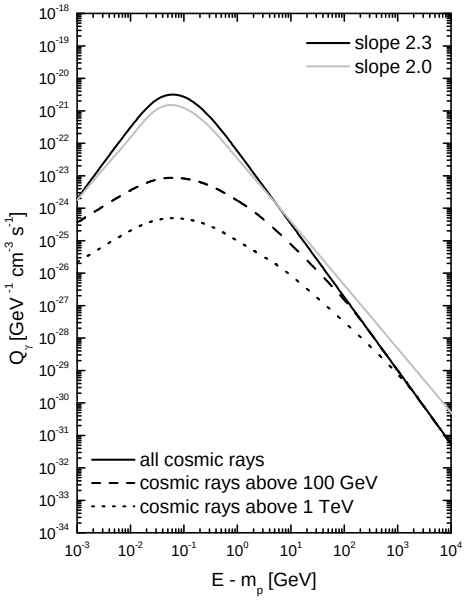

Figure 4.3: Contribution of cosmic rays of different energies to the hadronic γ-ray emissivity. The medium density is normalized to 1 cm^{-3} and the cosmic ray spectrum is proportional to $E^{-2.3}$ (black) and $E^{-2.0}$ (grey), with an enhancement of a thousand when compared with the Earth-like one above 1 GeV. The normalization of each spectrum (of each slope) is chosen to respect the value of enhancement. In the case of the harder spectrum of $\alpha = 2.0$, only the results for the whole cosmic ray spectrum are shown, but a similar decrease in emissivity to that of $\alpha = 2.3$ can be observed if lower energy cutoffs are imposed.

the enhancement, due to the steep decline ($\propto E^{-2.75}$) of the local cosmic ray spectrum. In what follows, as an example, enhancements of the full cosmic ray spectrum (for energies above 1 GeV) of a 1000 are considered. With such fixed ς, the normalization of the cosmic ray spectrum, K_p, can be obtained from Equation (4.38) for all values of the slope. Note that $K_p \propto \varsigma$, and thus the flux and γ-ray luminosity, F_γ and L_γ, are linearly proportional to the cosmic ray enhancement.

4.5.2 Emissivities

The γ-ray emissivity produced by a power law spectrum, with a cosmic ray enhancement of 1000 above 1 GeV, and $\alpha = 2$ and 2.3 is shown in Figure 4.3. This Figure shows the results for the whole spectrum of cosmic rays (all cosmic rays, i.e., all energies above 1 GeV) and for cases when the spectrum has a low energy cutoff (100 GeV and 1 TeV). For the production of secondary electrons, knock-on and pion processes are taken into account, as explained in previous Chapters and their corresponding Appendices. Numerical results for the knock on emissivity are shown in Figure 4.4 left panel for the same spectra. If the cosmic ray spectrum is modulated, the low energy yield of knock-on electrons are dramatically reduced. Only when the electron energies (E_e) are sufficiently large so that the minimum proton energy required to generate them (E_p^{min}) is larger than the modulation threshold, do the emissivities obtained with and without modulation converge.

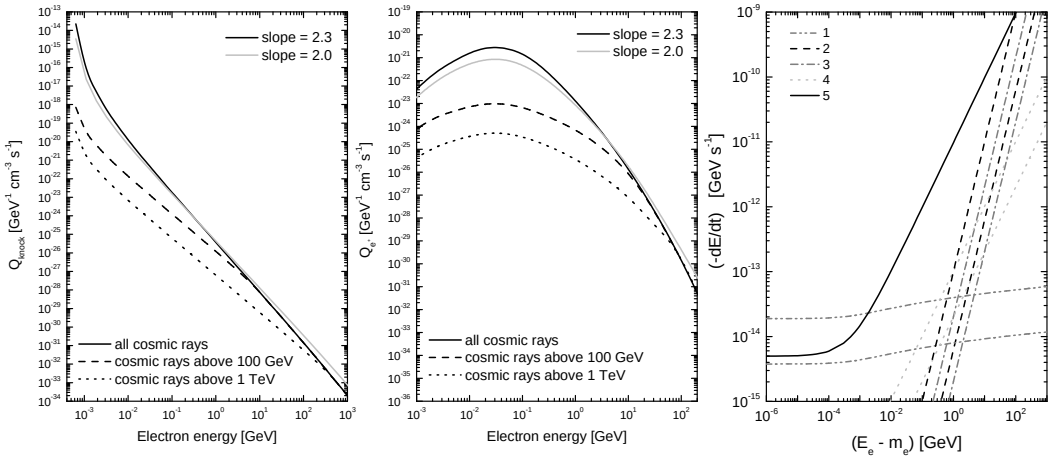

Figure 4.4: The effect of a modulated cosmic ray spectrum (the same as in Figure 4.3 with $\alpha = 2.3$ and 2.0) over the electron knock-on emissivity (*left*) and the positron emissivity (*middle*) of a medium with density $n = 1$ cm^{-3}. Right: Different losses for assumed parameters: Curves 1 correspond to ionization losses for $n = 100$ and 20 cm^{-3}. Curves 2 correspond to synchrotron losses for $B = 50$ and 200 μG (see text). Curves 3 correspond to inverse Compton losses for a photon energy density of 20 and 100 eV cm^{-3}. Curves 4 correspond to Bremsstrahlung losses for $n = 100$ and 20 cm^{-3}. Curve 5 corresponds to adiabatic losses having a ratio V(km s^{-1})/R(pc)=300 (e.g., a wind velocity of 1500 km s^{-1} and a size relevant for the escape of the electrons of 5 pc).

For the charged pion emissivity, numerical results for the case of positrons are presented in Figure 4.4 middle panel. As in the case of the neutral pion photon emissivity, a modulated spectrum would produce much smaller electron and positron emissivities at relatively low energies. This difference can reach several orders of magnitude compared with the spectrum obtained when all cosmic rays interact.

4.5.3 Electron energy losses and distribution

Having the emissivities of secondary electrons, the electron distribution is solve through the diffusion-loss equation. This is $\frac{N(E)}{\tau(E)} - \frac{d}{dE}\left[b(E)N(E)\right] = Q(E)$, where $Q(E)$ represents all the source terms appropriate to the production of electrons and positrons with energy E, $\tau(E)$ stands for the confinement timescale, $N(E)$ is the distribution of secondary particles with energies in the range E and $E+dE$ per unit volume, and $b(E) = -\left(dE/dt\right)$ is the rate of energy loss. The energy losses considered are those produced by ionization, inverse Compton scattering, bremsstrahlung, synchrotron radiation, and the expansion of the medium. A number of uncertain parameters enters into the computation of these losses. Most notably, these parameters are the medium density n affecting bremsstrahlung and ionization losses, the magnetic field B affecting synchrotron losses, the photon target field affecting inverse Compton losses, and the velocity of the expanding medium and the size relevant for escape, affecting the expansion losses.

Figure 4.4 right panel shows the rate of energy loss for a range of parameters. Results are for $n = 100$ and 20 cm^{-3} and magnetic fields are allowed to reach up to 200 μG in the collective wind region. The latter is made to enhance –on purpose– the synchrotron loss and to better shown the dominance of the other loss mechanisms over them. Inverse

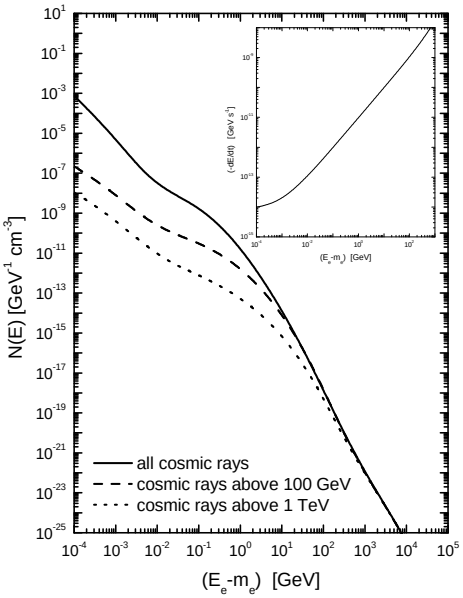

Figure 4.5: Secondary electron distribution obtained by numerically solving the loss equation. The primary cosmic ray spectrum is the same as in Figure 4.3 with $\alpha = 2.3$, and results are shown for different low energy cutoffs. The average density is assumed as $n = 20$ cm^{-3}, the magnetic field is assumed as 50 μG, and the size relevant to escape the modulating region is 5 pc. The inset shows the total energy loss rate $b(E)$.

Compton losses are computed using two different normalization for the energy density when the photon target is considered to be a blackbody distribution with $T_{\rm eff}$=50000 K. The expansion losses have the form

$$-\left(\frac{dE}{dt}\right)_{\rm Adia,}{}_{e} = \frac{V}{R}\left(\frac{E}{\rm GeV}\right) \rm GeV\ s^{-1}$$
$$= 3.24\times10^{-14}\left(\frac{V}{100\,\rm km\ s^{-1}}\right)\left(\frac{100\rm pc}{R}\right)\left(\frac{E}{\rm GeV}\right) \rm GeV\ s^{-1} \qquad (4.39)$$

where V is the velocity of collective wind in the region, and R its relevant size. In Figure 4.4 right panel, and to be conservative, a ratio $V(\rm km\ s^{-1})/R(\rm pc)$=300 (e.g., a –single or collective– wind velocity of 1500 km s^{-1} and a size relevant for the escape of the electrons of 5 pc) has been chosen. Figure 4.4 right panel shows that the expansion dominates the electron losses $b(E)$, as well as the confinement timescale $\tau(E)$, throughout a wide range of energies. An example of the resulting secondary electron distribution obtained by numerically solving the loss equation is shown in Figure 4.5. Only at high energies the effect of the cutoff is unnoticeable, whereas it greatly affects the production of secondaries (up to several orders of magnitude) below 10 GeV.

The radio emission from the electron population of Figure 4.5 is well below the upper limits imposed with VLA at the location of the Cygnus unidentified HEGRA source (see below for a more detailed discussion, $<$ 200 mJy at 1.49 GHz, Butt et al. 2003). Even assuming a rather high magnetic field of 50 μG as in Figure 4.5, that in the case of the HEGRA source is ruled out by X-ray and radio observations, one obtains a flux density of $\sim$ 50 mJy at the quoted frequency for the non-modulated cosmic ray population. A smaller magnetic field, as is probably found in the outer regions, or a modulated

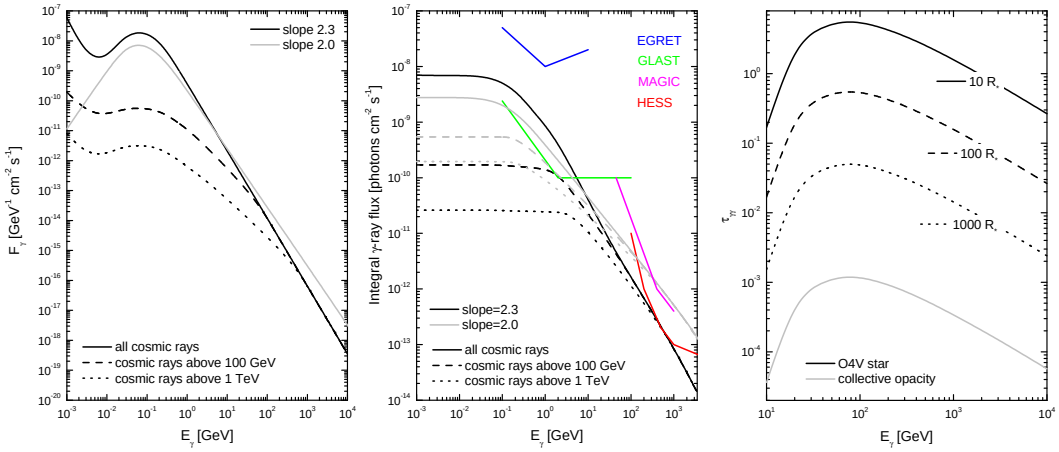

Figure 4.6: Differential (left panel) and integral (right panel) fluxes of γ-rays emitted in a non-modulated and a modulated environment. The bump at very low energies in the left panel is produced because leptonic emission coming only from secondary electrons is shown. Above $\sim$ 70 MeV the emission is dominated by neutral pion decay. Also shown are the EGRET, GLAST, MAGIC and HESS sensitivities. Note that a source can be detectable by IACTs and not by GLAST, or viceversa, depending on the slope of the cosmic ray spectrum and degree of modulation. Right: Opacities to $\gamma\gamma$ pair production in the soft photon field of an O4V-star at 10, 100 and 1000 $R_\star$, and in the collective photon field of an association with 30 stars distributed uniformly over a sphere of 0.5 pc. The closest star to the creation point is assumed to be at 0.16 pc, and the rest are placed following the average stellar density as follows: 1 additional star within 0.1, 2 within 0.25, 4 within 0.32, 8 within 0.40 and 14 within 0.5 pc.

production of secondaries will diminish this estimation. This limit is respected even when considering that the primary electron population (particularly at low energies) is at the same level as the secondary electron distribution.

4.5.4 Total γ-ray flux from a modulated environment

To compute γ-ray fluxes in a concrete example, it is here considered that $\sim$2 $M_\odot$ of target mass is being modulated within $\sim$1 pc. The average density is $\sim$ 25 cm^{-3}. This amount of mass is typical of the configurations studied previously within the innermost $20\,R_c \sim 2-8$ pc. To fix numerical values, it is considered that the group of stars is at a Galactic distance of 2 kpc. Using the computations of secondary electrons and their distribution, the left panel of Figure 4.6 shows the differential (hadronic and leptonic) γ-ray flux when the proton spectrum has a slope of 2.3 and 2.0. In the latter case, to simplify, only the pion decay contribution produced by the whole cosmic ray spectrum –which dominates at high energies– are shown.

The differential photon flux is given by

$$F_\gamma(E_\gamma) = [V/4\pi D^2]Q_\gamma(E_\gamma) = [M/m_p\,4\pi D^2][Q_\gamma(E_\gamma)/n], \tag{4.40}$$

where V and D are the volume and distance to the source, and M the target mass. In those examples where the distance, volume, mass and/or the medium density are such that the differential and integral flux above 100 MeV obtained from them with the full cosmic ray

Table 4.3: Examples of results of detection in different telescopes when the configuration of collective stellar winds generates a target of about 2 $M_\odot$, located at 2 kpc, and bombarded with a cosmic ray spectrum having an spectral slope $\alpha = 2.3$ and 2.0 enhanced a factor of 10^3 above 1 GeV. The full cosmic ray spectrum and different modulated cases, at 100 GeV and 1 TeV, are shown; except in the case of EGRET, when $\alpha = 2.3$ sensitivities are barely above the expected fluxes (see Figure (4.6).

Telescope	All	100 GeV	1 TeV
$\alpha = 2.3$			
EGRET ($E > 100$ MeV)	×	×	×
GLAST ($E > 100$ MeV)	√	×	×
MAGIC ($E > 50$ GeV)	×	×	×
HESS/VERITAS ($E > 100$ GeV)	×	×	×
$\alpha = 2.0$			
EGRET ($E > 100$ MeV)	×	×	×
GLAST ($E > 100$ MeV)	√	×	×
MAGIC ($E > 300$ GeV)	√	√	√
HESS/VERITAS ($E > 200$ GeV)	√	√	√

spectrum are greater than the instrumental sensitivity, a modulated spectrum with a 100 GeV or a 1 TeV energy threshold might not produce a detectable source in the 100 MeV – 10 GeV energy range. However, the flux will be essentially unaffected at higher energy (see the high energy end of Figures 4.3, 4.4, and 4.5). The left panel of Figure 4.6 shows that wind modulation can imply that a source may be detectable for the ground-based Cerenkov telescopes without being close to be detected by instruments in the 100 MeV – 10 GeV regime (like EGRET or the forthcoming GLAST). The middle panel of Figure 4.6 presents the integral flux of γ-rays as a function of energy, together with the sensitivity of ground-based and space-based γ-ray telescopes. The sensitivity curves shown are for point-like sources; it is expected that extended emission would require about a factor of 2 more flux to reach the same level of detectability. Table 4.3 summarizes the results. From Table 4.3 and Figure 4.6 it is seen that there are different scenarios (possible relevant parameters are distance, enhancement, degree of modulation of the cosmic ray spectrum and slope) for which sources that shine enough for detection in the GLAST domain may not do so in the IACTs energy range, and viceversa.

4.6 Opacity to γ-ray escape

The opacity to pair production of γ-rays in the UV stellar photon field of an association can be computed as (Reimer 2003, Torres et al. 2004)

$$\tau(E_\gamma) = \sum_{i=1}^{N} \int \int_{R_{c,i}}^{\infty} N_i(E_\star) \sigma_{e^-e^+}(E_\star, E_\gamma) dE_\star dr_i, \tag{4.41}$$

where $E_\star$ is the energy of the soft photons, E_γ is the energy of the γ-ray, $R_{c,i}$ is the place where the photon was created with respect to the position of the star number i, r_i is the distance measured from star number i, and $\sigma_{e^-e^+}(E_\star, E_\gamma)$ is the cross section

for $\gamma\gamma$ pair production (see C.57). Note that the lower limit of the integral on $E_\star$ in the expression for the opacity is determined from the condition that the center of mass energy of the two colliding photons should be such that $(1 - (mc^2)^2/(E_\star\, E_\gamma)) > 0$. The stellar photon distribution of star number i at a position r_i from the star is that of a blackbody peaking at the star effective temperature ($T_{\mathrm{eff}\,i}$) and diluted by the distance factor, $N_i(E_\star) = (\pi B(E_\star))/(hE_\star c) \cdot (R_{\star_i}^2)/(r_i^2)$, where h is the Planck constant, $R_{\star_i}$ is the star number i radius, and $B(E_\star) = (2{E_\star}^3)/((hc)^2) \cdot (e^{E_\star/kT_{\mathrm{eff}\,i}} - 1)^{-1}$.

The size of the emission region (where the target gas mass is located) considered as an example in the previous sections is of the order of 1 pc. The typical radius of a massive star is 10–20 solar radius $\sim 5 \times 10^{-7}$ pc, so that the most likely creation sites for photons will be far from individual stars. In Figure 4.6 (right panel) the value of $\tau(E_\gamma)$ for different photon creation sites distant from a O4V-star 10, 100, and 1000 $R_\star$, with $R_\star = 12R_\odot$ and $T_{\mathrm{eff}} = 47400$ K, are shown. Unless a photon is created hovering the star, well within 1000 $R_\star$, γ-ray opacities are very low and can be safely neglected. This is still true for associations in which the number of stars is some tens. Consider for instance a group of 30 such stars within a region of 0.5 pc (the central core of an association). The stellar density is given by Eq. (4.1); and the number of stars within a circle of radius R progresses as $\mathcal{N} = N(R/R_c)^3$. Figure 4.6 (right panel) shows that the collective contribution to the opacity obtained from Eq. (4.41) in this configuration is also very low, since the large majority of the photons are produced far from individual stars. However, this is not the case if one considers the collective effect of a much larger association like Cygnus OB2, particularly at its central region (Reimer 2003). Reimer demonstrated that even when a subgroup of stars like the ones considered here is separated from a super cluster like Cygnus OB2 by about 10 pc, the influence of the latter produces an opacity about one order of magnitude larger than that produced by the local stars. Even in this case, Figure 4.6 (right panel) shows that this opacity is not enough to preclude escape from the region of the local enhancement of stellar density. This is not the case at the center of Cygnus OB 2.

4.7 Candidates: Cygnus OB 2 and Westerlund 1

Extensive studies of Galactic and LMC/SMC star clusters and OB associations suggest that star formation occurs almost instantaneously (Massey et al. 1995, Leitherer 1999). Typical age spreads are about 2 Myr or less. This is short in comparison with stellar evolutionary timescales, except for the most massive stars, and so a coeval star formation seems appropriate. In addition, one is particularly interested in the case in which at the position of the stars that are being illuminated by cosmic rays there is no current star formation. If that is not the case, the amount of gas and molecular material in the ISM would be larger than that contained in the winds, and would make the latter a subdominant contribution in the generation of the total TeV flux. In particular, should collision between cosmic rays and nuclei in the ISM be dominant, there would be no modulation. This fact and the opacity to γ-ray escape that is found at the center of a very massive cluster points to the scenario: a sub-group of stars located in the outskirts of an association, close to an accelerator region, perhaps a SNR, or the association superbubble itself. The case of Cygnus OB 2 and the TeV source detected by HEGRA, TeV J2032+4131 (Aharonian et al. 2002, 2005b), seems to be a possible realization of this scenario. This TeV source, for which no counterparts at lower energies

are presently identified (Butt et al. 2003), constant during the three years of data collection, extended (5.6±1.7 arcmin, $\sim$ 2.7 pc at 1.7 kpc), separated in about 10 pc (at 1.7 kpc) from the core of the association, and coincident with a significant enhancement of the star number density (see Fig. 1 of Butt et al. 2003) might be suggestive of the scenario outlined in the previous sections. TeV J2032+4131 presents an integral flux of about 3% of that of the Crab [$F_\gamma(E_\gamma > 1\mathrm{TeV}) = 4.5(\pm1.3) \times 10^{-13}$ photons cm^{-2} s^{-1}], and a γ-ray spectrum $F_\gamma(E_\gamma) = B(E_\gamma/\mathrm{TeV})^{-\Gamma}$ photons cm^{-2} s^{-1} TeV^{-1}, where $B = 4.7\,(\pm2.1_{\mathrm{stat}} \pm 1.3_{\mathrm{sys}}) \times 10^{-13}$ and $\Gamma = 1.9(\pm0.3_{\mathrm{stat}} \pm 0.3_{\mathrm{sys}})$. Within the kind of models studied here, it would be possible to explain, apart from consistency with the flux level, spectrum, and variability, why there is no detectable TeV source at the central core of Cygnus OB 2 (large opacity to photon escape), and why there is no EGRET (and will not be a GLAST source) or other significant radio or X-ray diffuse emission at the position of the HEGRA detection (modulation of cosmic rays).

However, the only stars quoted by Butt et al. (2003) at the position of TeV J2032+4131 are 10 O and 10 B stars, and not all of them are within the contours of the source. The quoted stars are similar, late O and early B, and together produce a mass-loss rate of about 1×10^{-5} M$_\odot$ yr^{-1}. This mass-loss rate is low and produces not too dense collective wind, according to the simulations of Section 2. In addition, typical distances between these stars are of the order of a parsec, so that a central core radius is not well defined. Thus, if there is no additional significant stars in this region, what currently is being investigated in newest and deeper Chandra and XMM observations of the region (Butt et al., and Reimer et al. both in preparation) as well as on the expected star density, a better approach to study the possible contribution of stellar winds to this source is to add that of individual stars (Torres et al. 2004). If only the currently known stars exist, the produced flux is too low to produce the source unless a larger enhancement or a low ISM density are invoked. A simple hadronic scenario where an enhanced spectrum interacts with more abundant ISM nuclei cannot be discarded at this point, since there is no need to use modulation to explain why there is no source detected by EGRET (the predicted flux in this model is below EGRET sensitivity). However, this model can be tested with GLAST observations (see the example of Figure 4.6). Also, MAGIC observations of this region are crucial. Further data will allow one to reach a definitive answer.

Knödlseder (2003) has compiled a sample of massive young star clusters (Cygnus clones) that have been observed in the Galaxy (see his table 2). Westerlund 1 (Wd 1) is a prominent member. The usually adopted distance to the latter is $D \sim 1.1\pm0.4$ kpc (Piatti et al. 1998), although Clark et al. (2005) favor a distance between 2–4 kpc. The known population of massive stars, clearly a lower limit in each category, includes 7 WN, 6 WC, 5 Early transition stars (like luminous blue variables (LBV), or sgB[e]) and more than 25 OB (Clark and Negueruela 2002, Clark et al. 2005). A LBV (W243) apparently undergoing an eruption event was also found (Clark & Negueruela 2004). W243's mass-loss rate alone can be as high as $3 - 6 \times 10^{-4}$ M$_\odot$ yr^{-1}. The stellar population of Wd 1 appears to be consistent with an age of the order 4–8 Myr if the cluster is coeval, and with a lower limit for a total mass of about a few thousand M$_\odot$, most likely to be around a few $\times 10^5$ M$_\odot$ (Clark & Negueruela 2002, Clark et al. 2005). Thus, Wd 1 is likely to be one of the most massive young clusters in the Local Group, and in contrast to Cygnus OB2, it is much more compact (a radius of about 0.6 pc) –and thus a better target for pointing instruments. A few stars farther from the center (so that high opacities are avoided) subject to illumination by a cosmic ray population with a hard slope would make Wd 1 a γ-ray source. The HESS observatory has covered the position of Wd 1 when doing the

galactic plane scan, although with just a few hours of observation time (Aharonian et al. 2005e). Based on the arguments presented in this Chapter, pointed observations to Wd 1 might result in its detection.

Finally, special interest in this model may appear given the serendipitous discovery of HESS J1303-631 TeV γ-ray source (Aharonian et al. 2005f), extended and still unidentified, which is in spatial coincidence with the OB association Cen OB6 (see their Figure 7), that contains at least 20 known O stars and even 1 WR star.

4.8 Concluding Remarks

Collective wind configurations produced by a number of massive stars were studied, and densities and expansion velocities of the stellar wind gas that is target for hadronic interactions in several examples were obtained. The model presented takes into account secondary particle production, electrons and positrons from charged pion decay, electrons from knock-on interactions, and solves the appropriate loss equation with ionization, synchrotron, bremsstrahlung, inverse Compton and expansion losses to obtain expected γ-ray emission from these regions, including in an approximate way the effect of cosmic ray modulation. Examples where different stellar configurations can produce sources for GLAST and the MAGIC/HESS/VERITAS telescopes in non-uniform ways, i.e., with or without the corresponding counterparts were shown. Cygnus OB2, Cen OB6 and Westerlund 1 are associations where this scenario could be tested. In the latter case, it was here proposed that it is a suitable target for HESS.

Part II

The MAGIC Telescope and data analysis method

Chapter 5

The Čerenkov technique and the MAGIC Telescope

The Čerenkov technique for γ-ray astronomy, which allows an Imaging Air Čerenkov Telescope (IACT) to indirectly detect γ-rays entering the Earth atmosphere, is described. The main features of Extended Air Showers (EAS) are briefly commented, stressing the differences between EAS induced by primary γ-rays and the several orders of magnitude more numerous EAS induced by charged cosmic ray (CR) nuclei, which constitute the background. The production of Čerenkov radiation in an EAS is described, together with the subsequent detection of the Čerenkov flashes by an IACT. Finally, the MAGIC Telescope, the detector on which the experimental part of this Thesis is based on, is introduced.

5.1 Extended Air Showers

The physics of EAS is reviewed in detail by Longair (1997), Gaisser (1990) among others. CRs –mainly atomic nuclei (98%, from which 87% H, 12%He, 1% C,N,O,Fe), electrons (2%), γ-rays and neutrinos– are emitted by a diversity of astrophysical objects. Some of them reach the Earth. On their way they interact with the interstellar and intergalactic medium and charged CRs are quickly deflected by galactic and intergalactic magnetic fields. Therefore, the distribution of CR incident directions on top of the atmosphere is isotropic, with the exception of the small flux of (neutral) γ-rays and neutrinos. The most energetic (> 1 GeV) among these CRs constitute the primary particles of the EAS that develop in the atmosphere.

An EAS consists of the particles produced by the interaction of a single high energy primary CR on top of the atmosphere (~ 25 km above sea level). In the first interaction, several secondary particles are generated, which again interact with the molecules and ions of the atmosphere. The secondary products once more interact and generate new particles, and, as this process repeats, an EAS is generated. At the beginning of the process the number of particles in the shower rapidly grows. But, since the energy of the primary particle is distributed over all the generated particles, at some point their energy falls below the threshold for production of further particles. Eventually energy losses through ionization and Compton scattering dominate and the shower dies out.

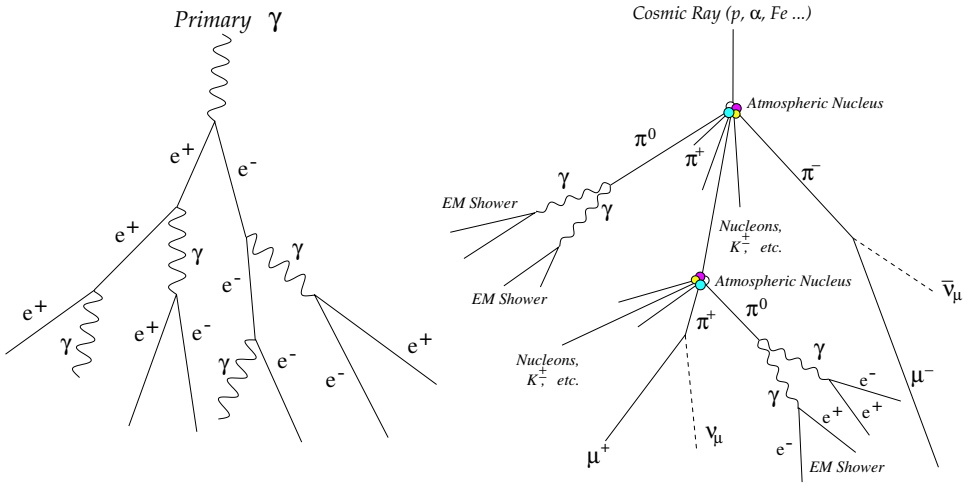

Figure 5.1: Sketch of the structure and the interactions present in an EAS, induced by a cosmic γ-ray (left) and by a charged cosmic nucleus (right).

5.1.1 Electromagnetic EAS

When a cosmic γ-ray or an energetic electron enters into the atmosphere develops an electromagnetic EAS, that to first order only contains electrons, positrons and photons. The primary γ-ray interacts with the strong Coulomb field of an atmospheric nucleus and, in order to conserve momentum, an electron-positron pair is produced from the emission of a virtual photon. If the energy of the resulting $e^{\pm}$ is sufficient, they will be accelerated in the presence of the Coulomb field of other atmospheric nuclei. As a result of this acceleration, a fraction of their kinetic energy is emitted in the form of real photons, i.e., they undergo bremsstrahlung radiation. If the energy of the secondary γ-rays is still higher than 1.022 MeV, they produce again $e^{\pm}$ pairs, which in turn can suffer further bremsstrahlung processes. The result of this recursive process is an avalanche of photons, electrons and positrons, which roughly follow the direction of the original γ-ray and share its total energy. A sketch of an electromagnetic EAS is shown in Figure 5.1. On the other hand, if a cosmic electron is the primary particle, an electromagnetic cascade, analogous to the one described but starting with bremsstrahlung emission, will develop. Electron-induced EASs are in fact an irreducible background for ground-based γ-ray detectors although their flux is much lower than that of hadronic CRs. For completeness, it should be mentioned that also muon-antimuon pair production and photo-production ($\gamma + nucleus \rightarrow hadrons$) processes may occur in an electromagnetic shower. They would lead to a muonic and hadronic component of the shower. However, these contributions can be neglected since the cross section of these reactions are much smaller than that of $e^{\pm}$ pair production and bremsstrahlung.

All the shower particles are strongly collimated along the incident direction of the primary γ-ray, i.e., the shower axis, due to the relativistic energies involved. The main process that broadens the shower transversely is multiple scattering and, in second order, the deflection of the charged particles by the Earth magnetic field. As the EAS develops, the energy of the secondary particles decreases, while the number of particles increases until the shower maximum. This maximum is reached when the mean energy of the electrons and positrons in the shower falls below a critical energy E_c (about 83 MeV for e^- in air), which defines the moment when ionization becomes the dominant energy loss

process, instead of bremsstrahlung. At the same time, the mean energy of the shower photons has decreased and the cross section for production of $e^{\pm}$ pairs becomes of the same order of the one for Compton scattering and photoelectric absorption (also for energies around 80 MeV). From this stage on, fewer secondaries are produced and the remaining particles rapidly loss their energy in the medium.

The development of electromagnetic EASs was first theoretically modelled by Rossi and Greisen (1941). Assuming several simplifying approximations they found an analytical solution for the longitudinal development of the shower. The Greisen equation (see Greisen 1956 or Gaisser 1990) describes the distribution of electrons and positrons with an energy above E_c as a function of the shower depth (the so-called longitudinal development),

$$N_e(t, E_0) = \frac{0.31}{\sqrt{\ln(E_0/E_c)}} e^{t[1-1.5\ln(s)]}\,, \tag{5.1}$$

where E_0 is the energy of the primary γ-ray, t is the depth along the shower axis in units of radiation lengths, and s is the shower age, which is a dimensionless quantity defined as

$$s(t, E_0) = \frac{3t}{t + 2\ln(E_0/E_c)} \tag{5.2}$$

and ranges from 0 to 2. The derivative of the number of $e^{\pm}$ with respect to the shower age, $dN_e(t, E_0)/ds$ is positive, i.e., the number of particles is growing, while $s < 1$; it is zero for $s = 1$, at the shower maximum; and becomes negative for older ages as the shower dies out. According to the definition of the shower age, the depth at which shower maximum occurs t_{max} only depends on the energy of the primary photon: $t_{max} = \ln(E_0/E_c)$.

The lateral distribution of electrons can be modeled using the NKG-formula, which was derived by Nishimura and Kamata (1952) and modified by Greisen (1960). It describes the $e^{\pm}$ density as a function of the distance r from the shower axis:

$$\rho(r, t, E_0) = \frac{N_e(t, E_0)}{r_M^2} \left(\frac{r}{r_M}\right)^{s-2} \left(1 + \frac{r}{r_M}\right)^{s-4.5} \frac{\Gamma(4.5 - s)}{2\pi\Gamma(s)\Gamma(4.5 - 2s)}\,, \tag{5.3}$$

where r_M is the multiple scattering Molière radius (about 79 m at sea level), and Γ is the Gamma function.

5.1.2 Hadronic EAS

An EAS induced by a charged cosmic hadron has three components, a hadronic, an electromagnetic, and a muonic one. The shower starts with the collision of the incident high energy hadron with an atmospheric nucleus, mainly producing pions, but also kaons and ions lighter than the incident nucleus. If the products of the first interaction have enough energy, they undergo successive nuclear collisions, leading to the hadronic high energy core of the shower.

About 90% of all secondary particles produced in the hadronic core of the shower are pions, out of which 2/3 are charged pions and 1/3 neutral pions. As discussed in Appendix B, the π^0 has a very short lifetime ($\tau \sim 10^{-16}$ s) and rapidly decays, in most of the cases, into two photons ($\pi^0 \longrightarrow \gamma + \gamma$). Each of the resulting high energy photons will initiate an electromagnetic sub-shower, so with each hadronic interaction, approximately one third of the energy goes into the electromagnetic component of the shower. On the other hand, secondary charged pions and kaons may decay into muons and neutrinos

($\pi^{\pm} \longrightarrow \mu^{\pm} + \nu_{\mu}(\bar{\nu}_{\mu})$, $K^{\pm} \longrightarrow \mu^{\pm} + \nu_{\mu}(\bar{\nu}_{\mu})$, $K^{\pm} \longrightarrow \pi^{\pm} + \pi^{0}$), feeding the muonic component of the shower. Muons only lose their energy via ionization or decay through the channel $\mu^{\pm} \longrightarrow e^{\pm} + \nu_e(\bar{\nu}_e) + \bar{\nu}_{\mu}(\nu_{\mu})$, thus an additional fraction of energy is released into the electromagnetic component of the shower. However, the muon lifetime ($\tau = 2.2 \times 10^{-6}$ s) is about two orders of magnitude higher than that of the pion and kaon ($\tau \sim 10^{-8}$ s), and, as many muons are produced with very high energy in the upper layers of the atmosphere, frequently they have high enough Lorentz factors to reach the Earth surface before decaying. These muons, together with the neutrinos, prevent a sizeable fraction (about 5%) of the initial CR energy from being absorbed in the atmosphere (Risse 2004).

Hence the three components of a hadronic EAS are the electromagnetic sub-showers originated from π^0 decays, the hadronic core built up from high energy nucleons and mesons (which usually re-interact and mostly become electrons and positrons whose energy is mostly dissipated through ionization), and a fraction of nearly non-interacting muons and neutrinos.

Figure 5.2 shows a lateral view of a simulated electromagnetic EAS and a hadronic EAS. It can be noticed that hadronic showers are broader, as their lateral spread is mainly caused by the transverse momentum get by the secondary hadrons in the hadronic interactions, which is substantially larger than the scattering angle generated from multiple scattering (the dominant process in the much slimmer electromagnetic showers). It is also worth mentioning that the nuclear interaction lengths of hadrons in air are substantially larger (almost double) than the radiation length for bremsstrahlung and the interaction length for $e^{\pm}$ pair production ($\xi_{nuclear} \sim 83\ g/cm^2$, $\xi_{brems} \sim 37\ g/cm^2$, $\xi_{pair} \sim 47\ g/cm^2$), what implies that the starting point and the maximum of the shower of hadron-induced EAS occurs deeper in the atmosphere than in the case of a shower induced by a γ-ray of the same initial energy.

5.2 The Imaging Atmospheric Čerenkov Technique

5.2.1 Čerenkov radiation in an EAS

When a charged particle travels through a medium with a speed $v = \beta c$ that exceeds the speed of light in that medium (i.e., $v > c/n$, where n is the refractive index of the medium), it emits light. This light emission, called Čerenkov radiation, is the result of the reorientation of the electric dipoles induced by the charged particle in the medium molecules. At low velocities, charges around the position of the incident particle are symmetrically distributed so as to cancel out, implying no net effect, and no radiation occurs. Only when the velocity of the charged particle is high enough, a net polarization of the medium briefly remains along the trajectory of the particle and, consequently, short electromagnetic impulses are emitted when the molecules rapidly turn back to their ground state (see a sketch of the process in panels a and b of Figure 5.3). As a result, the particle suffers a continuous energy loss while its energy is above the Čerenkov threshold. As the charged particle crosses the medium, a shock-wave is created behind it. The wavefront propagates at a fixed angle $\theta_{\check{c}}$ with respect to the track of the particle. The reason is that light emitted from different points of the particle trajectory only can add up coherently in Huygens construction for a very concrete angle, as is shown schematically in panel c of Figure 5.3. Requiring coherence, the Čerenkov angle can be deduced only

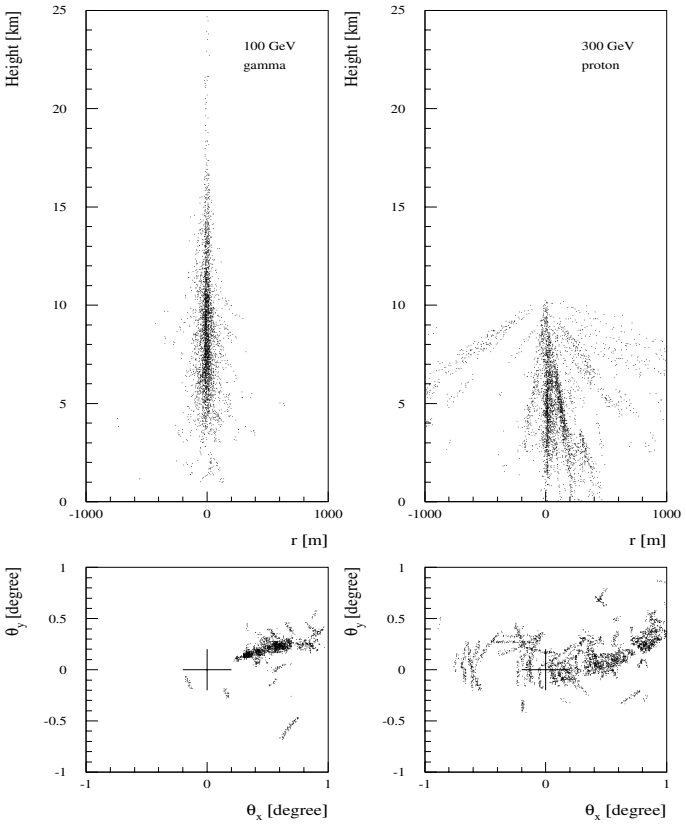

Figure 5.2: Simulation of an electromagnetic (left panels) and hadronic (right panels) Extended Air Showers. The top panels show the development of the shower in the atmosphere and the bottom ones the angular distribution of the Čerenkov photons at ground levels. Evident morphological differences can be seen which are crucial for imaging-based background substraction methods.

from geometrical considerations:

$$\cos\theta_{\check{c}} = \frac{\frac{c}{n}\cdot\Delta T}{\beta c\Delta T} = \frac{1}{\beta n}\,. \tag{5.4}$$

Thus, the maximum angle of Čerenkov emission is observed for ultra-relativistic charged particles ($\beta \backsimeq 1$), and is given by:

$$\cos\theta_{\check{c}}^{max} = \frac{1}{n}\,, \tag{5.5}$$

while the threshold energy of the incident particles to emit Čerenkov light ($v > c/n$) is:

$$E_{\check{c}}^{thr} = \frac{m_0c^2}{\sqrt{1-\beta_{min}^2}} = \frac{m_0c^2}{\sqrt{1-(1/n)^2}}\,, \tag{5.6}$$

where m_0 is the rest mass of the charged particle.

As the refractive index depends on the density of the medium, it changes with the atmospheric altitude. Therefore, the Čerenkov emission angle and the energy threshold for Čerenkov production take different values along the path of the shower. In order to better

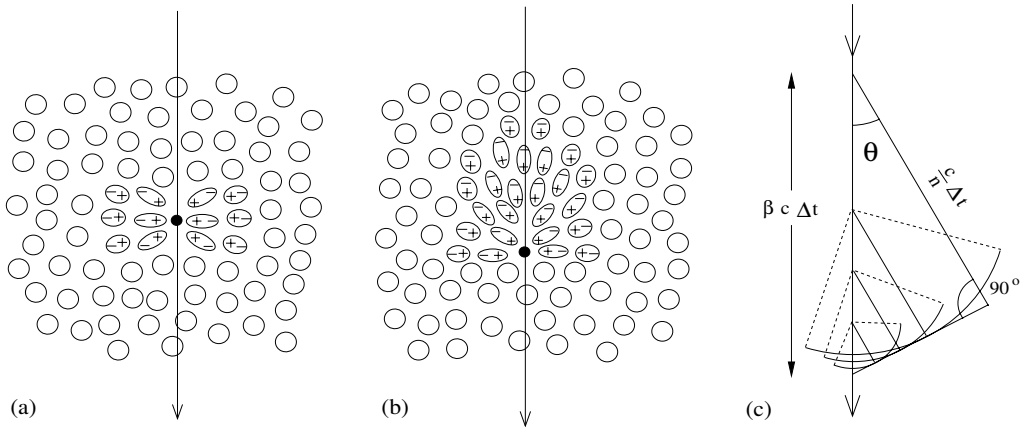

Figure 5.3: Polarization of the medium induced by a charged particle with low velocity (a) and with high velocity (b). Huygens construction of Čerenkov waves that only finds coherence for the Čerenkov angle $\theta_{\check{c}}$ with respect to the charged particle trajectory (c).

understand the evolution of the Čerenkov emission and to compute the Čerenkov radiation parameters for different atmospheric depths, a simplified model of the atmosphere can be used. In what follows, it is assumed an exponential variation of the atmospheric density with height h, i.e., and isothermal atmosphere,

$$\rho(h) = \rho_0 \cdot \exp\left(-\frac{h}{h_0}\right) , \tag{5.7}$$

where $h_0 = 7.1$ km and ρ_0 is the air density at sea level, 0.0013 g/cm^3. Then, the refractive index of the air as a function of height can be expressed as:

$$n(h) = 1 + n_h = 1 + n_0 \cdot \exp\left(-\frac{h}{h_0}\right) , \tag{5.8}$$

where $n_0 = 2.9 \times 10^{-4}$. Equations 5.7 and 5.8 show that the refractive index depends linearly on the air density, decreasing at the higher layers where the atmosphere is less dense. Smaller dependencies of the refractive index on other factors, such as the air temperature or the wavelength of the radiation, can be neglected.

Using Equation 5.8 in Eq. 5.5 and Eq. 5.6 and the fact that $n_h \ll 1$, the maximum Čerenkov emission angle and the Čerenkov energy threshold can be expressed in terms of the height in the atmosphere:

$$\cos\theta_{\check{c}}^{max} \simeq \sqrt{2n_h} , \tag{5.9}$$

$$E_{\check{c}}^{thr} \simeq \frac{m_0 c^2}{\sqrt{2n_h}} . \tag{5.10}$$

On one hand, as n_h decreases with height, the energy threshold for Čerenkov emission is higher in the upper layers of the atmosphere and decreases as the EAS develops on. As an example, at 10 km above the sea level, $n_h = 7.1 \times 10^{-5}$ and the $E_{\check{c}}^{thr}$ for electrons, muons and protons is 42.9 MeV, 8.9 GeV and 78.8 GeV, respectively, about two times larger than the threshold values found at sea level ($h = 0$ km). It is also worth noticing that nearly all the Čerenkov light in an EAS is produced by the secondary electrons and positrons, as they form an overwhelming fraction of the particles in the shower and they

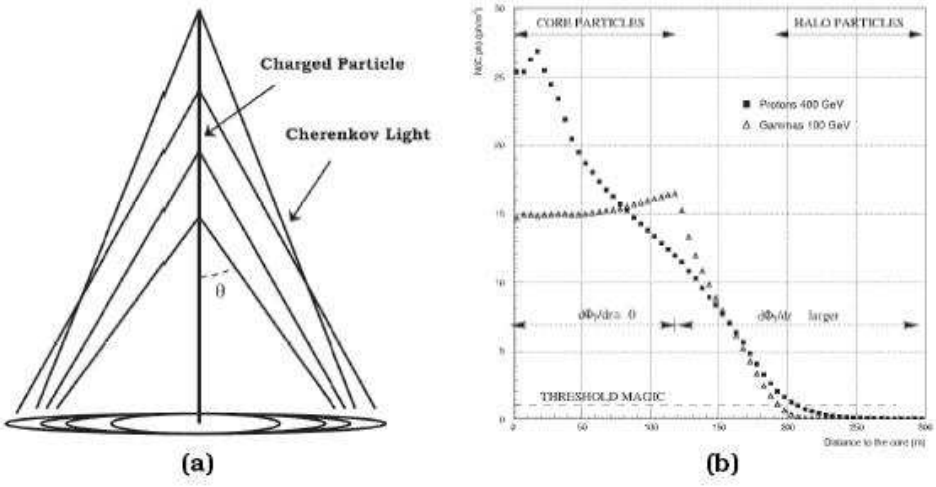

Figure 5.4: Scheme of the Čerenkov light ring produced by an ultra-relativistic charged particle at the observation level. The first two beams on panel (a) hit the ground at roughly the same radial distance even if they are produced at different heights. Panel (b) shows the simulation of the Čerenkov light pool produced by γ-ray and proton showers. The γ-induced Čerenkov light profile is practically constant until a radius of a hundred meters, where the hump occurs, and then decay rapidly for higher radius. Taken from Paneque (2004).

are more likely to be above the threshold of Čerenkov emission. At 10 km the Čerenkov energy threshold for electrons is still below the critical energy which indicates the shower maximum ($E_c \sim 83$ MeV), so most of the electrons and positrons still emit Čerenkov radiation when the electromagnetic EAS is already dying out. Muons from hadronic EAS can also emit a non negligible fraction of the Čerenkov light and occasionally produce a fake light distribution of a γ-ray induced shower. However, as muons travel through the atmosphere undeflected and with almost negligible energy loss, they constitute at the end a very powerful tool to understand the performance and calibrate ground-based γ-ray detectors.

On the other hand, the maximum angle of Čerenkov emission is smaller at the beginning of the shower than in the shower tail due to the change of n_h with height. This height dependence of the angle is responsible for the fact that the light emitted by shower electrons and positrons at a range of different heights reaches the ground at approximately the same distance from the axis of the shower, an effect that produces a characteristic enhancement of the Čerenkov light density. This effect is illustrated in Figure 5.4. EAS simulations show that this ring structure, also called hump, typically occurs for a radius between 100 and 130 m from the center of the Čerenkov light pool. The Čerenkov light at the ground is the superposition of all the light emitted in cones integrated over the whole shower longitudinal path. However, in a real EAS, due to multiple scattering the trajectories of secondary $e^{\pm}$ are slightly deviated from the track of the incoming primary γ-ray, and consequently, the ideal ring light pattern is somehow spread out. For hadron-induced EAS, the hump structure is less visible as $e^{\pm}$ directions are even more dispersed due to the high transverse momentum kick of nuclear interactions and $e^{\pm}$ scatter away from the shower axis.

In general, the differences in the shower development between a hadron-induced and a γ-induced EAS, which are reflected in the shape and the time structure of the Čerenkov light distribution at ground level, can be used to distinguish between them with a sensitive enough ground-based instrument. Air showers develop practically at the speed of light, resulting therefore in very short Čerenkov flashes. Typically the front of Čerenkov photons produced in an electromagnetic EAS arrives at the ground in 2-5 ns, whereas hadronic showers have a wider time spread (10-15 ns) due to the development of many electromagnetic sub-showers. As an example, a 1 TeV γ-ray induces an EAS which emit a Čerenkov flash in a cone with an opening angle of the order of 1°, which lasts about 5 ns, and yields about 50 photons per m^2 on the ground within 100 m around the shower axis.

For detection purposes, it is also important to know the spectrum of the Čerenkov radiation produced in an EAS. The number of Čerenkov photons emitted per unit of path length and per unit of photon energy (or, equivalently, photon wavelength λ) by a particle with charge Ze is given by:

$$\frac{dN^2}{dxd\lambda} = 2\pi\alpha Ze^2 \left(1 - \frac{1}{\beta^2 \cdot n^2(\lambda)}\right) \frac{1}{\lambda^2}\,, \tag{5.11}$$

where $\alpha = \frac{e^2}{\hbar c}$ is the fine structure constant. Equation 5.11 shows that the emission is restricted to those frequency bands for which $n(\lambda) > 1/\beta$. The radiation occurs in the visible and near visible regions of the spectrum, for which $n > 1$. In the X-ray band, n is always < 1, so the emission is forbidden. The $1/\lambda^2$ dependency of the spectrum indicates that most of the Čerenkov photons are emitted at short wavelengths, in the ultraviolet range, and that it decreases along the visible region. However, due to the interactions of the Čerenkov photons with the air molecules in their travel through the atmosphere, the spectrum observed at ground level is quite different from the emitted one (see Figure 5.5) and it peaks at around 330 nm. Čerenkov photons suffer the following attenuation processes in the atmosphere:

- Absorption in the Ozone layer, mainly in the upper part ($\gtrsim 10$ km) of the atmosphere. Practically all photons with wavelength lower than 290 nm are absorbed through this process ($O_3 + \gamma \longrightarrow O_2 + O$).

- Rayleigh scattering, which occurs on polarizable molecules with sizes smaller than the photon wavelength. If the atmospheric conditions are good, this is the process responsible for most of the Čerenkov light attenuation from 15 to 2 km above sea level, with a cross section $\propto \lambda^4$.

- Mie scattering, which takes place on polarizable molecules with sizes comparable or larger than the photon wavelength, basically aerosol particles present in the atmosphere. Its effect is especially important when atmospheric conditions are not optimal, i.e., if there is dust, pollution, clouds, fog, etc. The spectral dependence of the cross section is $\propto \lambda^{-a}$, with $1 \lesssim a \lesssim 1.5$

- Absorption by H_2O and CO_2 molecules, only important for photon wavelengths above 800 nm. These wavelengths are outside the sensitive range of the photosensors which are typically used for Čerenkov detection.

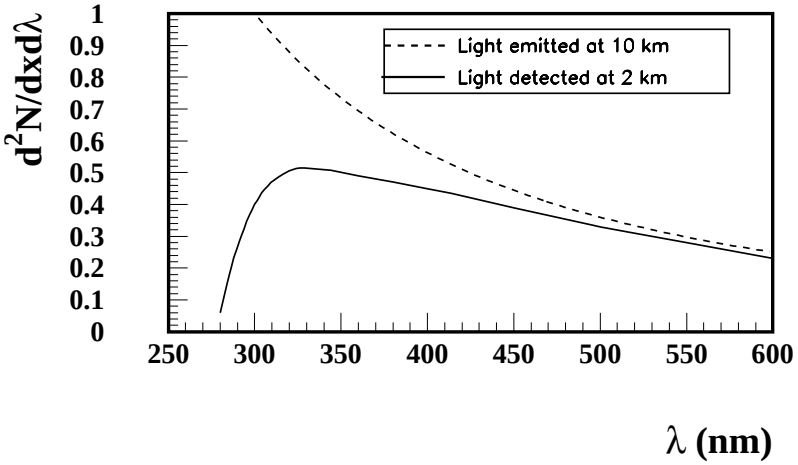

Figure 5.5: Differential Čerenkov photon spectrum in arbitrary units in the ultraviolet and visible wavelength ranges, emitted at 10 km above sea level (dotted line) and detected at 2 km (solid line) after suffering absorption in the Ozone layer and Rayleigh and Mie scattering. Graphic taken from Moralejo (2000).

5.2.2 Imaging Air Čerenkov Telescopes: detection technique

Imaging Air Čerenkov Telescopes (IACTs) are currently the most efficient ground-based experiments for the detection of cosmic γ-rays. As any other optical or radio telescope, an IACT consists of three basic elements: a tracking mechanical system, which counteracts the Earth rotation to track an astrophysical object in the sky; a collecting surface, which gathers the incident electromagnetical radiation and focuses it for its registration; and a receiver element, which converts the collected light in a recordable image of the observed field of view (FOV). A peculiar feature of Čerenkov telescopes is that they do not detect directly the photon flux under study, but instead detect the Čerenkov light which is produced in the EAS that the primary photons gives rise to in our atmosphere. A mirror surface collects a fraction of the Čerenkov light pool and at the focal plane a set of light detectors converts the incident Čerenkov photons into electric pulses which together conform an encrypted image of the EAS. The very short time response ($\sim$ ns) of the light detectors chosen for IACTs is another important characteristic of these telescopes and is key for background rejection.

The image formed in the camera of photosensors (generally photomultiplier tubes (PMT)[1]) is a geometrical projection of the atmospheric shower as can be schematically seen in Figure 5.6. Čerenkov photons emitted at different heights reach the telescope mirror dish with different angles and, therefore, will be focused on different positions in the camera of the telescope. As a consequence, the image contains information of the longitudinal development of the EAS, i.e., the number of particles emitting Čerenkov light as a function of the height in the atmosphere. Light coming from the upper part of the shower, where the secondary particles are more energetic, has smaller Čerenkov angles and is mapped onto a region close to the camera center, whereas light emitted from the last stages of the shower, from less energetic secondary charged particles, has larger

[1]Past and current IACTs use PMTs in their cameras, but new higher sensitivity light detectors, like Hybrid PhotoDetectors (HPD), Avalanche PhotoDiodes (APD), or Silicon Photomultipliers (SiPM), are currently under study.

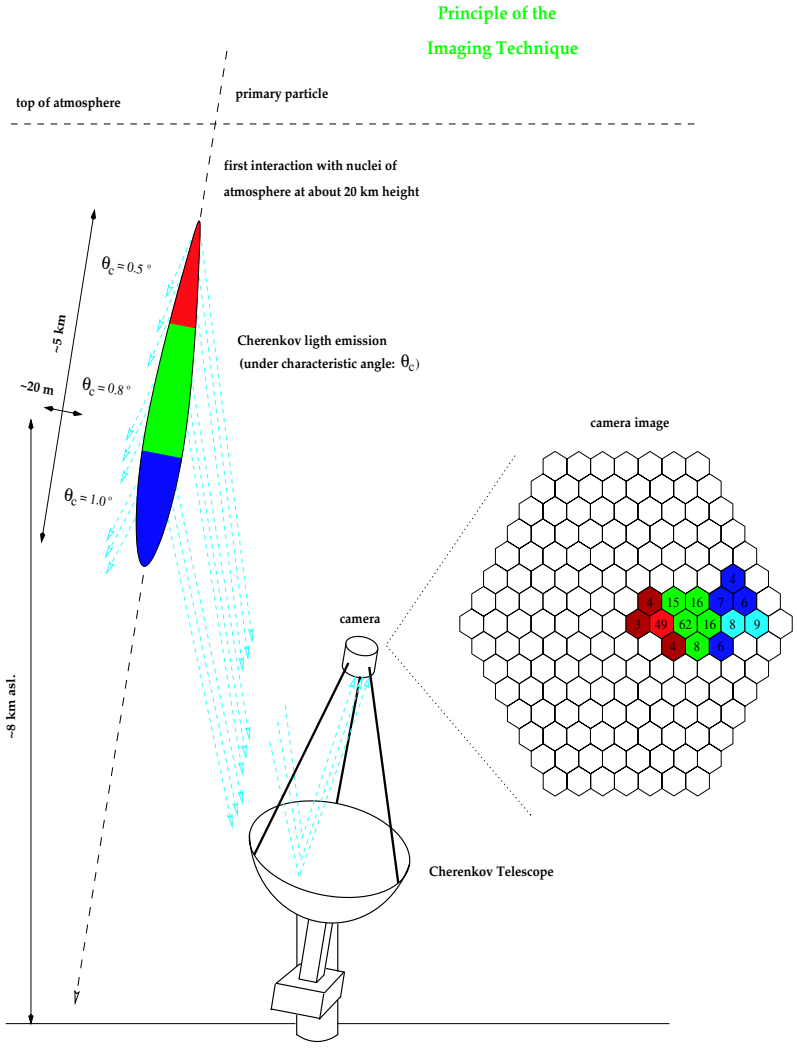

Figure 5.6: Sketch of the principle of the Čerenkov technique, through the formation of the image of an EAS in an IACT pixelized camera. The numbers in the figure correspond to a typical 1 TeV γ-ray induced shower.

Čerenkov angles and is mapped further away from the camera center (see Figure 5.6). For the larger showers (i.e., the ones induced by more energetic particles) or for showers with high impact parameters[2], due to this directionality of the Čerenkov radiation, Čerenkov photons from some parts of the EAS may not reach the reflector of the telescope and, therefore, parts of the shower may be not contained in the recorded image.

The Čerenkov technique relies on the shower development information that is contained in the images formed in the telescope to infer the characteristics of the particle that originated the EAS, as will be explained in more detail in the following Chapters on image analysis methods. On one hand, the total amount of light contained in the image is the main estimator of the energy of the primary particle. This is true because, although the fraction of initial energy lost in form of Čerenkov radiation is about 3 or 4 orders of magnitude smaller than the energy lost through ionization, the ratio between the Čerenkov

[2]The impact parameter of an EAS is defined as the distance between the telescope location and the point where the shower axis intersects the plane perpendicular to the telescope axis.

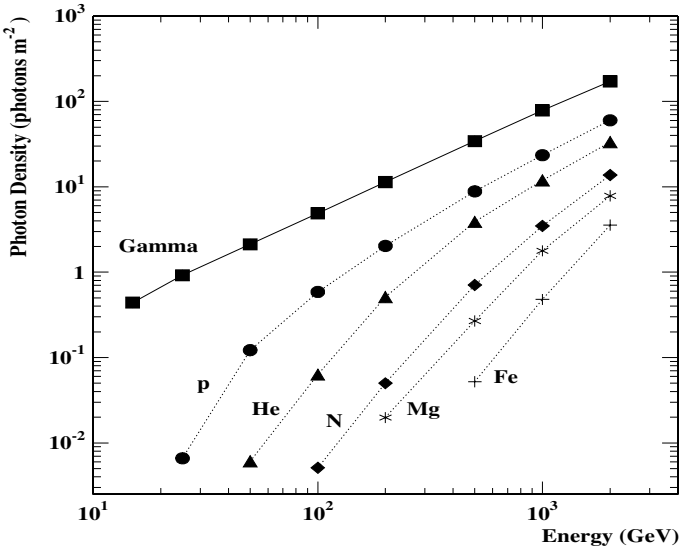

Figure 5.7: Čerenkov photon density at 2km height above sea level for different type of incident primary particles and as a function of their energy. Figure taken from Ong (1998).

energy losses and ionization losses is in first order constant, so a measure of the Čerenkov light provides a good estimation of the energy absorbed in the atmophere, which is in fact acting as a calorimeter. On the other hand, the orientation and shape of the image are indicators of the nature and the incoming direction of the primary particle.

With this technique, the first clear detection of a γ-ray source was achieved in 1989, when the Whipple telescope claimed a 9 sigma detection of the Crab Nebula (Weekes et al. 1989). Since then, much progress has been made, as discussed in the Introduction.

Two main parameters characterize an IACT: its sensitivity, i.e., the minimum detectable γ-ray flux in a given number of observation hours, and its energy threshold, i.e., the minimum energy of the primary particle to which the telescope is able to disentangle the signal from the background. The dispersion of the Čerenkov light generated in an EAS in a large pool over the ground at the observation level crucially influence these two parameters. On one hand, the light spread allows the IACT to detect EASs over a large range of impact parameters, from $\sim$ 30 to $\sim$ 150 m.[3] This provides IACTs with huge collection areas (of the order of 10^5 m^2). [4] Such collection areas of the IACTs turn into high sensitivities in comparison with γ-ray detectors mounted on satellites, whose dimensions are clearly limited by space-launching requirements to $\sim$ 0.01 - 1 m^2. On the other hand, the dilution of the Čerenkov radiation over the large light pool makes its detection more difficult and necessitates large mirrors and high sensitivity photodetectors. Figure 5.7 shows how the photon density at an observation site at 2 km above sea level diminishes as the energy of the EAS precursor particle is lower, going below 10 Čerenkov

[3]Although the efficiency of detection of showers with impact parameters larger than $\sim$ 150 m is quite low, i.e., when the light arriving to the IACT is outside the brightest region of the Čerenkov pool, beyond the hump, the large amount of showers arriving with these larger impact distances makes them to be still a significant fraction of the total amount of detected showers.

[4]It is worth mentioning that the area covered by the EAS light pool and, therefore, also the IACT collection area, depends on the energy of the primary particle and on the zenith angle of observation. At zenith angles $\gtrsim 60^\circ$ the collection area can increase by one order of magnitude.

photons per m^2 for γ-rays of less of 100 GeV. An efficient reconstruction of the primary particle characteristics through the image analysis requires a minimum number of detected Čerenkov photons per image (typical numbers are at least 60 equivalent photoelectrons in camera photodetectors). This implicitly means that an IACT is able to recognize γ-ray induced showers only for energies above a given threshold (E_{th}), which is basically limited by the size of the collection mirror area and the efficiency of conversion from incident Čerenkov photons to detected photoelectrons. As the number of Čerenkov photons is proportional to the energy of the primary γ-ray, the telescope energy threshold inversely depends on the mirror surface, A, and the light detection efficiency, ϵ. It also depends, directly, on the background flux from the night sky, ϕ, the solid angle on the sky subtended by the collection mirror, Ω, and the integration time of the signals in the camera, τ, as the larger these factors the larger is the amount of background light collected by the telescope which makes it more difficult to detect the signal (Longair 1997):

$$E_{th} \propto \sqrt{\frac{\phi\Omega\tau}{\epsilon A}}\,. \tag{5.12}$$

Although the sensitivity of IACT grows when observing at high zenith angles due to the increase on collection area, their energy threshold moves to higher energies, as the Čerenkov light spreads in a larger area.

The more usual convention for the definition of E_{th} is the γ-ray energy for which the differential trigger rate distribution peaks. As this definition makes the E_{th} dependent on the slope of the γ-ray spectrum coming from the source, a reference object (a so-called standard candle) is needed to compare different IACTs. For northern hemisphere IACTs, the source widely chosen as reference is the Crab Nebula, which is introduced in more detail in Chapter 7.

Only two years ago, the lowest energy threshold reached with an IACT had been the one obtained by the WHIPPLE telescope, about 300 GeV. Nowadays, a new generation of Čerenkov telescopes are pushing down in energy. Both the HESS array and the MAGIC telescope have reached 100 GeV. Even further progress in lowering the energy threshold is the goal of the MAGIC collaboration, as its mirror collection area is substantially larger than any other existing IACT.

To conclude, observations with IACTs require clear moonless nights if the optimal sensitivity is required. In addition, Čerenkov light attenuation due to Ozone absorption and Rayleigh scattering when propagating from the emission point and through the atmosphere to the detector location is predictable, but the Mie attenuation factor highly depends on the atmospheric conditions which indeed are usually highly variable. Therefore, reliable observations require good weather and atmospheric conditions.

5.3 The MAGIC Telescope

The MAGIC Telescope (Major Atmospheric Gamma Imaging Čerenkov Telescope) is one of the latest generation of Čerenkov telescopes. It is located at the Roque de los Muchachos Observatory, in the Canary island of La Palma (at a latitude of 28.8° North, longitude of 17.9° West, and 2200 m above sea level). Its 17-m diameter reflector dish turns it into the largest Čerenkov telescope ever. The initial ideas of the project came with a "Letter of Intent" in 1995 (Bradbury et al. 1995), and the detailed Technical Design Report (Barrio et al. 1998) was ready in 1998. The telescope construction

started in September 2001 and took basically two years. The official inauguration was in October 2003 although the first Čerenkov images were recorded already in March that year. The commissioning phase of the telescope started right after the inauguration and was concluded one year after, at the beginning of autumn 2004. Since then, the telescope is running in normal operation mode, with only technical accesses during full moon periods between data taking shifts. MAGIC is an international collaboration of physicists and technicians from 17 institutions based in 10 different countries (Germany, Spain, Italy, Switzerland, Poland, USA, Armenia, Finland, South Africa and Bulgaria).

The MAGIC Telescope represents a challenge in technological innovations and testing of new techniques never used before in the field of IACTs. The commitment to technological improvement was forced by the goal of the experiment: to push down the energy threshold as much as possible, below the values achieved by WHIPPLE, to almost cover, with the highest sensitivity possible, the still unexplored energy gap between 10 GeV and 300 GeV in γ-ray astronomy (see the Introduction for discussion about the importance of this energy range). With a high conversion efficiency from Čerenkov photons to photoelectrons and the world-wide largest collecting mirror area, an E_{th} close to 30 GeV is the ultimate target for MAGIC.

In the following subsections, the most relevant elements of the MAGIC Telescope are described, with emphasis in the technological innovations and the system on which the author has been particularly involved.

5.3.1 The telescope frame, reflector mirror dish and drive system

One of the main goals of the MAGIC Telescope is to reposition to any direction in the sky in less than one minute, in order to make follow up observations of the prompt emission of Gamma-Ray Bursts (GRB) after an alert from an X-ray or γ-ray satellite. To achieve this goal, the weight of the moving parts of the telescope is required to be as low as possible, especially the mirror frame. The choice was to support the mirror dish with a three layer structure made of low-weight carbon fiber-epoxy tubes joined by aluminum knots.[5] Carbon fiber is rigid enough and at the same time provides MAGIC with low enough inertia.

The frame design follows the concept of a pre-existing 17-m solar collector with alt-azimuth mount. It is important to keep the Čerenkov time distribution narrow to minimize the effect of the Night Sky Background, so in order to minimize the spread in the arrival times at the camera plane, the overall curvature of the octagonal tessellated 239 m^2 reflector area is parabolic. The focal length to diameter ratio, f/D, is about 1. This ratio ensures that the effect of the optical aberrations in the shower images is smaller than the pixel size.

The telescope reflector is composed of 964 mirror elements of 49.5 $\times$ 49.5 cm^2 area each, 892 of them grouped in 4-element panels, and the rest in 3-element panels at the rim of the reflector dish. Each mirror panel is equipped with an internal heating system to prevent dew and ice formation. The curvature of the individual mirror elements is spherical. Due to the overall parabolic shape of the reflector, their focal length is gradually increased (from 17 to 18 m) when moving out from the center of the dish. The construction of these individual mirror elements is another of the technical innovations adopted by the MAGIC Telescope. An aluminium box filled by an aluminium honeycomb structure,

[5]The weight of the combined frame and mirror dish is less than 20 tons, and the final weight of the telescope is about 64 tons.

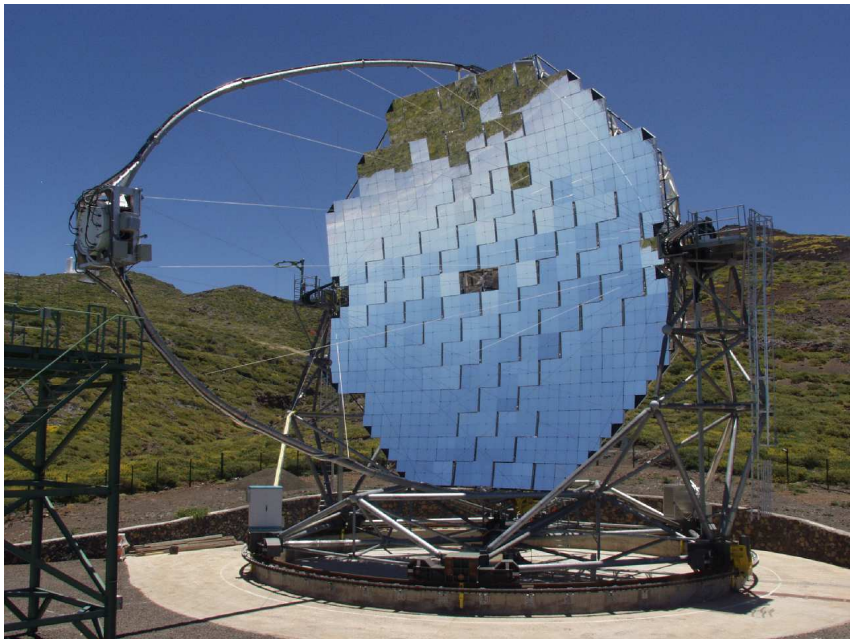

Figure 5.8: The MAGIC Telescope at "El Roque de los Muchachos" site in the canary island of La Palma.

which is light but rigid enough, constitutes the base of each mirror element. An AlMgSi1.0 alloy front plate is glued to the honeycomb. The 5 mm thick mirror front plate surface is polished and shaped with diamond milling and afterwards quartz coated to protect it against aging and scratches. The final assembly weights less than 4 kg. The mean reflectivity in the range of interest ($\sim$ 300-650 nm) is about 85% and the roughness of the mirrors surface is below 10 nm. 90% of the light of a parallel incident beam is collected in an area smaller than a small pixel of the MAGIC camera (Tonello 2005).

Another novel technique related to the reflector surface has been introduced in the MAGIC Telescope. Although the frame is rigid enough, the huge structure still suffers residual deformations when moving from one to another position. To correct for them, an Active Mirror Control (AMC) system has been developed. Each mirror panel is equipped with a switchable laser pointer. The spot that this laser makes in the focal plane is monitored by a CCD camera and used as a reference for the original position of the mirror panel. Two stepping motors can tilt the panel in both directions to adjust its position until the laser spot shifts to its nominal position. The readjustment operation of the whole reflector surface is controlled remotely and it is automatically done in less than 3 minutes.

The drive system of the MAGIC Telescope has been another challenging issue due to the high pointing accuracy required, the large dimensions of the telescope and the fast repositioning goal. The azimuth axis of the telescope is equipped with two 11 kW motors, while the elevation axis has a single motor of the same power. The position of the telescope is measured in the mechanical frame by three absolute 14-bit shaft encoders. With this configuration it is possible to measure the telescope position with an accuracy of about 0.02 degrees. The current maximum repositioning time is about 120 seconds[6],

[6]Recent tests have shown, however, that an azimuth speed twice the current speed is possible, so a maximum repositioning time well below one minute is achievable.

while the average is around 40 seconds. By using a CCD camera mounted on the reflector frame, it has been established that the telescope tracks to better than a 1/10 of a pixel size (Riegel et al. 2005).

5.3.2 The camera of the MAGIC Telescope

The camera is a decisive element in the general performance of an IACT. First of all, it is the device where Čerenkov photons are collected and converted to photoelectrons, so its efficiency strongly determines the energy threshold. Secondly, the γ/background separation power is highly dependent on the quality of the shower images so it also directly influences the sensitivity of the telescope.

Historically, IACT cameras developed from a single PMT to an array of a few hundred pixels. The progress of the last years can mainly be attributed to finer pixelization, allowing the subtle differences between hadron and gamma showers to be better revealed. Finer pixels have implied an improvement in the trigger efficiencies for γs, in the angular resolution, in the γ/h separation, and also some modest noise reduction by limiting the image to its minimal necessary size. In turn, also the energy resolution is slightly improved due to the better determination of the shower maximum location, particularly for low energy events.

An optimal IACT camera should be able to register both the low energy and the high energy showers with comparable efficiency. High energy showers generate more light and develop along larger depth range in the atmosphere, therefore their images in the camera are more extended (up to $\sim 1.5°$), so only a large field of view (FOV) camera ensures full containment of the higher energy showers images ($\sim 4\,^{\circ}$ ø FOV for $E_\gamma \lesssim 10$ TeV). Additionally, the information of any shower tail is very useful to improve the γ/h separation and the energy and angular resolution of the telescope. Moreover, the larger the FOV of the camera, the better sensitivity for studying γ-ray emission from extended objects (e.g., Galactic SNRs can have an angular extension larger than one degree). On the other hand, images from low energy showers (<100 GeV) are smaller so they demand a finer pixelization at least in the central region. A small pixel size also helps to reduce of the light of the night sky (LONS) background. This allows to reduce the trigger threshold preset on the discriminator level, which in turn implies a reduction in the E_{th}. Due to the high cost of each photosensor, the layout of the camera is always a compromise between a large FOV and a finer pixelization.

5.3.2.1 Camera layout and main design choice

The chosen design for the camera of the MAGIC Telescope also contributes to the general philosophy of a minimum weight telescope for a fast repositioning. Most of the trigger and readout electronics were not housed inside the camera but in the central data acquisition building, located 100 m away from the telescope. This choice minimizes the weight and size of the camera, and also reduces pickup noise, as the final processing signal electronics, which use to be noisy systems, are placed far away. Additionally, this design allows to reduce substantially the complexity of the camera, which is typically the element of the telescope that is more difficult to access. The camera contains no signal processing electronics, which simplifies maintenance and repairs.

The layout of the camera is schematically shown in Figure 5.9. Due to the compromise between telescope performance and cost, the hexagonal detecting area was split into two

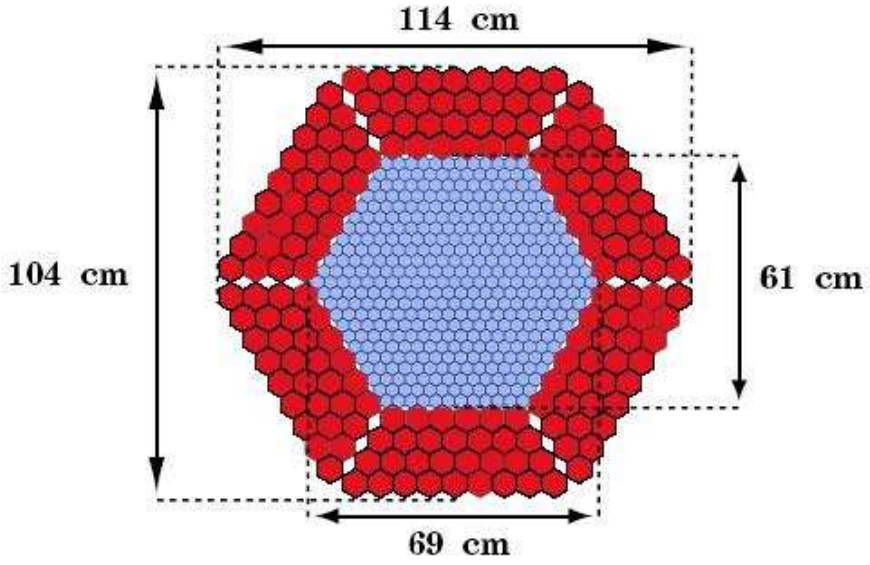

Figure 5.9: Scheme of the MAGIC camera layout. The inner region (in blue) is equipped with 0.1° ø FOV pixels to get a better sampling of the low energy showers. The outer region (in red) is segmented in 0.2° ø FOV pixels. The whole camera FOV is 3.5-3.8° in diameter.

regions: an inner part, segmented in 396 hexagonal finer pixels[7] of 0.1° angular diameter ($\sim$ 30 mm ø at the camera plane), which covers up to 2.1° (2.3°) ø FOV for the short (long) hexagonal camera axis; and an outer part with 180 hexagonal bigger pixels of 0.2° angular diameter ($\sim$ 60 mm ø at the camera plane), to cover up to 3.5° (3.8°) ø FOV. The trigger region consists only of the central 325 pixels, as described in Section 5.3.3.

The MAGIC camera configuration allows, with the finer inner pixels, a good sampling of the small images that are produced by low energy γ-rays. Although the shower tails of the larger images will be mapped into the outer region which is equipped with large pixels, the quality of the images of the higher energy showers is not substantially deteriorated, as the light density is also larger. The cost and complexity saved with respect to a uniform segmentation of the camera with finer pixels accounts on 540 photodetectors and all the elements of their corresponding readout channels.

Another crucial element conforming the layout of the MAGIC Telescope camera is a plate of light guides in front of the photodetector pixel matrix. Light concentrators provide two important benefits: a nearly 100% active area camera by minimizing the dead space between photosensors, and the rejection of a large fraction of the background light coming from outside the incident angle defined by the edge of the reflector dish. MAGIC light concentrators are made of a plastic material covered with aluminized Mylar foil of $\sim$ 85% reflectivity. They were especially designed to maximize the probability of double-crossing of the photons in the PMT cathode. Their entrance window is hexagonal. The output window of each concentrator cone is circular, matching the round active area of the photosensor. The use of this plate of light concentrators implies an increment of the photon detection efficiency of about 50%.

[7]The central pixel is left empty and is currently equipped with a higher sensitive photodetector devoted to optical studies.

Figure 5.10: Front view of the MAGIC Telescope camera. The plexiglas window protects the camera interior where the light concentrators collect the incident light onto the camera photosensors.

Finally, the light guides, the photosensors and, in fact, the whole camera are protected from the external environment by a 2 mm thick window made of UV transmitting plexiglas (all the described elements can be seen in the photograph showing the front of the MAGIC camera in Figure 5.10). Both sides of the plexiglas window are slightly reflective ($\sim$4%) so its overall transmission is 92%.

5.3.2.2 The camera photosensors

Photomultiplier tubes (PMTs) are the photosensors used for the 576 pixels of the camera. PMTs quantum efficiency (QE) is typically lower than the one achieved by HPDs and APDs, but the latter were too expensive and their active area was still limited. The MAGIC collaboration started a R&D program together with the English company Electron Tubes (ET) in order to design a model of PMT which fulfils all the requirements of the telescope:

- A diameter smaller than 30 (60) mm to achieve a FOV of 0.1 (0.2) °.
- Good photon collection once inside the light concentrator cones.
- Low gain ($\lesssim 2 \times 10^4$) compared to typical PMTs to avoid that the light of the night sky (LONS) induces photoelectron rates in excess of a few hundred MHz.

- Good time resolution with a pulsed FWHM close to 1 ns in order to exploit the differences in time spread of the Čerenkov flashes, allowing an efficient coincidence trigger design for the detection of γ-ray signals and an efficient suppression of background induced triggers.

- Wide dynamic range up to 5×10^3 to detect the largest expected signals ($\sim 5 \times 10^3$ phe per camera pixel for a ~ 10 TeV γ-induced shower), and still resolve signals of just few $\gtrsim$ phe.

- Good QE in the range of wavelengths of the showers Čerenkov light (i.e., roughly between 300 and 600 nm).

- Low afterpulse rate to avoid limiting the minimum trigger threshold setting for individual PMTs.

- Single photoelectron response, as it makes the calibration of the detection chain much more simple.

Two new models of PMTs were developed and constructed by Electron Tubes for the MAGIC Telescope: ET9916A (25 mm ø) for the inner pixels , and ET9917A (38 mm ø) for the outer pixels. These PMTs have two peculiarities that distinguish them from conventional PMTs and make them suitable to fulfil most of the MAGIC requirements: a hemispherical photocathode and an only 6-stage dynode system in circular-focused configuration. The advantage of a hemispherical-shaped photocathode compared to the flat entrance window of the conventional PMTs is, on one hand, a higher aperture solid angle which provides better light collection once inside the light guides, and, on the other hand, a reduced time jitter as the produced photoelectrons travel roughly the same distance between the photocathode and the first dynode. On the other hand, in a 6-stage dynode system it is easier to obtain a low gain and still to have good interdynode electron collection efficiency than in a typical 10 or 12-stage photomultiplier. Additionally, a 6-dynode PMT provides a lower interdynode time spread. All in all these PMTs are capable to produce signals with rise times as short as $\sim$ 700 ps and FWHM $<$ 1-1.2 ns (Ostankov et al. 2000).

The hemispherical shape of the photocathode has an additional advantage: for some incident angles, photons cross the photocathode twice. In these cases, if the photon is not absorbed in the first crossing it still has a second chance of being absorbed at the other side of the hemispherical sensitive area. Therefore, double-crossing photons have a higher probability to create a photoelectron and hence be detected by the PMT. The QE enhancement due to this double crossing effect can be as high as 20%. Once this effect was known and characterized, the design of the light concentrator guides was adapted to maximize the number of photons which suffer double crossing.

The photocathode of the PMTs provided by ET is bialkali with enhanced green sensitivity. Its uniformity and its QE as a function of the wavelength of the incident light have been measured in detail for a sample of PMTs (Paneque 2000). The mean QE exceeds 20% in the 330 - 470 nm range (25% at the peak), which matches quite well the expected Čerenkov photon spectrum range. A further substantial enhancement of the effective QE of the PMTs used in MAGIC was achieved with the application of a light scattering lacquer mixed together with a wavelength shifter (Paneque 2004). After coating manually the PMT photocathode with the lacquer, the mean QE improves up to 23% (the peak value arriving close to 30%).

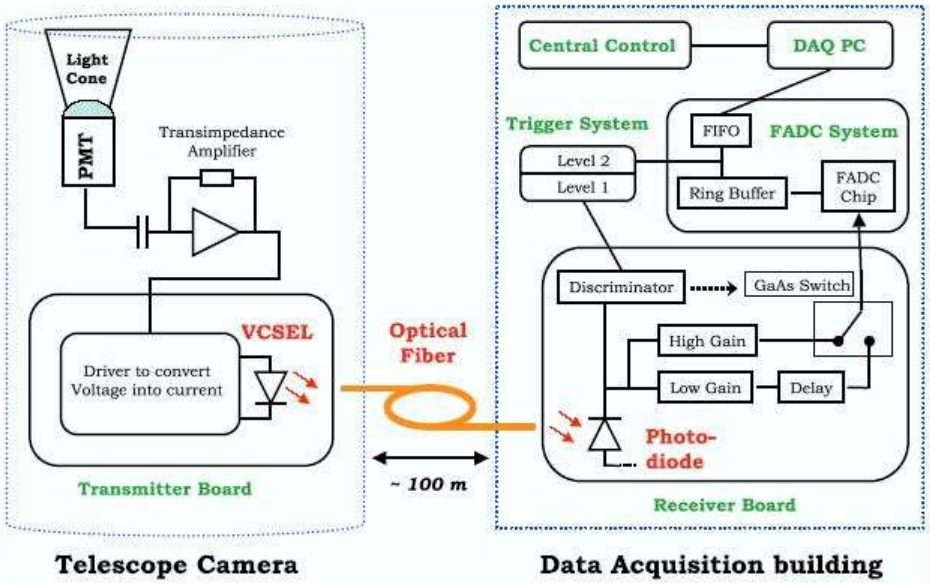

Figure 5.11: Scheme of the signal flow and the data readout in the MAGIC Telescope.

Ideally, photosensors should allow single phe detection, which makes the calibration of the camera much more simple, but also should have low afterpulsing probability to avoid spurious triggers. Unfortunately, these are contradictory requirements: a high amplification in the first dynode provides a good single phe response, but goes against a low afterpulse rate. The approach chosen for the ET PMTs was to use a 3R-R-R-R-R-R-R base with an overall HV of $\sim$ 1.1 kV (i.e., $\sim$ 120 V between dynodes and $\sim$ 360 V between the photocathode and the first dynode). It was also found that increasing by about 50 V the voltage applied to the 5^{th} and 6^{th} dynodes a linear behavior over the whole desired dynamic range is achieved. This is achieved by using an active load system which fixes the last two dynodes to -350 V and -175 V with respect to the anode, and a zener diode which sets the photocathode to 1^{st} dynode voltage to 350 V. With this configuration the overall PMT gain is within the required values, but it is still possible to resolve single phe signals, and the afterpulsing rate is below an acceptable level.

5.3.2.3 The analog optical transmission of the PMT signals

The decision of housing the main readout electronics outside the camera of the telescope implied a major challenge: the substantial distortion and attenuation that the PMT pulses suffer when they are transmitted through a 150 m long coaxial cable to the data acquisition building. A distortion of a few ns of the fast Čerenkov optical flashes can reduce the efficiency of the time coincidence based trigger. The MAGIC collaboration decided to drive the transmission of the PMT signals over such a large distance through optical fibers, for which the degradation of analog signals is significantly lower than in coaxial cables. The use of optical fibers for the signal transmission has additional advantages: there is no crosstalk between different channels (which are typically packed very close to each other in their way to the data acquisition building), signals can not be affected by external electromagnetic interferences, optical fibers are much lighter, and individual channels can be packed more compactly. This idea was first proposed and developed by

the AMANDA collaboration (Karle 1997).

The electrical PMT pulses are converted into light pulses. Each PMT output pulse is passed through the following stages still inside the camera (a scheme of the complete signal readout chain is shown in Figure 5.11). Right after the PMT base, the signal is amplified by a fast low noise transimpedance amplifier. The coupling of the PMTs working in low gain regime to this fast low noise amplifier is crucial when we want to operate at manageable anode currents and still detect the smallest Čerenkov light flashes. After the amplification, the pulse enters a *transmitter board* where it is transformed to a light pulse by means of a Vertical Cavity Surface Emitting Laser (VCSEL). The output of the VCSEL is coupled to an optical fiber, which brings the out from the camera. In the transmitter board, the voltage signal from the PMT base is converted into a current signal which modulate the current flowing through the VCSEL and hence its light output. The main technical innovation brought by MAGIC to this analog optical transmission technique has been the use of VCSELs instead of Light Emitting Diodes (LEDs) or other conventional lasers. It was found that VCSELs match the dynamic range and bandwidth provided by the transimpedande amplifier. Unexpected instabilities in the performance of the VCSELs showed up but, fortunately, slight modifications of the design were found (Blanchot et al. 1998 and Rose et al. 2000) to bring the instabilities below the statistical fluctuations of the PMT signals.

5.3.3 The trigger and the data acquisition systems

The signals from all the channels arrive through the optical fibers to the data acquisition building. To begin with, the optical pulses have to be reconverted into electrical pulses. This process is done by photo-diodes inside the so-called *receiver boards*. Still inside these boards, each electrical pulse is duplicated: the "trigger signal", from which the trigger system will decide if the event has to be recorded, and the "FADC signal", which will be digitized and subsequently stored by the data acquisition system (DAQ).

Only the signals from the innermost 325 pixels of the camera are considered for the trigger. As shown in Figure 5.12, the trigger pixels are grouped in 19 overlapping macrocells of 36 pixels each. Then, the decision of the whole trigger system is segmented in several levels. The level 0 trigger is located still within the receiver boards and acts on each individual PMT signal. Each channels analog pulse passes through a discriminator and, if its amplitude is larger than a tunable threshold, a square digital gate is opened and sent to the trigger system. The gate width is also adjustable (normally set to 6 ns). The discriminator threshold level can be tuned remotely so it can be changed during data taking according to the needs of each observation (e.g., observations of extragalactic sources imply a lower level of LONS than galactic observations, so the discriminator thresholds can be set lower to increase the sensitivity). After the level 0 trigger, the digital signal generated for each pixel is split in two, one entering the first level trigger and the other one to be used in the second level trigger. The level 1 trigger searches for coincidences of neighbor pixels independently in each defined macrocell. After a logical comparison of the digital outputs coming from the receiver boards, clusters of 2, 3, 4 or 5 next-neighbor in a short (few ns) time interval are required. If the cluster multiplicity is larger than 2, it is additionally required that each pixel in the cluster has at least two next-neighbors. This is the so-called closed-packed trigger configuration which helps to reduce the rate of triggers caused by muons. The level 1 configuration which is used for normal data taking is four closed-packed pixels, although the lowest energy showers can

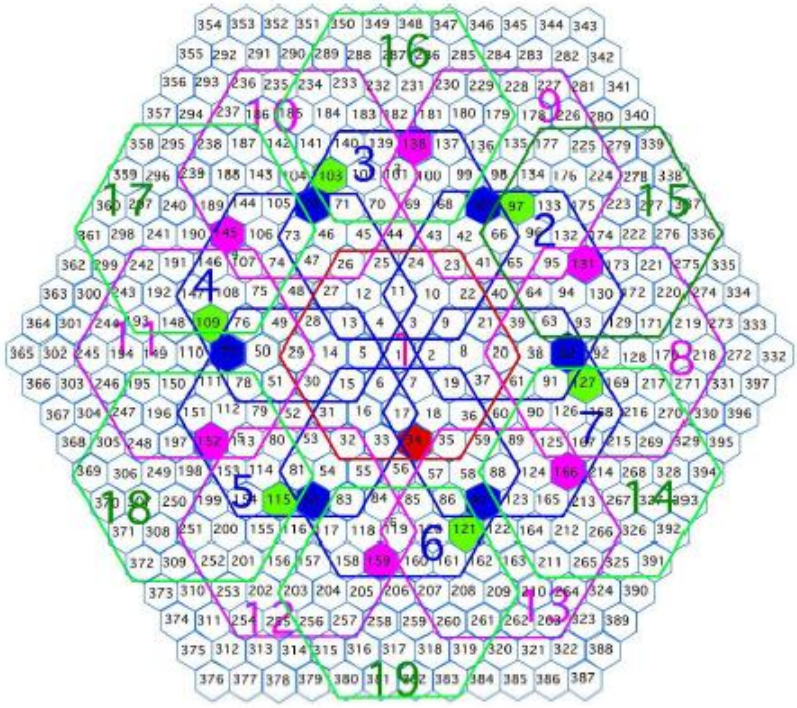

Figure 5.12: The trigger macrocells in the inner region of the MAGIC camera.

be partly rejected by this trigger level configuration selection so other possibilities are currently under study. The second level trigger can perform a "digital analysis" of the shower image which considers the topology of the event. For the time being, the level 2 trigger is just an inclusive 'OR' of the 19 macrocells.

The Second part of the analog signal coming from each pixel is sent to the Flash Analogic-to-Digital Converter (FADC) system. But still in the receiver board, the analog FADC signal is again duplicated into a "high-gain" and a "low-gain" channel. The high-gain signal is amplified by a factor of 10 whereas the low-gain signal is delayed by 50 ns. If the high-gain signal exceeds a preset threshold, a switch is actuated and the delayed low-gain signal is added right afterwards the high-gain. The combination of both signals with different gains is then digitized by the same FADC channel. This procedure substantially extends the dynamic range of the 8-bit FADCs.

The level 2 trigger directly communicates with the FADC system and enables the acquisition of the data whenever an event passes all the trigger system levels. It should be mentioned that the level 2 trigger has a prescaler board to scale down the number of triggers in order not to overcome the maximum continuous acquisition rate of 1 kHz allowed by the DAQ system in normal operation conditions. The DAQ system of the MAGIC Telescope consists on 18 crates of 4 FADC boards and a dual processor PC. Each FADC board digitizes the signals coming from 8 channels. Since the digitization speed is limited to 300 MSamples/s, the analog signals must be stretched in the receiver board to $\gtrsim$ 6 ns FWHM, so that at least 4 points can be measured for each pulse, and the pulse shape can be reconstructed. The FADC chips are continuously digitizing the analog signals of each pixel and storing them in an intermediate ringbuffer. When the level 2 triggers, the FADC chip stops digitizing, the position in the ringbuffer of the signal that

made trigger is determined and 30 time slices for each pixel (15 for each of the high and the low-gain channels) are written to a 512 kBytes FiFo buffer. The DAQ procedure has zero dead-time readout at the design trigger rate of 1 kHz. Finally, the digitized pulse is formatted into the standard raw event data format, saved to disk, and in a few hours-days written to tape. Up to 150 GBytes of rawdata can be generated in one data taking night.

5.3.4 The calibration system

The telescope signal readout digitizes the electronic pulse produced at each of the pixels of the camera for each event that produces trigger. From this information the characteristics of the incident primary particle should be reconstructed. In order to be able to do so it is mandatory to calibrate the camera and the readout chain with respect to the incident light flux, i.e., to determine the conversion factor between number of recorded FADC counts and number of incident photons for each individual pixel.

The MAGIC calibration system provides fast light pulses at different wavelengths and variable intensity in order to calibrate the whole dynamic range of the camera photosensors and their readout chain. The system consists in a box located at the center of the telescope mirror dish which houses 64 LEDs emitting at three different wavelengths: 370 nm (UV LEDs), 460 nm (blue LEDs) and 520 nm (green LEDs). They are arranged in 16 slots of 1, 2 or 5 LEDs that can be switched on independently. The light pulses have about 3-4 ns FWHM duration, which is nearly as short as the Čerenkov light flashes reaching the individual pixels from the air showers. The calibration box is equipped in addition with a continuous light source with the purpose of simulating and calibrating the PMTs response for different conditions of background light, as different levels of the light of the night sky or the presence of the moon or stars in the camera FOV. A diffusor placed at the window of the calibration box provides a uniformity of the light illumination better than 3% along the whole camera.

When calibration data are taken, a train of trigger pulses (of adjustable frequency) is sent to the calibration box via an optical fiber. At the same time, the same trigger pattern is sent to the general signal readout trigger system with an additional delay to readout the appropriated calibration pulse signals and reject accidental triggers due to cosmics. This dedicated calibration trigger line allows to take calibration data even during normal data taking. Calibration events are indeed interleaved within the cosmic events and used afterwards in the data analysis to ensure the stability of signal calibration along the whole data taking.

The calibration of the signals recorded by each pixel of the camera is done basically in two steps: first a relative calibration and then an absolute calibration. The relative calibration is essential in order to equalize the response of different channels when subjected to the same input signal. The complexity of the readout chain for each pixel makes it natural that the signals obtained from different pixels are not directly comparable (the PMTs are hand-made devices so a sizeable spread on the quantum efficiency, the photo collection efficiency and other characteristics is expected; the electrical to optical conversion of the signal in the VCSELs is also expected to be slightly different for different channels...). When the telescope is observing a region of the sky, the camera is not uniformly illuminated, so a source as the one provided by the calibration system is essential to correct for the differences that exist between the pixels. Periodically, with intervals of several months, a general flat-fielding of the pixel high voltages is performed to make the response of the camera uniform. It is illuminated with pulsed light of a certain

intensity and the high voltage settings of each PMT are adjusted in order to obtain the same response in the whole camera. Additionally, every data taking night, dedicated calibration runs are taken to compensate for the different degradation with time of the characteristics of each PMT (nominal HV, quantum efficiency, gain, etc.), the VCSELs response and the evolution of the conditions of light collection by the light guides or the transmittance of the plexiglas. Moreover, the VCSELs and other parameters of the telescope change in time scales of hours, so the relative pixel calibration needs a frequent update along the night. These updates are performed using interleaved calibration events that are constantly generated with a rate of 50Hz.

On the other hand, an absolute calibration is also needed in order to convert the signal recorded by a pixel in FADC counts to physical quantities more related to the flux of photons impinging onto the camera. The calibration system of the MAGIC telescope provides three independent methods to perform the absolute calibration:

- The *Blind Pixel* is a non-coated inner-size PMT placed in the outermost ring of the camera with a filter that the incident light by a factor 100 over the PMT range of wavelengths. Additionally, the area illuminated of the blind pixel is well under control by the use of a diaphragm (1 cm^2), and the PMT quantum efficiency has been accurately measured. The large attenuation allows the blind pixel to resolve single photoelectrons. By analyzing the single phe spectrum recorded by the blind pixel, the mean number of photoelectrons produced in the photocathode can be estimated and, together with the well-known QE and the pixel geometry, the mean number of photons arriving from the calibration pulses per unit area can be computed.

- The *PIN diode*, Positive-Intrinsic-Negative diode, is a photodiode that exhibits an increase on its electrical conductivity as a function of the intensity and wavelength of the incident light, with an overall detection efficiency very close to 100%. The PIN diode is calibrated with a ^{133}Ba source, and is located 110 cm from the calibration box. By monitoring the light pulses emitted by the calibration pulser, the mean number of photons that arrive per unit area onto the camera plane can be estimated from the number of phe generated in the PIN-diode, its QE, the LED emitted light spectrum and the geometry of the system.

- Traditionally, Čerenkov telescopes have followed the *Excess Noise Factor* or *F-Factor* method to perform their absolute calibration. The method is based on the fact that a PMT adds only a small excess noise to the intrinsic fluctuations of the photoelectron flux, excess noise which is linearly related to the initial number of phe that produces the PMT output signal pulse. The F-Factor of any electronic device is simply defined as:

$$F = \frac{(\text{Signal/Noise}) \text{ at the input}}{(\text{Signal/Noise}) \text{ at the output}} , \tag{5.13}$$

  being therefore a numerical value which account for the additional noise introduced by the readout and amplification chain, assuming it is independent on the signal intensity. From the knowledge of the F-Factor of the PMTs and the analysis of the output signal of each pixel, one can extract the average number of phe impinging on the first dynode of each PMT. In the case of the PMTs of the MAGIC camera, the F-Factor has been measured for a sample of 20 PMTs (Paneque et al. 2003) giving a value of 1.15 ± 0.02. Further details on the usage of this method are given in Chapter 6, where the data analysis procedure used for this Thesis is described.

The advantage of the F-Factor method is its simplicity and robustness. Its disadvantage is that it does not implicitly include the QE and phe collection efficiency of the PMTs (which can vary from one PMT to another) nor the transmission efficiency of the light guides, whereas the Blind Pixel and the PIN-diode methods do. Therefore, the F-Factor method measures the number of phes arriving to the first dynode of the PMTs and the other two methods measure the photon flux. Currently, although both the blind pixel and the PIN diode are already operative, the F-Factor method is the calibration procedure followed in the MAGIC data analysis.

5.3.5 The control system

The MAGIC Telescope is automatically controlled from a central PC. The control system is split up into functional units which correspond to the independent subsystems of the telescope already described (DAQ, Camera, Calibration, Drive, Level 2 trigger, AMC, Starguider). A central control computer coordinates all the subsystems, which have no intercommunication, and provides the user interface during normal data taking. The operator has access to all the subsystem functionalities from the central control program, which is written in Labview 6i and steers the subsystems over 100 Mbit/s Ethernet connection and a custom TCP/IP protocol communication.

Another dedicated control program steers the camera of the telescope. It is also written in Labview 6i and offers the shifters an independent user interface with more detailed information about the camera status. It is based in the same concept of the central control program: every functionality of the camera is controlled by independent camera subsystems which are managed by a "central" camera control. Each camera subsystem control software is written in C/C++ and accesses the hardware through basically two communication buses and protocols:

- Two CANbus lines of about 200 meters long with a total of 16 nodes are used for the regulation of every pixel HV setting and to monitor each pixel HV and DC current every 3 seconds. The remote control of devices which have serial port access is also done through these CANbus lines by using CANbus to RS-232 converters, as is the case of the remote control of the HV camera power supply and the setting of the pixels discriminator threshold.

- Two RS-485 bus lines of about 200 meters long are used to communicate the camera control program with two autonomous Programmable Logic Controllers (PLCs). Through these lines and with the Modbus protocol the cooling system of the camera, the camera lids, the camera Low Voltage power supplies and other auxiliary camera subsystems are controlled.

The author of this work has been the responsible for the control of the camera subsystems steered by the PLCs. A more detailed description of this control, the involved subsystems, their required specifications and their current performance is given in Appendix D, with special emphasis on the cooling system.

Chapter 6

Data analysis method

This Chapter describes the steps followed in this Thesis for the analysis of the MAGIC Telescope data, from the checks to ensure the quality of the data to the data reduction chain: the signal extraction, calibration, image cleaning and parameterization, γ/hadron separation and final signal evaluation.

6.1 Sources of background

One of the major challenges of the Imaging Air Čerenkov technique is the background characterization and subtraction. IACTs have to deal with two types of background:

Cosmic ray showers As already described in detail in the previous Chapter, the EASs initiated by the much more abundant hadronic component of the cosmic rays generate images in the camera of the IACTs which are similar to those produced by γ-induced showers. However, the substantial differences of the processes participating in the development of both types of EAS allow to discriminate γ-induced images from hadronic, as is explained in more detail later in this Chapter. It is worth to remind here that the EAS induced by cosmic ray electrons represent an irreducible background as they develop an electromagnetic shower completely undistinguishable from γ-induced showers.

Background light Čerenkov photons produced in the EAS are far from being the unique source of signal in the PMTs of an IACT, in fact Čerenkov light has been estimated to only contribute a factor $\sim 10^{-4}$ to the total of light of the night sky (LONS). All the other sources of light should be, therefore, taken into account as they can interfere in the detection of the EAS. There are two kinds of night-sky background (NSB): a diffuse component, also called LONS, both from an artificial (human-made light pollution, usually low near astronomical sites), and a natural origin (diffuse moonlight, sunlight scattered by interplanetary dust, zodiacal light, ionospheric fluorescence, etc.); and the NSB due to starlight (bright stars present in the FOV). Therefore, the intensity of the NSB depends on the observation conditions at the astronomical site, on the moment of the day and epoch of year when the observation is done, and on the portion of the sky which is observed, decreasing with increasing galactic latitude as we move far away from the stars crowded galactic sky coordinates. "El Roque de los Muchachos" observatory on the Canary Island of La Palma provides one of the best sky conditions for astronomical observations in the world.

Several studies has been performed to measure the intensity of the LONS at the site (e.g. Mirzoyan and Lorenz 1994) and it is estimated to produce an average of ~ 0.15 phe/ns for a 0.1° ø inner pixel of the MAGIC camera for moonless nights and pointing outside the galactic plane. The NSB photons increase the noise level of the output signal registered by the PMTs and therefore makes more difficult the detection of the showers initiated by the lowest energy γ-rays. A proper evaluation of the NSB and subtraction of its effect on the data are essential for the data analysis, as is explained in Section 6.4.2.

The presence of the moon increases the brightness of the night sky. Nevertheless, observations with moonlight are possible to be carried on depending on the moon phase and its angular distance to the telescope pointing FOV. The influence of the moon on the level of LONS is minimum at 90° angular distance. The moonlight flux also depends on the zenith angle of the observations and the atmospheric conditions. Rayleigh scattering results in a loss of 10-20% of the light flux even for a clear atmosphere. Unavoidable Mie scattering results in quite some strong light intensity close to the moon direction. At around 25° angular distance away from the moon, the direct scattered moonlight diminishes to below the level of the moonless LONS. The presence of thin high altitude haze layers of clouds (which can be recognize by the weak halo that is formed around the moon) may act as scatters of the moonlight and imply an increase of the PMTs DC current although observing at enough large off angle from the moon. The current conditions for observations during moon shine are the following: do not observe during full moon or moon illuminated by more than 70% (not more than 30% if haze layers of clouds are present), and never observe below 25° or above 130° angular distance to the moon (in the latter, direct moonlight may directly hit the camera). The value of the pixels level 1 trigger discriminator thresholds should be adjust by looking at the mean DC current level monitored in the PMTs, so too high trigger rates due to accidentals are avoided.

6.2 Monte Carlo simulation

Differently to other detector physics fields, in IACTs it is not possible to characterize the detector response with a controlled flux of known primary particles (a so-called test beam). Realistic and detailed Monte Carlo (MC) simulations are crucial for the data analysis. Moreover, the complexity of the processes involved in the generation of the shower images in the camera of an IACT, and the large number of parameters playing a role in the development of an EAS and the subsequent detection of its Čerenkov light, make the Monte Carlo simulations a must.

The MAGIC Telescope is not an exception and a lot of the steps of its data analysis are based on or make use of MC simulations. A chain of programs simulates the properties of different physics processes and detector parts:

- Simulation of EAS: The development of atmospheric EAS, either from primary γ-rays and hadronic cosmic rays, is done with the CORSIKA package (Heck and Knapp 2002), version 6.019, which was developed by the KASKADE collaboration. In the simulations, each particle is treated individually, when calculating the tracks and the interactions it can undergo, and its characteristic parameters (as energy, propagation direction, time, etc.) are stored. The output file contains all the Čerenkov photons arriving on the ground around the telescope location.

- Simulation of the Mirror Dish: In this step the propagation of Čerenkov photons through the atmosphere and their reflection in the mirror up to the camera plane are simulated. The output of this program corresponds to the photons hitting the camera.

- Simulation of the FOV star field: This program is needed to add light from the non-diffuse part of the NSB to the images recorded by the telescope. It reads data from a star catalogue and calculates, from the given position of the telescope's optical axis, the time of day, and the positional and spectral data for each star from the catalogue, how many photons of which wavelength hit a certain surface (mirror dish) over a given time (integration time). For each photon the direction cosines are calculated. Arrival time, wavelength and ground position are randomized.

- Simulation of the electronic chain response to background photons (both from the diffuse NSB and from individual stars): This program simulates the analogue signal at the entrance of the trigger discriminator and the digitized signal at the output of the FADC for phe coming from stars and the diffuse NSB. This is done for a much longer time window than that used for each simulated shower and stores the result in a database. The camera program subsequently selects randomly a smaller time window corresponding to the length of the FADC time window and adds it to the shower simulation. This pre-calculation saves substantial computing time as the Camera program does not have to generate the background photons for each event.

- Simulation of the camera response: The Camera program simulates the PMTs and the behavior of the trigger and FADC systems. In addition it also allows to combine it with the NSB. The output of the program is written in the same format as the real data, which allows to test the entire analysis software chain.

The detector simulation reproduces the effects that the different elements of the read-out chain produce in the signal. The mirror reflectivity, the efficiency of light collection of all the parts involved, the gain of the PMTs, the noise introduced by the electronic chain, etc., all these parameters are adjusted to match the behavior of the telescope when the data were collected. A particularly important parameter to be tuned in the MC simulation is the width of the Point Spread Function (PSF) distribution of the light collected by the mirror dish and focused onto the camera. Twice or three times per year, a major access to the telescope is done to adjust those mirror panels that have deviated too much from their nominal position. Mirror disaligment makes the Čerenkov photons focus into a wider region of the camera. The resulting shower images get also wider. As MC simulated images are used as a reference in several steps of the data analysis, it becomes essential to estimate the quality of the telescope focusing for the periods in which the analyzed data sample was taken, and generate MC simulations accordingly to that focusing quality. Several independent methods are being used to characterize the PSF of the telescope:

- The detection of strong γ-ray sources, as the Crab Nebula (see Chapter 7) and Active Galactic Nuclei in flare state, allows to obtain quite pure samples of real γ-ray shower images, which can then be compared to MC images simulated with different values of the width of the PSF distribution, looking for the best agreement.

Table 6.1: Parameters for the generation of the MC sample used in the analysis of the data presented in this Thesis.

Primary particle	**γ-ray**	**proton**
Energy range	10 GeV - 30 TeV	30 GeV - 30 TeV
Spectrum slope	$E^{-2.6}$	$E^{-2.75}$
Impact parameter range	0 - 300 m	0 - 400 m
Zenith angle range	0 - 30°	0 - 30°
Num. simulated showers	$\sim$ 10 M	$\sim$ 30 M
Num. triggered showers	$\sim$ 300 k	$\sim$ 200 k
diffuse NSB level	0.178 phe/ns for 0.1×0.1 deg^2	
σ of the PSF[a]	14 mm	

[a] See Appendix E.

- The width of the ring-shaped images generated by muons in the camera are also used as an estimator of the focusing quality of the telescope for different data taking periods. MC simulations of muons again look for the best match with the real images.

- Direct measurements with a CCD camera of the image of bright stars projected onto a panel placed at the camera plane is a third independent method used to monitor the telescope focusing.

In this work, the first of these three methods has been used to estimate the best match value of PSF for the different observation periods under consideration. The results are reviewed in Appendix E and compared with muon studies.

Table 6.1 summarizes the parameters of the Monte Carlo sample used in this work. Analogous samples have been also generated to look for the best match with real data events and for moon data studies, changing respectively the sigma of the PSF distribution and the level of diffuse NSB.

The software package for data analysis developed by the MAGIC collaboration is called MARS (MAGIC Analysis and Reconstruction Software), and works in the ROOT framework (Brun et al.). The analysis performed in this Thesis is based on version Mars V0-11-1.

6.3 First selection of the data sample

The first step in the data analysis is the selection of the data sample that one wants to analyze. The selection is limited to the availability of each type of data that is needed to perform a complete unbiased analysis, which unfortunately is often not fulfilling all the desired requirements.

6.3.1 Types of data runs

As explained in the previous Chapter, events are stored by the DAQ into raw data files, which contain for every pixel the information of the signal readout in 30 digitized FADC time slices. The DAQ system closes the file when a maximum number of events are stored

or if an inconsistency occurs in the system. Each raw data file is called a run and a run number is assigned to it.

During normal data taking of MAGIC, three different kind of raw data files are stored:

Data runs The telescope tracks a position in the sky and an event is generated when a trigger occurs (see Section 5.3.3 for details of the trigger conditions). Special calibration events are interleaved with the cosmic events at regular time intervals.

Calibration runs The calibration box emits light pulses and an event is recorded after a synchronized trigger signal is sent to the DAQ (see Section 5.3.4). At least one dedicated calibration run using UV light is mandatory before the observation of each of the scheduled sources every night. If a source is tracked for more than one hour or if the data taking conditions change substantially (e.g., the zenith angle of observation of the source, or the weather conditions), extra calibration runs are taken in between data runs to recalibrate accordingly.

Pedestal runs Information of the NSB and other sources of noise is taken during a so-called pedestal run. The trigger is activated randomly, 1000 events are recorded with a trigger rate of 500 Hz. These data allow to determine the baseline of the signal and its fluctuations for the NSB conditions of the current observations. At least one pedestal run is taken right before a group of calibration runs.

Alternatively raw data files can be classified according to the telescope pointing position respect to the source:

ON data runs The telescope is tracking and pointing the source.

OFF data runs The telescope is pointed to a position in the sky with no known source contained in the FOV but with similar background and zenith angle conditions of the ON runs.

Wobble mode data runs Observation technique where the source is tracked a fixed angular distance off-axis from the center of the FOV, so the source position can be treated as ON and the symmetric position respect to the camera center as OFF.

6.3.2 Run selection

Ideally, one would like to use for the analysis as many hours of ON data as possible, and several times more OFF data in order to reduce the effect of the background fluctuations on the analysis results. However, if the source of interest has not been observed in Wobble mode, often the quantity of dedicated OFF data available is not larger nor even equal to the quantity of ON data. In order to enlarge the statistics of OFF data, OFF data runs specially taken for other sources observed during the same data taking period can normally be used, or even data runs on faint sources.

Once the data samples to be used for the analysis have been established, a first selection of runs based on the quality of the data taking should be done.

- The rate of events that trigger (trigger rate), which is monitored during data taking, can be checked along each data taking night and compared between different nights. A low trigger rate points to bad atmospheric conditions or to deficient data taking

due to some telescope system misbehavior. Additional checks are needed to find out the reason of the problem and decide if these data runs can still be used in the analysis or they should be excluded.

- In order to confirm or discard if bad atmospheric conditions were the responsible for those localized low rate data taking nights or hours, the parameters recorded by the weather station (such as the relative humidity), the operator reports, and the atmospheric extinction coefficients should be checked. The Mercator and the Carlsberg Meridian optical Telescopes, which are also located at the Roque de los Muchachos Observatory in La Palma, provide daily measurements of the atmospheric extinction coefficient. The values are accessible from their web pages.[1] An extinction below 0.2 magnitude in the r' passband provided by the Carlsberg Meridian Telescope (CMT) has been required to accept a data taking night as good. Nights excluded from the analysis due to a too high extinction coefficient coincide with days were a red sunset was observed, pointing to the presence of "calima" (dust, fine sand) in the air. As reference of the typical behavior, Figure 6.1 shows the extinction coefficient measured by the CMT during the last two decades.

- The online runbook that the shifters fill up each data taking night has been checked for each night of the selected data sample. There, technical problems occurred during data taking and any other issue affecting the quality of the data is written down. Runs for which the DAQ was aborted, calibration runs where the box failed to fire, runs where the lids were closed or the PMTs HV was reduced automatically for safety reasons, etc. were correspondingly excluded thanks to this check.

- The general MAGIC Telescope database, which is automatically filled up the day after of the data taking, allows to easily check for runs with too few events, others that has been tagged as test runs, and runs with wrong loaded trigger table, calibration script or discriminator threshold settings.

6.4 Calibration, cleaning and image parameterization

Once the first run selection is complete, we proceed to transform the raw data into pixelized images in the camera of the telescope which can be related to the development of an EAS. The following subsections explain step by step how this is accomplished.

6.4.1 Signal extraction

The MAGIC telescope uses a 300 MHz FADC system to sample the air shower signals. 30 FADC samples are recorded for each pixel. There are different methods implemented in the MARS package to extract the charge and the arrival time information of the signal, all of them with the aim of minimizing the effect of the NSB. In this work, the "digital filter" signal extractor, currently the most widely used in the MAGIC data analysis, has been applied. In the "digital filtering", the signal is calculated as the weighted sum of n consecutive FADC slices, being the number of slices to be summed up a tunable parameter

[1] Mercator Telescope web page: http://www.mercator.iac.es/extinction/extinction.html, the extinction coefficient data is only available for few days as it is tabulated on-line only when the photometer is used for the observations and the sky presents photometric conditions. Carlsberg Meridian Telescope web page: http://www.ast.cam.ac.uk/∼dwe/SRF/camc_extinction.html

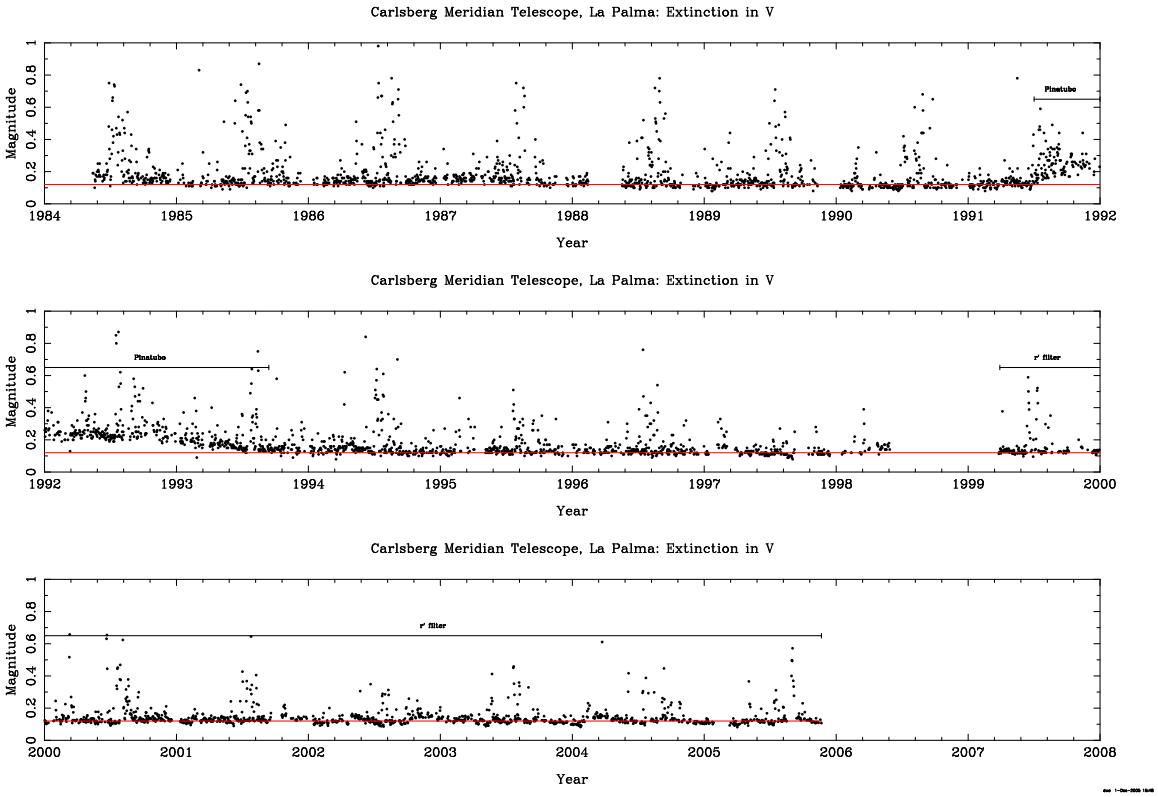

Figure 6.1: The V extinction coefficient from 1984 to 2005 as measured by the Carlsberg Meridian Telescope. The effect of the eruption of Mount Pinatubo in June 1991 is clearly visible. The number of high extinction values that occur every summer is normally caused by Saharan dust.

of the extractor. Since the pulse shape is dominated by the electronic pulse shaper, a numerical fit is possible. The weights are determined by taking into account the expected pulse shape, known from the pulse shaper and from MC γ simulations. A more detailed description of this extraction method is given in Bartko et al. (2005). In order to reduce the bias introduced by the signal extractors that imply a search of the signal maximum before extracting (since positive fluctuations of the background are then favoured), a pulse position check is previously done. The first 100 events of the run are readout and the mean position of the pulse maximum is evaluated. Then a searching window of limited width around the determined pulse position is defined for the signal extraction of all the events and pixels. The digital filter extractor is requested to fit its pulse shape only for the FADC slices included in the searching window.

The disadvantage of the digital filter signal extractor is that it can not efficiently extract pulses which are out of range of the recorded window. As explained in more detail in Section **??**, a hardware problem in the time delay setting of one of the trigger macrocells affected most of the 2005 data. As a consequence, those events triggered by the misbehaving macrocell tagged the starting point to register the pulses too late and the position of the pulses appeared shifted to the left even by two FADC time slices. For the case of the data sample analyzed in this work which was registered during period P29, the problem is even worse: the "normal" position of the pulses was around the second and third FADC slices (instead around the 5th or 6th as it is for the rest of the data samples

analyzed) and therefore the pulses of events triggered by macrocell 19 were partially or even totally outside the FADC 30 slices registration time. For these cases, the digital filter is no more the more appropriate extractor as it is not capable to make a good fit. Other signal extractor algorithms, as an integrating spline over only 1 FADC slice, would be more convenient.

For the signal extraction of all the data samples analyzed in this work a digital filter fitting 4 FADC slices has been used. To partially cure the misbehavior of the macrocell number 19, the size of the window for pulse searching around the determined pulse position has been increased from the standard values of 2.5 slices to the left and 4.5 slices to the right to the values of 4.5 slices to the left and 5 slices to the right. This slightly enhance the bias as the region for maximum signal searching is larger, but it is still expected to be lower than the case when no position check is performed.

6.4.2 Pedestal evaluation and subtraction

Shower signals are always inmersed in a background of NSB photoelectrons. Since the output of the PMT is AC-coupled, the NSB does not modify the level of the FADC pedestal. Contrariwise the NSB alters the size of the fluctuations. These fluctuations are proportional to the square root of the NSB phe rate. Only pulses whose charge is significantly above the level of noise fluctuations are interpreted as signal. This procedure is referred to as image cleaning. The noise fluctuation is characterized through the pedestal RMS.

Two ways are used to compute the pedestal level within the MAGIC data analysis: from a dedicated pedestal run, as the mean signal (with its corresponding RMS) per FADC slice recorded (no cosmic signals are expected to be caught by the random trigger); or directly using the events in the data runs, from the registered FADC slices in the low-gain region (last 15 slices) if no saturation occurs in the high-gain channel (as happens for most of the events) and thus no switch to add up the low-gain pulse is done. The average mean pedestal for each pixel is evaluated in the low-gain region from 2000 measurements with no saturated high-gain.

6.4.3 Calibration of the signal

The integrated charge of the extracted signal is given in units of FADC counts. It has to be converted to number of photoelectrons arriving at the first dynode of the PMTs. As explained in Section 5.3.4, after the relative calibration of the pixels to make their response uniform for a same input light, an absolute calibration is needed to compute the conversion factors from digitalized charge in FADC counts to number of phe. Dedicated calibration runs are used and the F-Factor method is applied. The number of phe arriving to the first dynode of each pixel can be derived from Equation 5.13:

$$N_{phe} = \frac{(< Q > - < Q_{ped} >)^2}{\sigma^2} F^2 \,, \tag{6.1}$$

where F is the quantity representing the excess noise introduced by the readout chain ($\sim$ 1.15 for the MAGIC PMTs), $< Q >$ is the mean charge in FADC counts of the pulse signal registered by the pixel calculated from calibration pulses and to which the mean pedestal $< Q_{ped} >$ is subtracted, and σ^2 is defined as the reduced variance calculated from the charge distribution and corrected for the contribution of the pedestal variance

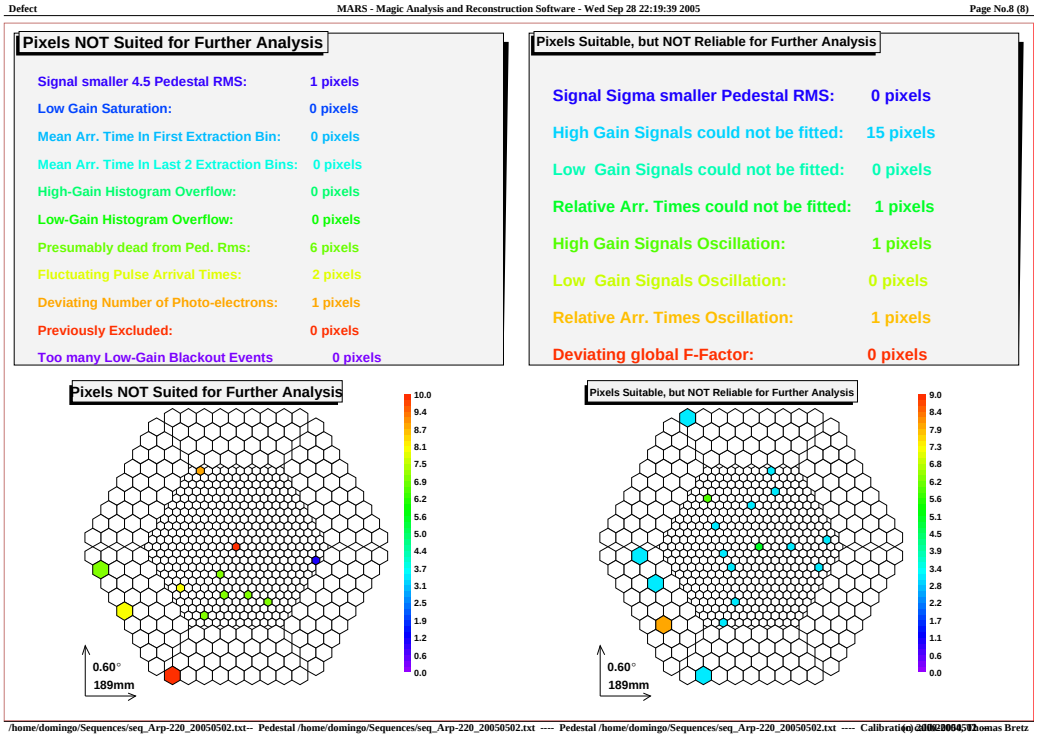

Figure 6.2: Identification of bad pixels from the analysis of a calibration run. On the left, the excluded pixels are colored in the camera layout drawing and the reason for their tagging as *unsuitable* is given in the list above. On the right, pixels showing a behavior deviated from the expected mean are tagged as *unreliable* but still keep by default for further analysis.

($\sigma^2 \equiv \sigma_Q^2 - \sigma_{ped}^2$). Then, the conversion factor from FADC counts to phe for each pixel is directly obtained from:

$$C_{phe}^{FF} = \frac{N_{phe}}{< Q > - < Q_{ped} >} = \frac{< Q > - < Q_{ped} >}{\sigma^2} F^2 \,. \tag{6.2}$$

6.4.4 Identification of bad pixels

Some pixels can not be calibrated due to a malfunction of some of the elements of its readout-chain. Those pixels have to be recognized to diagnose the hardware problem and repair it, but also to treat them in the more convenient way to avoid biases in the analysis. On top of this we also need to identify pixels which are affected by a bright star (which implies an increase of the pixel DC current and subsequently a higher pedestal RMS). Too large fluctuations on the charge extracted from the pulses of a calibration run, too low extracted mean charges, fluctuating arrival time of the pulses for the same pixel, too high or too low pedestal RMS, are reasons to tag a pixel as *bad*. Figure 6.2 shows an example of the list of pixels identified as not suitable for further analysis as resulted from the processing of a given calibration run. Above the camera layout, there is the list of conditions that are used to classify a pixel as bad.

The software can proceed in two ways with bad pixels: they can be completely excluded from the calculation of the image parameters, i.e. their signal is ignored in the following analysis steps; or the signal can be interpolated, i.e., their signal, pedestal

and pedestal RMS values are substituted by the average quantities from their neighbor pixels. By default, a pixel is interpolated if none of the neighbor pixels has been tagged as unsuitable, and the pixel with its new content is once again included in the regular analysis data chain.

6.4.5 Image cleaning

After the calibration of the signal, the next step in the analysis is to determine which pixels should be considered part of the recorded image, with the goal of keeping those pixels which contain information about the EAS and rejecting those ones whose signal is more likely due to NSB fluctuations. This procedure is called image cleaning. The pixel content is compared to two cleaning levels: in a first loop those pixels with a signal larger than the highest level are kept (and are classified as *core* pixels), and in a second loop pixels that are adjacent to the core image are rescued if they pass the second cleaning level. As a general rule, all isolated core pixels are excluded from the image. Two basic types of cleaning can be performed:

Relative The cleaning levels are determined by the mean pedestal RMS, σ_{ped}, of the pixel. Those pixels with a signal above r_1 times the noise level are selected as the core of the image, their neighbors with a signal above r_2 times the pedestal RMS are also kept. Typically r_1=3 and r_2=2.5.

Absolute A fixed threshold in number of phe is defined for a pixel considered as a core pixel, and a lower threshold for the surrounding pixels to be accepted. 10 phe for the core and 5 phe for the boundary pixels are the standard values currently used in the MAGIC data analysis.

The disadvantage of relative image cleaning is that the pedestal RMS noticeably depends on the NSB conditions. For example, it is different for galactic and extragalactic sources. If the same levels of relative image cleaning are applied to data taken with different background conditions, the resulting images can present large differences. This problem can be partly avoided with the absolute image cleaning, which does not take into account the magnitude of the pedestal fluctuations, but which is in turn sensitive to pixels with especially high pedestal RMS (e.g. those affected by stars).

The arrival time of the signal in each pixel can also be used to define an image cleaning method. Presently several timing based cleanings are under study and are already giving promising results specially for the smaller images. The analysis of the islands of pixels of the resulting image to discriminate if they are from noise origin or not is also another possible tool to improve the image definition. But neither the arrival time nor the islands will be considered in our analysis.

6.4.6 Parameterization of the EAS shower images: Hillas parameters

After calibration, pedestal subtraction and rejection of suspected NSB pixels, the shower image is integrated by the number of phe N_i registered at each pixel i which survives the image cleaning. In 1985 Hillas proposed a parameterization based on the first, second and third moments of the two-dimensional distribution of the signal along the image. For the moment calculation, the position of each pixel included in the image is weighted with the fraction of the image signal content in it, $\omega_i = \frac{N_i}{\sum_k N_k}$. The shower image is parameterized

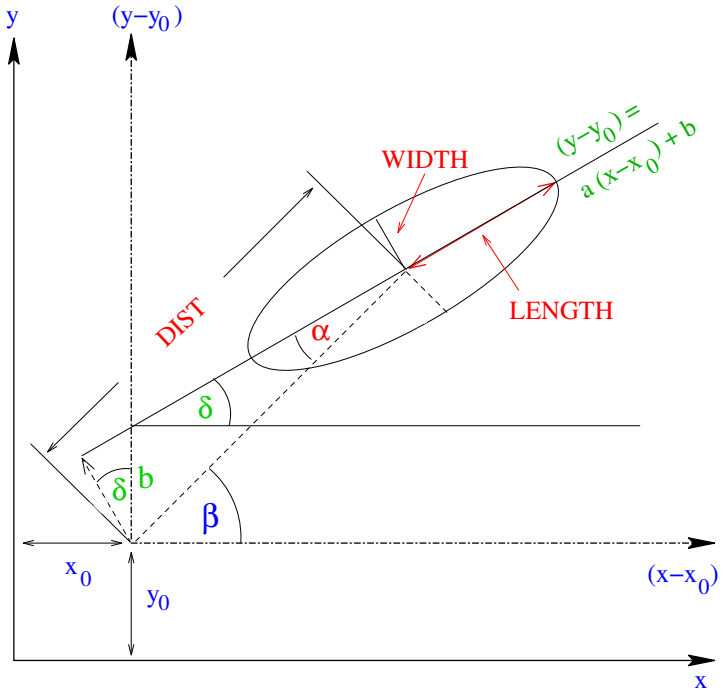

Figure 6.3: Scheme of the parameterization of shower images with an ellipse as proposed by Hillas.

as an ellipse and the moments are estimated with respect to a system of coordinates with center at the center of gravity of the image, x-axis along the major axis of the ellipse, and y-axis along the short axis. A set of so-called Hillas parameters are computed for each image. They can be grouped into two classes: those describing the shape of the shower and therefore independent of any reference point, and those depending on a reference point. The image parameters most commonly used for IACTs data analysis and the information they contain about properties of the primary particle that initiated the shower are compiled in the following list. Figure 6.3 schematically shows some of them.

SIZE Total number of phe on the image. It keeps direct information about the energy of the primary particle.

LENGTH Half length of the major axis of the shower ellipse. It is related with the longitudinal development of the shower in the atmosphere.

WIDTH Half width of the minor axis of the shower ellipse. It provides information of the transversal development of the EAS. As we have seen in Chapter 5, the lateral spread of a γ-induced EAS is substantially lower than that corresponding to a hadron.

CONC Fraction of phe contained in the two brightest pixels. It gives information about the core of the shower.

M3LONG Third moment of the image along the ellipse major axis. It can help to distinguish which of the two ellipse ends represents the shower head and which one

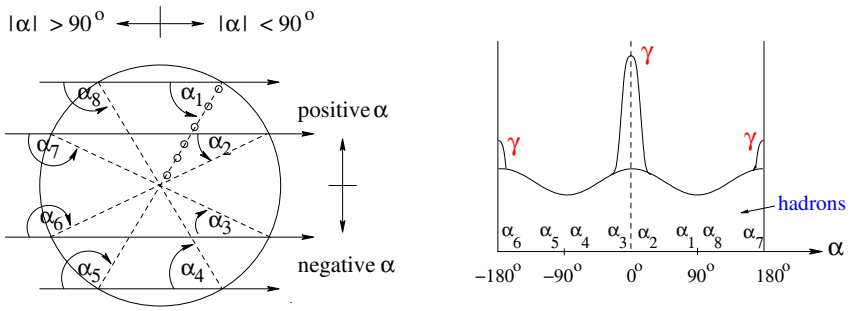

Figure 6.4: Illustration of the different values that ALPHA (α) may have, according to its definition, for different shower images.

the shower end or tail. When the head of the shower is closer to the camera center, the properly corrected M3LONG (according to its definition and the image position in the camera) is positive.

ASYM Vector between the image center of gravity and the brightest pixel. It informs about the asymmetry of the phe distribution along the major axis. It points to the part of the shower corresponding to the maximum development and helps to discriminate between the shower's head and tail.

LEAKAGE Fraction of the total signal contained in the pixels of the outermost ring of the camera. High LEAKAGE values indicate that the image is truncated, so information from some parts of the shower is not contained in the camera. Fully contained images have zero or very small values of LEAKAGE. It is a crucial parameter for the reconstruction of the primary particle energy, specially for the highest energies. In this work the LEAKAGE2 parameter is used, which is the fraction of signal contained in the 2 outermost rings of pixels.

DIST Distance between the image center of gravity and a reference point in the camera plane, normally the camera center. It is related with the shower impact parameter.

ALPHA Angle between the major shower axis and the direction determined by the image center of gravity and a reference point in the camera plane, normally the source position in the camera, which in most of the cases coincides with the camera center. Figure 6.4 shows the typical values of ALPHA that shower images may have. ALPHA tells by which angle the main axis of the image misses the reference point. γ-induced images point towards the position of the source in the camera, while hadron-induced ones are randomly distributed. Thus, ALPHA becomes the most powerful parameter for γ/hadron separation.

Figure 6.5 shows the differences in the distributions of the Hillas parameters that can be found between γ and proton-generated images (results from MC simulations). These differences are the feature that the γ/hadron separation techniques exploit to discriminate between both types of shower images.

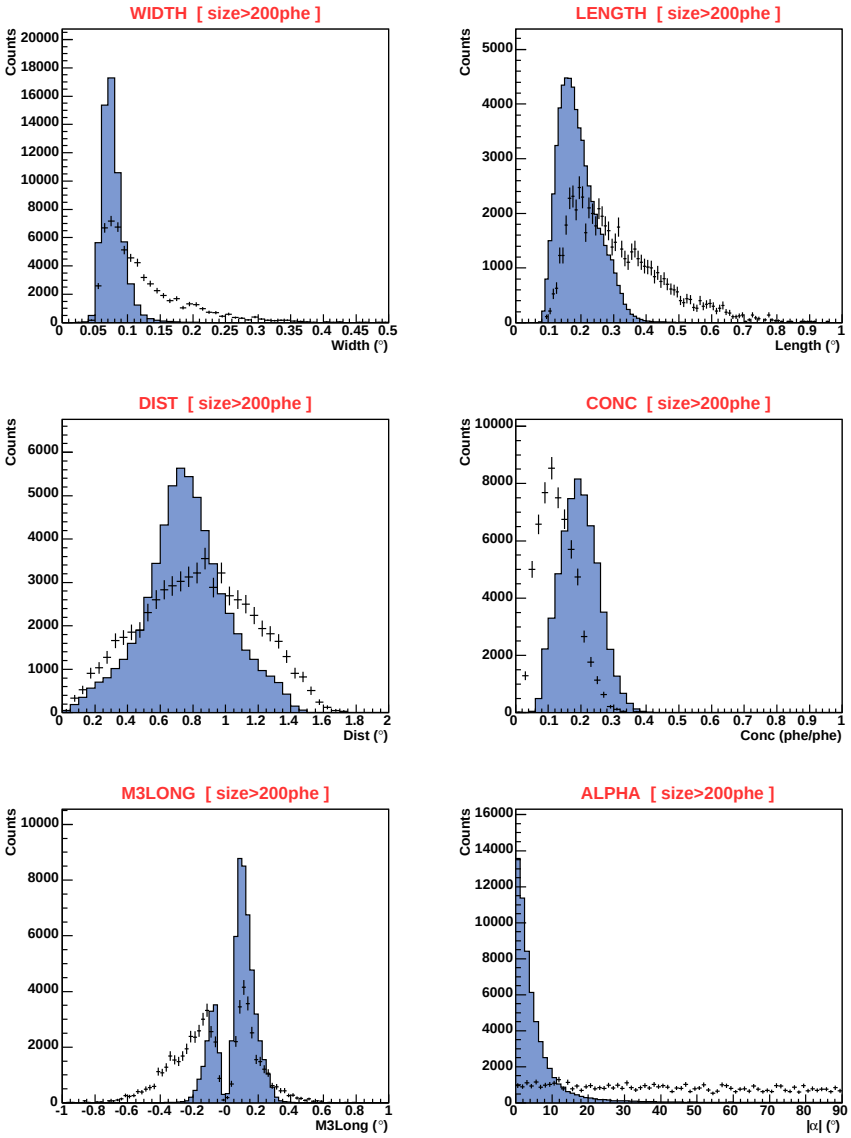

Figure 6.5: Comparison of the distributions of Hillas parameters between MC simulated γs (histograms) and MC simulated protons (dots), for SIZE values above 200 phe. Substantial differences can be observed, which points to a non negligible γ/hadron separation power of the chosen image parameters.

6.5 Second selection

Once the data stored in each pixel is fully processed and each image is parameterized, different procedures of selection of events are followed in order to eliminate as many background events as possible.

6.5.1 Run quality checks

Before applying the γ/hadron discrimination cuts, further quality cuts are still applied to reject runs for which the analysis has failed.

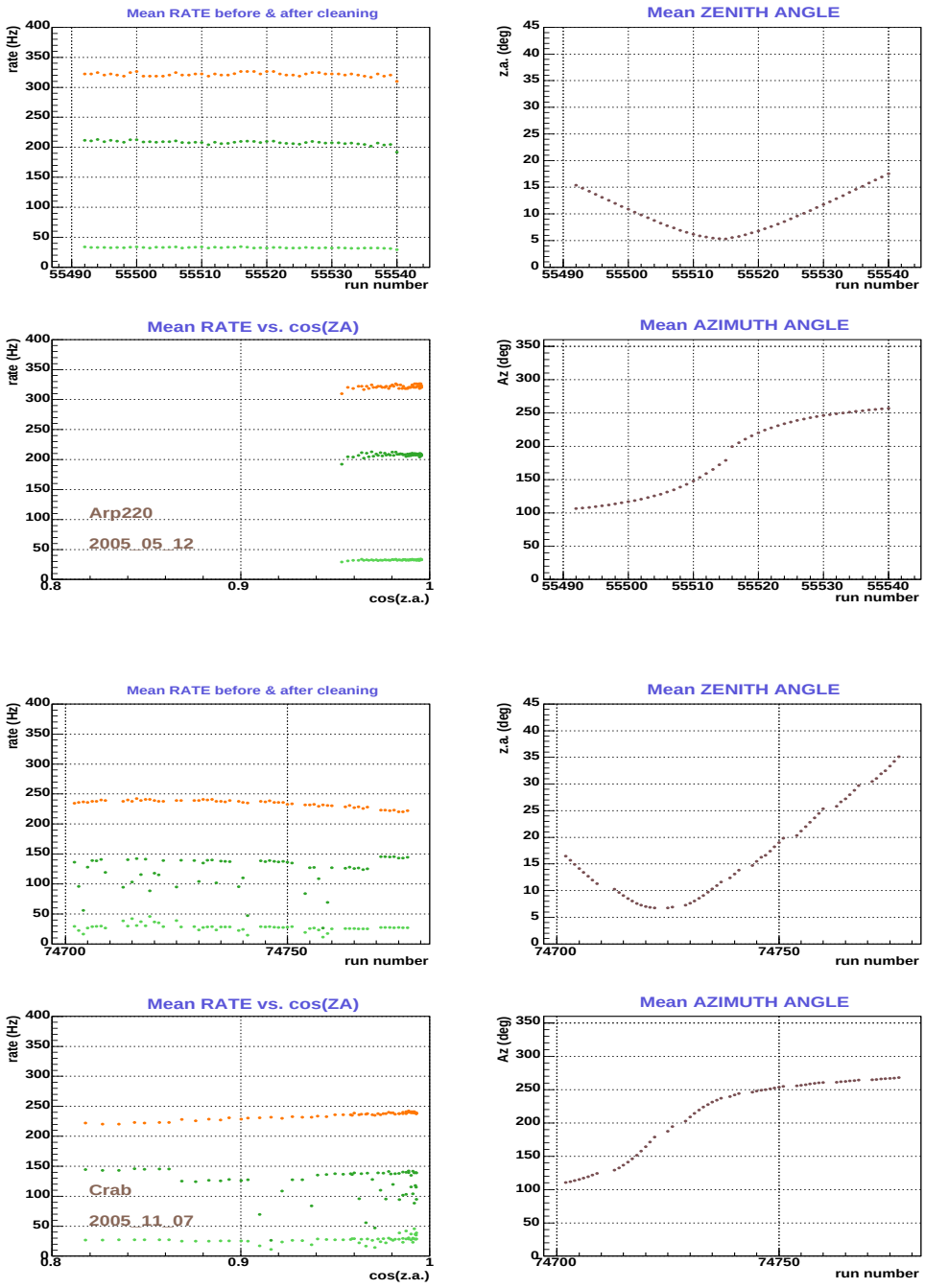

Figure 6.6: Rate of events per run as observed (orange dots), and after image cleaning (dark green dots). Light green dots show the rate after cleaning for SIZE values above 400 phe. The evolution of the zenith and azimuth angles during the observation is also shown, as well as the dependency of the rate with the cosine of the zenith angle. The four top panels correspond to an observation of Arp 220 on May the 12th 2005, which presents normal rates before and after cleaning. The four bottom panels are from an observation of Crab Nebula on November the 7th 2005, and although the trigger rate behaves as expected, the check makes evident a deficient processing of the data for some of the runs.

- The rate of events surviving the image cleaning is checked and compared with the rate before image treatment. Runs with problems in the signal extraction or the calibration will end up with a lower rate after cleaning than normal data runs, so can easily be detected and removed from further analysis if the data processing problem can not be solved. The rate after cleaning is also checked for high SIZE values, as well as the expected linear dependency of the rate with the cosine of the zenith angle (see Figure 6.6 for examples of a good night and a night with problematic runs, and the corresponding graphics in the following Chapters).

- The distribution of events in the camera plane should be uniform. However, the camera has shown up to be more efficient in some regions than in others. These inhomogeneities can be related to trigger macrocells misbehavior, dead pixels, etc. The distribution of centers of gravity (COG) of the images along the camera plane and the corresponding projected angular distribution (Φ plot) are used to make a diagnosis of this problem. Sometimes the origin of the non-uniformity is found and the data can be reprocessed accordingly. However, still some inefficiencies in the camera response have remained and are yet not fully understood. Figure 6.7 shows the COG distribution and the Φ plot for two of the analyzed days as an example. The large inefficiency affecting the upper right region of the camera on May the 12th was noticeably cured for the events on June the 7th, but still some inhomogeneities can be observed (apart from the peaks appearing in the Φ plot due to the flower shaped trigger).

- A comparison of the Hillas image parameters of the different data samples used in the analysis also allows to detect days for which the data processing has failed or the telescope had hardware problems which had not been tagged in the first data selection. Bad quality data show different Hillas parameters distributions than good quality data from the same source. Therefore, the Hillas parameters distributions of the different data taking nights of a same source are compared (see the corresponding figures in the following Chapters). In addition to this day-by-day Hillas distributions check, a comparison in this sense of the ON and OFF data samples is also essential. After calibration and image cleaning, and before any event selection cut, the hadronic showers largely dominate the number of γ-ray showers present in any data sample, either it is ON or OFF. Therefore, the image parameters are expected to show the same distribution independently of the pointing mode. This check allows to determine if a data sample chosen as OFF for a concrete ON sample is really suitable. If the ON and OFF data samples are not compatible, posteriori γ/hadron separation will have different efficiencies for both samples. This is why we restrict ourselves to check the compatibility of the main image parameters used in the γ/hadron separation procedure.

6.5.2 Event quality cuts

There are still some images that can be excluded from the sample before the events are subject to the γ/hadron separation process. Those that are already known not to originate from EAS Čerenkov light and those whose information is known to be poor and can diminish the efficiency of the γ/hadron separation method, are selected beforehand and rejected from the data sample.

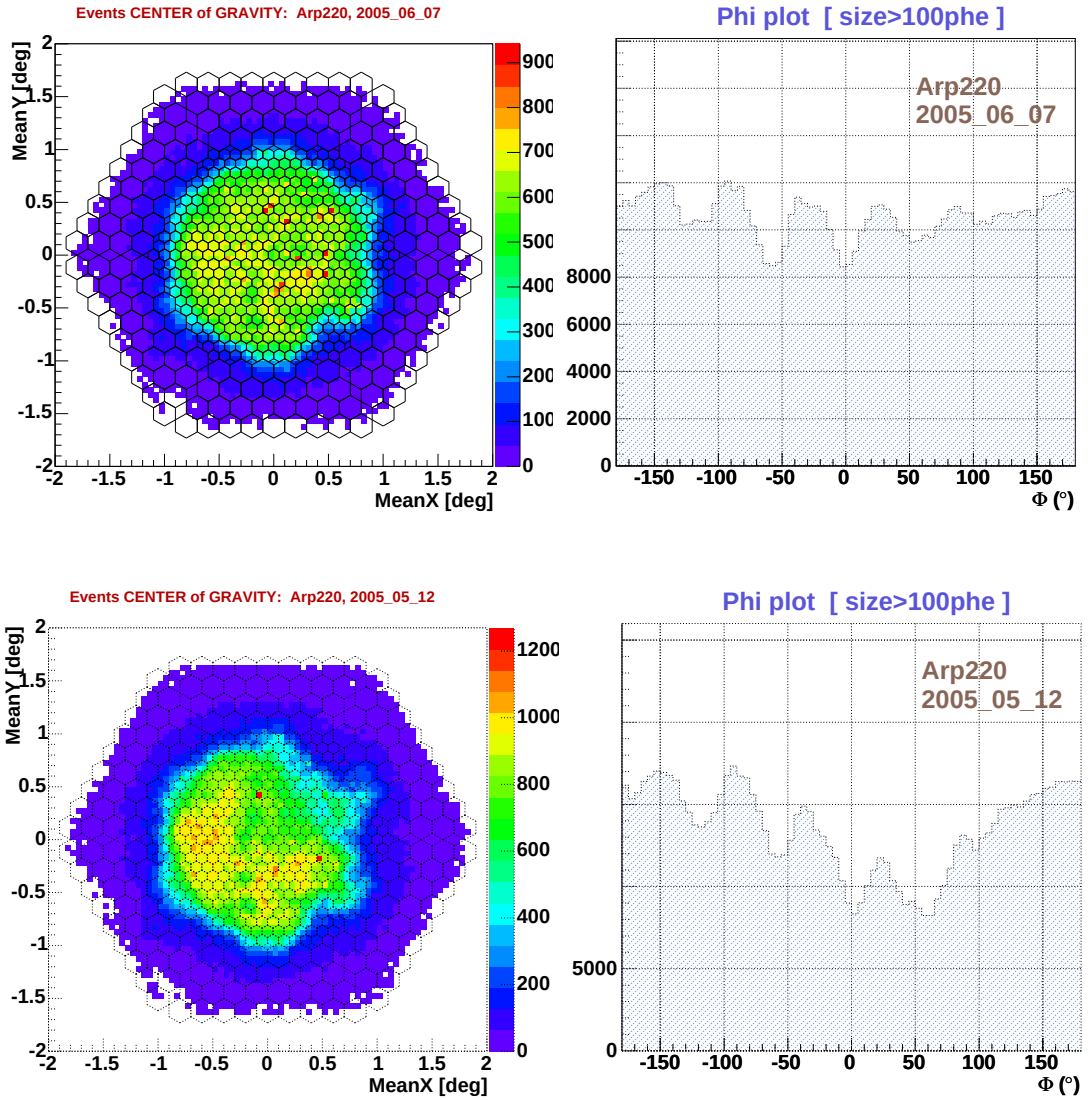

Figure 6.7: Distribution of COG of the shower images in the camera (left panel) and their angular distribution with Φ defined as the angle between the positive x-axis and the line from the center of the camera to the COG of the event (right panel). Some inefficiencies can be clearly seen, especially for the night of May the 12th. Also the flower shape feature of the trigger macrocells configuration can be slightly recognized.

An example of this undesired events are the so-called "spark" events. Already in the first MAGIC data analysis it was found that a group of events, not present in the MC simulations, appeared in the real data. They are roundish images, with small WIDTH and LENGTH, but high SIZE and CONCENTRATION for their reduced dimensions. They have been associated to sparks inside the camera, probably caused by discharges between the PMTs shielding and some other metallic element. The hypothesis points to a fast flash of light due to the spark which is partially reflected towards the PMTs by the plexiglas window and illuminates the few closest pixels were the spark occurred. These events can be clearly selected using a logarithmic SIZE versus CONC graph, as it is shown in Figure 6.8. They are rejected in all the data samples under consideration.

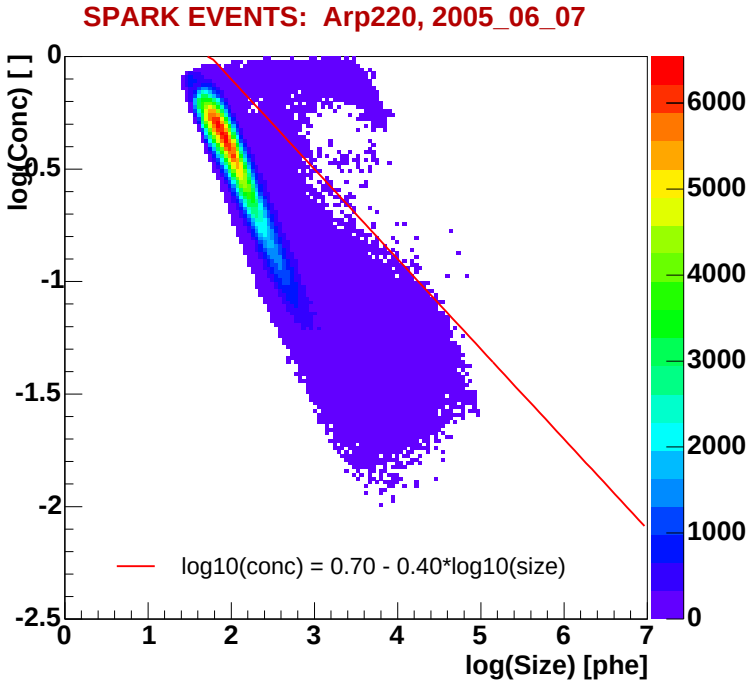

Figure 6.8: The so-called "spark" events are practically completely removed from the data sample with the cut in log(SIZE) and log(CONC) shown in the figure. This quality cut has been applied to all the data analyzed.

6.5.3 γ/hadron separation

Once the images have been treated and parameterized, comes the key point of the analysis: the discrimination between events generated by incident γ-rays, the signal, and the ones generated by primary hadrons or not rejected NSB fluctuations, the background.

The γ/hadron separation methods exploit the differences in shape and position of the images in the camera. In order to determine the features that distinguish γ-ray- and hadron-induced events, a sample of pure γ-ray events is necessary. As already mentioned, due to the impossibility of having a controlled flux of known primary particles, the γ/hadron separation has to rely on the Monte Carlo simulations. In only some cases real γ events from a data sample particularly reach on γ-ray showers (e.g. from Crab Nebula data or from a well-known Active Galactic Nuclei in flaring state) can be used for the optimization of the γ/hadron separation cuts. OFF data runs from real observations are usually taken as hadronic sample for the training of the γ/hadron separation method.

Many different methods have been tested to maximize the power of γ/hadron separation of the technique. Here just the more commonly used are reviewed, with emphasis in the Random Forest method which is the one used in this work.

Supercuts: static cuts In the n-dimensional space of Hillas image parameters, a set of hyper-planes select a subhyper-space. This method was successfully introduced by the WHIPPLE collaboration (Reynolds et al. 1993). As only one constant minimum and maximum cut value is set for each image parameter, the γ/hadron separation is optimized for the region of the parameter space with more statistics, i.e., for the most frequent showers: small energy showers and low observation zenith angles. The efficiency of supercuts worsens for other regions.

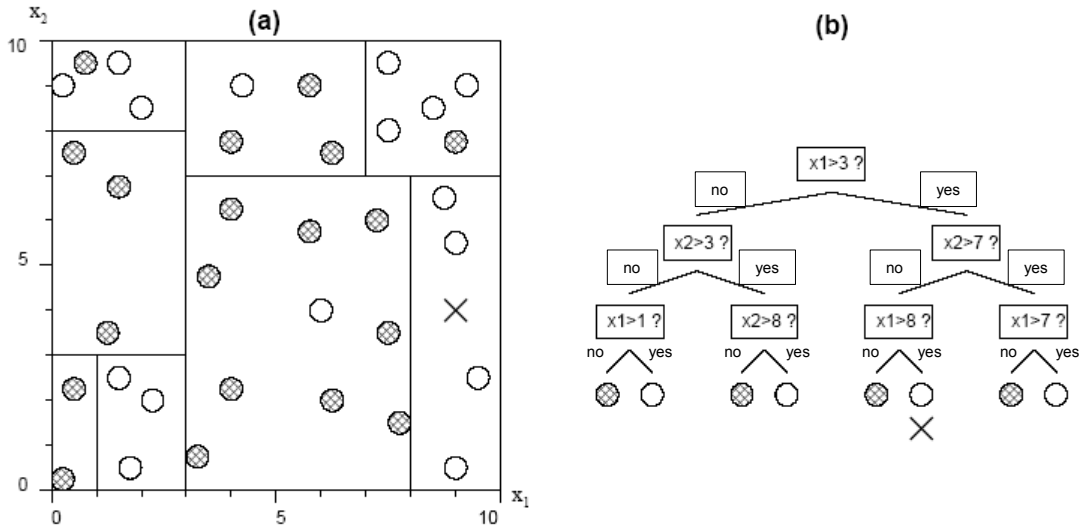

Figure 6.9: Sketch of the classification procedure followed in the growing of one Random Forest tree. Taken from Zimmermann (2005).

Dynamic cuts In order to improve the γ/hadron separation performance, the different parameter dependencies on the energy of the primary particle (represented by the SIZE parameter), the observation zenith angle and the impact parameter (represented by DIST) are taken into account in the so-called dynamic cuts, i.e., the cut limits on each Hillas parameter space are functions of SIZE, DIST and zenith angle.

Random Forest More sophisticated classification methods are widely used in high energy physics. One of these methods, the Random Forest (RF), is commonly used in MAGIC. The separation method is trained with two samples of data, each of them belonging to one of the two categories that need to be classified. In our case, they are a sample of pure γ showers (from MC) and a sample of hadron showers (from OFF real data). The method performs then the following iterative process:

- A certain number of image parameters are selected and will be used for the classification of the events. They must be at least partially independent.
- Three of the training parameters are randomly chosen and a classification tree is grown as follows (see Figure 6.9 for a sketch of a RF tree growing):
  - For each of the three variables of the tree, all the events (from both samples together) are sorted in order of increasing value of the variable in use.
  - A quantity called gini-index is then defined and it is calculated for each variable and for each position in the ordered list of events, which defines a separation in left (L) and right (R) events (equivalently, events below and above a cut value in one of the image parameters used):

$$g_j = \frac{n_{\gamma_L}^2 + n_{h_L}^2}{n_{\gamma_L} + n_{h_L}} + \frac{n_{\gamma_R}^2 + n_{h_R}^2}{n_{\gamma_R} + n_{h_R}}\,, \tag{6.3}$$

  with j an index running along the list of n events.

  - For each of the three tree variables, an optimal cut is estimated: that which maximizes the gini-index. For example, if WIDTH is the parameter used to order the events and the gini-index has been found to be maximum if the list is separated in right and left at the position j, the corresponding cut value in WIDTH is:

$$WIDTH_{cut} = \frac{WIDTH_j + WIDTH_{j+1}}{2} \,. \tag{6.4}$$

  - Once all the events are analyzed with respect to the three variables of the tree, a first division of the data is done with the variable that gets the highest gini-index and at the calculated corresponding cut value. Thus, from the initial node two branches are created with two new nodes, one containing the events below the cut value and the other with the ones above it.
  - For each of the new nodes again three of the image parameters are chosen and the classification and optimal separation of the subsample of events starts again.
  - No further subdivision of the nodes is performed when the population of events of a node is purely of one of the two initial categories. Then the node is called terminal node.
  - In order to avoid overtraining of the classification tree (i.e., to avoid that it grows until it selects individual events and not populations in its nodes), an additional condition is added to set a node as terminal: if the number of events in a node goes below a predetermined number (typically 10 events), the growing is stopped.

- One RF tree is then a set of nodes where the initial sample of events is subdivided according to cuts in different image parameters, which altogether looks for the best separation of the initial samples of events.
- To test as well as possible all the combinations of the multiparameter space and increase the chance of finding better γ/hadron separation, a lot of RF trees are grown (typically 100).
- Finally, a quantity called HADRONNESS is assigned to each terminal node of each RF tree:

$$HADRONNESS_i = \frac{N_h^i}{N_h^i + N_\gamma^i} \,, \tag{6.5}$$

  which expresses the probability of an event that will be classified in the terminal node i to be a hadron. By definition, all MC γ events have HADRONNESS equal to 0 whereas all MC hadrons have HADRONNESS equal to 1. A HADRONNESS value is assigned to each event of the real data being analyzed by passing it through the RF classification trees.
- The Random Forest provides a tool to quantify which are the used image parameters that provides better γ/hadron separation. For each tree and each node the increment of gini-index, Δg, is defined as the difference of gini-index of the node before and after cutting the population of the events with the analyzed variable. Summing up all the gini-index increments a graphic with the separation power of each parameter can be constructed (see Figure 6.10 for an example).

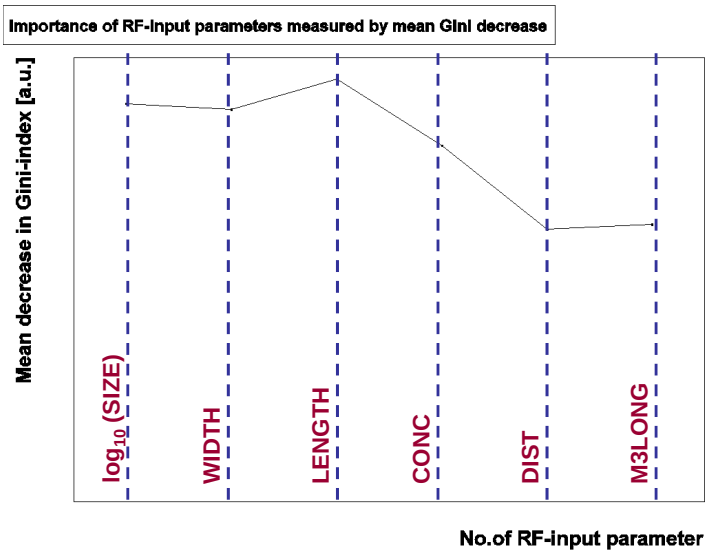

Figure 6.10: Total increments of gini-index for all the image parameters used in a Random Forest γ/hadron separation training. WIDTH and LENGTH are the parameters with higher separation power.

In order to avoid a selection of the candidates γ events as those with a specific range of SIZE, before starting the training procedure the samples of MC γs and OFF data hadrons are normalized as to have the same shape of the initial SIZE parameter distribution.

All the data analysis presented in this work make use of the Random Forest as γ/hadron separation procedure. Therefore a cut in only one parameter is applied to the events, a HADRONNESS cut, but as we have seen it does the work of an static or a dynamic cut in each of the image parameters used for the RF training. A recent study (Zimmermann 2005) concludes that RF gives comparable results as neural networks in terms of γ/hadron separation power, and improved results compared to static and dynamic cuts, especially at low energies.

6.5.4 Optimization of hadronness and alpha cut

Generally the higher the energy the higher the chances to extract a more pure sample of γ-ray images from the initial sample of events. Images generated from low energy induced showers contain only a few pixels and the distinctive features between hadron and γ showers are diluted. Therefore, in the final steps of the analysis it is convenient to classify the sample in bins of SIZE (which is in first order equivalent to the primary particle energy). For the analysis included in this work, six different bins of SIZE, with limits increasing logarithmically in SIZE, have been used. These are from 100 to 200 phe, from 200 to 400 phe, from 400 to 800 phe, from 800 to 1600 phe, from 1600 to 3200 phe, and from 3200 to 6400 phe.

In order to choose the more convenient HADRONNESS cut in each selected SIZE bin, two different approaches have been considered:

- Based on the maximum acceptance of γ events together with the best quality of the γ/hadron discrimination. Figure 6.11 resumes the procedure. Test samples of MC

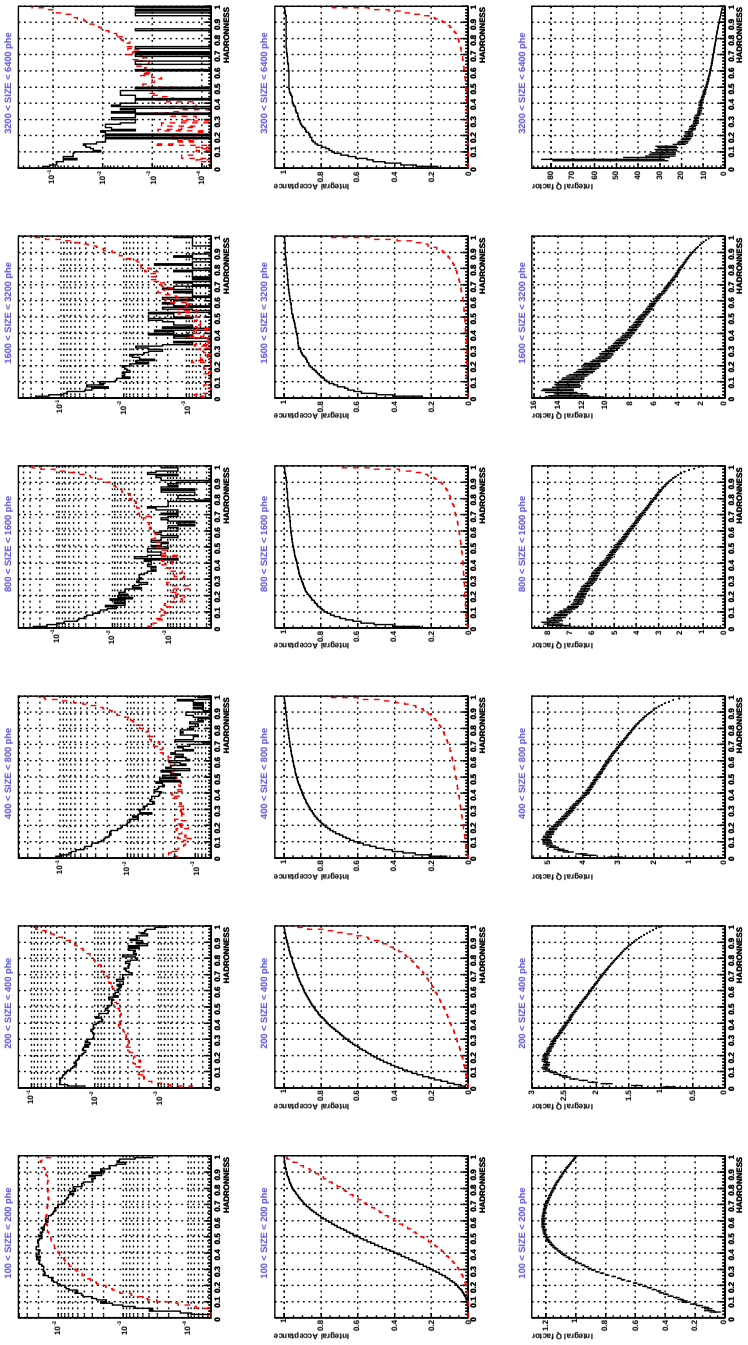

Figure 6.11: Diagnosis of the quality of the γ/hadron separation achieved when applying a certain HADRONNESS cut. Top panels show, for each SIZE bin, the distribution of HADRONNESS for a test sample of MC γs (black histogram) and a subsample of OFF data (red dashed histogram). Middle panels give the acceptance of MC γ-ray and background events as a function of the HADRONNESS cut applied. Bottom panels provide the Q factor values achieved for each HADRONNESS cut at each SIZE bin. Different values of HADRONNESS cut provide the best performance of γ/hadron discrimination for different bins of SIZE.

γs and OFF data events as hadrons, independent of the samples used for the RF training, are used to evaluate the distributions of the HADRONNESS parameter for a pure sample of γ-rays and of hadrons. The higher the SIZE the better the separation of both populations, being the HADRONNESS of the MC γ events closer to 0 (their ideal value) and that of the OFF data hadrons closer to 1 (see top panels of Figure 6.11). For each HADRONNESS cut value, h_{cut}, the efficiency of the cut or acceptance of γs is evaluated as follows:

$$Acc_{\gamma} = \frac{N_{\gamma}(h < h_{cut})}{N_{\gamma}^{total}} \,. \tag{6.6}$$

The acceptance of hadrons, Acc_h, for the same HADRONNESS cut is correspondingly computed. Then, the so-called "Q-factor" is calculated from this two quantities:

$$Q = \frac{Acc_{\gamma}}{\sqrt{Acc_h}} \,, \tag{6.7}$$

which quantifies the quality of the γ/hadron separation achieved by using the HADRONNESS cut, taking into account not only the acceptance of γ events it provides but also the fraction of hadrons that are still not removed with the cut. Middle and bottom panels of Figure 6.11 show the acceptances and Q-factors get with the RF tree grown and used for the analysis of this Thesis. Generally, the optimal HADRONNESS cut is that which provides the maximum Q-factor, but a minimum γ acceptance (typically 80%, or at least not less than 50%) is usually required in order to keep enough statistics of γ events for the signal evaluation.

- Based on the maximum significance or the best achievable sensitivity from the signal of a known source. The events of the ON data sample of a reference source (in this case the Crab Nebula) and from the selected OFF data sample are subject to the RF grown decision trees to evaluate their corresponding HADRONNESS value. The ALPHA parameter distribution for the ON data sample is then compared with the ALPHA distribution of the OFF data sample, cutting the events above different values of HADRONNESS. The procedure consists in evaluating the signal obtained from the so-called ALPHA plots, i.e. the excess events that may show up in the ON data distribution above the normalized OFF data distribution for low values of the ALPHA parameter. See the corresponding subsections of Section 6.7 for the details about significance and sensitivity estimations from an ALPHA plot. Changing the HADRONNESS cut between 0 and 1 with steps of 0.025, the cut value that provides the maximum significance is selected. Figure 6.12 shows the result of the HADRONNESS cut optimization obtained for the Crab Nebula data that is used as reference for the analysis of the sources of interest. A table with the final values used for the analysis can be found in the following Chapter, where the previous method based on the Q-factor and acceptances values have been also taking into account.

But still another parameter can be adjusted to optimize the sensitivity of the analysis: the cut in ALPHA which defines the region in the ALPHA plot considered as signal region, where the number of excess events is extracted from the subtraction of the OFF ALPHA histogram to the ON ALPHA histogram. As it is expected, and as it can be seen in the several ALPHA plots presented in the following Chapters, the peak at 0 of

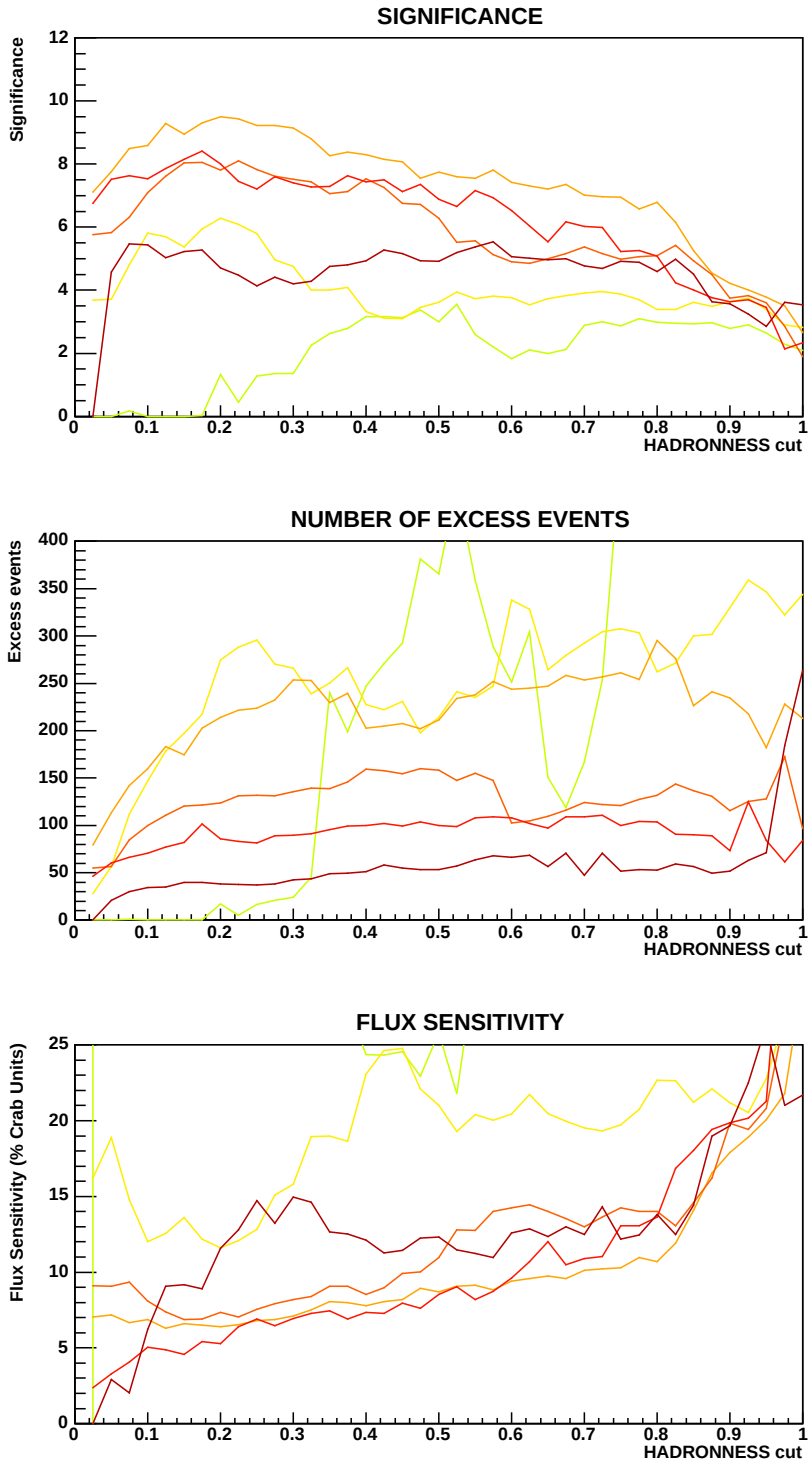

Figure 6.12: Results of significance (top panel), number of excess events (middle panel), and sensitivity (bottom panel) extracted from the signal of Crab Nebula varying the cut in HADRONNESS. The redder the line, the highest bin of SIZE it refers. The cut in HADRONNESS that maximizes the significance of the signal (top panel) is the one selected for further analysis.

the ALPHA distribution for γ events is narrower for higher energies of the primary γ-ray. This effect is due to the fact that showers induced by lower energy γ-rays are subject to more fluctuations and, therefore, their subsequent images in the camera present a larger dispersion in the orientation of their major axis. For this reason, it is generally convenient to extract the signal with a smaller cut in ALPHA for higher SIZE bins than for lower ones. A similar approach of the one explained for the optimization of the cut in HADRONNESS has been followed to optimize the cut in ALPHA. The ALPHA cut is decreased, starting from 20°, in steps of 1.25 degrees for each trail of HADRONNESS cut. The number of excess events, significance and sensitivity in Crab Units are evaluated for each trail. The combination of HADRONNESS cut and ALPHA cut that provides the best significance of the Crab Nebula excess signal is the one chosen for further analysis. The two-dimensional plots showing the result of this optimization process are shown in the following Chapter, together with the optimal values of ALPHA and HADRONNESS cut chosen for each SIZE bin.

6.6 Reconstruction of primary parameters

The energy of the primary γ-ray and its arrival direction can be reconstructed by several methods that make use of the image parameters.

6.6.1 Energy reconstruction

As is shown in Figure 6.13 for MC γ-ray showers, in first order, the logarithm of the energy of the primary γ-ray is linearly related to the logarithm of the SIZE of the image that it generates.

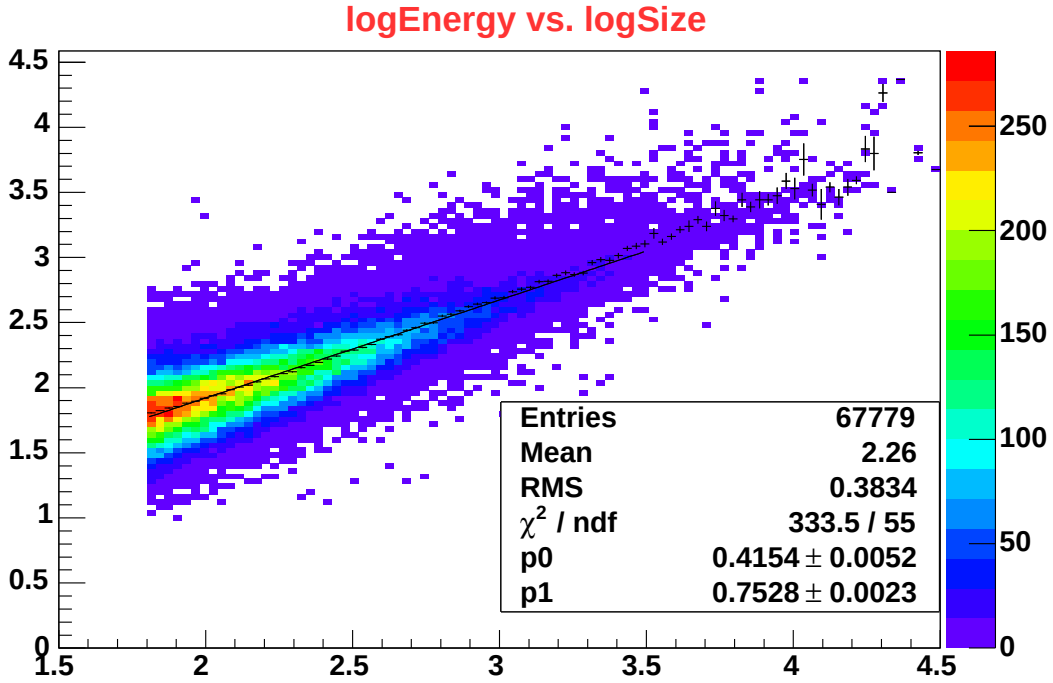

Figure 6.13: Linear relation between the SIZE of the shower images and the energy of the primary γ-rays. MC simulations.

However, if one tries to determine the typical energy of the events contained in a certain SIZE bin, it is not defined at once by a simple gaussian distribution around its more probable value given from the previous linear law. Figure 6.14 shows the energy distributions of MC γ-ray events for different bins of SIZE. Large tails can be observed especially for the highest SIZE bins.

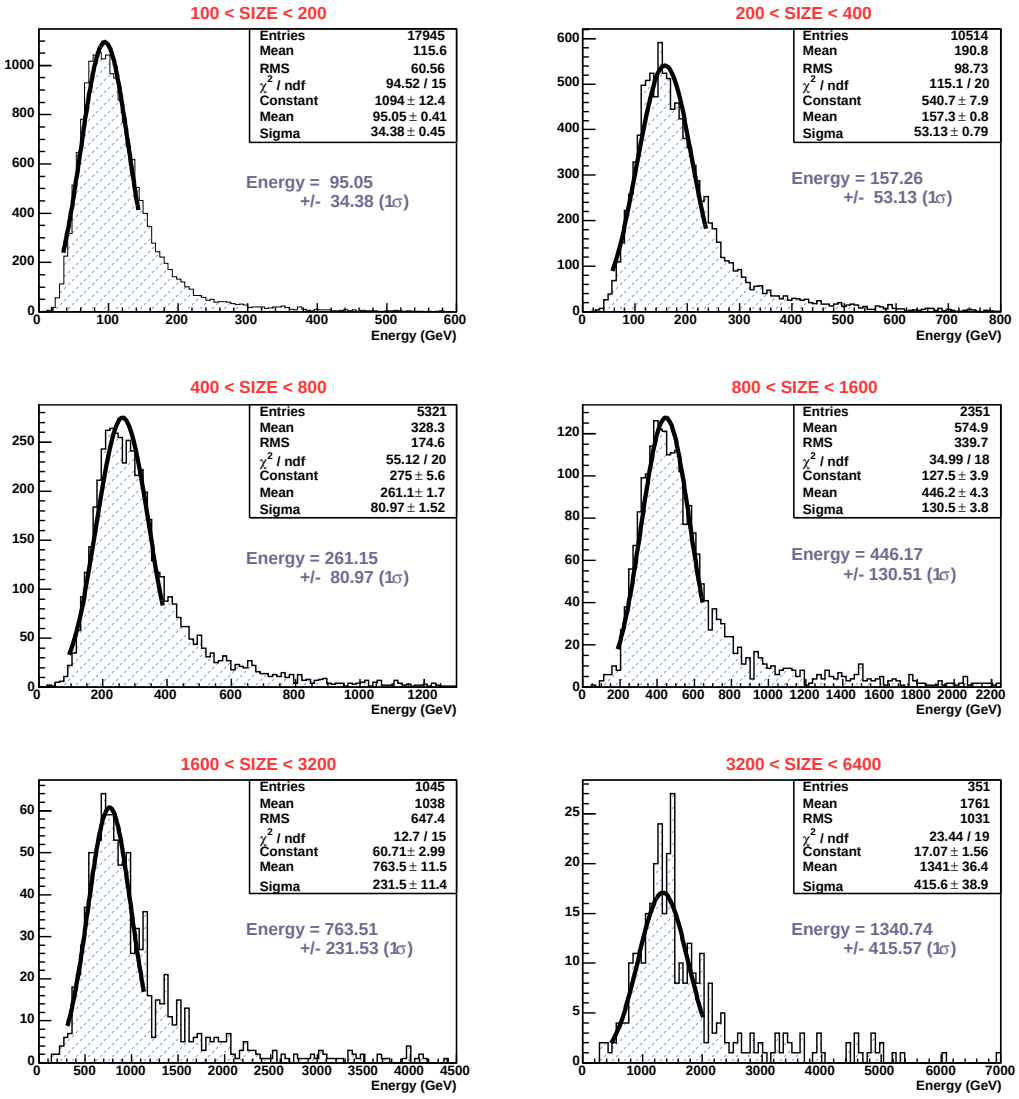

Figure 6.14: Distribution of true energy of MC γ events for the SIZE bins used in the data analysis of this Thesis. Tails of not well assigned events are seen especially for the highest SIZE bins.

The events at these tails correspond to images with a non negligible level of LEAKAGE. The not fully containment of the shower image in the camera makes these showers to be classified in a SIZE bin with typical energy of the primary γ-ray lower than their real energy. Thus, a reconstruction of the SIZE in terms of the LEAKAGE2 of the image has been tested to resort the events in their corresponding SIZE bin. Figure 6.15 shows that images with LEAKAGE2 larger than 0.06 present a linear relation between their assigned SIZE and their level of LEAKAGE2, implying that a correction for the non-contained

part of the shower can be applied.

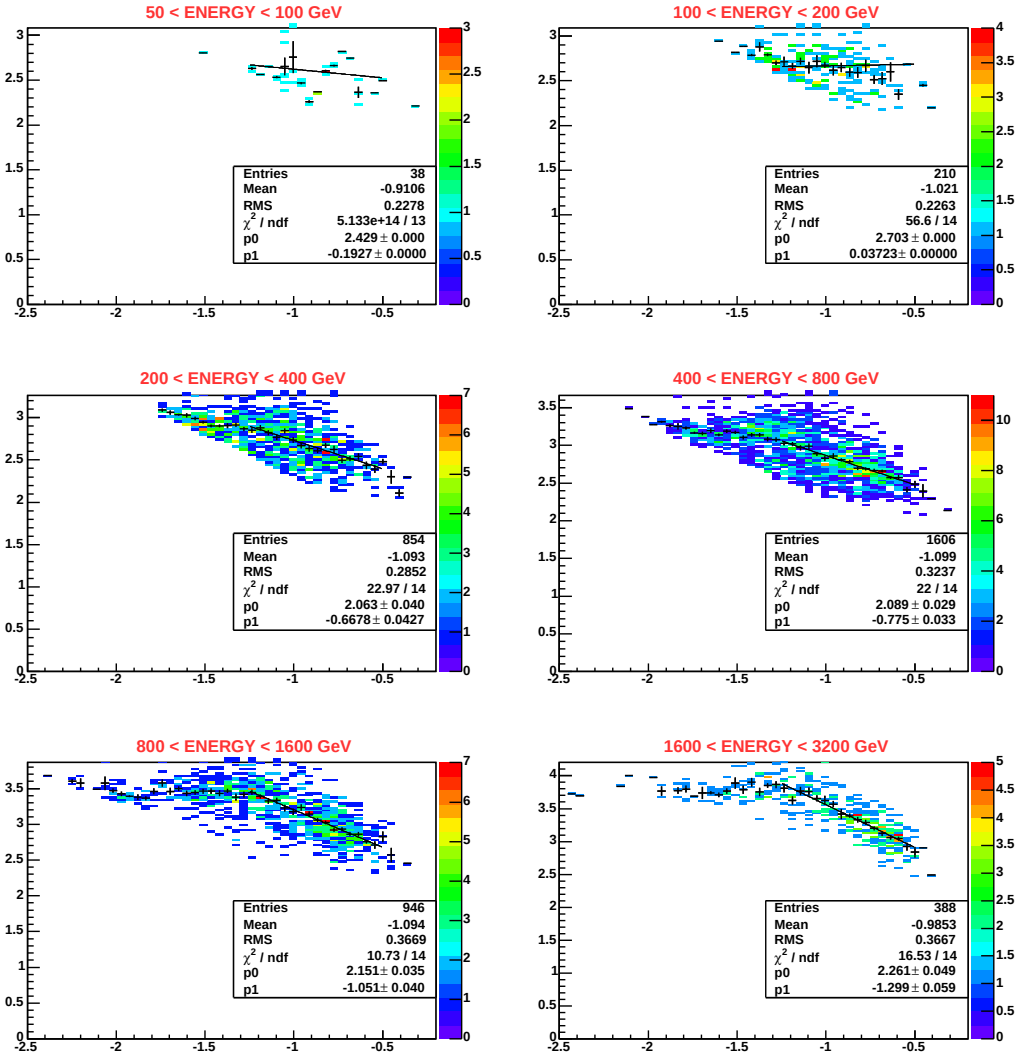

Figure 6.15: Linear correlation between the logarithms of SIZE and LEAKAGE2 for images with sizable non-containment in the camera.

The linear correlation between log(SIZE) and log(LEAKAGE2) is similar but still different for the different SIZE bins. However, as the true energy is not known for the real data events, there is no way to apply different corrections for different events, and the result of the linear fit from the energy bin from 800 to 1600 GeV[2] has been chosen to correct all the images with LEAKAGE2 larger than 0.06:

$$\log \mathrm{SIZE}_{rec} = \log \mathrm{SIZE} + 1.314 + 1.051 \log \mathrm{LEAKAGE2}\,. \tag{6.8}$$

The typical value of energy obtained for each bin of SIZE, once applied the SIZE reconstruction for the events with high values of LEAKAGE (Figure 6.16), has been used as reference value for the setting of the differential flux upper limits. The exact values,

[2]This priority responds to the fact that the higher energy showers are the ones suffering more for the non-containment in the camera, and that this energy range is the one with highest interest for the analysis of the TeV J2032+4130 source.

as well as the correction applied to consider a slope of the source under study different from the one used for the MC γ simulations (α=-2.6), are reviewed in Section 8.4.

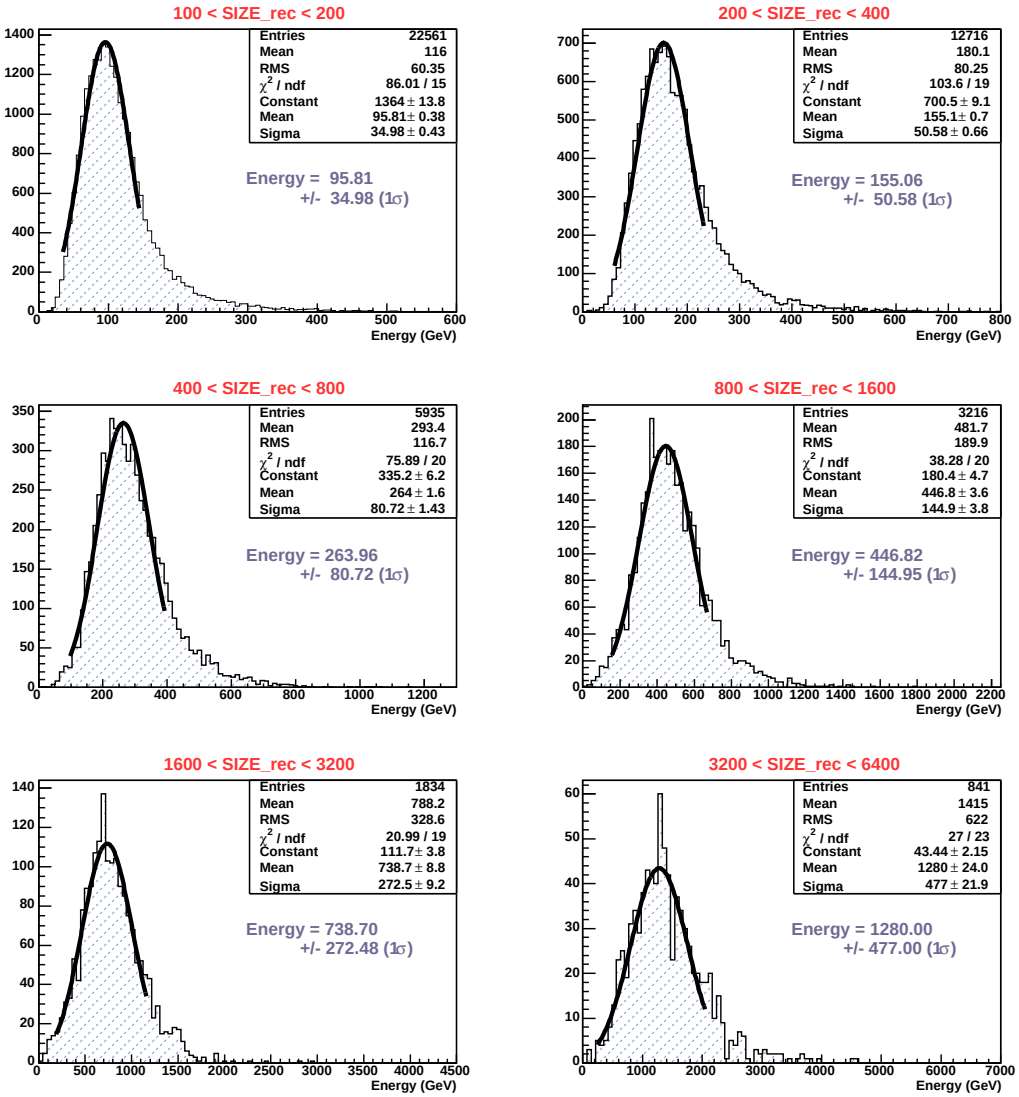

Figure 6.16: Distribution of true energy of MC γ events for the SIZE bins used in the data analysis of this Thesis. The SIZE of the showers with large amount of LEAKAGE has been reconstructed. The more probable value of true energy for each SIZE bin is estimated with a gaussian fit.

More complex parameterizations and reconstruction methods based in the Random Forest algorithm are being currently used for the energy reconstruction within the MAGIC collaboration. However, as no significant signal have been found in the analysis presented in this work and still there are features to be understand about the achieved energy resolution and bias, it is beyond the scope of this Thesis to perform a more exhaustive energy reconstruction of the analyzed showers.

6.6.2 Source position reconstruction

In its standard operation mode, an IACT points to the source under study, and it is assumed that the source position coincides with the camera center. Therefore, the reconstruction of the source position for a large amount of observations is reduced to check for a possible mispointing of the telescope and correct for it. Once this is done, the analysis can go on just assuming that the source is at the center of the camera, and an analysis based on an ALPHA plot computed with respect to that position can be performed. Even Wobble mode observations of well known point-like sources can be analyzed with the standard ALPHA-based analysis. However, analysis methods which assume that the position of the source in the camera is known a priori can not be used for many other observations: extended sources, as galactic SNRs or dark matter searches; sources whose position is poorly known, as is the case of unidentified EGRET sources or Gamma Ray Bursts; or new sources in the camera FOV, for example when doing a sky scan or serendipitously found in the FOV of another source. For all these cases the Hillas image parameters dependent on the source position can not more be well determined (as no reference position can be defined) and, thus, an ALPHA-based analysis makes no longer sense. Analysis methods which reconstruct the individual γ-ray arrival direction are essential to treat these particular cases.

6.6.2.1 The DISP method

The author has taken part in the development of an analysis method, called DISP, that uses the information of the shower image shape to reconstruct the position of the source for each detected shower. Starting from the previously successful application by the Whipple Collaboration, the DISP method has been improved and adapted to MAGIC.

The DISP method reconstructs the arrival direction of the primary γ-rays on an event-by-event basis. The source position is assumed to lie on the major axis of the Hillas ellipse that parametrizes the shower image in the camera, at a certain distance (DISP) from the image center of gravity (COG). Fomin et al. (1994) proposed the use of the "ellipticity" of the shower images (defined as the ratio WIDTH/LENGTH) to infer the position of the source of individual showers using a single IACT. The idea behind this is that shower images which are closer to the source position in the camera are more roundish, whereas showers which are further away from the camera position are more elliptical. The method was applied, among other IACTs, by the Whipple collaboration (Lessard et al. 2001) and the HEGRA Collaboration for the stand-alone CT1 telescope (Kranich et al. 2003). It provided a good angular resolution for single IACTs ($\sim$0.12° above 500 GeV).

Lessard et al. (2001) proposed the following parameterization of the DISP quantity:

$$\mathrm{DISP} = \xi \left(1 - \frac{\mathrm{WIDTH}}{\mathrm{LENGTH}}\right) , \tag{6.9}$$

where the ξ parameter has to be determined from a pure sample of γ events (commonly MC γ simulations).

Because of the different features of the MAGIC Telescope, such as its parabolic reflector and its lower energy threshold, we have adopted a more general parameterization. It has been seen to describe better the correlation between the shower elongation and the distance shower-COG/source-position for the MAGIC camera, providing an improvement

of the angular resolution:

$$\mathrm{DISP} = A(\mathrm{SIZE}) + B(\mathrm{SIZE}) \cdot \frac{\mathrm{WIDTH}}{\mathrm{LENGTH} + \eta(\mathrm{SIZE}) \cdot \mathrm{LEAKAGE2}} \,. \tag{6.10}$$

The new parameterization includes a second order polynomial dependence of the A, B and η parameters on the logarithm of the total image SIZE. We have also included a correction term in LENGTH to account for images truncated at the edge of the camera, similarly to the correction introduced by Kranich et al. (2003) for the CT1 HEGRA telescope. The correction is proportional to the LEAKAGE2 parameter (the ratio between the charge content in the two outermost camera pixel rings and SIZE). The inclusion of the camera leakage correction allows a better reconstruction of the arrival direction of the more energetic showers, which implies also an improvement of the angular resolution of the telescope with increasing energy.

Optimal values for the DISP parameter functions (A, B and η) can be determined from Monte Carlo simulations or real data from a strong well known point-like source. In this work, a sample of MC simulated γ-rays (zenith angle $< 30°$) has been used for the DISP parameters optimization. The average angular distance (θ^2) between the real and the estimated source position is the parameter required to be minimized. The optimization results are:

- For shower images with LEAKAGE2 = 0:

$$\begin{aligned} A &= 0.925 + 0.530\,(\log \mathrm{SIZE} - 2) - 0.300\,(\log \mathrm{SIZE} - 2)^2 \,, \\ B &= -0.639 - 0.805\,(\log \mathrm{SIZE} - 2) + 0.364\,(\log \mathrm{SIZE} - 2)^2 \,. \end{aligned}$$

- For shower images with LEAKAGE2 not null:

$$\begin{aligned} A &= 1.441 + 0.026\,(\log \mathrm{SIZE} - 2) - 0.044\,(\log \mathrm{SIZE} - 2)^2 \,, \\ B &= -1.891 - 2.224\,(\log \mathrm{SIZE} - 2) + 0.826\,(\log \mathrm{SIZE} - 2)^2 \,, \\ \eta &= 3.524 + 2.218\,(\log \mathrm{SIZE} - 2) + 1.339\,(\log \mathrm{SIZE} - 2)^2 \,. \end{aligned}$$

The DISP calculation, Eq. 6.10, provides two possible source positions along the shower major axis. Therefore, a method to select the correct one is needed. As mentioned, images in the camera contain information about the longitudinal development of the shower in the atmosphere. Čerenkov photons from the upper part of the shower create a narrower section of the image with a higher photon density (head), photons from the shower tail normally generate a much more fussy and spread image end (tail). Therefore, asymmetries in the charge distribution of the images can indicate to which image edge the source position is closer.

The ASYM parameter (see Section 6.4.6 for its definition) allows in most cases to determine the head-tail of a shower image, providing the selection efficiency for the photon density in the image is high. This is normally the case for high energy showers (more than 70% of correct head-tail reconstruction is achieved for SIZE>180 phe). New image asymmetry parameters are being tested to improve the head-tail discrimination, providing promising results.

To estimate the angular resolution of the telescope provided by the DISP method, the distribution of reconstructed arrival directions can be fitted by a two-dimensional gaussian function, leaving σ as a free parameter. Results for Crab Nebula data are shown

in the following Chapter. Previous studies (Domingo-Santamaría et al. 2005) resulted on a global σ for SIZE>180 phe (∼140 GeV) of 0.102 ± 0.008°. The improvement in the angular resolution is significant when compared to previous single IACT results.

6.6.2.2 Mispointing

An accurate knowledge of the position of the source under study in the camera coordinates is essential for a correct calculation of the image parameters that depend on the source position, like DIST and ALPHA, which in turn are key parameters for the γ/hadron separation and the signal evaluation. Therefore, information of the mispointing of the telescope and on the precision of the tracking is fundamental. The Starguider system of MAGIC monitors the mispointing of the telescope during the data taking. It consists of a high sensitivity CCD camera, installed at the center of the telescope mirror dish, which registers both the section of the sky containing the source and some reference LEDs placed on the camera frame. The pointing of the telescope is computed with a precision better than 0.01° from the position of the many stars in the FOV of the CCD camera (Riegel et al. 2005).

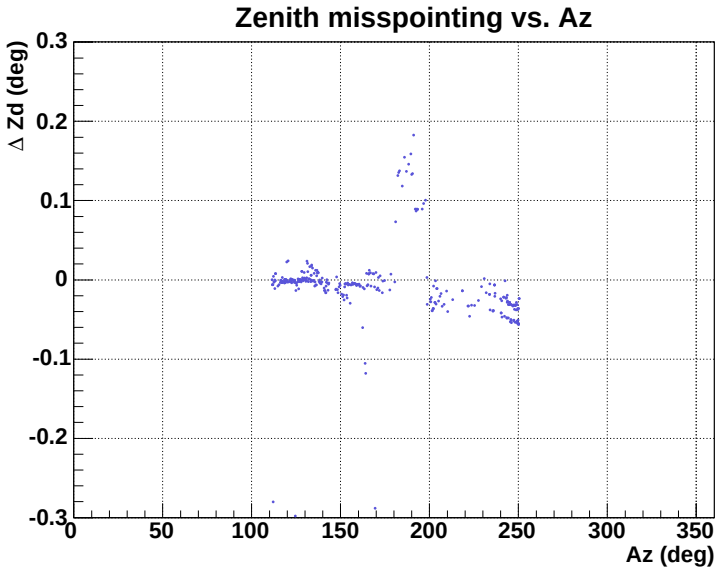

Figure 6.17: The Starguider monitors a deviation in the zenith axis of about 1.5 degrees when the azimuth axis crosses the 180 degrees value, i.e., when the source is culminating. After few minutes, the pointing is recovered.

Despite the high accuracy of the Starguider system, there are still few problems not yet solved concerning the pointing of the telescope. On one hand, an absolute calibration of the Starguider is not available, so the use of its information has to rely on the goodness of its adjustment. Assuming that the mispointing values provided by the system are unbiased, only relative corrections can be done in case a sudden increase of the mispointing occurs for part of the data taking. These jumps are in fact observed when a source is being tracked and it arrives to culmination. If the data taking is not stopped before arriving to culmination, the telescope continues tracking and at some point the movement in the zenith axis has to be inverted. Is in this moment when the Starguider system systematically registers a mispointing up to 0.15 degrees during few minutes of data taking. This disadjustment is due to the little movement that one shaft encoder

of the tracking system allows. After some minutes, the motors encoders seems to catch again the right position and rhythm and the mispointing disappears. An example of this culmination mispointing problem is shown in Figure 6.17. The mispointing only occurs during few minutes, just affecting therefore from two to three typical data runs. In the absence of reliable absolute information of the pointing, and mainly because of the small fraction of data runs affected by the culmination mispointing (only part of the nights the analyzed sources have been observed across their culmination), we have neglected its effect and no correction has been applied for the analysis herein presented.

6.7 Evaluation of the signal

The evaluation of the statistical reliability of a positive result in searching for a γ-ray source is an important problem in γ-ray astronomy. One must determine the confidence level of a candidate positive signal, that is, the probability that the excess count rate is due to a genuine γ-ray source rather than to a spurious background fluctuation. Using a reference source with a well known flux like the Crab Nebula allows to estimate the sensitivity of the instrument from the significance of the detection.

6.7.1 Significance calculation

In the standard Hillas analysis and after cutting in the optimal values of HADRONNESS, ALPHA plots for ON and OFF data samples are constructed. If the source under analysis is bright enough in γ-rays and the devoted observation time is enough, an excess at low ALPHA values appears for the ON data distribution respect to the normalized ALPHA distribution of the OFF data events. The signal region corresponds to ALPHA values below the predefined ALPHA cut and the background region to the remaining ALPHA values. Part of the background distribution is used to normalize ON and OFF.

The number of observed excess events can be computed just subtracting, in the signal region, the integrated number of events in the ON and OFF samples (respectively N_{ON} and N_{OFF}): $N_{exc} = N_{ON} - \alpha N_{OFF}$, where α is the normalization factor used to equalize the ON and OFF data statistics.[3]

There have been various procedures adopted by different experiments to estimate the statistical reliability of their signals. Here the two formulae adopted for the present analysis are reviewed:

- The first option adopted is to directly estimate the standard deviation of the observed signal N_{exc}. Since ON and OFF data are results of two independent measurements, the variance of the excess signal can be calculated by:

$$\sigma^2(N_{exc}) = \sigma^2(N_{ON}) + \sigma^2(\alpha N_{OFF}) = \sigma^2(N_{ON}) + \alpha^2\sigma^2(N_{OFF})\,. \tag{6.11}$$

  Then, the standard deviation of the excess signal, where both the fluctuations of the ON and the OFF samples contribute (which, from the poissonian law, are given by $\sigma(N_{ON}) = \sqrt{N_{ON}}$ and $\sigma(N_{OFF}) = \sqrt{N_{OFF}}$), can be estimated from:

$$\sigma(N_{exc}) = \sqrt{\sigma^2(N_{ON}) + \alpha^2\sigma^2(N_{OFF})} = \sqrt{N_{ON} + \alpha^2 N_{OFF}}\,. \tag{6.12}$$

[3]The normalization factor is normally computed from the integrated number of events of the ON and OFF ALPHA distributions in part of the background region: from 30 to 80 degrees of absolute ALPHA. The ratio of observation time devoted to the ON and OFF data samples is also used.

Defining the significance N_σ as the ratio of the excess counts above background to its standard deviation, it is given by:

$$N_\sigma = \frac{N_{exc}}{\sigma(N_{exc})} = \frac{N_{ON} - \alpha N_{OFF}}{\sqrt{N_{ON} + \alpha^2 N_{OFF}}}\,. \tag{6.13}$$

- Li and Ma (1983) made a critical examination of the methods that were used in the analysis of γ-ray experiments to estimate the statistical reliability of an observational result. They demonstrated that many of the used procedures often overestimated the significance of a positive signal. As a conclusion they proposed two formulae to correctly evaluate the statistical significance of a result. One of their options is the following:

$$N_\sigma = \sqrt{2}\left[N_{ON}\ln\left[\frac{1+\alpha}{\alpha}\left(\frac{N_{ON}}{N_{ON}+N_{OFF}}\right)\right] + \ln\left[(1+\alpha)\left(\frac{N_{OFF}}{N_{ON}+N_{OFF}}\right)\right]\right]^{1/2}. \tag{6.14}$$

Results from Equation 6.13 have been used for the next steps of the analysis presented in this Thesis. Equation 6.14 has only been computed for a check.

6.7.2 Flux sensitivity

The sensitivity of an IACT is defined as the γ-ray flux that a source should emit in a given range of energies (or above a given energy for an integral flux sensitivity) to achieve a 5 sigma detection in 50 hours of observation.

To extract the expression of the sensitivity that has been adopted in the current analysis, it is needed to explicitly derive the dependency of the significance of a signal with the devoted observation time. If we assume, to see the functional dependency, that the observation time for ON data taking, T_{obs}, is the same that for OFF data taking, and we express the number of events N_{ON} and N_{OFF} as the product of the detected event rates times the observation time, in Equation 6.13 we can factorize T_{obs} and get the following relation:

$$N_\sigma = \frac{\mathrm{rate}_{ON} - \alpha\,\mathrm{rate}_{OFF}}{\sqrt{\mathrm{rate}_{ON} + \alpha^2\,\mathrm{rate}_{OFF}}}\sqrt{T_{obs}}\,. \tag{6.15}$$

Therefore, knowing the significance of the signal detected for a source in a given observation time, one can easily estimate the number of sigmas that one should get for a 50 hours observation time:

$$N_\sigma|_{50\mathrm{h}} = \sqrt{\frac{50\mathrm{h}}{T_{obs}}}N_\sigma|_{T_{obs}}\,. \tag{6.16}$$

Then, the sensitivity S, in units of the flux of the detected source, is given by the number of times that one should increase or reduce the observed rate to have a 5 σ detection in 50 hours instead of $N_\sigma|_{50\mathrm{h}}$ sigmas:

$$5 = \sqrt{\frac{50\mathrm{h}}{T_{obs}}}N_\sigma|_{T_{obs}}(N_{exc} \Rightarrow S\cdot N_{exc})\,. \tag{6.17}$$

Solving the previous equation, the sensitivity in per cent of the flux of the observed source can be computed with the following formula:

$$S = \frac{1}{2N_{exc}}\left[\frac{T_{obs}(\mathrm{h})}{2} + \sqrt{\frac{(T_{obs}(\mathrm{h}))^2}{4} + 2\,T_{obs}(\mathrm{h})(1+\alpha)\alpha\,N_{OFF}}\right]\times 100\,, \tag{6.18}$$

and its error is given by:

$$\Delta S = \sqrt{\frac{(S/100)^2}{N_{exc}} + \frac{(T_{obs}(\mathrm{h}))^2(1+\alpha)^2\alpha^2\, N_{OFF}}{4N_{exc}^2\left[\frac{(T_{obs}(\mathrm{h}))^2}{4} + 2\,T_{obs}(\mathrm{h})(1+\alpha)\alpha\, N_{OFF}\right]}} \times 100\,. \tag{6.19}$$

6.7.3 Upper limit calculation

If we are analyzing a source and no signal is observed for the devoted observation time (as it is the case of the analysis done in this Thesis), an upper limit to the flux emitted by the source can be established.

A direct way to proceed is to compute the upper limit in terms of the sensitivity previously derived from a well known source that is going to be used as standard candle (in the case of this work, the Crab Nebula is used for the sensitivity calculation). Therefore, the 5σ upper limit (i.e., the upper limit with a confidence level, CL, of 99.9999%) for the flux arriving from a source observed during T_{obs} hours is given by:

$$F_{u.l.}|_{5\sigma} = S(\mathrm{Crab})\sqrt{\frac{50}{T_{obs}(\mathrm{h})}}\,, \tag{6.20}$$

expressed in units of per cent of the flux of the Crab Nebula (i.e., in Crab Units).

Often the upper limit to the fluxes are relaxed, requiring only that the detection is below 2 σ of significance (i.e., a CL of 95.45%) instead of 5 σ:

$$F_{u.l.}|_{2\sigma} = \frac{2}{5}F_{u.l.}|_{5\sigma}\,, \tag{6.21}$$

also expressed in Crab Units. To convert the estimated upper limits at a given energy into unambiguous flux units, the differential Crab spectrum extracted by from MAGIC data from 2004 and 2005 has been used (Wagner et al. 2005):

$$\frac{dF}{dE} = (1.50 \pm 0.18)10^{-3}\left(\frac{E}{\mathrm{GeV}}\right)^{-2.58\pm0.16} \mathrm{photons\,cm^{-2}\,s^{-1}\,TeV^{-1}}\,. \tag{6.22}$$

Part III

First MAGIC observations of regions of star formation

Chapter 7

Evaluating the MAGIC sensitivity with Crab

This Chapter reviews the results from the analysis of a data sample of the Crab Nebula observed with the MAGIC Telescope. The aim of this analysis is to be used as a reference for the rest of sources analyzed in this Thesis.

7.1 Characteristics of the source and previous observations

The Crab Nebula (also known as Messier Object 1, M1 or NGC 1952) is a gaseous diffuse nebula in the constellation of Taurus. It is the remnant of a supernova that was reported by Chinese and Arab astronomers in 1054 as being visible during daylight for 23 days. Located at a distance of about 6500 ly or 1930 pc from Earth, the nebula consists of the material ejected during the supernova explosion, which has spread over a volume approximately 3 pc in diameter, and is still expanding at a velocity of about 1800 km s^{-1}.

At the center of the nebula is the Crab Pulsar, also known as PSR B0531+21, a neutron star remnant of the supernova. It rotates once every 33 milliseconds, and the beams of radiation it emits interact with the nebular gases.

The Crab Nebula is often used as calibration source in X-ray and γ-ray ground-based astronomy. The pulsar provides a strong periodic signal that is used to check the timing of the X-ray detectors. In fact, 'Crab' and 'milliCrab' are often used as units of flux density. The overall luminosity of the object in the whole energy range is estimated to be about 5×10^{38} erg s^{-1}. Both ground and space-based observations have been carried out in every observationally accessible wavelength band. The resulting broad band spectral energy distribution (see Figure 7.2) is exceptionally complete. A recent review of the characteristics of the emission of Crab is given in Horns and Aharonian (2004). The origin of the high energy emission is commonly interpreted as non-thermal processes: synchrotron radiation and inverse Compton scattering.

The Crab Nebula is the reference TeV γ-ray emitter in the northern hemisphere sky. The first TeV detection of the Crab Nebula was achieved by the Whipple collaboration in 1989 (Weekes et al. 1989). Nowadays it has been detected by more than ten independent ground-based instruments dedicated to very high energy γ-ray astronomy.

The observation of the Crab Nebula from the Roque de los Muchachos Observatory at La Palma is possible approximately from September to March at nearly all zenith angles, as it culminates at 6.8°.Observations with the MAGIC Telescope have been carried out

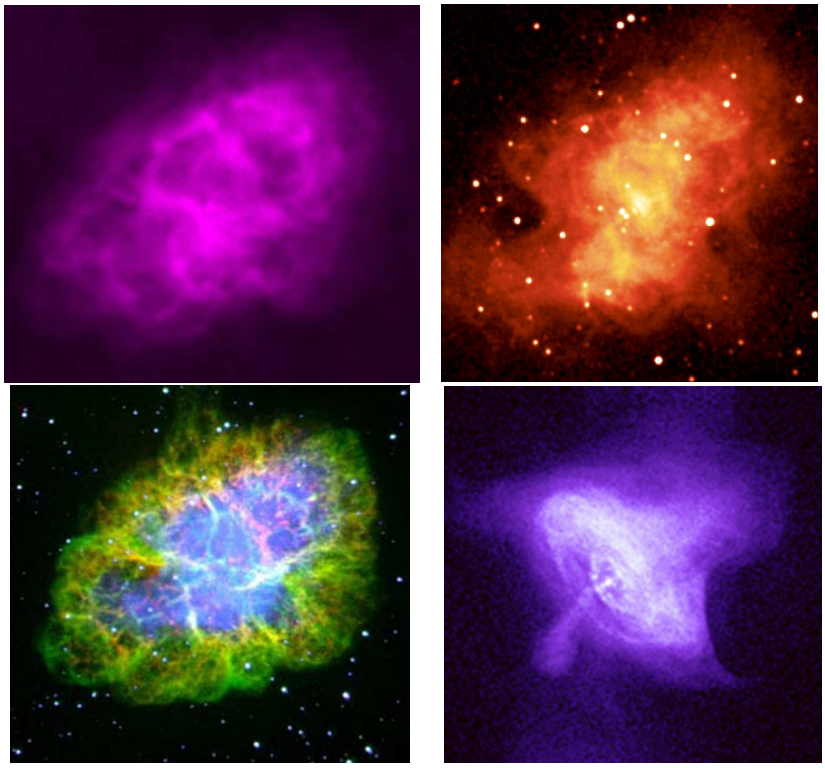

Figure 7.1: Multifrequency images of Crab: Radio (top-left), infrared (top-right), optical (bottom-left), and X-ray (bottom-right), in different scales.

since its first light at the beginning of 2004. Figure 7.3 shows the Crab Nebula spectrum measured by MAGIC (Wagner et al. 2005). It is in good agreement with the HEGRA (Aharonian et al. 2004c) and Whipple (Hillas et al. 1998) results and has been used in the present work to calibrate the telescope sensitivity.

7.2 Analysis procedure

A reference sample of Crab Nebula data has been used to evaluate the sensitivity of the analysis applied to the star forming region sources under study. If an excess signal is obtained, it will be compared to the Crab Nebula analysis results to set the flux level observed in Crab units, or failing that, an upper limit to the flux of the source will be set from the sensitivity shown by the Crab Nebula results.

Apart to be used for the evaluation of the results, the Crab Nebula data has been used to optimize the analysis, selecting the more convenient γ/hadron separation cuts, taking advantage of the strong signal that MAGIC detects already with only one hour of observation. Once the cuts are defined, they are applied to the data samples of the sources under study, which are completely independent of the data sample used for the cut optimization.

Next, the analysis options chosen for the different steps of the data analysis followed in this work are reviewed:

- First selection of runs according to the trigger rates, the atmospheric conditions and the comments in the corresponding shift runbooks.

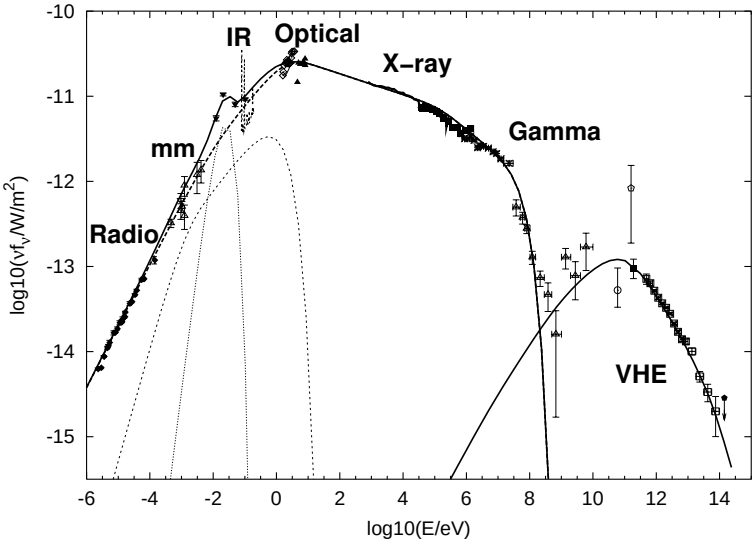

Figure 7.2: Crab Nebula spectrum from a compilation of data from many experiments at all accessible wavelengths. Taken from Horns and Aharonian (2004).

- Data processed with:
  - The Digital Filter as signal extractor algorithm. It integrates the content of 4 FADC slices in the high or low gain region. To avoid to lose the pulses for some events (see Section 6.4.1 for a description of the problem), the searching window has been increased to 4.5 and 5 FADC slices to the left and right of the most frequent pulse position, determined by a previous pulse position check.
  - Pedestal level for the calculation of the calibration constants has been extracted from dedicated pedestal runs, whereas pedestals for the data have been evaluated from the low-gain part of a sample of events of the data runs themselves.
  - Calibration constants are firstly calculated from a calibration run with light pulses generated by UV LEDs. Afterwards they are updated using interlaced calibration events.
  - Interpolation of the signal of next-neighbor pixels to treat and replace the content of detected bad pixels is applied when possible.
  - Absolute image cleaning, with pixels whose content is above 10 phe constituting the core of the images and one ring of next-neighbor pixels whose signal is above 5 phe.
  - Standard parameterization of the resulting images with Hillas parameters.
- Second selection of runs according to the rate of events surviving the image cleaning and the shape of the distributions of Hillas parameters.
- Cut of events related to "sparks".
- From the Random Forest trees, grown from MC γ events and a portion of events the OFF data sample (about 20000 events from each category), a HADRONNESS value is assigned to each ON and OFF data event. After testing different sets of

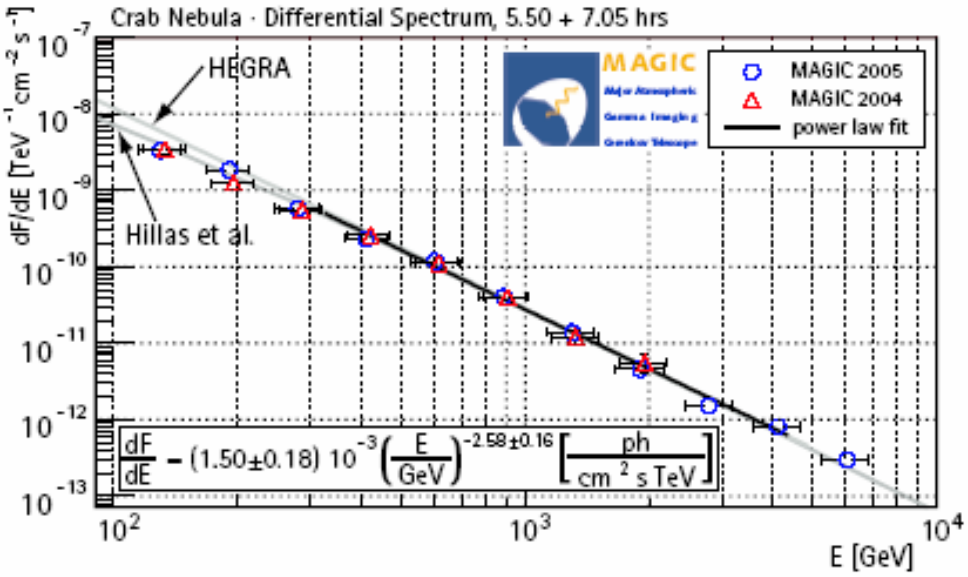

Figure 7.3: Crab Nebula spectrum from MAGIC observations carried out during 2004 and 2005. From Wagner et al. (2005). The spectrum, measured down to nearly 100 GeV, compare well with earlier observations at higher energies by Whipple and HEGRA experiments (shown in the figure with the faint extrapolated power-law lines).

Hillas parameters, the RF which has shown to provide better results has been the one trained with the following parameters: log(SIZE), WIDTH, LENGTH, CONC, DIST, and M3LONG.

- Reconstruction of the SIZE parameter for events not fully contained in the camera.
- ON and OFF data samples are divided in 6 bins of SIZE and, for each of them, the ALPHA plot is constructed and the HADRONNESS and ALPHA cuts are optimized as to provide the maximum significance of the Crab Nebula γ signal above the background.
- Finally, the optimal cuts are applied and the flux sensitivity of the analysis is evaluated for each bin of SIZE.

Plots and results from the most crucial steps already described are shown in the following Sections.

7.3 Data sample

Tables 7.1 and 7.2 review the characteristics of the data samples chosen for the Crab Nebula reference analysis.

Concerning the extragalactic source Arp 220, as no Crab Nebula data from the same data taking period is available [1], very recent Crab Nebula data (from late October and

[1] During May and June the Crab Nebula is no longer visible from the MAGIC Telescope site

November 2005) has been used for the analysis. It has been checked that the telescope performance was similar to that during the Arp 220 data taking (May and June 2005), basically regarding the quality of the telescope focusing (see Appendix E for the results of the study of the PSF among the concerning periods). In fact, both data samples (Crab Nebula and Arp 220) have been taken briefly after a technical access for general refocusing of the telescope mirror dish, one happening at the end of April and the other at mid October. The range of zenith angles of the Crab Nebula data has also been selected to match the one of the Arp 220 sample (relatively low zenith angles, below 30°).

On the other hand, the observations of the galactic source TeV J2032+4130 have been performed essentially under moon conditions, i.e., making use of the observation time slot when the moon is not completely below the horizon. As explained in Section 6.1, the presence of moonlight may increase the level of NSB and, therefore, may change the shape of the recorded images. For this reason, an analysis of Crab Nebula data taken under similar moonlight conditions becomes essential to evaluate the influence of different levels of moonlight on the telescope sensitivity. The TeV J2032+4130 data was taken along a large number of data taking periods, from the end of June until mid November 2005. As it is shown in Table 9.2, this implies a large variety of observational conditions: zenith angles from culmination (about 13°) up to 50°, mean DC current level from normal moonless observations ($\sim 1\mu$A) up to 6μA, different setting of the pixels discriminator thresholds, and different general performance of the telescope. Concerning this last point, the study evaluating the degradation of the telescope focusing (see Appendix E) has included also the intermediate months between June and November 2005, in order to check for the necessity of using different MC simulations for the analysis of the different data taking periods involved. Regarding the several levels of moonlight, unfortunately, when the analysis presented in this Thesis was performed, there was no Crab Nebula data after April 2005 taken under moon conditions inducing such high DC current levels as those found in parts of the TeV J2032+4130 data. See Chapter 9 for more details on the decisions taken for the analysis of this data.

In what refers to the OFF data sample for the Crab Nebula analysis, unfortunately no dedicated moonless OFF Crab data (i.e. pointing to a defined sky region with similar star content and zenith angle as the ON Crab Nebula observations) was taken during the whole considered periods, or at least not enough quantity or not of good enough quality (bad weather conditions). Neither other dedicated moonless galactic OFF data was taken for the same range of zenith angles. However, several nights of the end of October and November were devoted to dedicated OFF Crab observations with moderate moonlight. Having a closer look, it can be seen that slightly more than one hour of that data actually presents a mean DC current of the same order of the typical value observed for Crab Nebula no moon observations (i.e., between 1 and 1.3μA). Therefore, as a solution to the lack of a more convenient OFF data sample, that OFF Crab data runs tagged as moon data but with a mean DC current of the inner pixels below 1.3μA have been redefined, in this Thesis, as the OFF Crab no moon data sample (runs tagged as 'no moon' in Table 7.2).

7.4 Data quality checks

In this Section the checks performed to ensure the good quality of the selected data are shown.

Table 7.1: Crab Nebula data sample. The data taking conditions are reviewed (the weather status (Wea.), the CMT extinction coefficient, the range of zenith angles, if the source is observed during culmination, the mean trigger rate, the raw observation time, the setting of the discriminator thresholds, and the mean DC current level in the inner pixels), as well as the list of selected runs, if they are considered as 'moon' or 'no moon'[1], if the files provided from the online analysis are the ones used, and the final effective observation time included in the analysis for each night after the run selection and classification.

Date	Wea.	Ext.C. (mag)	ZA (°)	Culm.?	Rate (Hz)	Tobs (min)	DT (a.u.)	DC (μA)	Tagged[1]	Online A.used ?	selected runs	Eff. To (min
28/10/2005	OK	0.085	6.7-22.9	YES	243	157	40	1.28-1.30	no moon	NO[4]	71212-16	18.3
								1.30-1.60	moon		71217-18,21-29,32-37, 40-49,52-58,61-68	138.2
29/10/2005	OK	0.086	8.2-30.6	NO	235	110	40	1.21-1.30	no moon	YES	71408-15,18-30	71.2
								1.30-1.33	moon		71400-05	19.7
01/11/2005	OK	0.162	6.7-28.9	YES	226	176	40	1.04-1.20	no moon	YES	71718-20,22-25,28-32, 35-40,44-53,56-63,66-71,75-79	171.0
05/11/2005	OK	0.078	9.5-30.8	NO	237	100	40	1.10-1.25	no moon	YES	74339-44,47-55,58-63,66-72	100.4
07/11/2005	OK	0.085	6.7-36.0[2]	YES	236	212	40	1.10-1.22	no moon	YES	74702,05-08,14,16,18,22,26, 29,31-33,35-37,44-51,55-56,60,63-68	116.0
10/11/2005	OK	0.193	9.7-25.9	NO	208[3]	76	40	1.13-1.27	no moon	YES	75173-74,77-81,84-90,93-98	76.1
TOTAL:						831			no moon			553.1
									moon			157.9

[1] Independently of the official tag of the data runs concerning the moon conditions of the observation, they are reclassified as 'no moon' if DC<1.3μA and as 'moon' if DC=1.3-1.6μA.

[2] Only runs with zenith angle < 30° were selected.

[3] The trigger rate presents strange fluctuations.

[4] The automatic online analysis failed and its output files presented too low rate after calibration. The data runs were recalibrated with a more recent version of the MARS software analysis package.

Table 7.2: OFF Crab data sample. Same information as in Table 7.1.

Date	Weather	Ext.Coef. (mag)	ZA (°)	Culm.?	Rate (Hz)	Tobs (min)	DT (a.u.)	DC (μA)	Tagged[1]	Online A. used?	selected runs	Eff. Tobs (min)
29/10/2005	OK	0.086	7.8-19.7	YES	238	118	40	1.25-1.30	no moon	YES	71433-40	29.50
								1.30-1.43	moon		71442-54,57-67	87.77
08/11/2005	OK	0.134	6.7-12.2	YES	222	64	40	1.00-1.30	no moon	YES	74817-20,23-29	42.33
								1.30-1.40	moon		74813-16	16.03
26/11/2005	OK	0.161	9.3-23.3	YES	233	170	40	1.32-2.96	moon	YES	76000-01,04-11 14-18,20-22,25-29	80.88
TOTAL:						352			no moon			71.83
									moon			184.68

[1] Independently of the official tag of the data runs concerning the moon conditions of the observation, they are reclassified as 'no moon' if DC<1.3μA and as 'moon' if DC=1.3-1.6μA.

7.4.1 Event rate

The rate of events in the data samples has been inspected in search of runs with problems, either intrinsic to the data taking conditions or to the data processing. This information, together with the reported bad weather conditions, led to discard some days of the original data sample. The rest of the selected nights (those in Tables 7.1 and 7.2) present reasonable values of trigger rate, before any data analysis. However, when comparing the trigger rates with the event rates after image cleaning, several problems arise for some of the days. The bottom panels of Figure 6.6 are a clear example: the trigger rate seems quite stable among different runs, but the rate after cleaning drastically drops for some of the runs, and even more surprisingly, some of that problematic runs show a rate for SIZE values above 400 phe larger than the normal expected value.

The misbehavior observed in the rates for some runs after image cleaning points to a problem occurred during the processing of the data. In fact, both the Crab Nebula and the Off Crab data samples used in this work are the ones provided by the online analysis performed at the site the day after the data is taken. Automatic programs process the raw data to generate files with substantially reduced size which store the calibrated and parameterized shower images. At the moment this analysis was done, the online analysis was the only alternative to have a fast access to the data, as the raw data was written to tapes and was not immediately available. A disadvantage is that the analyzer is not able to change the options used during the data processing. Fortunately, the online analysis performed at that time was very compatible with the data processing which the author applied to older data samples such as the Arp 220 data: the Digital Filter integrating 4 FADC slices as signal extractor, a calibration based on an initial calibration run and subsequent updates with interlaced calibration events, and an absolute image cleaning with 10 and 5 phe thresholds.[2]

We have excluded for further analysis runs deviating from the average rate, in order to avoid possible uncontrolled effects in the results. The rates of the selected runs can be seen in Figure 7.4. The rejection of runs due to these problems is the main cause for the reduction in effective observation time compared to the raw observation time (see Table 7.1).

7.4.2 Hillas parameters distributions

An additional check involves the comparison of the different Hillas parameters distributions in all the bins of SIZE. As an example, Figure 7.5 shows that the distributions of CONC are consistent for all the nights of the Crab Nebula ON data sample. No additional runs were discarded by means of this check as no systematic discrepancy was found.

Finally, also the compatibility of the ON and OFF data samples is checked in terms of the distributions of Hillas parameters, especially for those parameters used in the Random Forest γ/hadron separation. Figure 7.6 shows that both samples agree well in the LENGTH parameter, which presents one of the highest γ/hadron discrimination power. The rest of image parameters used in the RF also show comparable good agreement.

[2] In fact, the problems shown in Figure 6.6 had been already detected in the output files of the online analysis for other observation periods and data samples. The problem is yet not completely understood, as calibration constants seem to be well calculated for the problematic runs. There are some indications that the origin is due to hot pixels appearing time to time, but the reason of them to eliminate so large amount of events when performing the image cleaning is still under investigation.

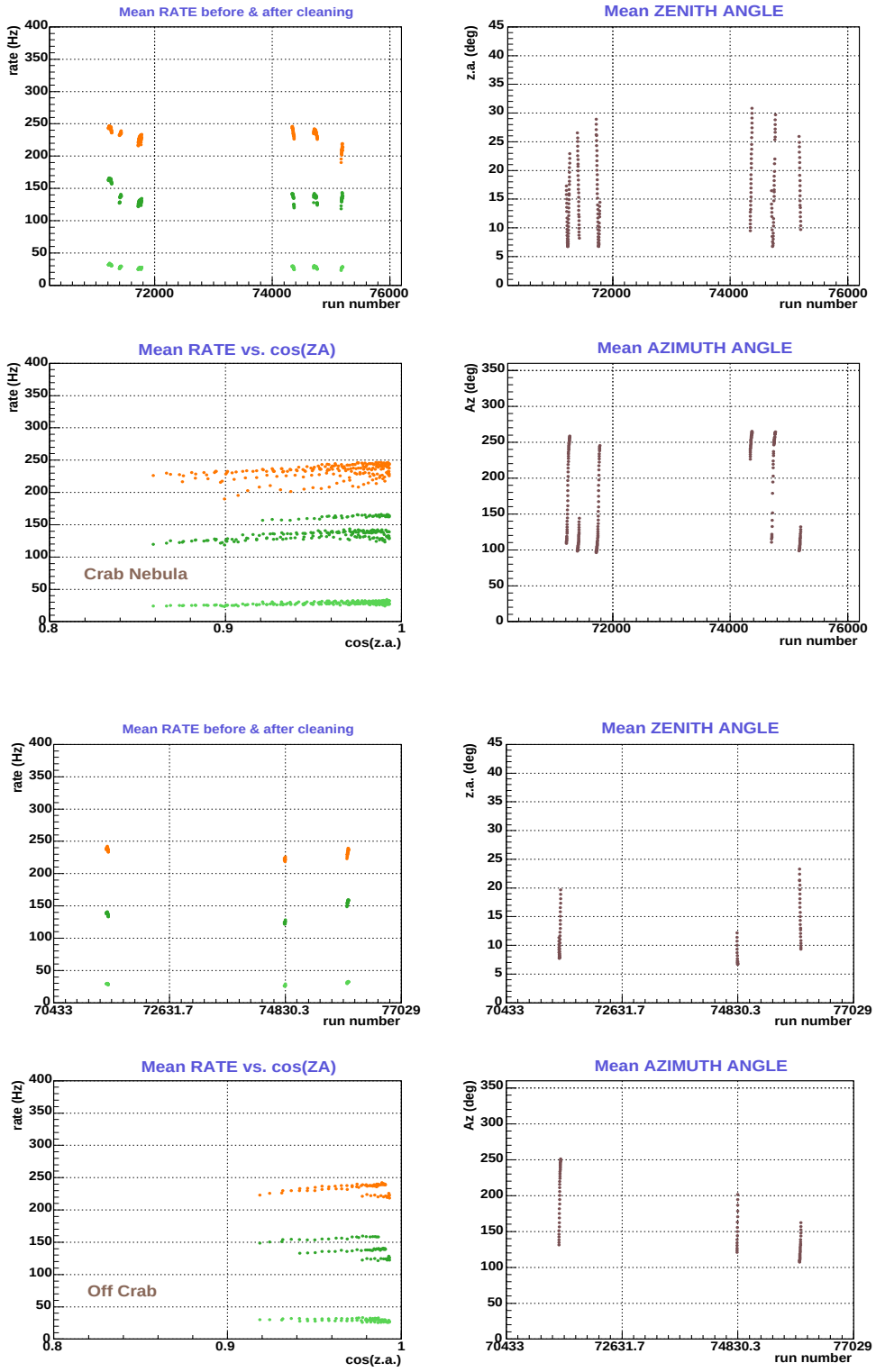

Figure 7.4: Each point in the top (bottom) graph is the mean rate of events for each data run selected from the Crab Nebula (Off Crab) observations. In orange, trigger rates; in dark green, rates after image cleaning; and in light green, rates surviving the image cleaning but with a SIZE above 400 phe.

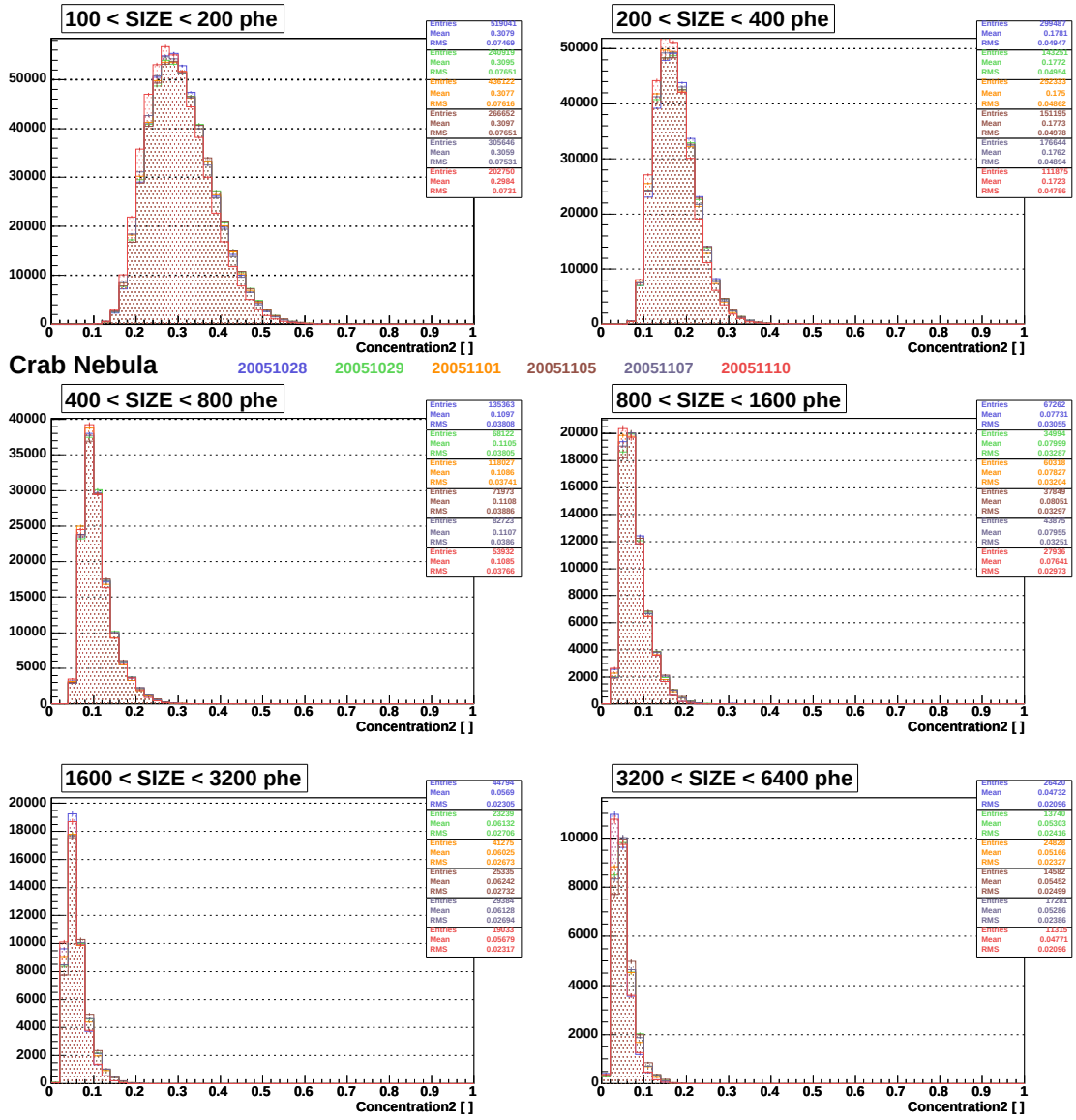

Figure 7.5: The CONC distribution for all days of the Crab Nebula ON data sample (see the legend for the color labelling) and different bins of SIZE. Good agreement is observed.

7.5 Optimal cuts and flux sensitivities

As explained in the previous Chapter, the HADRONNESS cut for γ/hadron separation and the ALPHA cut to define the signal region have been chosen to maximize the significance of the Crab Nebula signal. A grid of cut trail values for HADRONNESS, from 0 to 1, and for ALPHA, from 0 to 20 degrees, has been tested for each bin of SIZE. The results in terms of significance, computed as explained in Section 6.7, are shown as two-dimensional histograms in Figure 7.7 for the Crab Nebula analysis with no moon data, and in Figure 7.8 for the Crab Nebula analysis with moderate moon light.

It is worth checking whether the HADRONNESS cuts result on reasonable values of

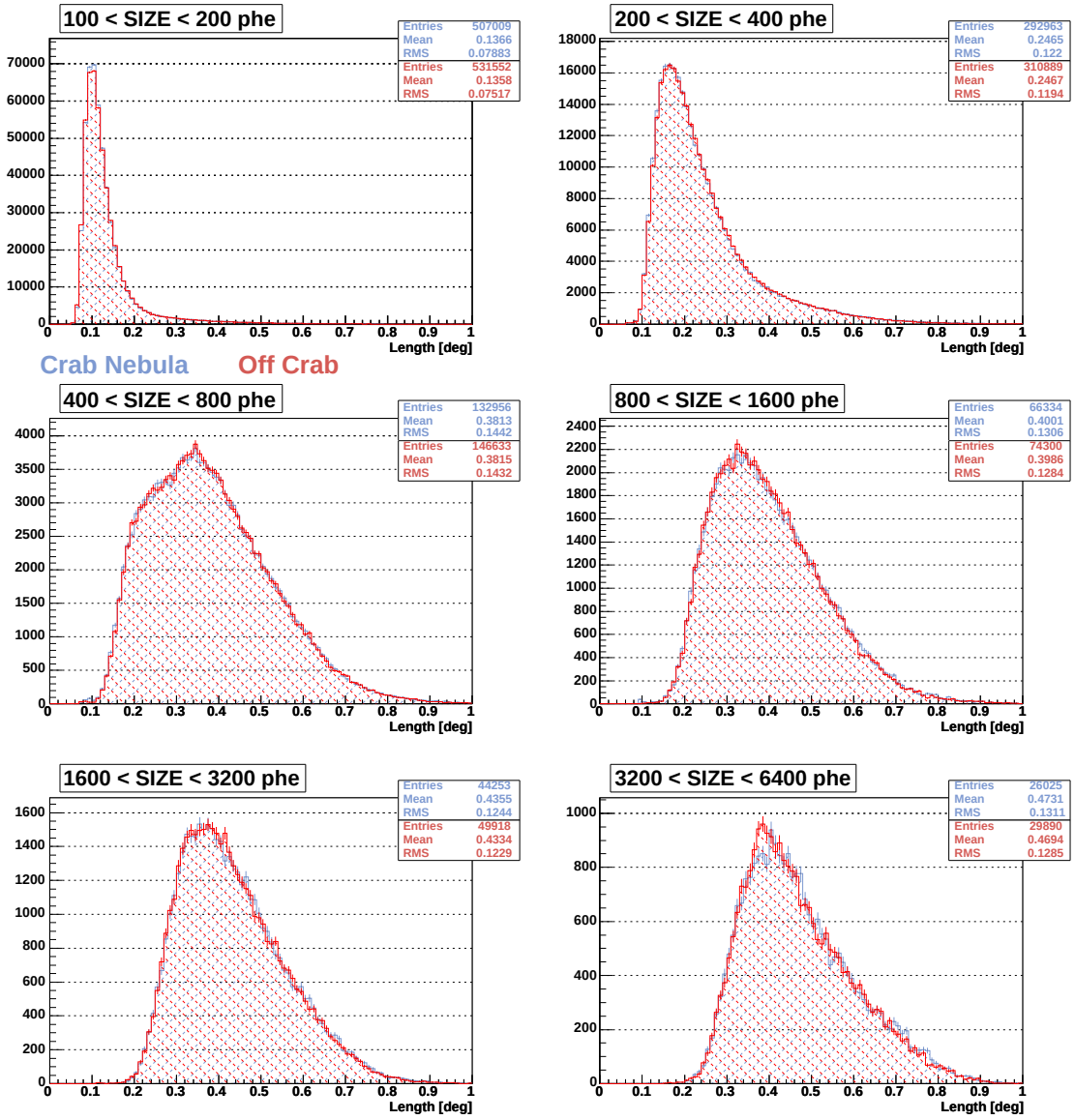

Figure 7.6: The LENGTH distribution for the ON and OFF Crab data samples with moon, for different bins of SIZE. Good agreement is observed.

γ acceptance and Q factor. Figure 6.11 shows the evolution of both quantities with the HADRONNESS cut. In general, the obtained cuts provide good γ acceptances together with high background rejection, and, for some of the SIZE bins, even higher acceptances were achieved by adjusting the HADRONNESS cut without noticeably degrading the significance of the Crab Nebula signal. The final cuts are reviewed in Table 7.3.

Figure 7.9 (7.10) shows the ALPHA plot obtained for the Crab Nebula no moon (moderate moon) data sample with the optimal HADRONNESS cut found in the previous analysis for each of the SIZE bins analyzed. The OFF ALPHA distributions have been normalized to the corresponding ON ALPHA histogram for the events between 30 and

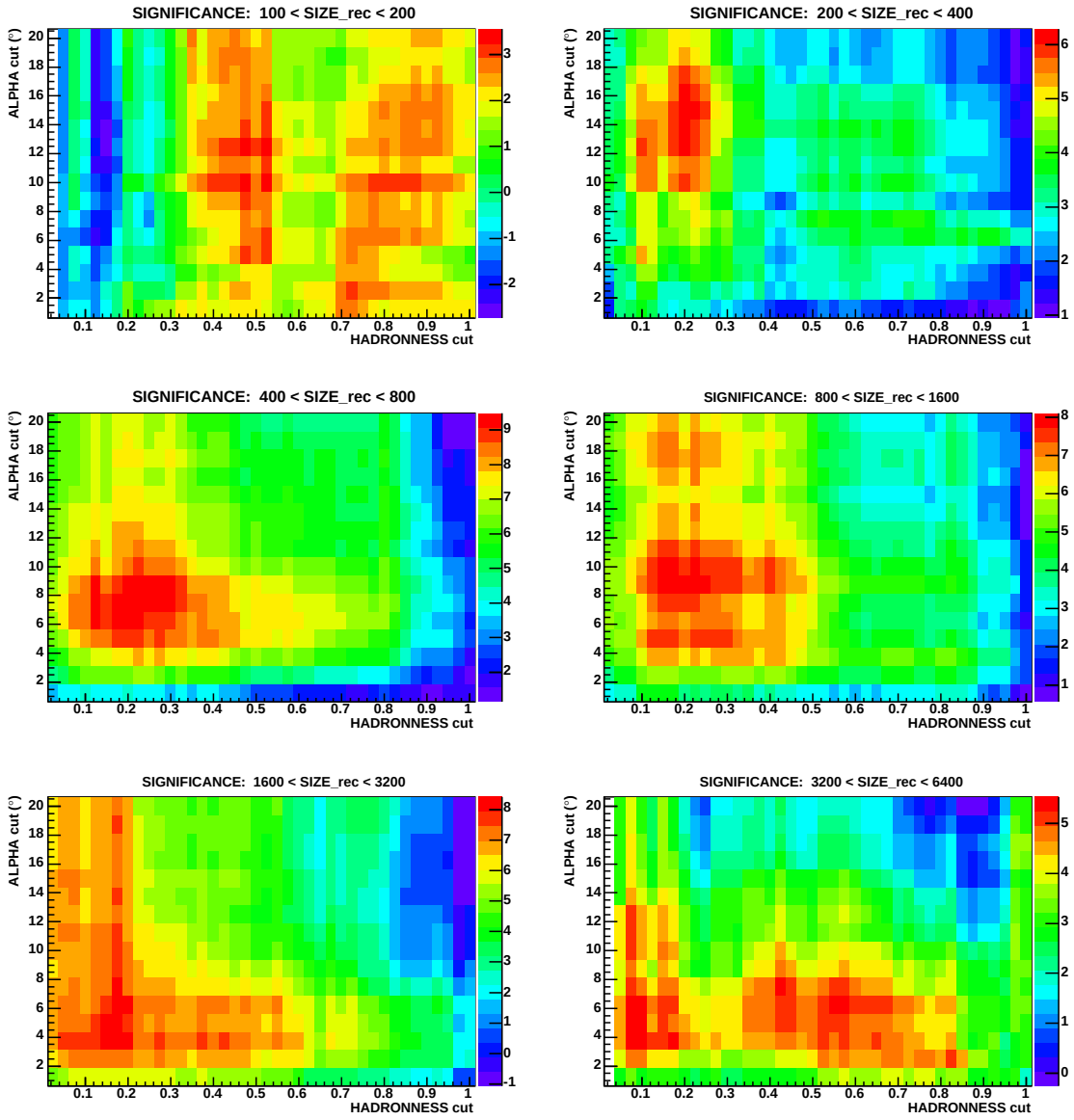

Figure 7.7: Searching for the HADRONNESS and ALPHA cuts which maximizes the significance of the signal obtained from the Crab Nebula no moon analysis for each of the considered bins of SIZE.

80°. The excess signal of the Crab γ-ray events arise for the lowest values of the ALPHA angle.

Finally, Table 7.4 summarizes the sensitivity and significance values obtained for each bin of SIZE and both of the moon conditions analysis, as well as reviews the HADRONNESS and ALPHA cuts used to get them and which are going to be applied to the analysis of the data of the following Chapters.

As can been seen from both the corresponding alpha plots and the numbers in Table 7.4, the analysis is not sensitive enough for the lowest SIZE bin (100-200 phe). It is true that in the case of the analysis of data with moderate moonlight, a significance a bit larger

Table 7.3: γ acceptance and Q factor obtained from the MC and OFF data test samples for each bin of SIZE when applying the corresponding optimal HADRONNESS cut.

SIZE bin (phe)	HADRONNESS cut	γ acceptance (%)	Q factor
NO MOON data analysis			
100 - 200	0.52	0.63	1.2
200 - 400	0.20	0.53	2.8
400 - 800	0.20	0.78	4.7
800 - 1600	0.16	0.84	8.6
1600 - 3200	0.20	0.87	11.0
3200 - 6400	0.18	0.87	18.0
MODERATE MOON data analysis			
100 - 200	0.72	0.90	1.2
200 - 400	0.32	0.67	2.6
400 - 800	0.20	0.79	4.8
800 - 1600	0.14	0.80	7.6
1600 - 3200	0.26	0.87	11.0
3200 - 6400	0.22*	0.85	17.0

* The optimization of the HADRONNESS cut (Figure 7.8) for the 3200-6400 phe SIZE bin shows a maximum of the significance for values of HADRONNESS around 4.5. However, another relative maximum of the significance appears for values close to 0.2 HADRONNESS, which is in better agreement with that found for the Crab no moon analysis.

Table 7.4: Differential flux sensitivity obtained from the analysis of Crab Nebula data taken with no moon and moderate moon conditions. The value of the significance quoted in parenthesis corresponds to the Li & Ma's approach.

SIZE bin (phe)	HADR. cut	ALPHA cut (°)	Norm. factor	N.excess events	N.bkg. events	N_σ (σ)	Sensitivity (% Crab)
Crab NO MOON data analysis (1.22 hours)*							
100 - 200	0.52	12.50	1.16	446	7399	3.5 (3.5)	22.18 ± 1.06
200 - 400	0.20	10.00	1.21	209	499	5.8 (5.8)	12.49 ± 0.91
400 - 800	0.20	8.75	1.18	223	162	9.3 (9.2)	6.71 ± 0.53
800 - 1600	0.16	7.50	1.02	110	44	7.8 (8.0)	7.05 ± 0.84
1600 - 3200	0.20	6.25	1.03	99	27	8.0 (8.2)	6.21 ± 0.84
3200 - 6400	0.18	6.25	1.67	41	11	4.9 (4.5)	11.31 ± 2.65
Crab MODERATE MOON data analysis (2.63 hours)							
100 - 200	0.72	12.50	0.97	1537	39532	5.4 (5.5)	20.89 ± 0.54
200 - 400	0.32	10.00	0.96	540	2418	7.4 (7.5)	14.74 ± 0.65
400 - 800	0.20	8.75	0.88	451	395	13.1 (13.4)	7.07 ± 0.37
800 - 1600	0.14	7.50	0.92	286	79	13.7 (14.5)	5.19 ± 0.41
1600 - 3200	0.26	6.25	0.82	206	70	11.3 (12.1)	6.62 ± 0.57
3200 - 6400	0.22	6.25	0.61	78	17	7.6 (8.9)	8.66 ± 1.21

* Due to the reduced amount of OFF Crab data available classified as 'no moon', only a comparable amount of ON Crab Nebula no moon data (about one hour, concretely the sample corresponding to November the 5th) has been used for the calculation of the signal significance and the flux sensitivity, in order to avoid being dominated by the fluctuations of the background.

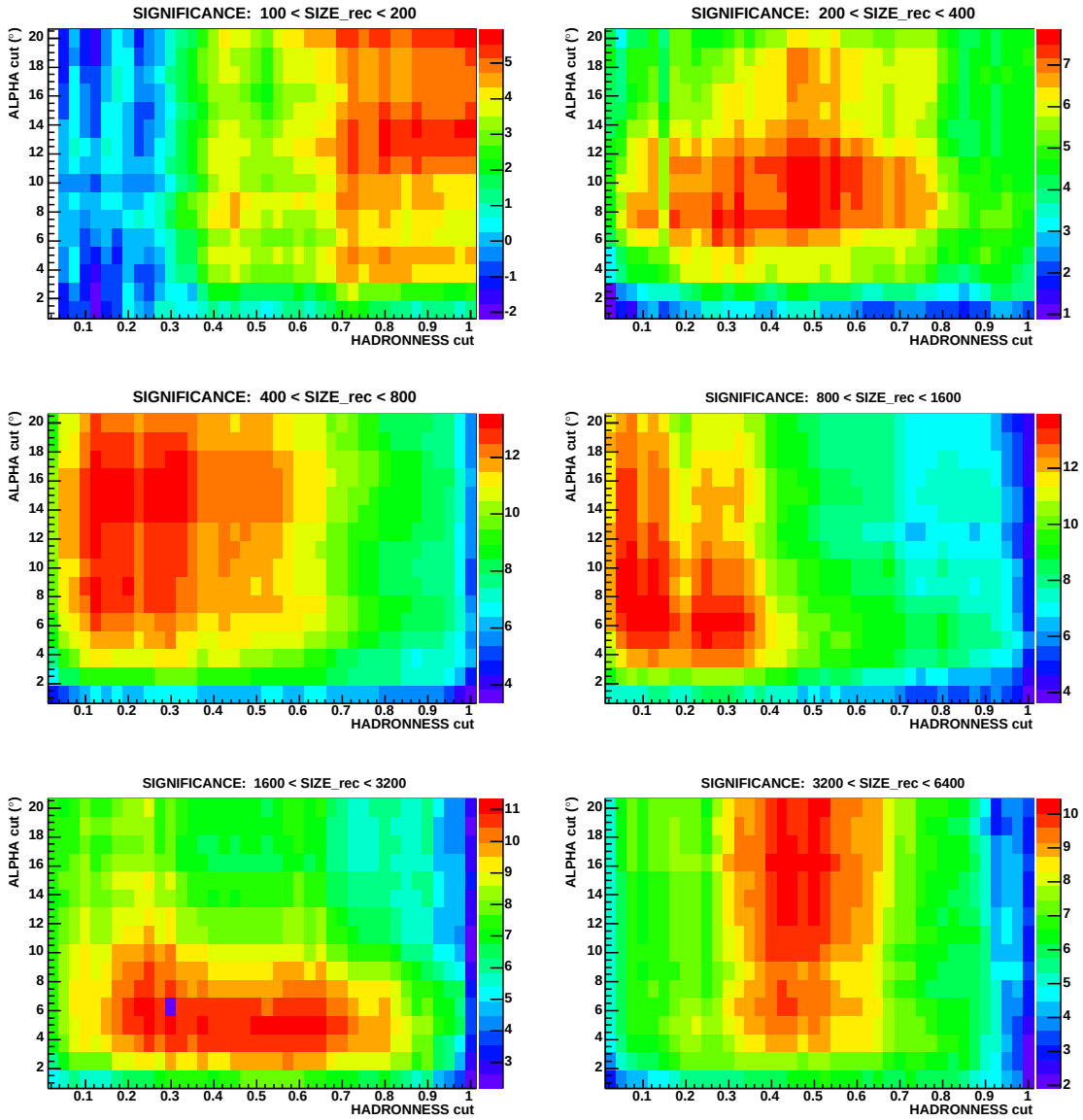

Figure 7.8: Searching for the HADRONNESS and ALPHA cuts which maximizes the significance of the signal obtained from the Crab Nebula moderate moon analysis for each of the considered bins of SIZE.

than 5σ has been found, but the small signal to noise ratio makes this result very sensitive to systematics in the background, so we have decided not to consider the lowest SIZE bin in the analysis. It is worth mentioning that the analysis has not been optimized for the lowest energies, as a robust but at the same time low energy showers suppressing image cleaning has been applied. Results can be improved for the lower SIZE bins if losser cuts in the image cleaning are used.However, this study is beyond the scope of this Thesis.

Finally, we would like to highlight that the results of flux sensitivity obtained for the data under moderate moonlight conditions are compatible within the errors with those from the no moon Crab Nebula data.As a consequence, we have decided to proceed as

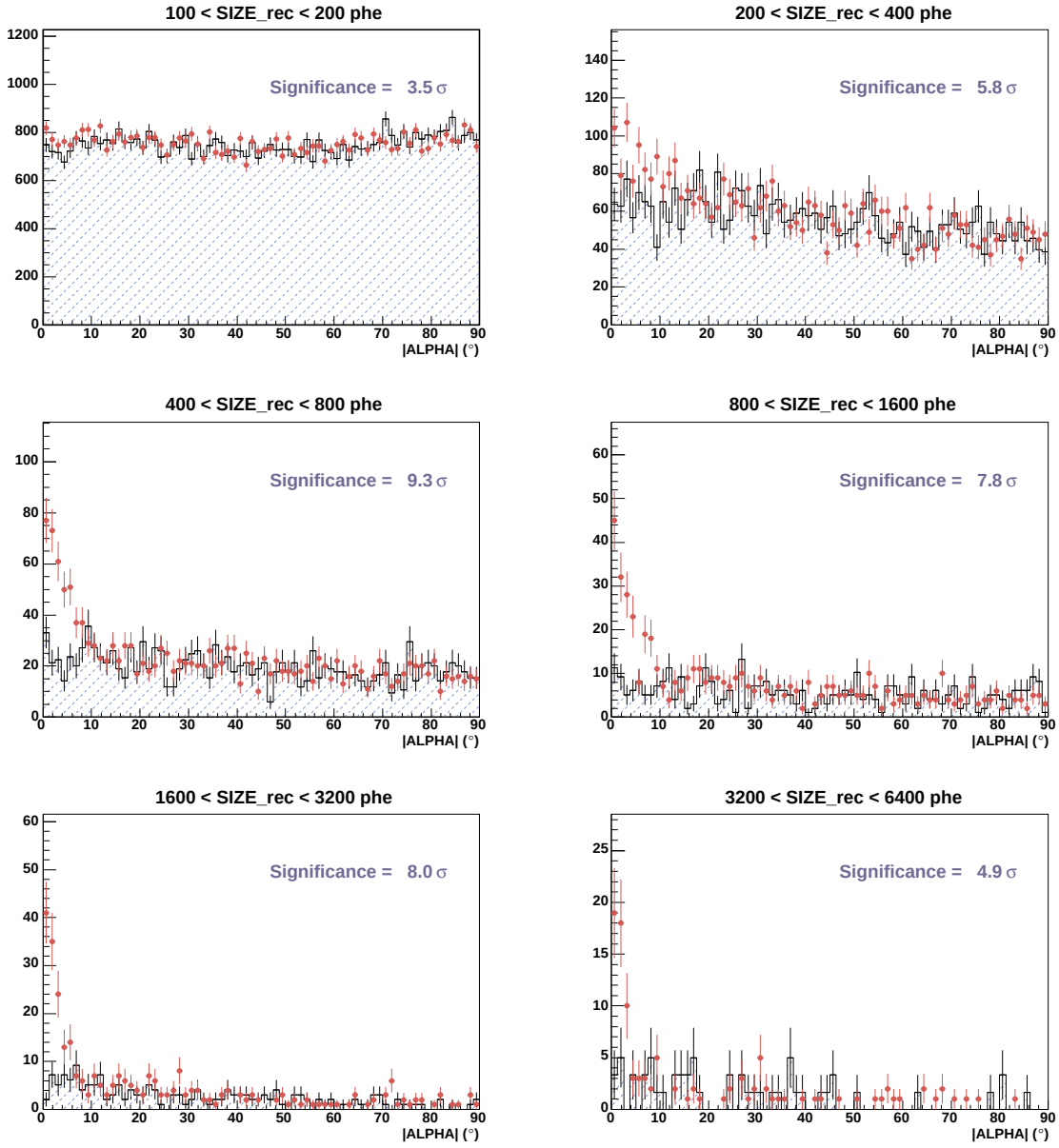

Figure 7.9: Crab data sample with no moon: ON and OFF data ALPHA plots for the different bins of SIZE with the corresponding optimized HADRONNESS cuts.

follows with the star forming regions data samples analysis: the results from the Crab Nebula data with no moon is applied for the analysis of the Arp 220 data sample, whereas only data runs with moderate DC current level are selected from the TeV J2032+4130 sample and they are analyzed using the Crab Nebula moon analysis as a reference.

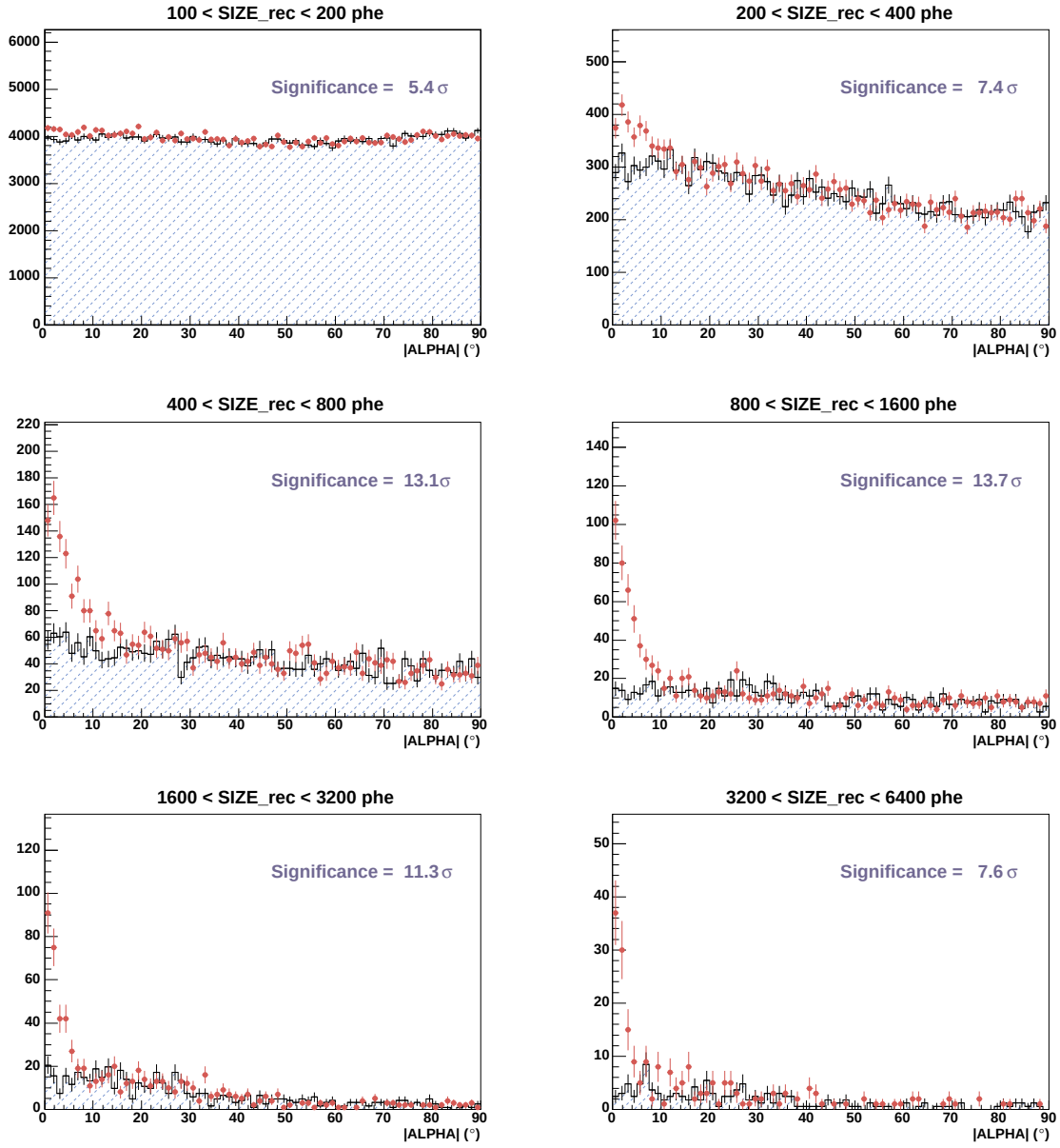

Figure 7.10: Crab Nebula data taken under moderate moon conditions: ON and OFF data ALPHA plots for the different bins of SIZE with the corresponding optimized HADRONNESS cuts.

7.6 Estimation of the telescope angular resolution

Before entering into the analysis of the observations of some particular regions of star formation, we would like to briefly report on an estimation of the MAGIC angular resolution using the DISP method for the reconstruction of each shower arrival direction. The Crab Nebula no moon ON and OFF data samples described in Tables 7.1 and 7.2 have been used. As it is described in Section 6.6.2.1, a source position is estimated for each selected shower image and the subsequent skymap is constructed. The HADRONNESS

cuts optimized for each SIZE bin have been applied to the ON and OFF data samples. Normalizing the ON and OFF Crab skymaps by means of the ratio of observation times, and substracting them, the skymap of excess events has been obtained. A clear excess is observed at the camera center, i.e. at the Crab Nebula position (see Figure 7.11).

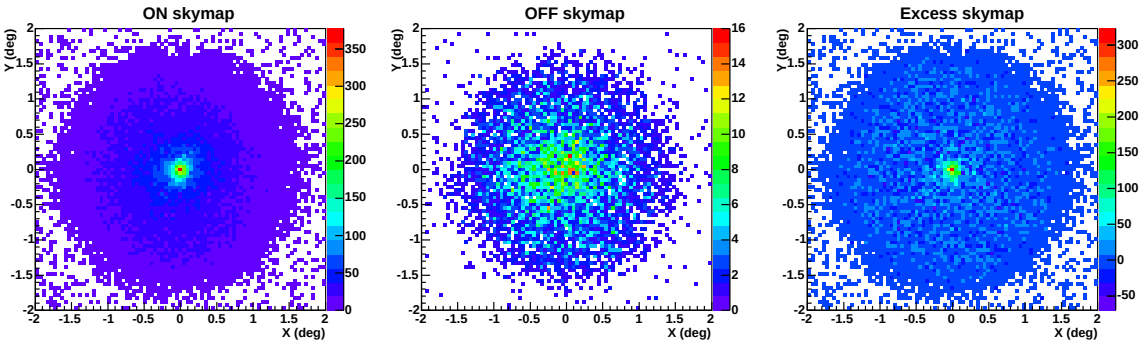

Figure 7.11: Skymaps of reconstructed arrival direction of the selected shower events for Crab ON (left) and OFF observations (middle), and the subsequent skymap of excess events (right). Each shower image contributes with one entry of source position in the skymap, which has been reconstructed by means of the DISP method.

The skymap of excess events can be interpreted as the PSF of the γ-rays detected by the telescope, analogously to the distribution of photons directly collected by an optical telescope. For point-like sources, the angular resolution of a detector is defined as the minimum angular distance by which two separate sources are resolved. The Rayleigh criterion is the generally accepted one for the minimum resolvable detail. According to it, the angular resolution is given by the full width at half maximum of the PSF distribution. However, Čherenkov astronomers often rather talk about σ of the PSF distribution when defining the angular resolution of their telescopes. The excess skymap for the Crab Nebula has been projected onto the x- and y-axis of the MAGIC camera. Both projections have been fitted with a gaussian. Figure 7.12 shows the results. A mean angular resolution (σ of PSF) of $0.112^\circ \pm 0.002^\circ$ for SIZE values above 200 phe (i.e., for energies above $\sim$ 160 GeV) is obtained, which is in good agreement with previous studies given in Domingo-Santamaría et al. (2005).

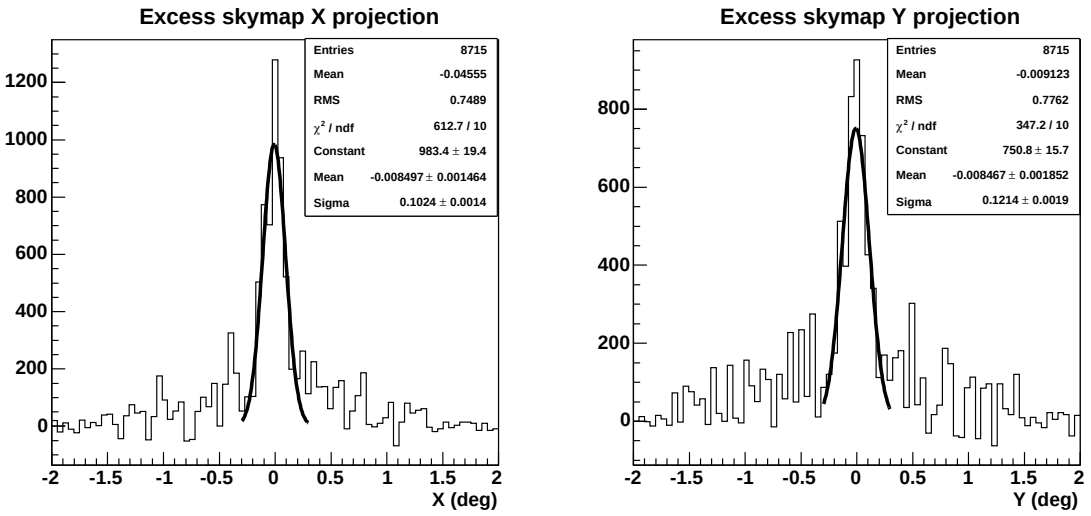

Figure 7.12: Left (right) panel shows the projection onto the X (Y) camera axis of the distribution of reconstructed arrival directions for the excess events of the Crab Nebula analysis, for SIZE values above 200 phe. As expected, the γ-ray signal is centered at the Crab position (camera center) and the mean value of both σ gaussian fits has been taken as estimation of the telescope angular resolution.

Chapter 8

MAGIC observations of Arp 220

The results of the analysis of 15 hours of observation of the ULIRG Arp 220 with the MAGIC Telescope are summarized. No signal was observed with the dedicated amount of observation time. Upper limits to the flux of Arp 220, based on the sensitivity extracted from the Crab Nebula data analysis, have been set.

8.1 Characteristics of the source and previous observations

For a description of the characteristics of Arp 220, the lector is referred to Section 3.2.1 within the theoretical Chapters, as well as to Section 2.2 where the main properties of Ultraluminous Infrared Galaxies (ULIRG) are reviewed.

No observations of Arp 220 have been reported at IACTs operation energies. Both the HESS array and the MAGIC Telescope have been observing this source during 2005. However, due to its declination[1] Arp 220 is a target especially suitable for northern hemisphere sites, and HESS can only observe it at large zenith angle values (above 46 °). Therefore, the upper limits resulting from the present study can be complementary to the results that HESS may provide.

8.2 Data sample

Tables 8.1 and 8.2 review the characteristics of the data samples chosen for the Arp 220 analysis, the ON and the OFF data samples respectively. In this case, there is dedicated OFF data taken specifically for Arp 220, but in order to enlarge the statistics of the OFF data sample and, therefore, reduce the background fluctuations, all the dedicated OFF samples of extragalactic sources taken during the same data taking periods (P29 and P30) have been included in the analysis. Figure 8.1 shows the range of zenith angles of the Arp 220 observations and the OFF data sample. All the observations were performed at zenith angles below 30°.

[1]The Arp 220 celestial coordinates are: RA = 15^h 34' 57.21", DEC = +23° 30' 09.5"

Table 8.1: Arp 220 ON data sample. The data taking conditions are reviewed (the weather status, the CMT extinction coefficient, the range of zenith angles, if the source is observed during culmination, the mean trigger rate, and the raw observation time), as well as the final effective observation time included in the analysis for each night after the run selection.

Date	Weather	Ext. coef. (mag)	ZA range (°)	Culm.?	Mean rate (Hz)	Tobs (min)	Eff. Tobs (min)
02/05/2005	OK	0.063	5.3 - 8.3	YES	335	37	36.83
08/05/2005	OK,few calima	0.178	5.3 - 17.2	YES	302	133	132.55
12/05/2005	OK	0.093	5.3 - 17.5	stopped	322	131	131.00
14/05/2005	OK	–	5.3 - 15.3	YES	319	95	94.52
15/05/2005	clouds	–	6.5 - 14.9	NO	308	57	35.40
31/05/2005	OK	0.088	5.3 - 16.7	stopped	304	117	117.10
02/06/2005	OK	0.087	5.3 - 13.7	YES	306	107	107.23
05/06/2005	OK	0.083	5.3 - 14.8	YES	316	103	103.48
07/06/2005	OK	0.167	5.3 - 15.1	stopped	293	109	109.02
12/06/2005	OK	0.088	5.3 - 11.0	YES	322	58	57.75
TOTAL:						947	924.88

Table 8.2: OFF data sample. Same information as in Table 8.1.

Date	Weather	Ext. coef. (mag)	ZA range (°)	Culm.?	Mean rate (Hz)	Tobs (min)	Eff. Tobs (min)
Off Arp 220							
06/05/2005	OK,few calima	0.197	5.3 - 14.2	YES	290	84	83.58
11/05/2005	OK	0.098	5.3 - 17.9	YES	334	149	148.65
03/06/2005	OK	0.084	5.3 - 16.2	YES	317	101	101.45
09/06/2005	OK	0.097	6.1 - 10.1	NO	321	27	26.75
Off 2E1415							
03/05/2005	OK	0.089	3.1 - 12.2	YES	332	66	66.32
07/05/2005	OK	0.196	3.2 - 26.0	NO	295	114	113.63
03/06/2005	OK	0.084	3.1 - 18.9	NO	307	79	77.38
06/06/2005	OK	0.089	3.1 - 15.8	YES	312	68	67.67
Off 1ES1426							
11/05/2005	OK	0.098	13.9 - 25.0	NO	320	113	111.48
Off HB1553							
07/05/2005	OK,few calima	0.196	17.7 - 23.2	YES	301	129	128.52
Off M87							
06/05/2005	OK,few calima	0.197	17.3 - 17.5	NO	303	76	73.58
Off W-Comae							
02/05/2005	OK,few calima	0.063	0.6 - 17.2	YES	336	111	110.67
TOTAL:						1117	1109.68

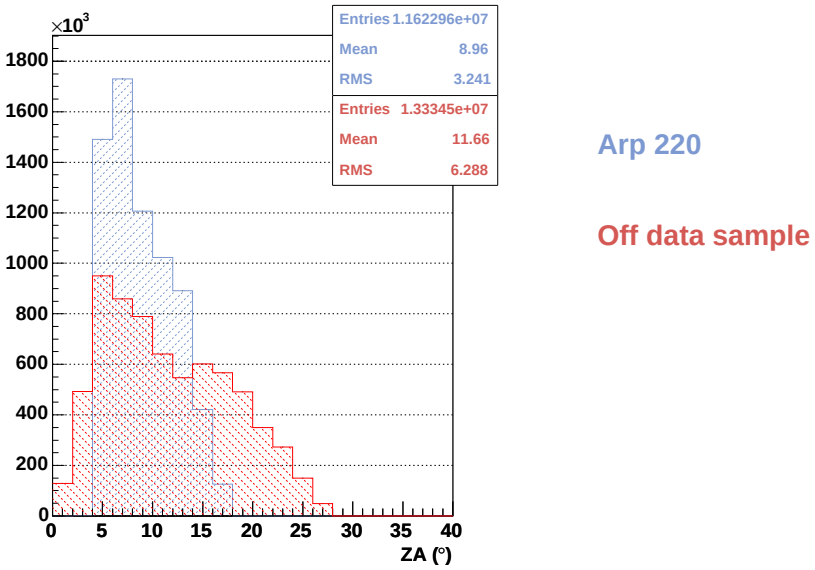

Figure 8.1: Zenith Angle distribution of the Arp 220 ON data sample and the selected set of extragalactic sources OFF data sample.

8.3 Data quality checks

In this Section the checks performed to ensure the quality of the data are described.

8.3.1 Event rate

Figure 8.2 shows the event rate for the data runs used in the analysis of Arp 220, before and after image cleaning. Only a few runs have been discarded due to abnormal values of the rate caused by technical problems. These technical problems were usually pointed out by operators in the data taking runbook.

8.3.2 Hillas parameter distributions

Analogously to the Crab analysis, an additional check consists in the comparison of the shape of the distributions of the Hillas parameters for the different bins of SIZE. Figure 8.3 shows, for example, the good consistency of the DIST distributions of the Arp 220 ON data sample for all nights. No additional runs were discarded. Figure 8.4 shows that of the ON and OFF data samples are compatible before applying event selection cuts in terms of the distribution of WIDTH, one of the Hillas parameters with higher γ/hadron separation power. Good agreement is observed also for the remaining image parameters used to train the RF.

8.3.3 Evaluation of the mispointing

The telescope mispointing during Arp 220 observations has been monitored using the Starguider system. Contrary to the Crab Nebula observations, basically all the Arp 220 data, except one night, is affected by mispointing during culmination of the source. Figure 8.5 shows the jump in the zenith pointing axis that affects about 6 minutes of each data taking night when the observation zenith angle passes through 180°. All the nine affected days are plotted. The magnitude of the mispointing is more or less the same for the

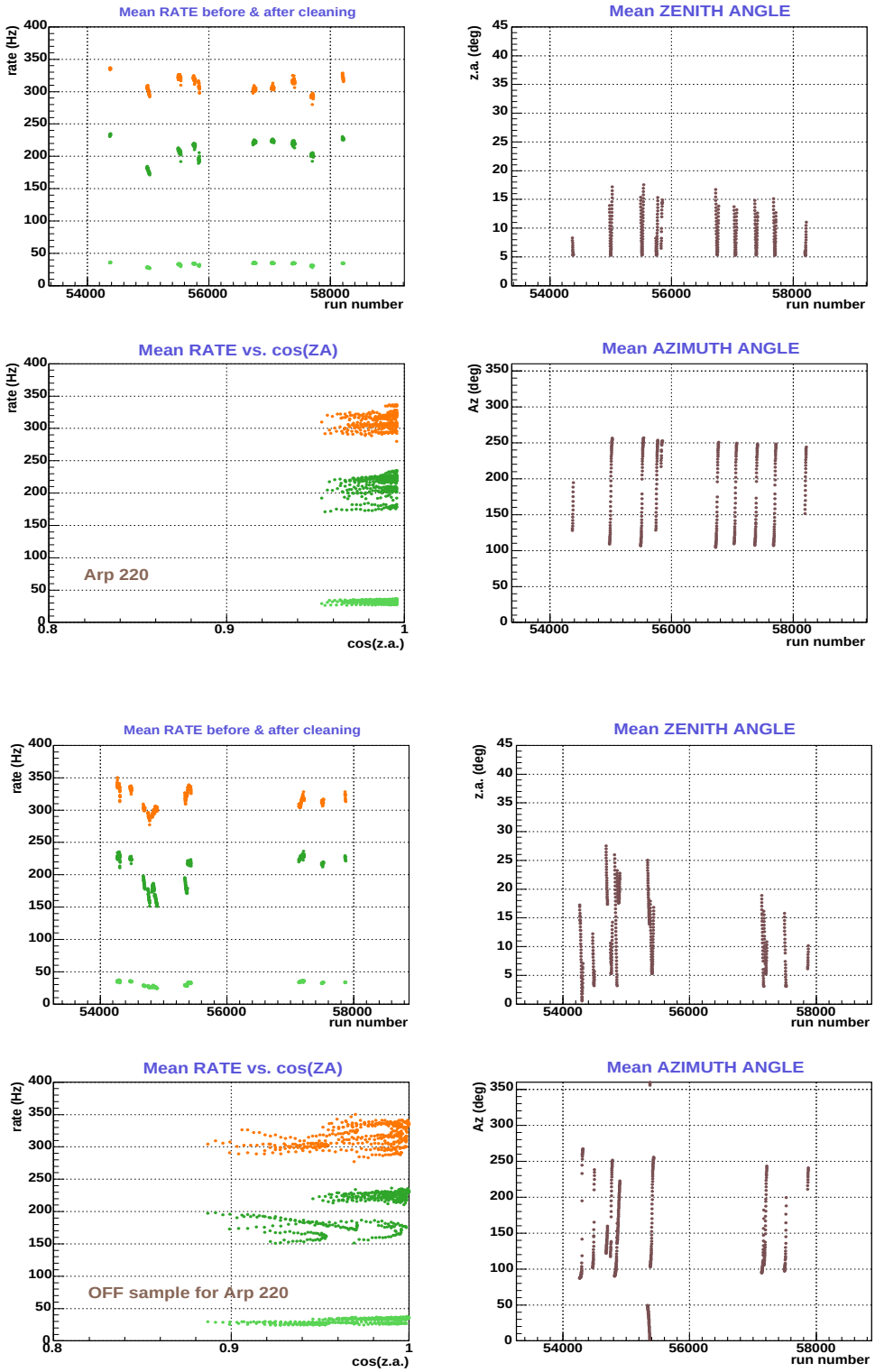

Figure 8.2: Each point in the top (bottom) graph is the mean rate of events for each data run in the ON (OFF) data sample used for the Arp 220 analysis. In orange, trigger rates; in dark green, rates after image cleaning; and in light green, rates surviving the image cleaning but with a SIZE above 400 phe.

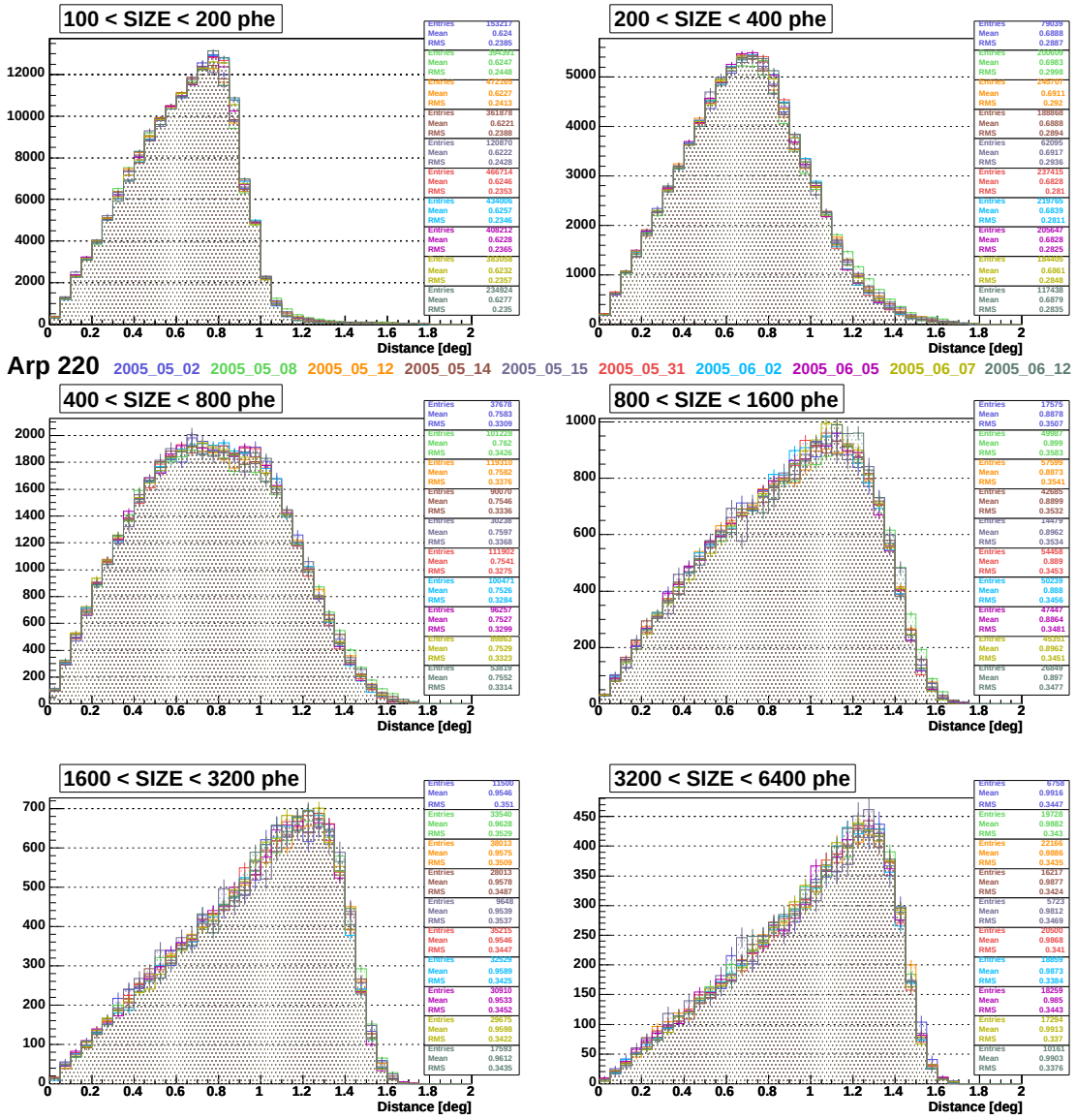

Figure 8.3: The DIST distribution for all days of Arp 220 ON data sample (see the legend for the color labelling) and different bins of SIZE. Good agreement is observed.

different days, between 0.09 and 0.15 degrees, i.e. about the size of one inner pixel of the MAGIC camera. For four of the days the data taking was stopped right before the tracking entered in culmination to avoid runs with the known problem, therefore, only about 3% of the events (30 minutes of the total of 925) included in the analysis are affected. However, Figure 8.5 indicates another possible problem: in the Starguider data two populations can be clearly distinguished, one with an initial bias in the zenith mispointing of about 0.06 degrees and the other with an absolute initial mispointing before culmination centered around zero. Interestingly, the biased sample corresponds to data from the first half of May 2005, before the end of Period 29. For the data from Period 30 the Starguider

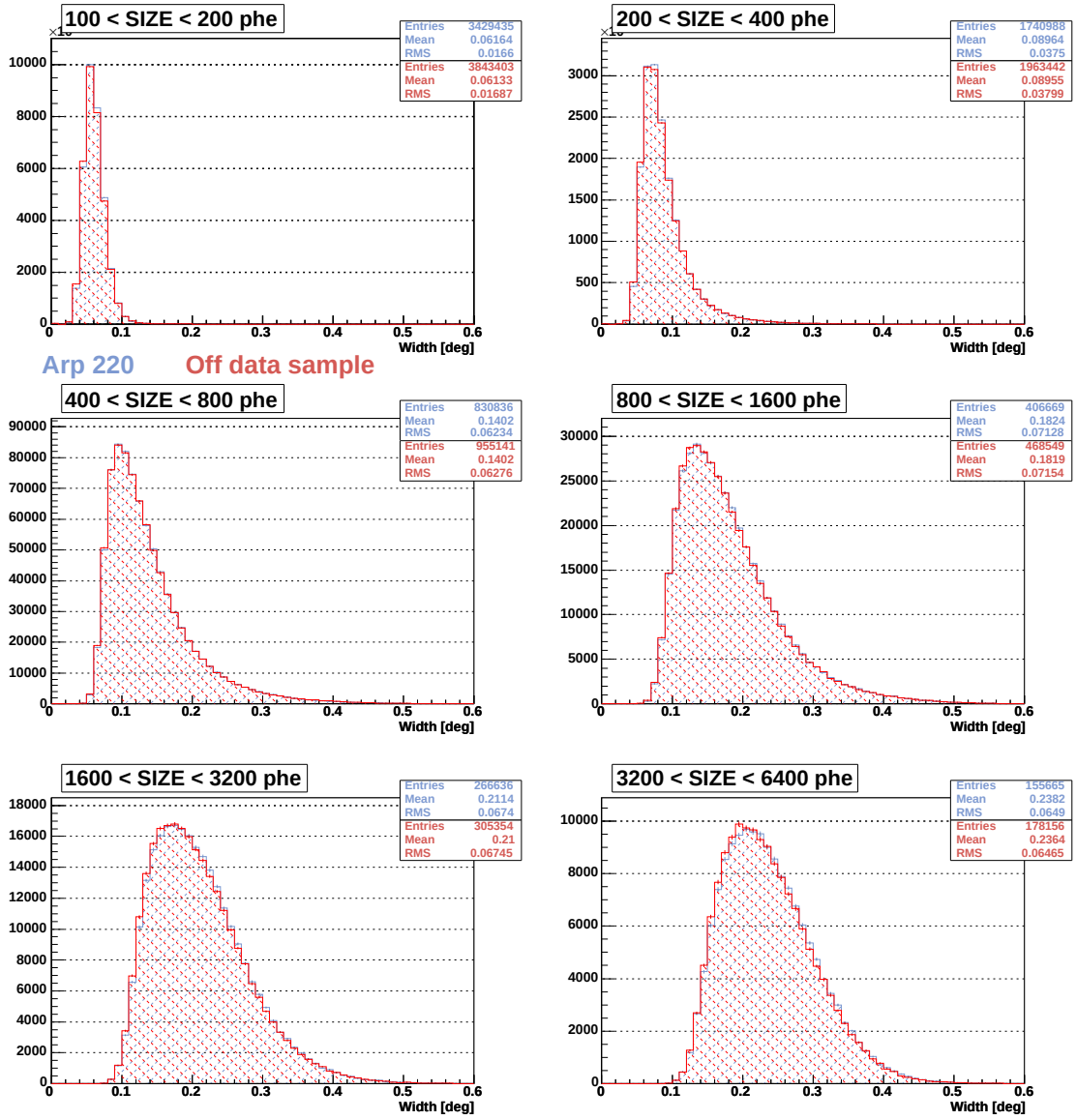

Figure 8.4: The WIDTH distribution for the ON (Arp 220) and OFF data samples and different bins of SIZE. Good agreement is observed.

system seems to be better calibrated. Indeed, during the moonless days between the two mentioned periods, there was a technical access where a misfocusing of the AMC system was found and corrected. It was very probably introduced during the previous major telescope focusing at the end of April 2005. Therefore, there is an indication that a global shift in the pointing takes place for the P29 data, although we would like to stress that, its magnitude is about half the size of an inner pixel and, therefore, a large effect on the ALPHA parameter computation is not expected.

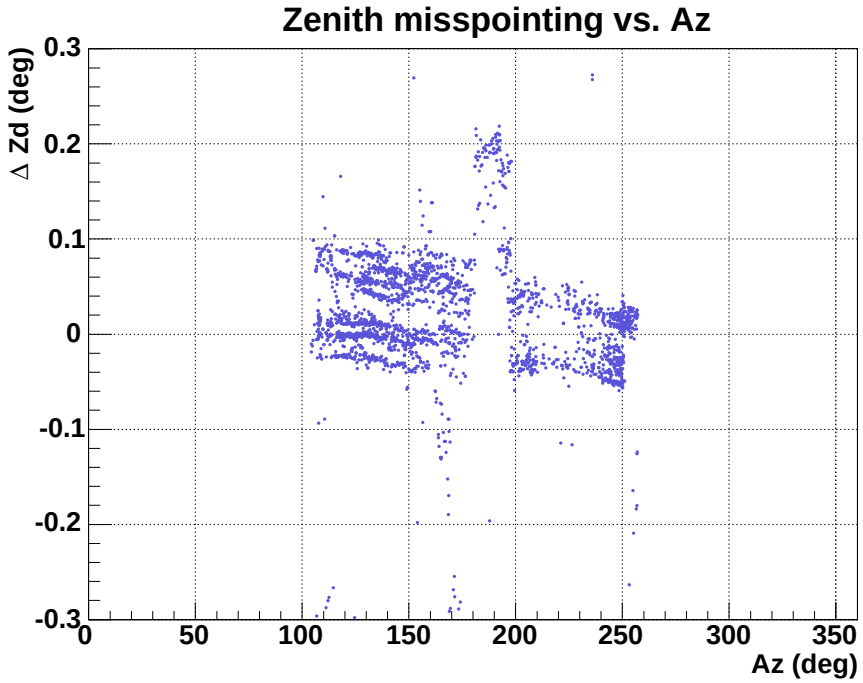

Figure 8.5: The top panel shows the mispointing in zenith angle as a function of the azimuth angle of the telescope. The so-called "culmination problem" is well visible after azimuth 180°.

8.4 ALPHA plots and Upper limits from Crab sensitivity

Figure 8.6 shows the ALPHA plots which were obtained for the whole sample of ON and OFF data, after applying the HADRONNESS cuts that were determined using the Crab Nebula no moon analysis, as it is explained in the previous Chapter. The ON and OFF ALPHA distributions match reasonably well within fluctuations. No signal above the background level is observed in any of the SIZE bins. The numbers are reviewed in Table 8.3.

The upper limits to the flux of Arp 220 can be calculated out of the sensitivity that was determined using the Crab Nebula sample, as explained in Section 6.7.3. Table 8.4 summarizes the results.

In order to compare with theoretical predictions of the differential γ-ray flux expected from Arp 220, SIZE must be converted into energy. As explained in Section 6.6.1, the SIZE of the images which are strongly truncated has been reconstructed according to the value of LEAKAGE2. As a first estimation, the mean of the distribution of true energy of the MC γs that lay on each bin of reconstructed SIZE is assigned as the energy position for each upper limit. One σ deviation of the gaussian fit to the MC true energy distribution is the error adopted for this energy estimation, in order to represent the dispersion of the energy of the events contained in each SIZE bin (see Figure 6.16).[2]

[2]This estimation is simpler than the reconstruction of the energy for each shower image and the reanalysis of the data sample in bins of energy instead of SIZE, but it should give roughly the same value of mean energy.

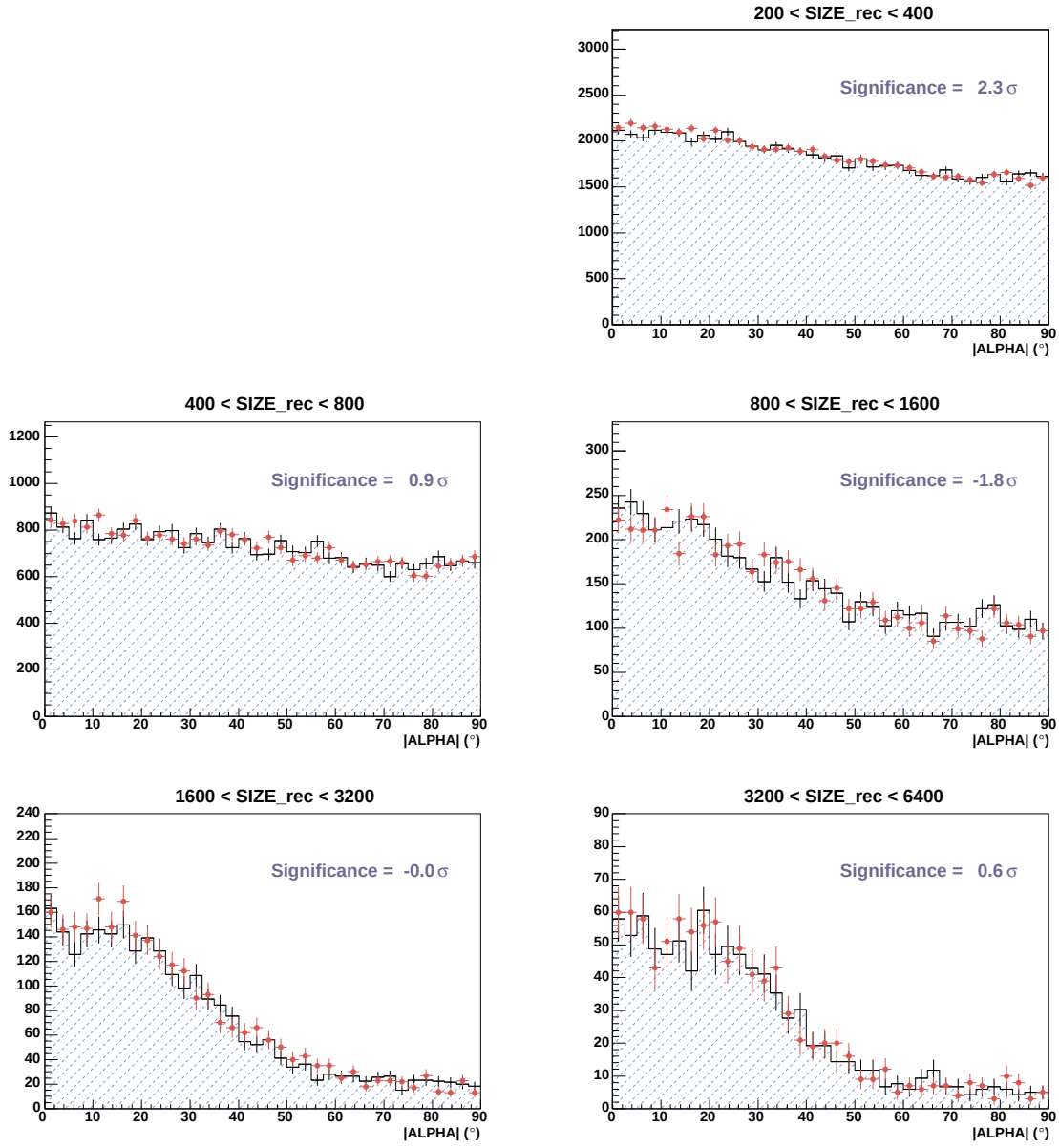

Figure 8.6: ALPHA plots for the Arp 220 data.

However, the estimation of the most probable energy of the γ-rays for each SIZE bin has been done with a MC γ sample simulated under the assumption of a certain spectral slope: -2.6. Therefore, if the source under study has a different slope, the best choice for the energy to be associated to each SIZE bin can be different. To account for the systematic effect of the spectral slope, the same distributions shown in Figure 6.16 have been computed weighting each event with a factor $E^{2.6-x}$, being x the new slope wanted to be evaluated. The results of this evaluation, together with the percentage of change of the estimated mean energy for each SIZE bin, can be found in Table 8.5.

Figure 8.7 shows the upper limits. Systematic and statistical errors are already

Table 8.3: Number of excess and background events and the corresponding significance obtained from the Arp 220 alpha plots analysis. The value of the significance quoted in parenthesis corresponds to the Li & Ma's approach.

SIZE bin (phe)	HADR. cut	ALPHA cut (°)	Norm. factor	N.excess events	N.bkg. events	N_σ (σ)
200 - 400	0.20	10.00	0.91	295	8343	2.3 (2.3)
400 - 800	0.20	8.75	0.88	51	2873	0.7 (0.7)
800 - 1600	0.16	7.50	0.87	-62	707	-1.8 (-1.8)
1600 - 3200	0.20	6.25	0.83	7	370	0.3 (0.3)
3200 - 6400	0.18	6.25	0.84	22	132	1.4 (1.4)

Table 8.4: 5σ and 2σ upper limits to the differential flux of Arp 220, derived from the sensitivity flux estimated from the analysis of the Crab Nebula data not affected by moonlight.

SIZE bin (phe)	Sensitivity (% Crab)	Sensitivity ($\times 10^{-14}$ ph cm^{-2} s^{-1} GeV^{-1})	5σ Upp.Limit ($\times 10^{-14}$ ph cm^{-2} s^{-1} GeV^{-1})	2σ Upp.Limit ($\times 10^{-14}$ ph cm^{-2} s^{-1} GeV^{-1})
200 - 400	12.49 ± 0.91	38.12 ± 2.78	68.65	27.46
400 - 800	6.71 ± 0.53	5.19 ± 0.41	9.34	3.74
800 - 1600	7.05 ± 0.84	1.40 ± 0.17	2.53	1.01
1600 - 3200	6.21 ± 0.84	0.33 ± 0.04	0.59	0.24
3200 - 6400	11.31 ± 2.65	0.14 ± 0.03	0.26	0.10

included. The differential γ-ray flux which was theoretically predicted and presented in Section 3.2.2 has been superimposed for comparison. The results obtained using the δ-function approximation and the total p-p cross-section for neutral pion production, as proposed by Aharonian and Atoyan (2000) are shown as a black curve. The estimation using the differential proton-proton cross-section proposed by Blattnig et al. (2000) is shown in red. The latter is shown here just for completeness, since we have already discussed that this parameterization of the cross section overestimates the γ-ray flux at high energies.

The upper limits imposed to the differential flux of Arp 220 with 15.4 hours of data are above the theoretical curves (even the one using Blattnig et al. parameterization) for all energies, getting closer to a possible experimental discard of the prediction obtained using the Blattnig et al. p-p differential cross-section for the highest energies analyzed ($\sim$ 1 TeV). However, all upper limits are at least about one order of magnitude above the curve estimated from the δ-function approximation. The current results imply that under the same conditions of telescope performance and sensitivity of the data analysis applied, the amount of observation time needed to be devoted to Arp220 in order to be at the level of confirming or rejecting the predictions from the model presented in Section 3.2.2 is too high for a detector with a typical duty cycle of about 1000 hours per year. [3]

[3]At the time the proposal of observation of Arp 220 was approved by the MAGIC collaboration, the Blattnig et al. (2000) cross-section approach was the one currently used for the theoretical estimation of the feasibility of detection. Only after the study presented in Appendix B was done we learned that the differential cross section parameterization proposed by Blattnig et al. overpredicts the highest energy pion yield, making the γ-ray emitted spectrum very hard and inducing, if extrapolated to energies above

Table 8.5: Effect of the spectral slope (α) on the most probable energy of the γ-ray images included in each bin of reconstructed SIZE. The quoted errors correspond to 1σ deviation of the gaussian fit to the MC true energy distributions.

SIZE bin (phe)	E(α=2.6) (GeV)	E(α=2.5) (GeV)	E(α=2.4) (GeV)	E(α=2.3) (GeV)	E(α=2.2) (GeV)	E(α=2.1) (GeV)	E(α=2.0) (GeV)	ΔE (%)	mean E (GeV)
100 - 200	96 $\pm$ 35	97 $\pm$ 35	98 $\pm$ 35	101 $\pm$ 35	102 $\pm$ 36	103 $\pm$ 36	104 $\pm$ 36	8.6	100 $\pm$ 36
200 - 400	155 $\pm$ 51	156 $\pm$ 52	158 $\pm$ 51	161 $\pm$ 52	163 $\pm$ 52	164 $\pm$ 54	166 $\pm$ 54	6.9	161 $\pm$ 54
400 - 800	264 $\pm$ 81	266 $\pm$ 83	271 $\pm$ 84	274 $\pm$ 84	277 $\pm$ 84	280 $\pm$ 85	283 $\pm$ 85	6.8	274 $\pm$ 86
800 - 1600	447 $\pm$ 145	452 $\pm$ 144	457 $\pm$ 143	462 $\pm$ 141	469 $\pm$ 144	474 $\pm$ 144	479 $\pm$ 143	6.9	463 $\pm$ 146
1600 - 3200	739 $\pm$ 272	750 $\pm$ 270	760 $\pm$ 269	770 $\pm$ 267	788 $\pm$ 274	798 $\pm$ 274	808 $\pm$ 273	9.0	773 $\pm$ 284
3200 - 6400	1280 $\pm$ 477	1312 $\pm$ 483	1332 $\pm$ 481	1350 $\pm$ 486	1370 $\pm$ 484	1389 $\pm$ 481	1429 $\pm$ 516	11.0	1352 $\pm$ 497

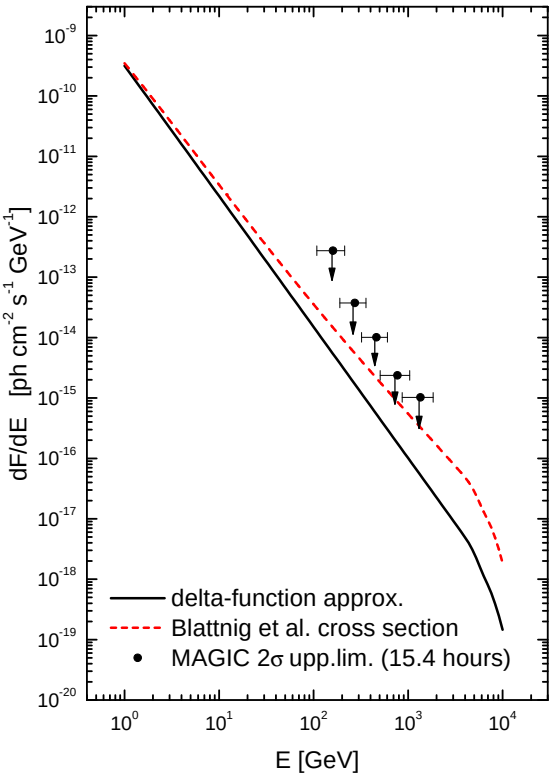

Figure 8.7: Upper limits to the differential γ-ray flux of Arp 220. The curves represent the theoretical predictions, in black using the δ-function approximation and in red dashed using the cross section proposed by Blattnig et al. (2000), extrapolated at high energies. The latter overestimates the flux, as discussed earlier in this Thesis.

In view of these results, and despite the scientific interest of the detection of the closest ultra-luminous infrared galaxy, we deem that this source should not be a prime target for observation with MAGIC in the future.

few hundreds of GeV, a significant overestimation of the γ-ray flux.

Chapter 9

MAGIC observations of TeV J2032+4130

The results of the analysis of 8.7 hours of observation of TeV J2032+4130 with the MAGIC Telescope are summarized. No significant excess was observed for the sample of data analyzed. Upper limits to the differential γ-ray flux, based on the sensitivity extract from the Crab Nebula data analysis, have been set.

9.1 Characteristics of the source and previous observations

In 2002 the HEGRA collaboration reported the serendipitous discovery of a TeV source in the Cygnus region (Aharonian et al. 2002), when analyzing data originally devoted to the microquasar Cyg X-3 and the EGRET source GeV J2035+4214. About 113 hours of data recorded during 3 years of regular observations (from 1999 to 2001) were analyzed. The detection was confirmed (Aharonian et al. 2005d) by follow-up observations (about 158 hours) carried out during the final season of operation of the HEGRA array (2002). A summary of the HEGRA final results for the spectrum is presented in Table 9.1.

Although it is apparent that the integral fluxes (for $E > 1$ TeV) derived from the first and the follow-up data samples differ by about 40%, the statistical errors, which are dominated by contributions near 1 TeV, suggest that this difference is not significant ($\sim 1\sigma$). Using all data (1999 to 2002) this source was determined as steady in flux over the four years of data taking, extended, with radius $6.2 \pm 1.2 \pm 0.9$ arcmin, and exhibiting a hard spectrum with photon index ~ -1.9 (Aharonian et al. 2005d). Its integral flux above energies $E > 1$ TeV amounts to $\sim 5\%$ of the Crab, assuming a Gaussian profile for the intrinsic source morphology. There is no obvious counterpart at radio, optical or X-ray energies (Butt et al. 2003, Mukherjee et al. 2003), leaving TeV J2032+4130 presently unidentified. It was, in fact, the first unidentified source found at TeV energies, before the set of discoveries brought out by the HESS array in 2004 and 2005.

Interestingly, earlier claims for a TeV source consistent with the HEGRA position were reported by other experiments. The Crimean group (using the Čerenkov imaging technique) reported a significant excess ($\sim +6.0\sigma$ pre-trial) at about 0.7° north of Cygnus X-3 from a two-dimensional study of data taken in 1993 (Neshpor et al. 1995). Flaring episodes coincident with a Cyg X-3 radio flare at energies above 40 TeV (Merck 1993, Krawczynski 1995) positionally consistent with the HEGRA COG have been also reported. Recently, after the HEGRA discovery claim, the Whipple collaboration also reported an

Table 9.1: Summary of the HEGRA final results for TeV J2032+4130

Spectral Cuts: Differential points

Energy E(TeV)	Flux $(E)^a$	Flux^a Error(E)	s	b	S^b
— 1999 to 2001 Dataset §1(120.5 h) —					
1.05	1.70	1.24	130	678	**+3.0**
1.82	1.94	0.91	107	531	**+3.1**
3.16	0.37	0.27	57	323	**+1.4**
5.50	0.30	0.11	33	117	**+3.2**
9.55	0.09	0.04	13	34	**+2.8**
— 2002 Dataset §2(157.8 h) —					
1.05	19.90	16.57	153	885	**+2.1**
1.82	1.85	1.56	152	913	**+1.7**
3.16	0.85	0.28	107	513	**+3.4**
5.50	0.28	0.10	44	174	**+3.2**
9.55	0.07	0.04	17	51	**+2.8**
— All Data (278.3 h) —					
1.05	11.98	10.80	283	1563	**+3.6**
1.82	1.89	0.97	259	1444	**+3.3**
3.16	0.64	0.20	164	836	**+3.6**
5.50	0.29	0.07	77	291	**+4.5**
9.55	0.08	0.03	30	85	**+3.9**

a: Flux and Errors in units $\times 10^{-13}$ ph cm^{-2}s^{-1} TeV^{-1}

b: Significance from Li&Ma using s, b and a normalization of 0.143

Fitted Spectrum: Pure Power-Law

dN/dE	=	$N\ (E/1\,\mathrm{TeV})^{-\gamma}$ ph cm^{-2} s^{-1} TeV^{-1}
— 1999 to 2001 Dataset §1(120.5 h) —		
N	=	$4.1\ (\pm 2.1_{\mathrm{stat}} \pm 1.3_{\mathrm{sys}}) \times 10^{-13}$
γ	=	$1.7\ (\pm 0.3_{\mathrm{stat}} \pm 0.3_{\mathrm{sys}})$
— 2002 Dataset §2(157.8 h) —		
N	=	$9.3\ (\pm 2.9_{\mathrm{stat}} \pm 1.4_{\mathrm{sys}}) \times 10^{-13}$
γ	=	$2.1\ (\pm 0.2_{\mathrm{stat}} \pm 0.3_{\mathrm{sys}})$
— All Data (278.3 h) —		
N	=	$6.2\ (\pm 1.5_{\mathrm{stat}} \pm 1.3_{\mathrm{sys}}) \times 10^{-13}$
γ	=	$1.9\ (\pm 0.1_{\mathrm{stat}} \pm 0.3_{\mathrm{sys}})$

Integral Flux^a (E>1 TeV)

— 1999 to 2001 Dataset §1(120.5 h) —		
$F(E > 1\,\mathrm{TeV})$	=	$5.86\ (\pm 3.91_{\mathrm{stat}})$
— 2002 Dataset §2(157.8 h) —		
$F(E > 1\,\mathrm{TeV})$	=	$8.45\ (\pm 3.05_{\mathrm{stat}})$
— All Data (278.3 h) —		
$F(E > 1\,\mathrm{TeV})$	=	$6.89\ (\pm 1.83_{\mathrm{stat}})$

a: Flux and Errors in units $\times 10^{-13}$ ph cm^{-2}s^{-1}

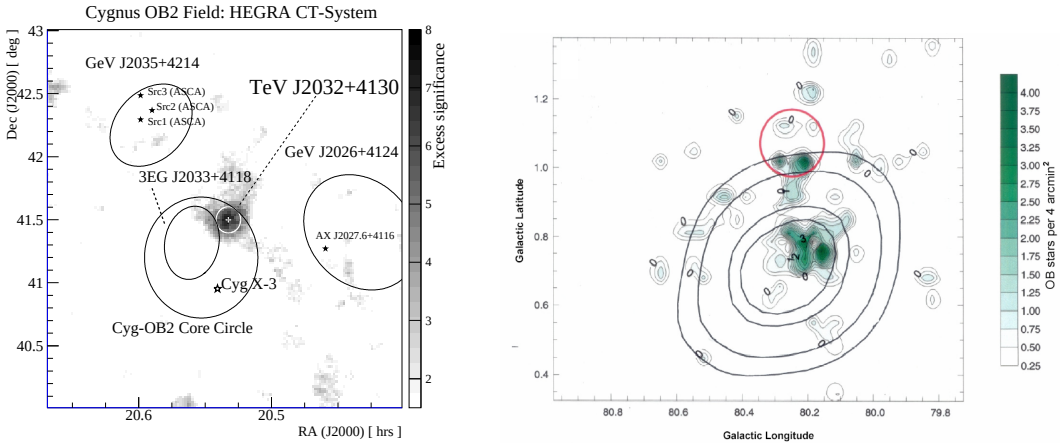

Figure 9.1: Left: From Aharonian et al. (2005d). Skymap of event excess significance from all HEGRA IACT-System data centered on TeV J2032+4130 ($3.0° \times 3.0°$ FoV). Nearby objects are indicated (EGRET sources with 95% contours). The TeV source centre of gravity with statistical errors, and the intrinsic size (standard deviation of a 2D Gaussian, σ_{src}) are indicated by the white cross and white circle, respectively. Right: From Butt et al. (2003). 110 cataloged OB stars in Cyg OB2 shown as a surface density plot (stars per 4 arcmin2). Note that many stars in Cyg OB2 remain uncatalogued, the total number of OB stars alone is expected to be ~ 2600, some of which will be coincident with the HEGRA source position (Knodlseder 2002). Although the extinction pattern towards Cyg OB2 may control the observed surface density of OB stars, it is generally assumed that the observed distribution of OB stars already tracks the actual distribution. If so, models relating the star density with the TeV source, as those discussed earlier in this Thesis, could have an additional appealing. The thick contours show the location probability (successively, 50%, 68%, 95%, and 99%) of the non-variable EGRET source 3EG 2033+4118. The red circle outlines the extent of the TeV source.

excess at the position of the HEGRA unidentified source ($+3.3\sigma$) in their archival data of 1989 and 1990 (Lang et al. 2004). However, as it is discussed below, these results are in conflict with the HEGRA estimates of flux level and steady nature of the TeV source, assuming they all have the same origin.

The TeV J2032+4130 unidentified source lies in the direction of the star-forming region Cygnus OB2. Figure 9.1 shows two skymaps of the region, representing detection significance as measured by the HEGRA system (left panel) and density of OB stars (right panel). The excess signal is clearly positioned a the edge of the error circle of the 3EG J2033+4118 source and of the core circle of the extremely dense Cygnus OB2 stellar association, while it is coincident with a outlying enhancement of the star density.

Multiwavelength observations of the region suggest a hadronic origin for the γ-ray emission (Butt et al. 2003, Aharonian et al. 2005d), although at the moment they do not completely rule out the possibility of a leptonic origin (see Figure 9.2). If the hadronic origin is confirmed by subsequent observations (implying the presence of protons with

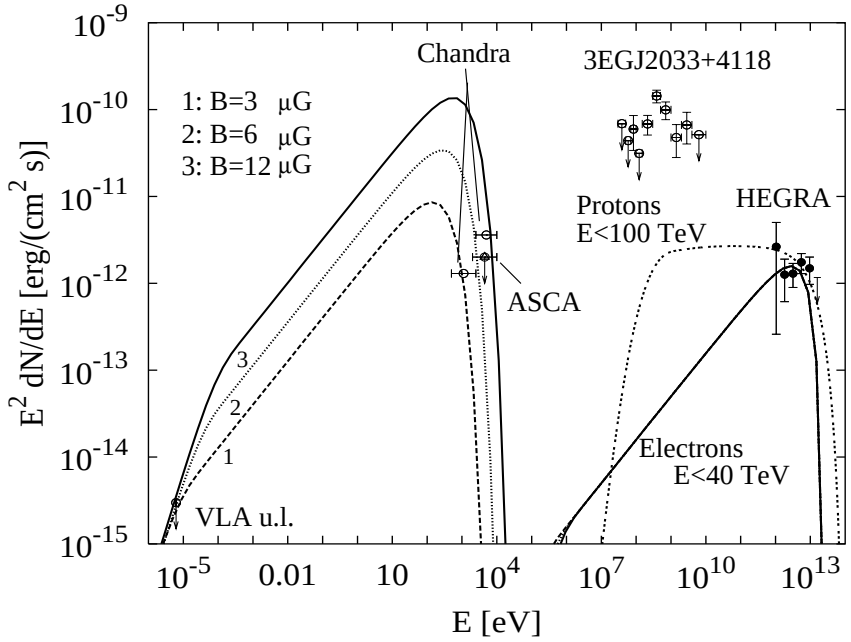

Figure 9.2: Spectrum of TeV J2032+4130 measured by HEGRA (Aharonian et al. 2005d) compared with simple, purely hadronic (protons E<100 TeV) and leptonic (electrons E<40 TeV) models. Upper limits, constraining the synchrotron emission (leptonic models), are from VLA and Chandra (Butt et al. 2003) and ASCA (Aharonian et al. 2002) observations. In the model, a minimum energy $\gamma_{min} \sim 10^4$ is chosen to meet the VLA upper limit. EGRET data points are from the 3rd EGRET catalogue. Taken from Aharonian et al. (2005d).

energies of $\sim$ 100 TeV), this would establish that OB associations compete with supernova remnants as the dominant sites for cosmic ray production in the Galaxy.

The average flux detected in 1989-1990 by Whipple ($\sim$ 12% of the Crab for E>600 GeV) is clearly well above the average steady flux reported by HEGRA over the four year observation period 1999-2002 ($\sim$ 5% of the Crab for E>1 TeV), but substantially below that reported by the Crimea group in 1993 ($\sim$ 1.7 Crab Units for E>1 TeV). Neither the Whipple nor the HEGRA experiments find any evidence for variability within their individual datasets. The large differences between the detected flux levels suggest episodic emission from TeV J2032+4130. However, variability is difficult to reconcile with the extended nature of the source as seen by HEGRA.

9.2 Data sample

Observations of TeV J2032+4130 with the MAGIC Telescope have been carried out during 2005. These observations were scheduled exclusively during moon time over several months from the end of June until mid November 2005. Table 9.2 reviews the characteristics of the data samples. As can be seen in the Table, the data sample is quite inhomogeneous in what refers to observation conditions. The zenith angle ranges

from culmination (about 13°) up to relatively large values ($\sim$ 50°). The mean DC current level registered in the PMTs goes from the typical values of normal moonless observations ($\sim$ 1μA) up to 6μA. For those nights affected by strong moonlight the discriminator thresholds were increased respect to the settings which are standard in galactic observations (40 a.u.). Besides the performance of the telescope was not stable during the five data taking periods involved in the observations. This heterogeneity of the sample makes the analysis more difficult. Yet, in the absence of a rigorous study of the moonlight influence on the sensitivity of the telescope and since Crab Nebula data was not available under strong moonlight circumstances we have restricted our analysis only to TeV J2032+4130 data taken under dim moonlight. This implies then that the analysis of the Crab Nebula data with moderate moon presented in Chapter 7 can be used as a reference to estimate the telescope sensitivity.

The following conditions were imposed to ensure the quality and homogeneity of the data sample:

1. Mean trigger rate above 200 Hz.
2. Mean DC current level at the inner PMTs lower than 2μA.
3. Observation zenith angle below 30°.
4. Good weather and atmospheric conditions.

From a total of about 28 hours of observations, only 8.7 hours of ON data runs have been finally considered in this Thesis under the strict criterion adopted. As reviewed in Table 9.2 most of the runs were discarded from this first analysis due to high moonlight conditions ($\sim$ 12.4 hours), and/or due to large zenith angle observations ($\sim$ 9.2 hours), and/or due to abnormal low trigger rate ($\sim$ 9.5 hours), and/or due to weather unstable conditions ($\sim$ 6.5 hours). The specific reasons for the exclusion of ON data runs for each of the nights are given in the Table in the 'selected runs' column, within parenthesis. Frequently a set of runs has been discarded due to more than one condition.

9.3 Data quality checks

In this Section, analogously to previous Chapters, the checks performed to ensure the quality of the selected data are briefly reviewed.

9.3.1 Event rate

Figure 9.3 shows the event rate for the data runs considered for the analysis of TeV J2032+4130, before and after image cleaning. The data taken during September and October 2005 was discarded by means of this check, as the mean trigger rate drops to about 150 Hz. As already mentioned, the rate reduction seems not to be related to a degradation of the telescope focusing (see Appendix E), but may be attributed to a reduction of the total reflecting area caused by mirror damage during the hot summer months. As the situation is not fully understood we have decided not to include the data of September and October.

Table 9.2: Features of the data from TeV J2032+4130 ON and OFF observations with the MAGIC Telescope. See Table 7.1 for a more detailed description of the columns content. Numbers in parenthesis refer to the failed criterium for inclusion of the runs in the analyzed sample.

Date	Weather	Ext.Coef. (mag)	ZA (°)	Culm.?	Rate (Hz)	Tobs (min)	DT (a.u.)	DC (μA)	Online A. used?*	selected runs	Eff.Tobs (min)
TeV J2032+4130											
30/06/2005	OK	0.073	12.8 - 23.0	YES	225	179	40	1.00 - 1.98	NO	59785-808,10-31	175.13
01/07/2005	OK	0.077	12.8 - 22.0	YES	228	116	40	1.12 - 1.50	NO	59905-36	113.57
03/07/2005	OK	0.081	15.1 - 25.0	NO	226	67	40	1.07 - 1.21	NO	60125-44	67.02
31/07/2005	OK	0.092	20.4 - 48.3	NO	219	146	40	1.10 - 1.48	YES	(3) 62923-40	55.17
02/08/2005	OK	0.095	40.0 - 50.4	NO	193	57	40	1.07 - 1.15	YES	(3)	0.00
11/09/2005	OK	–	12.8 - 15.1	YES	142	54	40	1.56 - 2.10	NO	(1)	0.00
12/09/2005	OK	–	12.8 - 18.7	YES	140	113	50-48	2.15 - 3.41	NO	(1,2)	0.00
13/09/2005	RH[a]	0.108	12.8 - 28.8	YES	123	146	55	3.30 - 4.72	NO	(1,2,4)	0.00
11/10/2005	OK	0.095	13.6 - 45.3	NO	173	183	50-45	1.57 - 3.11	YES	(1,2,3)	0.00
12/10/2005	OK	0.107	14.1 - 23.6	NO	147	72	57-60	4.67 - 5.00	NO	(1,2)	0.00
04/11/2005	RH[b]	0.103	25.0 - 38.2	NO	214	75	40	1.14 - 1.17	NO	(3) 74016-24	33.15
05/11/2005	OK[c]	0.078	17.1 - 23.3	NO	240	40	40	1.10 - 1.12	PART	74186-89,92,98-99	21.37
06/11/2005	OK	0.108	33.1 - 40.0	NO	218	40	40	1.20 - 1.21	YES	(3)	0.00
07/11/2005	OK	0.085	18.3 - 44.7	NO	222	147	40	1.14 - 1.69	PART	(3) 74583-91,95-98,00-01,04-05	57.41
08/11/2005	clouds	0.134	19.5 - 37.8	NO	177	91	45	2.61 - 3.79	YES	(1,2,3,4)	0.00
09/11/2005	clouds	–	21.2 - 49.2	NO	128	132	55	3.97 - 6.25	PART	(1,2,3,4)	0.00
18/11/2005	RH[d]	0.099	25.5 - 30.0	NO	249	25	52	4.11 - 6.28	YES	(2,4)	0.00
TOTAL:						1683					522.82
Off TeV 2032											
02/07/2005	OK	0.074	12.8 - 18.8	YES	222	98	40	0.86 - 1.09	YES	60018-43	94.42
04/07/2005	OK	0.080	19.3 - 21.5	NO	230	17	40	0.96	NO	60275-79	16.58
11/09/2005	OK	–	12.9 - 15.6	NO	137	38	40	0.98 - 1.30	YES	(1)	0.00
12/09/2005	OK	–	18.1 - 24.4	NO	138	45	48	1.12 - 1.76	NO	(1)	0.00
13/09/2005	RH[e]	0.108	27.5 - 35.3	NO	101	48	55	1.31 - 2.65	NO	(1,2,3,4)	0.00
02/11/2005	OK	0.086	24.4 - 37.2	NO	217	72	40	0.94 - 0.96	NO	(3) 71826-31,33-36,38-39,42-43	31.38
06/11/2005	OK	0.108	15.5 - 28.9	NO	234	80	40	1.05 - 1.26	YES	74377-85,88-96,99-03	80.20
TOTAL:						398					222.58

* 'YES' stands for online analysis output files used for the analysis; 'PART' means that a sizable amount of online analysis data runs were discarded because they present abnormal rates after cleaning; 'NO' indicates that recalibrated data runs have been used instead.
Comments regarding the weather: [a] ∼40%, later rain; [b] unstable; [c] windy; [d] ∼80%; [e] increasing, clouds

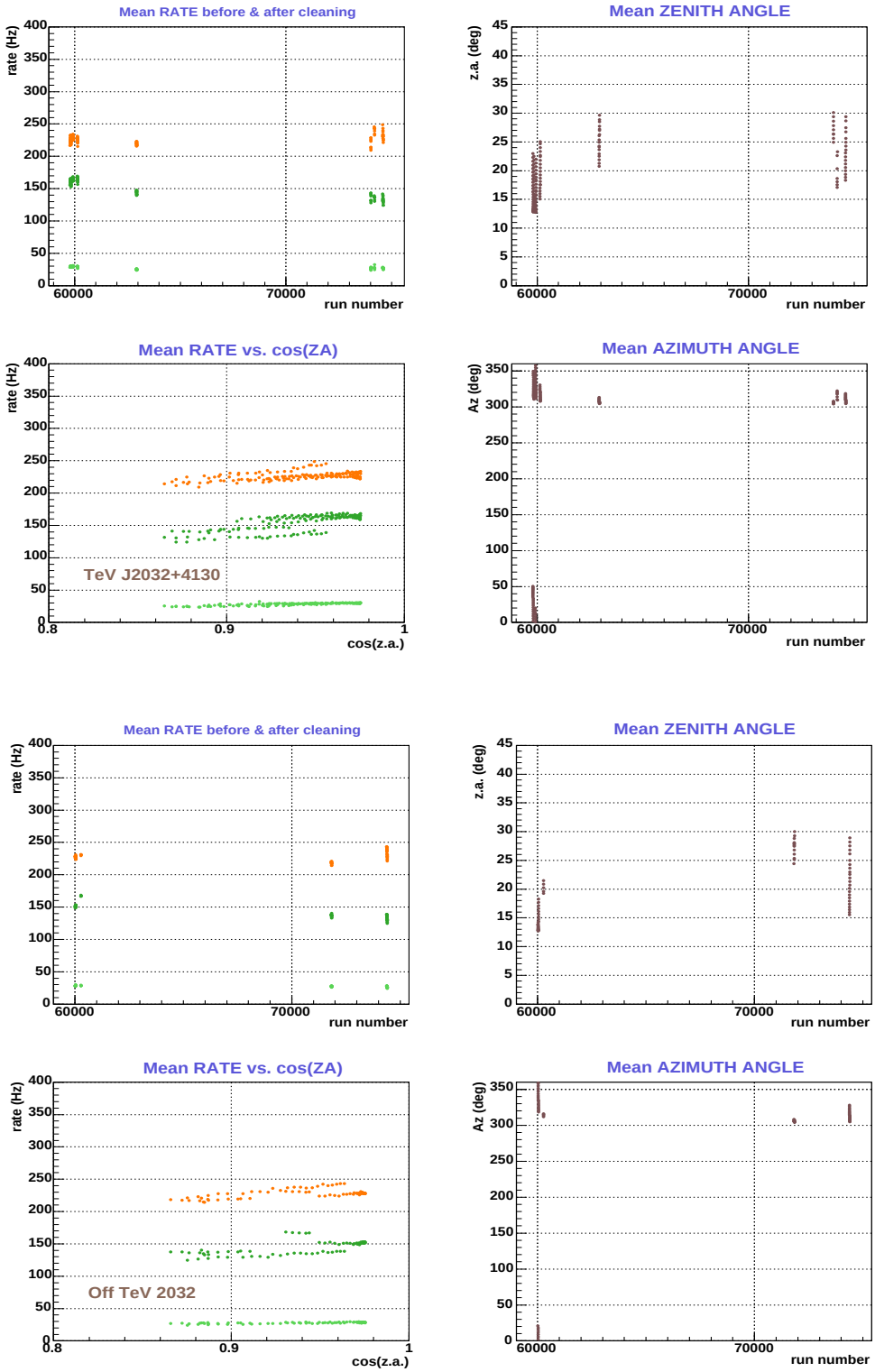

Figure 9.3: Each point in the top (bottom) graph is the mean rate of events for each data run in the ON (OFF) data sample used for the TeV J2031+4130 analysis. In orange, trigger rates; in dark green, rates after image cleaning; and in light green, rates surviving the image cleaning but with a SIZE above 400 phe.

9.3.2 Hillas parameter distributions

Figure 9.4 shows, as example, the good consistency of the WIDTH distributions of the TeV J2032+4130 ON data sample for all the analyzed data taking nights. As for the rest of data samples, no additional runs were discarded by means of this check. Figure 9.5

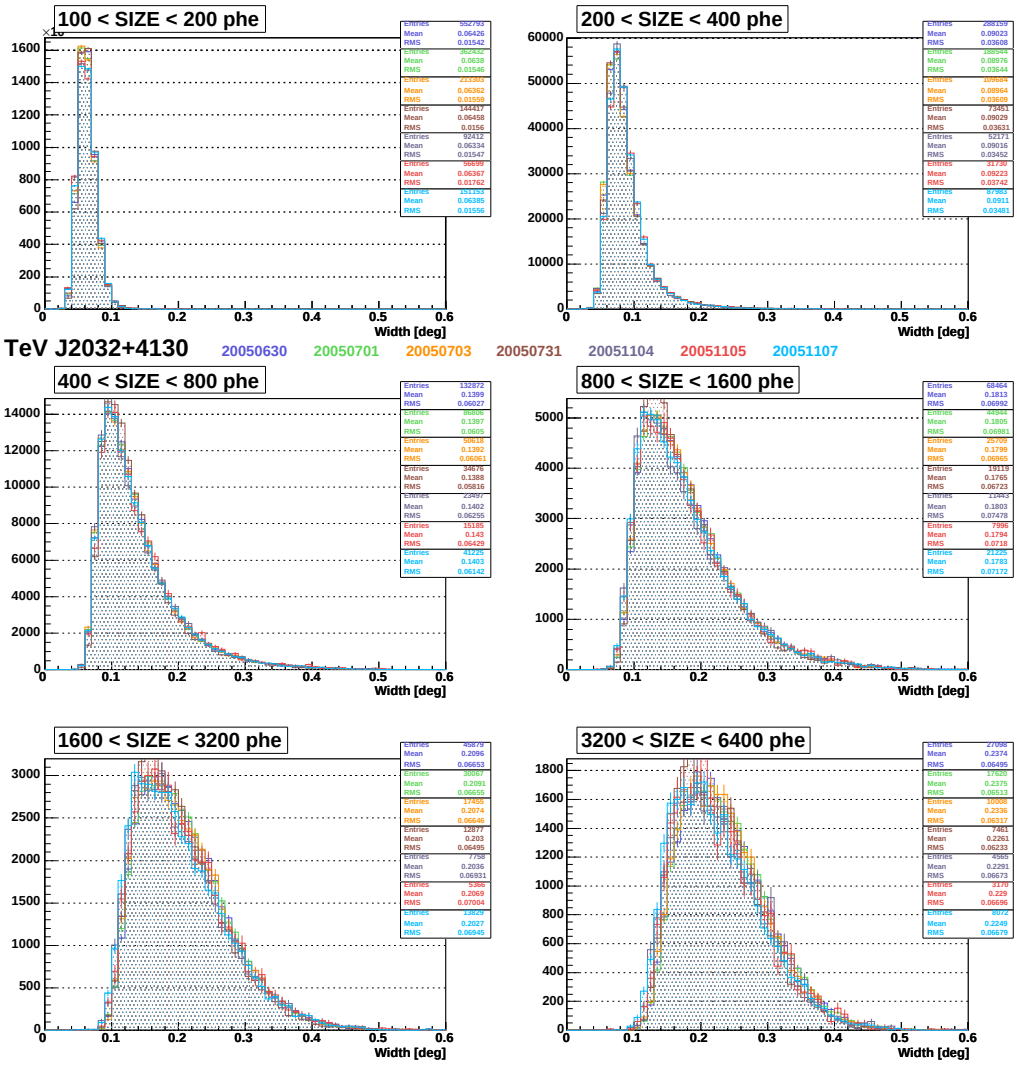

Figure 9.4: The WIDTH distribution for different bins of SIZE and all the days of the TeV J2032+4130 ON data analyzed (see the legend for the colors labelling). Good agreement is observed.

shows that the ON and OFF data samples are compatible before applying event selection cuts in terms of the distribution of LENGTH, one of the Hillas parameters with higher γ/hadron separation power. Good agreement is observed also for the remaining image parameters used to train the Random Forest.

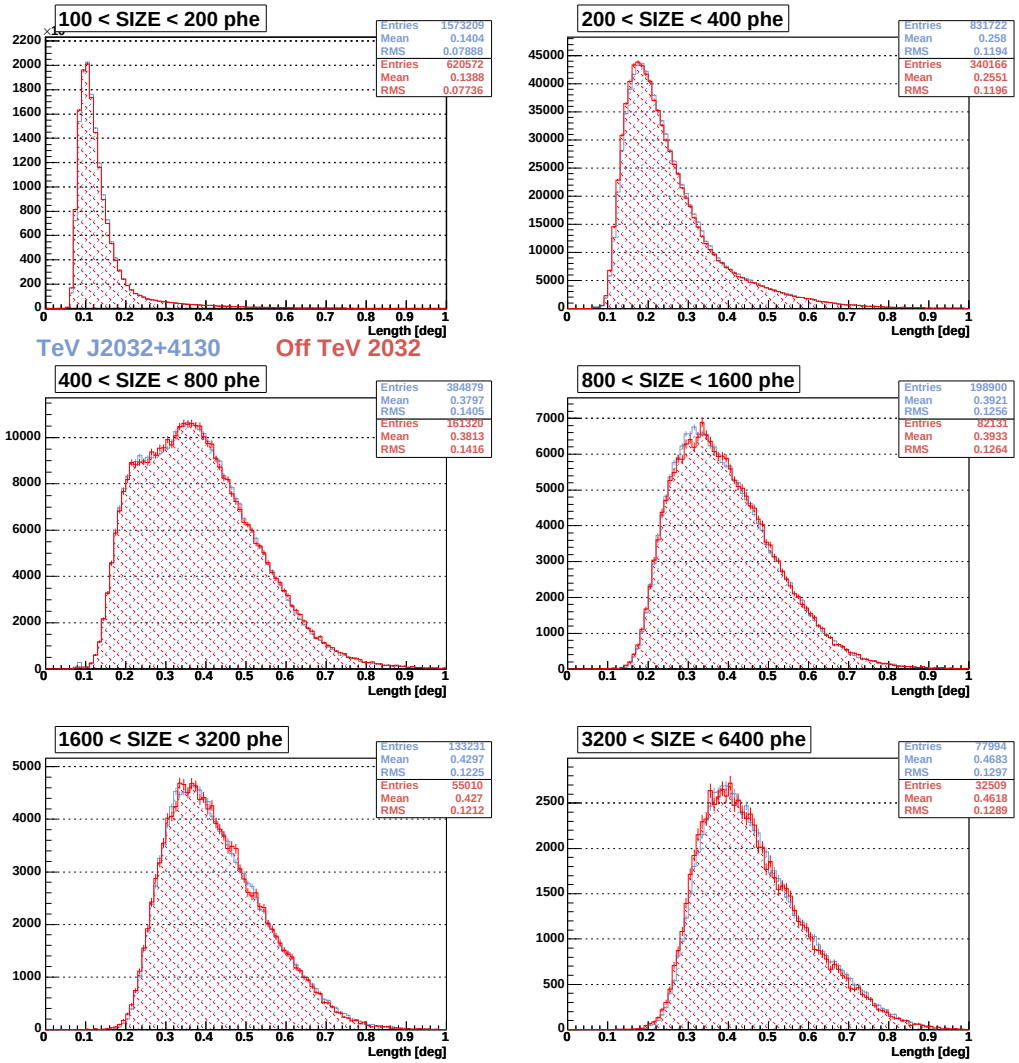

Figure 9.5: The LENGTH distribution for the ON and OFF TeV J2032+4130 data samples and different bins of SIZE. Good agreement is observed.

9.4 ALPHA plots and flux upper limits

Figure 9.6 shows the ALPHA plots which were obtained for the selected data sample of TeV J2032+4130 ON and OFF observations. The ON and OFF distributions match reasonably well within fluctuations, especially for the lower SIZE bins. No significant excess is observed for any of the analyzed SIZE bins. However, interestingly, a positive signal above 2σ over the background has been obtained for the two bins of higher SIZE values, although these results should be taken with caution (see more comments on this below). The numbers are reviewed in Table 9.3.

The upper limits to the flux of TeV J2032+4130 have been calculated out of the sensitivity obtained in the analysis of the Crab Nebula moon data sample, as explained in Section 6.7.3. Table 9.4 summarizes the results[1], and Figure 9.7 schematically shows

[1]Note that the extended character of the source, as reported by HEGRA, has not been considered in the current upper limits estimation. Assuming a Gaussian profile for the source morphology, HEGRA

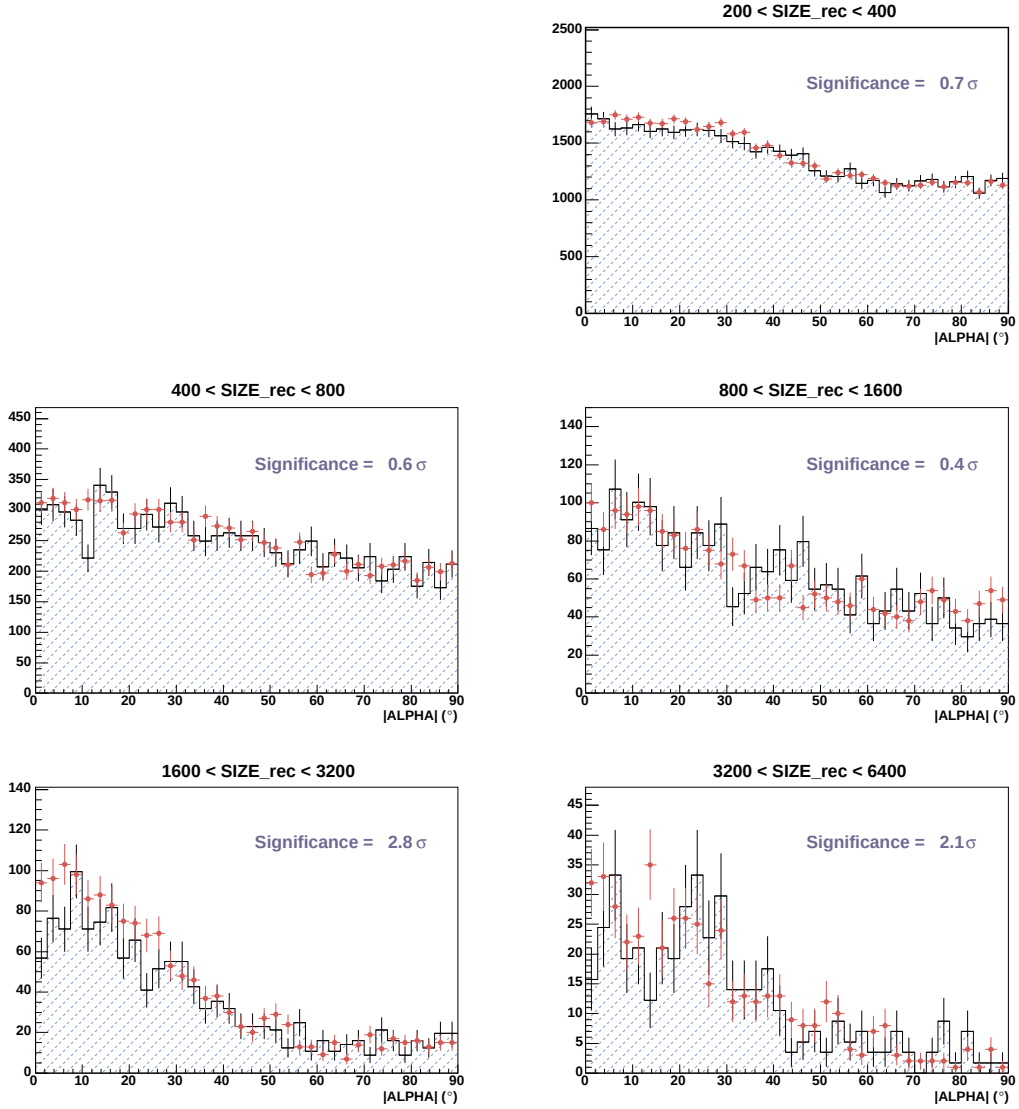

Figure 9.6: ALPHA plots for the TeV J2032+4130 data.

current and previous observations.

There, the blue points correspond to the HEGRA TeV J2032+4130 spectrum reported from the 4 year data set (a total of 278 hours of observation). The orange bar corresponds to the integral flux above 600 GeV reported by Whipple from the reanalysis of 1989-1990 data, which was converted into differential flux under the assumption of a photon index ranging from -1.9 to -2.1, following the HEGRA measurements. The pink bar corresponds to the integral flux above 1 TeV which is claimed by the Crimean group on the basis of the 1993 observations, under the same assumptions for the spectral index. The black points stand for the MAGIC upper limits as derived in this Thesis. These upper limits are in contradiction with the Whipple and Crimean measurements unless the source is variable.

reported a σ value of $0.104^\circ \pm 0.020^\circ$ for its intrinsic size. However, as the extension of TeV J2032+4130 is close to the angular resolution of MAGIC (which will be slightly better than that obtained in Section 7.6 for energies above 1 TeV), we do not expect substantial changes in the estimated sensitivities and upper limits.

Table 9.3: Number of excess and background events and the corresponding significance obtained from the TeV J2032+4130 alpha plots analysis. The value of the significance quoted in parenthesis corresponds to the Li & Ma's approach. The reliability of the excesses is discussed in detailed below.

SIZE bin (phe)	HADR. cut	ALPHA cut (°)	Norm. factor	N.excess events	N.bkg. events	N_σ (σ)
200 - 400	0.32	10.00	2.31	99	6729	0.7 (0.7)
400 - 800	0.20	8.75	2.30	35	907	0.6 (0.6)
800 - 1600	0.14	7.50	2.28	13	268	0.4 (0.4)
1600 - 3200	0.26	6.25	1.78	56	133	2.8 (2.7)
3200 - 6400	0.22	6.25	1.75	24	40	2.1 (2.0)

Table 9.4: 5σ and 2σ upper limits to the differential γ-ray flux of TeV J2032+4130, derived from the sensitivity flux estimated from the analysis of Crab Nebula data taken under moderate moonlight conditions.

SIZE bin (phe)	Sensitivity (% Crab)	Sensitivity ($\times 10^{-14}$ ph cm^{-2} s^{-1} GeV^{-1})	5σ Upp.Limit ($\times 10^{-14}$ ph cm^{-2} s^{-1} GeV^{-1})	2σ Upp.limit ($\times 10^{-14}$ ph cm^{-2} s^{-1} GeV^{-1})
200 - 400	14.74 ± 0.65	44.98 ± 1.98	107.78	43.11
400 - 800	7.07 ± 0.37	5.47 ± 0.29	13.10	5.24
800 - 1600	5.19 ± 0.41	1.03 ± 0.08	2.48	0.99
1600 - 3200	6.62 ± 0.57	0.35 ± 0.03	0.84	0.34
3200 - 6400	8.66 ± 1.21	0.11 ± 0.02	0.26	0.10

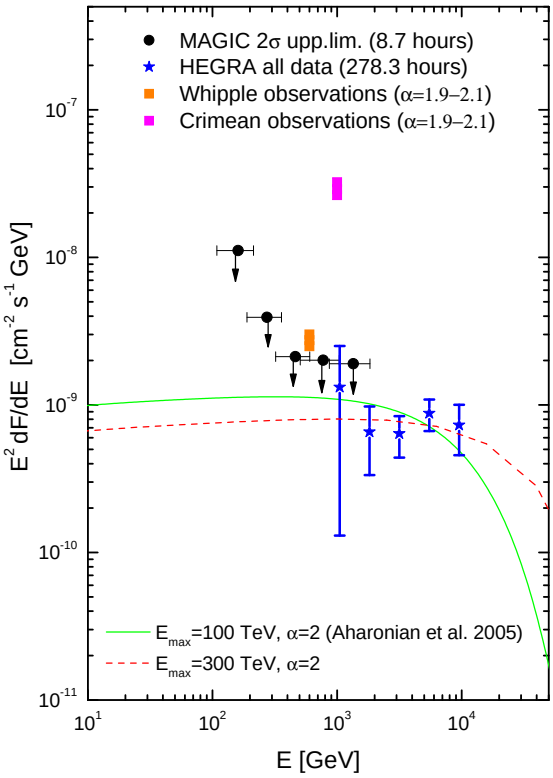

Figure 9.7: MAGIC upper limits to the flux of TeV J2032+4130. The curves represent theoretical hadronic models computed for comparison. HEGRA (stars), Whipple (orange bar) and Crimean (pink bar) observations are also included.

The curves correspond to purely hadronic models which are computed here to show that they can explain both the HEGRA flux points and the MAGIC upper limits under reasonable requirements, for instance, on the fraction of energy of a typical supernova explosion that is available for the acceleration of the parent cosmic ray population. The green curve has been obtained for a cutoff in the primary population of protons at 100 TeV while for the red curve the cutoff is at 300 TeV.

The analysis results in a more that 2 σ significant excess for the highest two SIZE bins. However this excess should be taken with caution. As can be seen in Figure 9.6 the shape of the ALPHA distribution for both the ON and OFF samples is far from being flat. Especially for the highest SIZE bins, there is an enhancement of events at lower values of ALPHA. This effect can be understood because a large fraction of the highest energy showers have values of DIST in excess of 1°, while the trigger region extends only to 1°, so high energy showers trigger more efficiently when they point to the center of the camera (i.e. have low ALPHA values). This represents a problem when we try to estimate the background at low ALPHAs out of a fit to the ALPHA distribution of the ON sample

Table 9.5: The influence of the chosen procedure for the normalization of the ON and OFF ALPHA distributions on the results for the bins of highest SIZE when few statistics is collected.

Normalization	**1600 - 3200 phe**		**3200 - 6400 phe**	
region or procedure	Norm.factor	N_σ (σ)	Norm.factor	N_σ (σ)
30° < |ALPHA| <80°	1.78	2.8	1.75	2.1
20° < |ALPHA| <30°	2.07	1.6	1.40	3.1
70° < |ALPHA| <80°	1.98	1.9	0.92	4.8
Norm.factor = Tobs(ON)/Tobs(OFF)	2.35*	0.6	2.35*	0.8

* Note that, for the lower SIZE bins, the normalization factors obtained considering the number of events in the 30 to 80° ALPHA region is very close to the ratio of observation time.

itself.[2] It is also problematic when we normalize ON and OFF using the number of events between 30 and 80° because this number is lower than the number of events at the signal region.

In order to quantify the systematics, the ON and OFF ALPHA distributions have been normalized using the background at two extreme regions: a region close to the signal region (ALPHA between 20 and 30°) and the outermost region (ALPHA between 70 and 80°). We have also normalized on the ratio of observation times of the ON and OFF samples. This ratio is completely independent of the shape of the ALPHA distributions and should be equivalent to a normalization based in the number of events if the rate of the ON and OFF samples is consistent (see the resultant ALPHA plots in Figure 9.8). The significance of the detections are summarized in Table 9.5 for the four normalization procedures. They vary strongly, suggesting that the detection is an artifact of the normalization method.

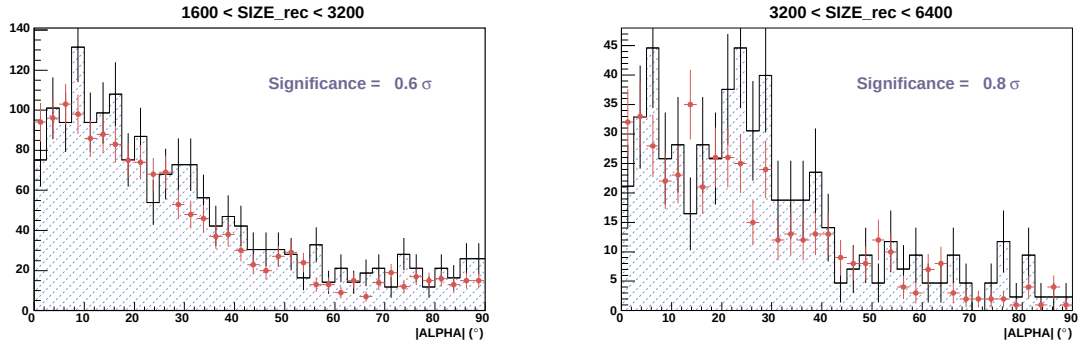

Figure 9.8: The two highest SIZE bins of the TeV J2032+4130 data analysis. ALPHA plots normalized according to the ratio of observation time included in the ON and the OFF data samples.

In addition, it is worth remembering that events are binned according to a reconstructed SIZE parameter that takes into account the value of LEAKAGE2. We have checked that 66% of the events in the bin from 1600 to 3200 phe had an original SIZE lower than 1600 phe. Something similar happens for 72% of the events in the bin from 3200 to 6400 phe.

[2] This approach is commonly used when not enough amount of OFF data is available (i.e., an analytical fit to the ON ALPHA distribution for values above 30° is used and extrapolated to the signal region).

This is another source of systematic effectswhose magnitude may differ for the ON and OFF samples.

9.5 Conclusions

In view of the results of the systematics evaluation, we conclude that no significant signal has been found in the highest SIZE bins and stick to the upper limits that can be found in Figure 9.7. However, these upper limits already constrain the source spectrum at energies lower than those measured by HEGRA and rule out that the source emitted during 2005 at the levels reported by the Whipple or Crimean telescopes.

The basic technical problem in the analysis at the highest energies have turned out to be that the highest energy showers are truncated at the edges of the camera and their trigger efficiency depends on their orientation. We would benefit from an extension of the trigger region up to 1.2-1.3°.

Considering that the upper limits are very close to the spectrum reported by HEGRA we can also conclude that it is crucial to try and include the complete set of 2005 data in a future analysis, and certainly, to extend the observations in 2006.

Chapter 10

Concluding remarks

The study herein presented intended to evaluate the possibility of regions of star formation to appear as sources of γ-rays for the new generation of γ-ray detectors, both ground and space-based, and both from a theoretical and an experimental point of view.

After a positive result from a phenomenological evaluation of the most powerful extragalactic sites of star formation, the detailed modeling of γ-ray emission for the best candidate galaxies has brought out concrete observational conclusions for these objects. The nearest starburst galaxy NGC 253, claimed to be detected by CANGAROO but not yet confirmed (in fact, contradicted at the reported flux level) for the moment by the HESS array, should be detectable by the HESS experiment if reasonable amount of additional observation time is devoted, as the theoretical predicted fluxes are just below the upper limits recently set. In what concerns the closest ultra-luminous infrared galaxy, Arp 220, the study presented here on the more appropriate proton-proton cross section for neutral pion production to be used in predictions of γ-ray emission above hundreds of GeV has shown that the initial prospects for its detection with the MAGIC Čerenkov telescope are no longer theoretically supported, unless a substantial improvement on the sensitivity is achieved. Nevertheless, both galaxies are indeed expected to be detected by GLAST already within its one-year all-sky survey.

Galactic OB associations have also been investigated as plausible γ-ray sources for the current and near future γ-ray detectors. A hadronic emission model which would be able to explain multi-GeV and TeV γ-ray detections with lack of strong lower energy counterparts has been presented. It gains interest on the light of the recent population of TeV unidentified sources discovered by HESS in the Galactic plane. However, although the requirements of the model are reasonably possible, the large uncertainties that exist on the properties and numeric content of OB stellar associations and on their surrounding interstellar medium prevent specific predictions. In terms of the best associations known, the southern cluster Westerlund 1 has been proposed as a good candidate for HESS, whereas Cygnus OB2 (for which already the HEGRA unidentified TeV J2032+4130 source suggests a possible relation with the OB association) appears as the best candidate for the MAGIC telescope northern observatory.

Building upon this theoretical framework, the available data from the first observations of the MAGIC Telescope of regions of star formation has been analyzed. It is to be remarked that the results herein presented did not pretend to be a conclusive analysis yet, but rather a robust first look to the data in order to provide a solid input for deeper analysis and further observations. In the case of Arp 220, the observations carried out by MAGIC have confirmed the conclusions theoretically reached already: the current

performance of the MAGIC Telescope is not enough to detect the γ-ray flux of this ULIRG within a reasonable amount of observation time. In any case, upper limits were imposed. In what refers to TeV J2032+4130, the situation is quite different: an analysis of only 8.7 hours of the available sample sets upper limits already at the level of the flux detected by HEGRA (what denotes the differences in capabilities between these two instruments). Moreover, unless the source presents occasional flaring episodes (not supported by the 4 years of steady HEGRA results), the Whipple and Crimean measurements are in contradiction with the MAGIC upper limits. In the light of these results, we would like to emphasize the interest in devoting deeper observations with the MAGIC telescope of this source, still unidentified, as well as performing a reanalysis of the existing additional data sample which has been preliminarily put aside here for technical reasons. Moreover, MAGIC-II is expected to be operative in 2007. The new telescope will be provided with a larger trigger area and the outer camera region will be equipped mostly with small pixels. This will increase the sensitivity for high energy showers and reduce the systematics. Besides, the operation of both telescopes in coincidence will improve the sensitivity by a factor two. A detection will probably be feasible, at the level of the HEGRA measured flux, within only $\sim$10 hours of observation.

Keeping faith that a modest contribution to the understanding of energetic processes in regions of star formation has been made, and hoping that at least this effort will motivate further and more complete studies, this Thesis ends here.

Appendix A

A numerical approach for multiwavelength modeling

In this Appendix, the set of numerical subroutines used to obtain some of the predictions included in the theoretical Chapters of this Thesis is briefly discussed.

A.1 $\mathcal{Q}$-DIFFUSE flow and concept

Theoretical predictions of this Thesis are mostly obtained with the numerical package $\mathcal{Q}$-DIFFUSE, a code described below, initially developed and first applied by Torres (2004). The aim of this set of numerical codes is to compute γ-ray spectra from astrophysical scenarios, including all energy losses and radiative processes that imply multifrequency emission. This approach tries to reduce as much as possible the number of hypothesis on which the emission model is based, requiring it to reproduce (or comply with) the experimental data available at all wavelengths. In this sense, $\mathcal{Q}$-DIFFUSE provides a self-consistent model of the astrophysical environment.

The logic of the code is shown schematically in Figure A.1. As starting point, an injection spectrum of primary cosmic rays is assumed. Its characteristics are estimated by linking the cosmic rays to the known (local to the source) acceleration processes that may have created them (e.g., supernova remnants induced shocks or collective effects of stellar winds), and thus using the related observational inputs, as the supernova explosion rate. The primary proton population is subject to energy losses (by ionization and pion production) and to escaping out from the emission region through diffusion or convection processes. From the proton steady state (i.e. the solution of the diffusion-loss equation), the computation of the secondaries is done. Secondary electrons and positrons are generated from knock-on interactions and decay of secondary charged pions. The contribution of secondary electrons and positrons is then summed up to the primary electron population, which is assumed to be the same than the proton injection spectrum but by a factor N_e/N_p. The whole electron/positron population is then let to evolve to its steady state, computing the energy losses that it is subject to (synchrotron emission, ionization, bremsstrahlung, inverse Compton and adiabatic losses) and the confinement timescale. The radio spectrum is then evaluated from the steady electrons synchrotron emission, modulated by free-free absorption of the medium plasma electrons. A comparison between the predicted radio flux and the existing data provides a direct feedback to some model parameters that appear in the computation of the electron steady state. They are

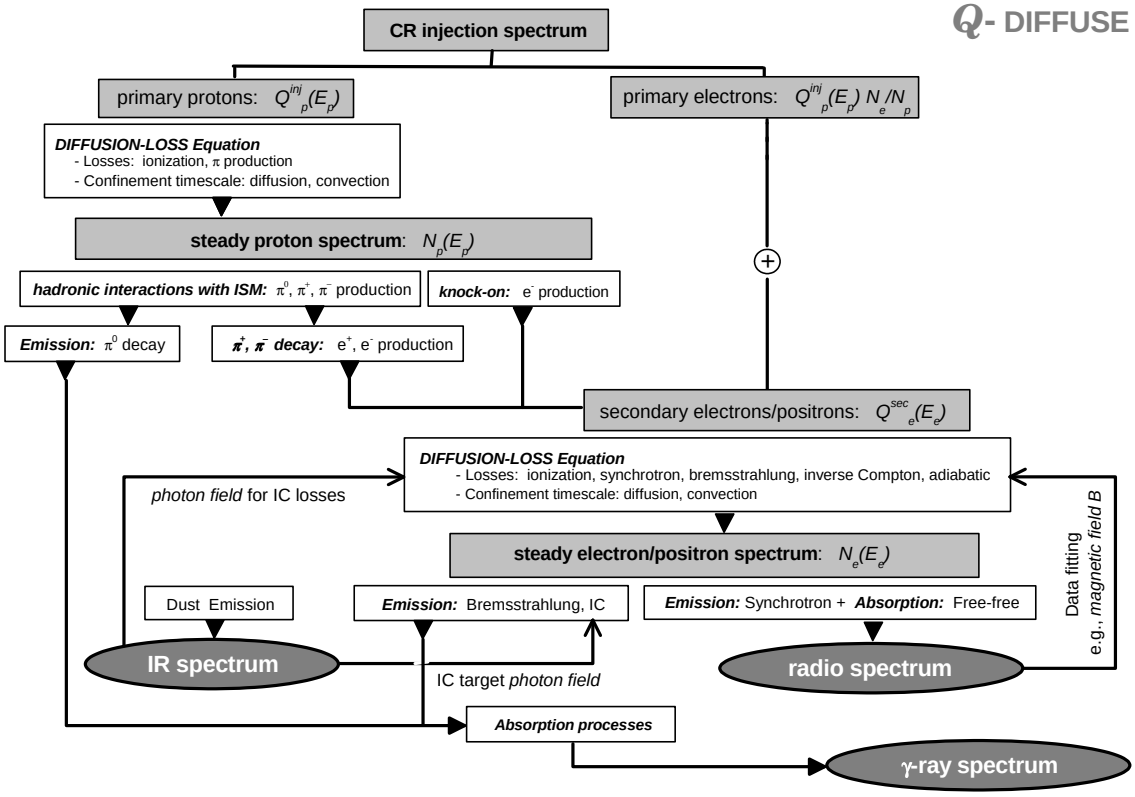

Figure A.1: $\mathcal{Q}$-DIFFUSE flow diagram.

tuned until a good agreement with the measured radio spectrum is achieved. For example, one of the crucial parameters, which indeed is hardly known with good precision in most of the scenarios but plays an important role both in the electron synchrotron energy losses and in the synchrotron radio emission, is the magnetic field. Other parameter crucial in explaining low frequency radio data is the absorption frequency of free-free radiation (alternatively, the emission measure and plasma temperature). These two, are determined within the code until an agreement with observations is reached. Infrared emission from dust existing in the region is also simulated with the parameters that characterize the infrared photon field being adjusted to describe the observational existing data. These photons (in addition to the CMB) are the seed for the inverse Compton process when considering the electron energy losses and the resultant high energy γ-ray emission. Once all the parameters have been fixed and the proton and electron steady populations have been determined, high energy γ-ray emission is evaluated. This includes the decay of neutral pions, which were generated in hadronic interactions of the cosmic rays with the interstellar medium, and leptonically-generated γ-rays, through bremsstrahlung and inverse Compton of the steady electron population.

Results from $\mathcal{Q}$-DIFFUSE were tested against other existing numerical codes, like GALPROP (Strong and Moskalenko 1997) for the neutral pion decay γ-ray emission.

Table A.1: Main symbols used in $\mathcal{Q}$-DIFFUSE, meaning and units.

$b(E)$	rates of energy loss	GeV s^{-1}
$\tau(E)$	confinement timescales	s
$Q(E)$	emissivities	particles GeV^{-1} s^{-1} cm^{-3}
$N(E)$	distributions	particles GeV^{-1} cm^{-3}
$J(E)$	intensities	particles GeV^{-1} cm^{-2} s^{-1} sr^{-1}
$F(E)$	differential fluxes	particles GeV^{-1} cm^{-2} s^{-1}
$F(E > \bar{E})$	integral fluxes above $\bar{E}$	particles cm^{-2} s^{-1}

The leptonic computation were also validated against other codes (see Torres 2004 for details). A good agreement was found for all the predictions in the different energy ranges. Symbols and units of the quantities more frequently used in the code and in this Thesis are summarized in Table A.1. In both the code and this Thesis, energies are given in GeV, variables describing distances in centimeters and time in seconds.

A dedicated follow-up appendix (Appendix B) extensively describes the hadronic γ-ray production from neutral pion decay and presents the related formulae in detail, as this process represents the most important contribution to the γ-ray spectrum in its relevant energy scale for the systems herein studied. The formulae for the rest of physics and other technical details included in $\mathcal{Q}$-DIFFUSE are described in Appendix C.

Appendix B

γ-ray emission from neutral pion decay

In this Appendix, the γ-ray emission produced from neutral pion decay is derived and reviewed. Some of the latest knowledge on the pp cross-section for π^0 production is also summarized. In order to obtain predictions with good reliability in the energy range of γ-ray satellites and ground-based Cherenkov telescopes, a convenient approach for the computation of high energy γ-ray emission is discussed.

B.1 Neutral pion and γ-ray emissivities

High energy cosmic ray nuclei interact with the matter they found when travelling through the interstellar medium. These, basically proton-proton and proton-nuclei interactions involve the production of neutral pions. Emissivity is defined as the number of particles having energies in the range between E and $E+dE$ that are produced per unit of volume and unit of time. In general, as stated by Stecker (1971), the emissivity –also known as source function– $Q(E)$ of any particle type is given by the product of the density of the target nuclei in the medium, the frequency ν of collision per target nucleus and the multiplicity $<\zeta>$ of particles with energy E produced per collision:

$$Q(E) = n\nu <\zeta> \ . \tag{B.1}$$

The frequency of the reaction of interest can be expressed in terms of the interaction differential inclusive cross section $d\sigma/dE$ and the incident intensity of primary particles $J_p(E_p)$ (in units of GeV^{-1} cm^{-2} s^{-1} sr^{-1}). Then, summing up the contribution of the whole incident population, the emissivity is given by:

$$Q(E) = 4\pi n \int_{E_p^{th}(E)}^{E_p^{max}} dE_p \, J_p(E_p) \frac{d\sigma(E, E_p)}{dE} \, , \tag{B.2}$$

in units of GeV^{-1} cm^{-3} s^{-1}, and with E_p^{th} the energy threshold of the reaction to occur. Therefore, for the case of the neutral pions resulting from an incident isotropic intensity of protons, $J_p(E_p)$, which interact with fixed target nuclei with number density n through the reaction $p + p \rightarrow p + p + \pi^0$, the expression for the neutral pion emissivity is the following:

$$Q_{\pi^0}(E_{\pi^0}) = 4\pi n \int_{E_p^{th}(E_{\pi^0})}^{E_p^{max}} dE_p \, J_p(E_p) \frac{d\sigma(E_{\pi^0}, E_p)}{dE_{\pi^0}} \, , \tag{B.3}$$

where E_p^{max} is the maximum energy of the incident protons, $E_p^{th}(E_{\pi^0})$ is the minimum proton energy required to produce a pion with total energy E_{π^0}, and $d\sigma(E_{\pi^0}, E_p)/dE_{\pi^0}$ is the differential inclusive cross section for the production of a pion with energy E_{π^0}, in the laboratory reference frame (LS), due to a collision of a proton of energy E_p with a hydrogen atom at rest.

The neutral pion is an unstable particle, with a lifetime of about $10^{-16}s$, that decays nearly 99% of the times into two γ-ray photons: $\pi^0 \rightarrow 2\gamma$.[1] When the π^0 decays at rest, or equivalently if the process is observed from the center of mass frame[2] (CMS), each γ-ray takes half of the energy of the pion:

$$E_\gamma^{'} = \frac{1}{2} m_{\pi^0} c^2 \,. \tag{B.4}$$

However, neutral pions are seldom created at rest in the LS rather, since they suffer no energy losses by ionization, they usually decay in flight. Therefore, as seen from the LS frame, the energy of the γ-ray is boosted by a factor β_{π^0}, being β_{π^0} the velocity of the pion in units of c.

In the CMS frame, the two γ-rays are emitted in opposite directions, with angles θ and $\pi - \theta$, being θ the angle of the γ-ray emission with respect to the pion velocity direction. Therefore, in the LS frame, the energy of a γ-ray photon emitted at an angle θ can be computed with a Lorentz transformation from the CMS frame to the LS frame, transformation described by a boost, assumed to happen along the x-axis[3]:

$$E_\gamma = \Gamma_{\pi^0} E_\gamma^{'} - \beta_{\pi^0} \Gamma_{\pi^0} (p_\gamma^{'})_x c = \frac{E_\gamma^{'}(1 + \beta_{\pi^0} \cos\theta)}{\sqrt{1 - \beta_{\pi^0}^2}} \,, \tag{B.6}$$

where relations $(p_\gamma^{'})_x = p_\gamma^{'} \cos\theta$ and $p_\gamma = E_\gamma / c$ –for photons–, have been used.[4] The angular distribution of the produced γ-rays is isotropic in the CMS, so the number of γ-rays emitted between θ and $\theta + d\theta$ is given by:

$$n_\gamma(\theta) d\theta = \sin\theta \, d\theta \,, \tag{B.7}$$

The number of γ-rays distributed in θ should sum up the same than those accounted for when distributed in energy. Therefore, using Equation (B.7) and the derivative of

[1] The remaining 1% of the times the neutral pion decay in an electron-positron pair and a photon: $\pi^0 \rightarrow e^+ e^- \gamma$. Other decay channels have negligible branching ratios (at least five orders of magnitude smaller) compared to these two main channels.

[2] CMS quantities will be quoted with a prime here on, whereas quantities without prime will refer to the LS frame.

[3] A boost is a Lorentz transformation between two reference frames moving with constant velocity v with respect to each other. If the x-axis is chosen such the relative movement of both reference frames runs along it, the boost that will transform the four-momentum of a particle, $p^\mu = (E, p_x c, p_y c, p_z c)$, is described by the following matrix:

$$\Lambda = \begin{pmatrix} \Gamma & -\beta\Gamma & 0 & 0 \\ -\beta\Gamma & \Gamma & 0 & 0 \\ 0 & 0 & 1 & 0 \\ 0 & 0 & 0 & 1 \end{pmatrix} \,, \tag{B.5}$$

where the Lorentz factor of a particle $\Gamma = 1/\sqrt{1 - \beta^2}$ is also known as boost factor, and $\beta = v/c$ is the boost velocity in units of c.

[4] Useful relations when describing relativistic particles: $E = m\Gamma c^2$, $| \overrightarrow{p} | = m\Gamma v$, and $E^2 = (| \overrightarrow{p} | c)^2 + (mc^2)^2$. The energy of massless particles can be computed as $E = | \overrightarrow{p} | c$.

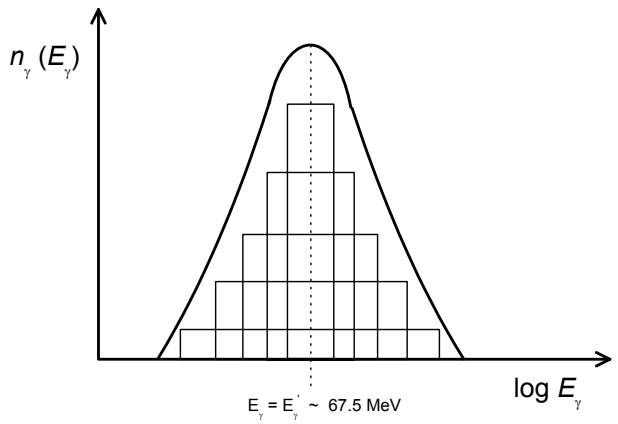

Figure B.1: Scheme of the γ-ray espectral distribution expected from the decay of a multienergetic population of neutral pions.

Equation (B.6), the energy distribution of γ-rays in the observer LS frame can be found:

$$n_\gamma(E_\gamma) = n_\gamma(\theta)\frac{d\theta}{dE_\gamma} = \frac{\sin\theta\, d\theta}{\frac{E'_\gamma \beta_{\pi^0}\sin\theta\, d\theta}{\sqrt{1-\beta^2_{\pi^0}}}} = \frac{\sqrt{1-\beta^2_{\pi^0}}}{E'_\gamma \beta_{\pi^0}}\,. \tag{B.8}$$

Note that the energy distribution of γ-rays emitted from the decay of a monoenergetic population of neutral pions is a flat distribution, i.e., energy independent, being symmetric around $E_\gamma = E'_\gamma = \frac{1}{2}m_{\pi^0}c^2$ if it is expressed in logarithmic scale. From Equation (B.6), the energy range to which the γ-ray emission is restricted can be easily obtained. The less energetic γ-rays will be emitted opposite to the pion incident direction ($\theta = \pi$), whereas the more energetic ones will travel in the same direction than the pion ($\theta = 0$):

$$E^{min}_\gamma = E'_\gamma \frac{1-\beta_{\pi^0}}{\sqrt{1-\beta^2_{\pi^0}}} = \frac{1}{2}m_{\pi^0}c^2\sqrt{\frac{1-\beta_{\pi^0}}{1+\beta_{\pi^0}}}\,, \tag{B.9}$$

$$E^{max}_\gamma = E'_\gamma \frac{1+\beta_{\pi^0}}{\sqrt{1-\beta^2_{\pi^0}}} = \frac{1}{2}m_{\pi^0}c^2\sqrt{\frac{1+\beta_{\pi^0}}{1-\beta_{\pi^0}}}\,. \tag{B.10}$$

Therefore, the energy distribution of γ-rays that results from the decay of a population of neutral pions with different β_{π^0} values will be the addition of many of such symmetric flat spectrum. Hence, the final distribution presents a maximum at the energy $\frac{1}{2}m_{\pi^0}c^2 \sim 67.5$ MeV, as can be seen schematically in Figure B.1.

Equation (B.8) can be expressed as a function of the total energy of the pion (use $E_{\pi^0} = m_{\pi^0}\Gamma_{\pi^0}c^2$, $E_{\pi^0} = \Gamma_{\pi^0}E'_{\pi^0}$ from the boost transformation from CMS to LS frame, and $E'_{\pi^0} = m_{\pi^0}c^2 = 2E'_\gamma$):

$$n_\gamma(E_\gamma) = \frac{2}{\sqrt{E^2_{\pi^0} - m^2_{\pi^0}c^4}}\,. \tag{B.11}$$

Then, the γ-ray emissivity from π^0 decay is obtained from the neutral pion emissivity, Q_{π^0}, multiplied by the energy distribution of γ-ray emitted by each π^0, and integrating

over all pion energies:

$$Q_\gamma(E_\gamma)_{\pi^0} = 2\int_{E_{\pi^0}^{min}(E_\gamma)}^{E_{\pi^0}^{max}(E_p^{max})} dE_{\pi^0} \frac{Q_{\pi^0}(E_{\pi^0})}{\sqrt{E_{\pi^0}^2 - m_{\pi^0}^2 c^4}}\,, \tag{B.12}$$

where $E_{\pi^0}^{min}(E_\gamma)$ is the minimum pion energy required to produce a γ-ray photon of energy E_γ, and $E_{\pi^0}^{max}(E_p^{max})$ is the maximum pion energy that the population of protons can produce.

B.1.1 Limits of the integrals

To have a complete description of the γ-ray emissivity coming from hadronic interactions of the cosmic rays with the medium, the limits of both the neutral pion and the consequent γ-ray emissivity integrals have to be computed. In this subsection the formulae of the several integral limits are derived in detail (see the appendices of Moskalenko and Strong 1998, and Blattnig et al. 2000b for alternative discussions).

The minimum energy of the produced pions can be determined from the lower limit of the resultant γ-ray energy distribution spectra (i.e., extracting β_{π^0} as a function of the γ-ray energies from Equation B.9), which sets a minimum π^0 velocity:

$$\beta_{\pi^0}^{min} = \frac{(E_\gamma^{'})^2 - E_\gamma^2}{(E_\gamma^{'})^2 + E_\gamma^2}\,, \tag{B.13}$$

Remembering that energy can be expressed in terms of the β velocity ($E_{\pi^0}^{min} = m_{\pi^0}\Gamma_{\pi^0}c^2 = m_{\pi^0}c^2/\sqrt{1-(\beta_{\pi^0}^{min})^2}$) and that the energy of the γ-rays in the CMS frame is $E_\gamma^{'} = (1/2)m_{\pi^0}c^2$, the minimum energy of the pion generated in the pp collision is:

$$E_{\pi^0}^{min} = E_\gamma + \frac{m_{\pi^0}^2 c^4}{4E_\gamma}\,. \tag{B.14}$$

On the other hand, the expression for the maximum energy of the produced neutral pions should be deduced from kinematic considerations. Consider the inelastic collision of two protons that generates one π^0. From here on, the rest of particles but the pion that appear in the final state will be included in a system denoted by X, such that $p + p \rightarrow \pi^0 + X$. Requiring total momentum conservation in the CMS reference frame, the modulus of the momentum vectors of the final state particles should be equal:

$$\overrightarrow{p_p^{'}} + \overrightarrow{p_p^{'}} = \overrightarrow{p_{\pi^0}^{'}} + \overrightarrow{p_X^{'}} = 0\,, \tag{B.15}$$

$$|\overrightarrow{p_{\pi^0}^{'}}|^2 = |\overrightarrow{p_X^{'}}|^2\,, \tag{B.16}$$

$$(E_{\pi^0}^{'})^2 - (m_{\pi^0}^{'}c^2)^2 = (E_X^{'})^2 - s_X\,, \tag{B.17}$$

where s_X is defined as the mass invariant square of the X subsystem.[5] Using the fact that in the CMS the mass invariant of the whole system is directly the sum of the total energy of all the particles of the starting or final state, we have the following relation:

$$\sqrt{s} = E_{\pi^0}^{'} + E_X^{'}\,. \tag{B.18}$$

[5] The mass invariant of a system of particles, $\sqrt{s}$, is a Lorentz invariant quantity and it is defined as the modulus of the total four-momentum, i.e., the sum of the individual four-momentum vectors of all the particles in the system: $s \equiv ({p_1}^\mu + {p_2}^\mu + ... + {p_N}^\mu)^2 = (E_1 + E_2 + ... + E_N)^2 - (\overrightarrow{p_1}c + \overrightarrow{p_2}c + ... + \overrightarrow{p_N}c)^2$.

Working on Equation (B.17), and using the previous relation, we can get:

$$E_{\pi^0}^{'} = \frac{s - s_X + m_{\pi^0}^2 c^4}{2\sqrt{s}} \,. \tag{B.19}$$

Therefore, as all quantities in the previous equation are positive, given a system with center of mass energy $\sqrt{s}$, the energy of the produced neutral pion will be maximum when the X subsystem has minimum energy: s_X^{min}. As s_X is Lorentz invariant, it can be evaluated in any reference frame. If we take the frame where the i particle of the X subsystem of N particles is at rest ($E_i = m_i c^2$, $\overrightarrow{p_i} = 0$, $\Gamma_i = 1$):

$$s_X \equiv \left(\sum_{i=1}^{N} p_i{}^{\mu}\right)^2 = \sum_{i=1}^{N}\sum_{j=1}^{N} p_i{}^{\mu} p_{j\,\mu} = \sum_{i,j=1}^{N} (E_i E_j - \overrightarrow{p_i} c \overrightarrow{p_j} c) = \sum_{i,j=1}^{N} m_i m_j \Gamma_j c^4 \,. \tag{B.20}$$

Given that the Lorentz factor Γ is always equal or bigger than 1, the minimum s_X will be:

$$s_X^{min} = \sum_{i,j=1}^{N} m_i m_j c^4 = \left(\sum_{i=1}^{N} m_i c^2\right)^2 \equiv M_X^2 c^4 \,, \tag{B.21}$$

where M_X depends on the reaction channel and represents the invariant mass of the system consisting of all particles except the pion. Consequently, in the CMS, the maximum energy of the produced neutral pion will be:

$$(E_{\pi^0}^{'})^{max} = \frac{s - M_X^2 c^4 + m_{\pi^0}^2 c^4}{2\sqrt{s}} \,. \tag{B.22}$$

But the upper limit of the γ-ray emissivity integral in Equation (B.12) is given with respect to the LS frame, so a boost transformation is still needed. The boost is characterized by the velocity of the incident protons in the CMS frame, $\beta_p^{'}$. Assuming that the incident proton move along the x-axis, by a Lorentz transformation (as described in footnote 3):

$$\begin{aligned} E_{\pi^0}^{max} &= (E_{\pi^0}^{'})^{max}\Gamma_p^{'} - (p_{x,\pi^0}^{'})^{max}(\Gamma_p^{'}\beta_p^{'}) \\ &= m_{\pi^0} c^2 [\Gamma_{\pi^0}^{'}\Gamma_p^{'} - (\Gamma_{\pi^0}^{'}\beta_{\pi^0}^{'})^{max}(\Gamma_p^{'}\beta_p^{'})] \,. \end{aligned} \tag{B.23}$$

Expressing everything in more convenient quantities and using the relations $\Gamma\beta = \sqrt{\Gamma^2 - 1}$, $\Gamma_p^{'} = E_p^{'}/m_p c^2$ and $E_p^{'} = \sqrt{s}/2$, the expression of the maximum energy of the pions that the population of incident protons generates becomes:

$$E_{\pi^0}^{max} = m_{\pi^0} c^2 \left[\frac{\sqrt{s}}{2m_p c^2}\frac{(E_{\pi^0}^{'})^{max}}{m_{\pi^0} c^2} + \sqrt{\left(\frac{s}{4m_p^2 c^4} - 1\right)\left(\frac{[(E_{\pi^0}^{'})^{max}]^2}{m_{\pi^0}^2 c^4} - 1\right)}\right] \,, \tag{B.24}$$

where the expression (B.22) of $(E_{\pi^0}^{'})^{max}$ can be substituted, taking into account that for the case of π^0 production the X subsystem of the final state is formed by two protons, so $M_X = m_p + m_p$. To explicitly introduce the energy of the incident cosmic ray proton in the formula, the relation $\sqrt{s} = \sqrt{2m_p c^2(E_p + m_p c^2)}$ can be used.[6]

Finally, the proton threshold energy for the production of a pion of energy E_{π^0}, which appear as the lower limit of the integral of the π^0 emissivity given in Equation (B.3), can

[6]In the particular case of a system of two particles with equal mass, one colliding onto the other assumed as a target at rest (as a target proton state in the LS frame), the general expression of the mass

be found by solving the $E_{\pi^0} = E_{\pi^0}(s)$ relation of Equation (B.24) to express –by inversion– s as a function of E_{π^0}. Then, $s = s(E_{\pi^0})$ can be made equal to $2m_pc^2(E_p + m_pc^2)$, which allows for the minimum proton energy to be derived.

Summarizing, the γ-ray emission expected from hadronic interactions of the cosmic ray nuclei with the medium can be computed with the following formulae:

$$Q_\gamma(E_\gamma)_{\pi^0} = 2\int_{E_{\pi^0}^{min}(E_\gamma)}^{E_{\pi^0}^{max}(E_p^{max})} dE_{\pi^0} \frac{Q_{\pi^0}(E_{\pi^0})}{\sqrt{E_{\pi^0}^2 - m_{\pi^0}^2c^4}}\,, \tag{B.26}$$

$$Q_{\pi^0}(E_{\pi^0}) = 4\pi n \int_{E_p^{th}(E_{\pi^0})}^{E_p^{max}} dE_p\, J_p(E_p) \frac{d\sigma(E_{\pi^0}, E_p)}{dE_{\pi^0}}\,, \tag{B.27}$$

$$E_{\pi^0}^{min} = E_\gamma + \frac{m_{\pi^0}^2c^4}{4E_\gamma}\,, \tag{B.28}$$

$$E_{\pi^0}^{max} = m_{\pi^0}\left[\frac{2m_pE_p^{max} - 2m_p^2 + m_{\pi^0}^2}{4m_pm_{\pi^0}} + \right. \tag{B.29}$$
$$\left. \sqrt{\left(\frac{E_p^{max} + m_p}{2m_p} - 1\right)\left(\frac{(2m_pE_p^{max} - 2m_p^2 + m_{\pi^0}^2)^2}{8m_pm_{\pi^0}^2(E_p^{max} + m_p)} - 1\right)}\right]\,,$$

$$E_p^{th}(E_{\pi^0}) = \frac{2m_p^3 - m_pm_{\pi^0}^2 + m_{\pi^0}^2E_{\pi^0} - 2E_{\pi^0}^2m_p}{2(m_{\pi^0}^2 - 2E_{\pi^0}m_p + m_p^2)} - \tag{B.30}$$
$$\frac{\sqrt{m_p^2(E_{\pi^0}^2 - m_{\pi^0}^2)(4E_{\pi^0}^2m_p^2 - 4m_{\pi^0}^2E_{\pi^0}m_p + 16m_p^3E_{\pi^0} + m_{\pi^0}^4 - 8m_p^2m_{\pi^0}^2)}}{2m_p(m_{\pi^0}^2 - 2E_{\pi^0}m_p + m_p^2)}\,.$$

Note that if E_p^{max} goes up to infinity (i.e., there is for instance an exponential cutoff in $J_p(E_p)$), then, also $E_{\pi^0}^{max} = \infty$. But still one crucial point needs to be clarified in order to have univocally described the γ-ray hadronic emission: the differential cross-section that describes the proton-proton π^0 production process. This is discussed in what follows.

B.2 Parameterizations of cross sections for neutral pion production in proton-proton collisions

For the kind of numerical computation codes that usually involve the use of pion production cross sections, which often imply many iterative loops, as the code used in this Thesis, a simple form for the cross section is desired in order to minimize computer time. Many algebraic parameterizations of the cross section have been provided until now by many authors, usually representing a Lorentz invariant differential cross section (LIDCS), a laboratory frame spectral distribution (i.e., an energy differential cross section) or a total cross section.[7] In what follows, two different approaches to compute the neutral pion

invariant of the system, given in footnote 5, reduces to:

$$\begin{aligned}\sqrt{s} &= \sqrt{(p_1+p_2)^2} = \sqrt{p_1^2 + p_2^2 + 2p_1p_2} = \sqrt{m_1^2c^4 + m_2^2c^4 + 2(E_1E_2 - |\,\vec{p_1}\,||\,\vec{p_2}\,|\cos\theta)} \\ &= \sqrt{2m_p^2c^4 + 2E_pm_pc^2} = \sqrt{2m_pc^2(E_p + m_pc^2)}\,. \end{aligned} \tag{B.25}$$

[7]The invariant single-particle distribution resulting from the production process of a particle C in a reaction of the type $A+B \rightarrow C+X$ (A and B being the initially colliding particles, C the produced particle

decay γ-ray emission are to be investigated, one using an energy differential cross section and the other a total cross section.

B.2.1 The δ-function approximation and a total cross section parameterizations

In this formalism, used for example by Aharonian and Atoyan (2000), the neutral pion emissivity of Equation (B.27), can be approximated by assuming that a fixed average fraction of energy is transferred from the proton to the pion,

$$\begin{aligned} Q_{\pi^0}(E_{\pi^0}) &= 4\pi n \int_{E_p^{th}(E_{\pi^0})} dE_p \, J_p(E_p) \, \delta(E_{\pi^0} - \kappa E_p^{\rm kin}) \, \sigma(E_p) \\ &= \frac{4\pi n}{\kappa} J_p \left(m_p c^2 + \frac{E_{\pi^0}}{\kappa} \right) \sigma \left(m_p c^2 + \frac{E_{\pi^0}}{\kappa} \right) , \end{aligned} \tag{B.33}$$

where σ is the total cross-section of inelastic pp collisions[8], and κ is the mean fraction of the kinetic energy $E_p^{\rm kin} = E_p - m_p c^2$ of the proton transferred to the secondary meson per collision. In a broad region from GeV to TeV energies, κ can be well approximated to 0.17. Then, in this formalism, an accurate knowledge of the total inelastic cross section is needed to compute the γ-ray emissivity.

Aharonian and Atoyan (2000) proposed that, since the cross section rises rapidly from the reaction energy threshold at $E_p^{\rm kin} \sim 0.3$ GeV to a value of about 30 mb for energies

---

of interest, and X representing all other particles produced in the collision) is defined by: $E\frac{d^3\sigma}{dp^3} = \frac{E}{p^2}\frac{d^3\sigma}{dpd\Omega}$, where $\frac{d^3\sigma}{dp^3}$ is the Lorentz invariant differential cross section (LIDCS), i.e., the probability per unit of incident flux for detecting a particle C within the phase-space volume element dp^3. E is the total energy of the produced particle C, and Ω is the solid angle. This cross section form is invariant under Lorentz transformations, so can be derived in any reference frame and then applied to any other one. This is an advantage because the data for pion production is basically given in terms of quantities expressed in the CMS frame. However, frequently, for numerical computations, probability density distributions integrated over solid angle are needed instead. Therefore, looking for an accurate parameterization of the spectral distribution or energy differential cross section, $d\sigma/dE$, and the total cross section, σ, becomes important. Both cross sections can be derived by integration from the LIDCS (which contains dependencies on the energy of the colliding protons (through the energy of the center of mass in the collision $\sqrt{s}$), on the energy of the produced pion (whose kinetic energy is T_π), and on the scattering angle of the pion, θ):

$$\frac{d\sigma}{dE}(\sqrt{s}, T_{\pi^0}) = 2\pi p \int_0^{\theta_{max}} d\theta E \frac{d^3\sigma}{dp^3} \sin\theta \, , \tag{B.31}$$

$$\sigma(\sqrt{s}) = 2\pi \int_0^{\theta_{max}} d\theta \int_{p_{min}}^{p_{max}} dp E \frac{d^3\sigma}{dp^3} \frac{p^2 \sin\theta}{\sqrt{p^2 + m_C^2}} \, , \tag{B.32}$$

where θ_{max}, p_{max} and p_{min} are the extrema of the scattering angle and momentum of the pion respectively, and m_C is the rest mass of the particle C. These extrema are determined by kinematic considerations (see Blattnig et al. 2000b for further details). Then, starting from different LIDCS parameterizations it is possible to integrate them over the kinematics to obtain the corresponding parameterizations for the total and differential cross sections. The accuracy of the latter forms will only depend on the accuracy of the parameterizations of the LIDCS.

[8]Full proton-proton interaction cross section includes both the elastic (pp interactions without secondaries generation, just elastic scattering of the incident protons) and the inelastic cross section (processes where secondary particles are generated). Inelastic cross sections can be diffractive or non-diffractive, if they account for interactions where the incident proton and/or the target proton suffer a transition to an excited state before dissociating in a proton and one or more pions, or not. Finally, inelastic cross sections can be inclusive, when they are multiplied by the average pion multiplicity, or not inclusive, when they are not. Note that $d\sigma/dE$ can be thought as containing the inclusive total inelastic cross section, as is stated explicitly for instance in Dermer's (1986a) equation 3.

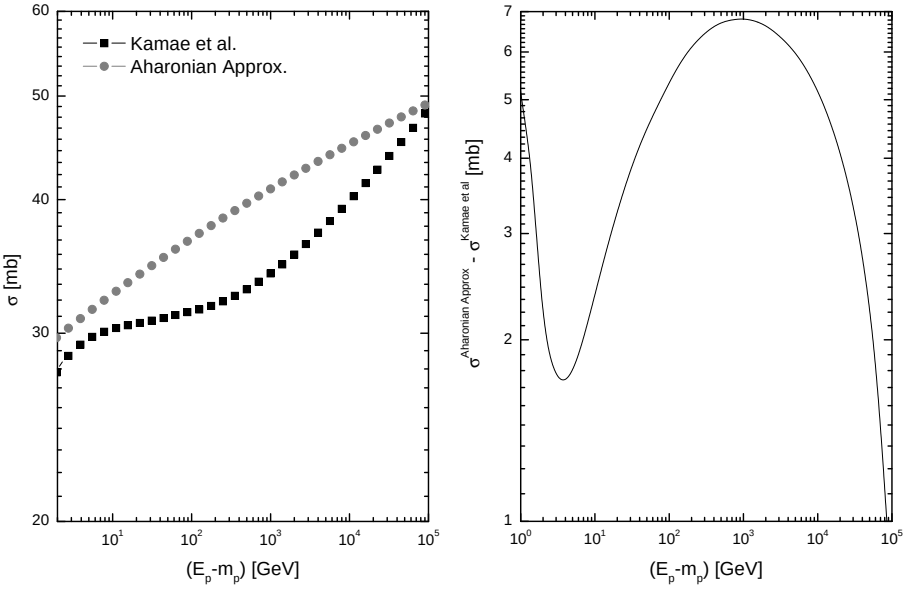

Figure B.2: Comparison between model A of Kamae et al., sum of diffractive and non-diffractive contributions, and Aharonian and Atoyan's formula for the total inelastic pp cross section.

around $E_p^{\rm kin} \sim 2$ GeV, and thereafter it increases only logarithmically, a sufficiently good approximation is to assume:

$$\begin{aligned} \sigma_{pp}(E_p) &\approx 30\,[0.95 + 0.06\ln(E_p^{\rm kin}/1{\rm GeV})]\ {\rm mb} \quad , \quad {\rm for} \quad E_p^{\rm kin} > 1{\rm GeV} \\ \sigma_{pp}(E_p) &\approx 0 \quad , \quad {\rm otherwise.} \end{aligned} \tag{B.34}$$

It can be seen (e.g., Dermer 1986a) that a more accurate approximation of the total cross section below 1 GeV does not noticeably affect the results of γ-ray emissivities, provided the spectrum of primaries is sufficiently broad, since most of the γ-rays are generated by primary protons having energy in excess of GeV.

In a recent paper, Kamae et al. (2005) introduced the effect of diffractive interactions and scaling violations in pp non-diffractive interactions. The diffractive interactions contribution to the total pp cross section was usually neglected in all other computations of γ-ray emissivity from neutral pion decay to date, and thus one would expect an increase in the predicted fluxes. Kamae et al.'s best model, dubbed A, for the inelastic (not inclusive) cross section is given in Table 1 of their paper, columns 2 and 3.

Figure B.2 shows the comparison of the sum of both diffractive and non-diffractive contributions of Kamae et al.'s model with Aharonian and Atoyan's formula, for proton kinetic energies above 1 GeV. Aharonian and Atoyan's approximation produces an actually larger (but quite close) cross section for all energies. Kamae et al. (2005) compared their model A with Hagiwara's (2002) compilation of pp cross section measurements and found a good agreement. When multiplicity is taken into account, Kamae et al.'s model also agrees with the data on inclusive cross sections, as can be seen in Figure B.4.

Figure B.3 left panel shows a comparison of the γ-ray emissivity obtained when using Kamae et al.'s model A or Aharonian and Atoyan's cross section in Equation (B.33). In this comparison, the proton spectrum is the Earth-like one, $J_p(E_p) = 2.2\,E_p^{-2.75}$ protons cm^{-2} s^{-1} sr^{-1} GeV^{-1} and $n = 1$ cm^{-3}. The resulting γ-ray emissivity is multiplied

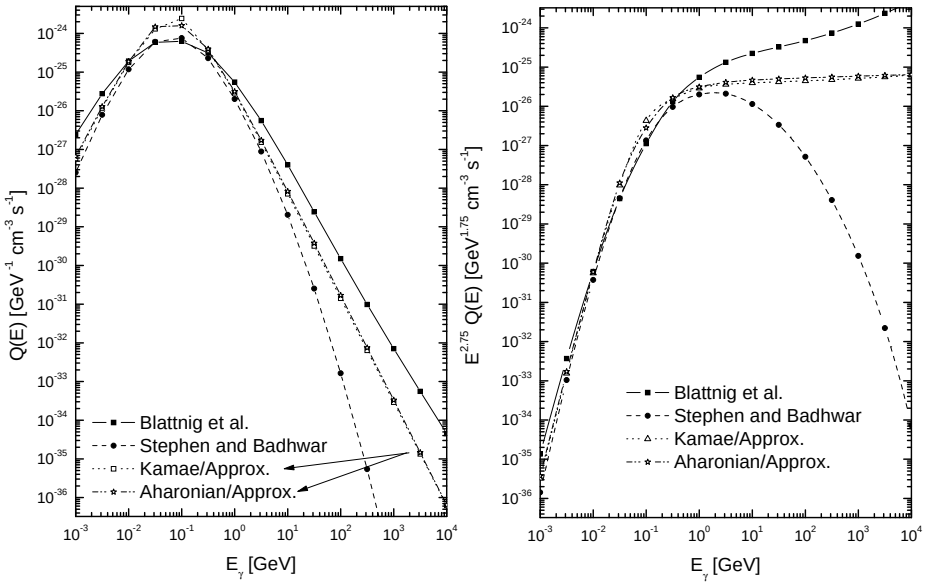

Figure B.3: Left: Comparison of the γ-ray emissivities computed with the δ-function approximation (Kamae et al.'s model A and Aharonian and Atoyan's formula for the inelastic total cross section) and the ones directly computated using differential cross section parameterizations. Right: γ-ray emissivities as in left panel multiplied by $E^{2.75}$, with 2.75 being the slope of the proton primary spectrum.

by 1.45 to give account of the contribution to the pion spectrum from the presence of heavier nuclei both as targets and as projectiles (Dermer 1986a). Curves are practically indistinguishable in this scale, and their ratio is well within a factor of ~ 1.3. Aharonian and Atoyan's expression for the cross section produces a slightly larger value of emissivity than that obtained with Kamae's model A, including non-diffractive interactions, but results are in quite good agreement.

B.2.2 Differential cross section parameterizations

Recently, Blattnig et al. (2000a) have developed parameterizations of the differential cross section regulating the production of neutral and charged pions from pp interactions. They presented a parameterization of the Stephens and Badhwar's (1981) model by numerically integrating their LIDCS. The resulting parameterization is given as a function of the incident proton kinetic energy in the LS frame, $T_{\rm lab}$, and the kinetic energy of the produced pion, T_π. It is divided into two regions, corresponding to low and high proton laboratory kinetic energies:
For the 0.3 - 2 GeV range:

$$\begin{aligned} F_2 &= A_1 T_\pi^{A_2} + A_3 T_{\rm lab}^{A_4}\,, \\ F_1 &= \exp(A_5 + \frac{A_6}{\sqrt{T_{\rm lab}}} + A_7 T_{\rm lab}^{A_8} + A_9 T_\pi^{A_{10}} + A_{11} T_\pi^{A_{12}})\,, \\ \left(\frac{d\sigma}{dE}\right)_{\rm lab} &= (A_{13}\frac{F_1}{F_2} + A_{14}\exp(A_{16}\sqrt{T_\pi} + A_{17} T_\pi^{A_{18}} T_{\rm lab}^{A_{19}}))T_\pi^{A_{15}}\,. \end{aligned} \qquad \text{(B.35)}$$

Table B.1: Constants in the Blattnig et al. (2000a) parameterization of the differential cross section for the production of neutral pions.

$A_1 = 6.78 \times 10^{-10}$	$B_1 = 1.3 \times 10^{-10}$
$A_2 = -2.86$	$B_2 = -2.86$
$A_3 = 1.82 \times 10^{-8}$	$B_3 = 4.27 \times 10^{-9}$
$A_4 = -1.92$	$B_4 = -2.4$
$A_5 = 22.3$	$B_5 = 22.3$
$A_6 = 0.226$	$B_6 = -1.87$
$A_7 = -0.33$	$B_7 = 1.28$
$A_8 = -1.75$	$B_8 = -1.25$
$A_9 = -32.1$	$B_9 = -33.2$
$A_{10} = 0.0938$	$B_{10} = 0.0938$
$A_{11} = -23.7$	$B_{11} = -23.6$
$A_{12} = 0.0313$	$B_{12} = 0.0313$
$A_{13} = 2.5 \times 10^6$	$B_{13} = 2.5 \times 10^6$
$A_{14} = 1.38$	$B_{14} = 0.25$
$A_{15} = 0.25$	
$A_{16} = -39.4$	
$A_{17} = 2.88$	
$A_{18} = 0.025$	
$A_{19} = 0.75$	

For the 2 - 50 GeV range:

$$\begin{aligned} F_2 &= B_1 T_\pi^{B_2} + B_3 T_{\rm lab}^{B_4}\,, \\ F_1 &= \exp(B_5 + \frac{B_6}{\sqrt{T}_{\rm lab}} + B_7 T_{\rm lab}^{B_8} + B_9 T_\pi^{B_{10}} + B_{11} T_\pi^{B_{12}})\,, \\ \left(\frac{d\sigma}{dE}\right)_{\rm lab} &= B_{13} T_\pi^{B_{14}} \frac{F_1}{F_2} + B_{15} T_\pi^{B_{16}} \exp(B_{17}\sqrt{T}_\pi)\,. \end{aligned} \tag{B.36}$$

Energies are given in units of GeV, and the differential cross section in mb GeV^{-1}. Constants are in Table B.1. The high end in energy of the parameterization is defined by the energy up to which it was tested against experiments by Blattnig et al. (2000a).

Blattnig et al., despite finding the Stephens and Badhwar's parameterization to be the best of all they analyzed, found that it dramatically underestimates the experimental data of LIDCS for transverse momenta of the produced pion larger than 2 GeV (see Blattnig et al. (2000b) figure 6). Hence, Blattnig et al. developed a new parameterization of the LIDCS; the resulting differential cross section, particularly in the case of neutral pions, shows a much simpler analytical form than Stephens and Badhwar's model shown above, and does not require to be divided into two energy ranges:

$$\frac{d\sigma(E_{\pi^0}, E_p)}{dE_{\pi^0}} = e^A \quad \text{mb GeV}^{-1}\,, \tag{B.37}$$

where

$$A = \left(-5.8 - \frac{1.82}{(E_p - m_p)^{0.4}} + \frac{13.5}{(E_{\pi^0} - m_{\pi^0})^{0.2}} - \frac{4.5}{(E_{\pi^0} - m_{\pi^0})^{0.4}}\right).$$

Table B.2: Integrated emissivities for an Earth-like spectrum. Values are in units of photons $\mathrm{cm}^{-3}\ \mathrm{s}^{-1}$.

Parameterization/Approx.	$E > 100$ Mev	$E > 100$ GeV	$E > 300$ GeV
Blattnig et al.	3.2E-25	2.2E-28	4.7E-29
Kamae et al.	4.8E-25	1.8E-29	2.6E-30
Aharonian and Atoyan	4.0E-25	2.2E-29	3.1E-30
Stephens and Badwhar (Blattnig et al.)	2.2E-25	1.8E-31	1.9E-33

Despite the differences between both parameterizations, they integrate to nearly the same total cross section and a single expression is needed to represent the total inclusive cross section:

$$\sigma_{\pi^0}(E_p) = \left[0.007 + 0.1\frac{\ln(E_p - m_p)}{(E_p - m_p)} + \frac{0.3}{(E_p - m_p)^2}\right]^{-1} \mathrm{mb}\,, \tag{B.38}$$

where rest masses and energies must be given again in units of GeV.

The inclusive total inelastic cross section deduced by Blattnig et al. seems to work well for energies even higher than 50 GeV, as can be seen in Figure B.4, together with a compilation of experimental data (Dermer 1986b). We also show in the same Figure the results for the inclusive total cross section from model A of Kamae et al. (2005), obtained from his figure 5. Indeed, Kamae et al.'s model produces a slightly higher cross section, although both correlate reasonably well with experimental data, at least up to 3 TeV. This Figure enlarge the comparison of Blattnig et al. (2000a) inclusive cross section with experimental data (see their figure 4), where only three low-energy data points from Whitmore (1974) were considered.

However, the differential cross section parameterizations proposed by Blattnig et al. are not deprived of problems if extrapolated to high energies. As already mentioned, the parameterization of the Stephen and Badhwar's model grossly underpredicts, whereas the newest Blattnig et al. (Equation B.37) overpredicts, the highest energy pion yield. The γ-ray photon emission that is output of the use of these two differential cross sections in Equations (B.26) and (B.27) is shown, for an Earth like spectrum, in Figure B.3 left panel, together with the previous δ-approximation formalism predictions. Figure B.3 right panel shows the emissivities as computed in the different approaches multiplied by $E^{2.75}$. As expected, Stephen and Badhwar's parameterization falls quickly at high energies whereas both Kamae et al.'s and Aharonian and Atoyan's cross sections secure that the γ-rays emitted maintain an spectrum close to that of the proton primaries. For γ-rays above few TeV, i.e., γ-rays mostly generated by protons above few tens of TeV, Blattnig et al.'s differential cross section parameterization makes the γ-ray emitted spectrum much harder than the proton spectrum that produced it. This indicates that a direct extrapolation of Equation (B.37) for computing γ-ray emissivity above TeV energies from Equation (B.26) induces overpredictions of fluxes.

Table B.2 presents the results for the integrated emissivity, $\int_{E_\gamma} Q_\gamma(E_\gamma)\, dE_\gamma$, with $Q_\gamma(E_\gamma)$ being the different curves of Figure B.3 left panel. To obtain integrated fluxes from a source of volume V at a distance D one has to multiply by the constant $V/(4\pi D^2)$, so that the difference in integrated emissivities indeed represent those among integrated fluxes. As Table B.2 shows –disregarding Blattnig et al.'s parameterization of Stephen

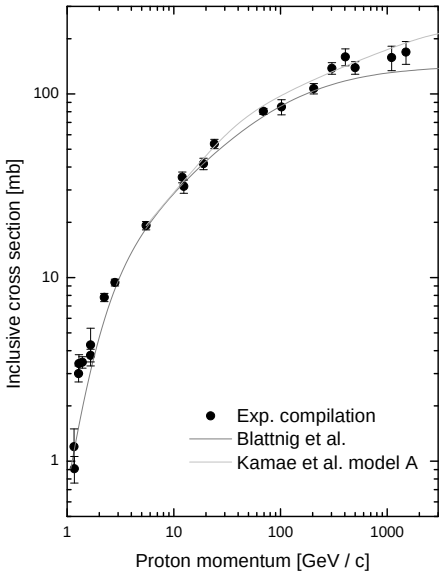

Figure B.4: Comparing inclusive cross sections. Kamae et al.'s model A data come from their figure 5, Blattnig et al.'s curve is obtained from Equation (B.38) and experimental compilation is from Dermer (1986b).

and Badwhar's results, quoted here just for completeness–, above 100 MeV differences are less than a factor of 1.5, which most likely are within other uncertainties in any given model. But above 300 GeV, differences are much larger.

If interested in the GLAST-domain predictions (say, $E > 100$ MeV, $E < 50$ GeV), and up to the moment where a better and more complete parameterization exists, the most conservative choice seems to use Blattnig et al.'s new differential cross section parameterization (Equation B.37) with no other approximation in Equations (B.27) and (B.26). This choice, while not taking into account diffractive processes, will possibly slightly underpredict the integrated flux (as shown in Table B.2). The advantage is that by using Blattnig et al.'s approach there is no δ-function approximation involved nor an ad-hoc histogram of particle numbers as proposed in the treatment of Kamae et al. (2005), but one has an analytical expression that can be directly used in the numerical estimates of Equation (B.26). However, the price to pay is that this form of computation cannot be considered reliable at higher energies and should not be used.[9] For the IACTs-domain ($E > 100$ GeV) the safest and also computationally-preferable choice appears to be to take either Kamae et al.'s model A, or even the simpler Aharonian and Atoyan's expression (Equation B.34), and a δ-function approximation. This approach would probably be slightly underestimating the integrated flux at such high energies. Both parameterizations yields to the same results, within typical uncertainties in other model parameters. To conclude, assuming either Kamae et al.'s or Aharonian and Atoyan's expression for all energies does not imply substantial differences for the calculation of fluxes, as Table B.2 shows, and it is computationally preferable.

[9] At the moment of writing, Kamae et al. are developing a differential cross section parameterization of their model A.

Appendix C

Physics included in the numerical modeling

This Appendix compiles the physics contained in the numerical package $\mathcal{Q}$-DIFFUSE*, and presents the relevant formulae as they are included there. Energy losses both for protons and electrons, electron and positron production, bremsstrahlung and inverse Compton radiation, dust and radio emission, free-free absorption, and the equation of radiation transport are covered in some detail. Since the first application of* $\mathcal{Q}$-DIFFUSE *was made by Torres (2004), this Appendix draw upon his own, while expanding it, in describing the code physics.*

C.1 Energy loss processes

C.1.1 Proton losses

Proton losses are produced mainly by ionization and, at higher energies, by pion production (e.g., Ginzburg & Syrovatskii 1964, p.120ff, Mannheim & Schlickeiser 1994). Collisions with stars and dust, synchrotron proton emission, Coulomb, photo-pair, and photo-hadron processes play a much subdominant role in the absorption of proton cosmic rays under the global scenario studied, and are not considered.

C.1.1.1 Ionization

During the motion of a proton through a neutral medium, the ionization loss rate is given by (e.g., Ginzburg & Syrovatskii 1964, p.120ff)

$$-\left(\frac{dE}{dt}\right)_{\mathrm{Ion},p} = \sum_j \frac{4\pi e^4 n_j}{mv}\left\{\ln\left[\frac{2mv^2}{I_j}\left(\frac{E}{m_p c^2}\right)^2\right] - \frac{v^2}{c^2}\right\}$$

$$\sim 1.83\times 10^{-17}\left(\frac{n_{\mathrm{H}}+2n_{\mathrm{H_2}}}{\mathrm{cm}^3}\right)\frac{c}{v}\left\{10.9+2\ln\left(\frac{E}{m_p c^2}\right)+\ln\left(\frac{v^2}{c^2}\right)-\frac{v^2}{c^2}\right\}\ \mathrm{GeV\ s^{-1}}, \quad \text{(C.1)}$$

where v is the velocity of the cosmic ray, e and m are the charge and mass of an electron, I_j is the mean ionization energy of the species j ($I \sim 15$ eV for hydrogen and ~ 41.5 eV for helium), and n_j is the concentration of j-atomic electrons. In units of c, the velocity is $\beta = \left(1-{\Gamma_p}^{-2}\right)^{1/2}$ —with $\Gamma_p = E_p/m_p c^2$—. The numerical factor results in assuming a medium composed of hydrogen and helium in a ratio 10:1. For extremely energetic

protons, such that $E \gg (m_p/m)m_p c^2 \sim 2$ TeV, the ionization losses expression changes to take into account that a proton can transfer all its energy to the electron

$$-\left(\frac{dE}{dt}\right)_{\mathrm{Ion},p} = \sum_j \frac{2\pi e^4 n_j}{mc}\left\{\ln\left[\frac{2mc^2}{I_j^2}\left(\frac{E^3}{m_p^2 c^4}\right)\right] - 2\right\}$$
$$\sim 9.17\times 10^{-18}\left(\frac{n_{\mathrm{H}} + 2n_{\mathrm{H}_2}}{\mathrm{cm}^3}\right)\left\{19.22 + 3\ln\left(\frac{E}{m_p c^2}\right) + \ln\left(\frac{m_p}{m}\right)\right\}\ \mathrm{GeV\ s^{-1}}. \quad \text{(C.2)}$$

Ionization losses are commonly given using the medium grammage. This form can be obtained by dividing the previous expressions by c, so that losses are given in units of GeV cm^{-1}, and then, using the Avogadro's conversion, by multiplying the latter by $6\times 10^{23}/n$, so that losses (in hydrogen) are given in units of GeV g^{-1} cm^2, or GeV per unit of hydrogen grammage, where n is the hydrogen number density.

C.1.1.2 Pion production

The energy loss by pion production is given as (Mannheim and Schlickeiser 1994, Schlickeiser 2002, p. 125 and 138)

$$-\left(\frac{dE}{dt}\right)_{\mathrm{Pion},p} = \int_0^{E_{\pi\mathrm{max}}} dE_\pi P(E_\pi, E_p), \quad \text{(C.3)}$$

where, $P(E_\pi, E_p)$ is the pion power of a relativistic proton with total energy $E_p = \Gamma_p m_p c^2$, and it is given by $P(E_\pi, E_p) \sim 1.3\, n\, c\, E_\pi\, \xi(E_p)\, \sigma_{pp}\, \delta(E_\pi - \bar{E}_\pi)\, \Theta(E_p - E_{\mathrm{th}})$. Here, $\delta(E_\pi - \bar{E}_\pi)$ stands for the δ-function between the energy E_π and the mean energy of the produced pion. $\Theta(E_p - E_{th})$ is a Heaviside step-function which ensures that the energy is above the threshold energy of the reaction, $E_{\mathrm{th}} = 1.22$ GeV. The factor $\xi(E_p)$ is the pion multiplicity, which up to protons energies of 10^4 GeV, can be approximated by an increasing power law

$$\xi(E_p)^{\pi^\pm} \sim 2\left[\frac{E_p - E_{\mathrm{th}}}{\mathrm{GeV}}\right]^{1/4} \quad \text{and} \quad \xi(E_p)^{\pi^0} \sim \frac{1}{2}\,\xi(E_p)^{\pi^\pm}. \quad \text{(C.4)}$$

In any case, the way in which the energy is distributed onto pions during the hadronic interaction is not relevant for the total energy loss. The limiting value of the inelasticity is 1/2, i.e., a leading nucleon plus a pion cloud, each carrying half of the incident total energy, leave the interaction fireball. Then, the energy dependence of the mean pion energy is

$$\bar{E}_\pi = \frac{1}{2}\frac{(E_p - m_p\, c^2)}{\xi(E_p)} \sim \frac{1}{6}(E_p - m_p\, c^2)^{3/4}. \quad \text{(C.5)}$$

The cross section is approximated as $\sigma_{pp} \sim 30$ mb. The error introduced here by assuming a constant cross section through the whole energy range is only mildly (logarithmically) dependent on energy. In any case, note that this approximation applies only to compute the loss rate, not to compute actual pion emissivities, for which a more advanced treatment is provided in Sections B.1 and C.2.2. Finally, the factor 1.3 in the pion power corrects the hydrogen density of the medium to account for heavier components (here $n = n(\mathrm{H}) + n(\mathrm{HII}) + 2n(\mathrm{H_2})$). Eq. (C.3), (C.4) and (C.5) then give (Mannheim and Schlickeiser

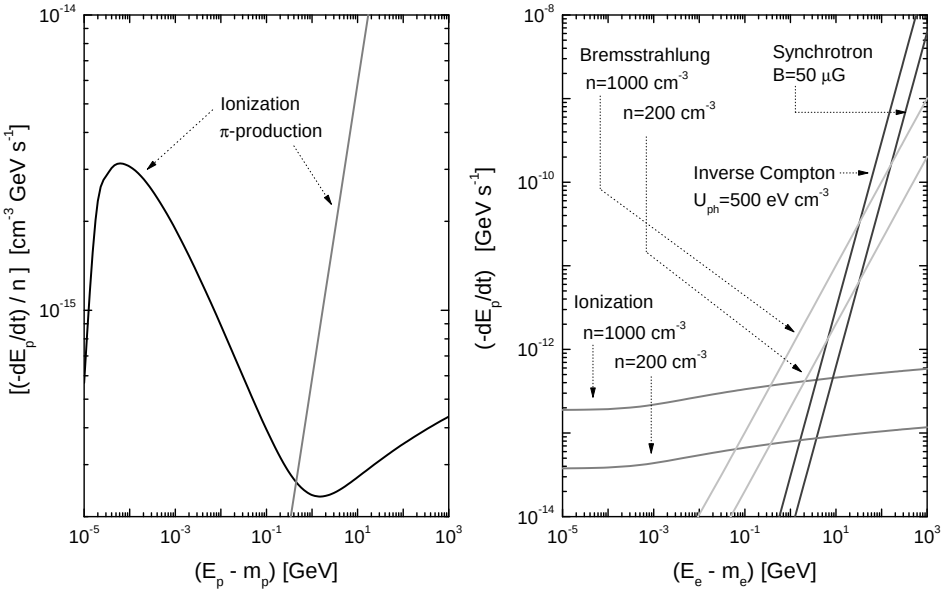

Figure C.1: Example of the rate of energy loss for protons (left panel) and electrons (right panel) considered in this work. Protons losses are mainly produced by ionization and pion production. Both are proportional to the medium density, and this is factored out (in units of cm^{-3}). Electrons losses correspond to synchrotron and bremsstrahlung radiation, inverse Compton scattering, and ionization. A set of random parameters is assumed for this example –shown in the figure–, additionally to the assumption that the average density of the photon target is $\bar{\epsilon} = 1$ eV. From Torres (2004).

1994),

$$-\left(\frac{dE}{dt}\right)_{\mathrm{Pion},p} = 0.65\, c\, n\, \sigma_{pp}\, (E_p - m_p)\, \Theta(E_p - E_{\mathrm{th}})$$
$$\sim 5.85 \times 10^{-16} \left(\frac{n}{\mathrm{cm}^3}\right) \left(\frac{E_p - m_p c^2}{\mathrm{GeV}}\right) \Theta(E_p - E_{\mathrm{th}})\, \mathrm{GeV\ s}^{-1}. \quad \text{(C.6)}$$

C.1.2 Electron losses

During their motion through the ISM, electrons are affected by ionization, bremsstrahlung, Inverse Compton, and synchroton emission. The formulae used to compute these losses are provided below, as they is implemented in the code. Throughout this Section, E represents the electron energy E_e, and m stands for the electron mass.

C.1.2.1 Ionization

In the ultrarelativistic case ($E \gg mc^2$), the ionization losses in neutral atomic matter (e.g., Schlickeiser 2002, p. 99; Ginzburg & Syrovatskii 1964, p. 140ff)

$$-\left(\frac{dE}{dt}\right)_{\mathrm{Ion},e} = (mc^2)\frac{9}{4} c\sigma_T \sum_j n_j Z_j \left[\ln\left(\frac{E}{mc^2}\right) + \frac{2}{3}\ln\left(\frac{mc^2}{I_j}\right)\right]$$
$$\sim 2.75 \times 10^{-17} \left[6.85 + \ln\left(\frac{E}{mc^2}\right)\right] \left[\frac{n_{\mathrm{H}} + 2n_{\mathrm{H}_2}}{\mathrm{cm}^{-3}}\right] \mathrm{GeV\,s}^{-1}. \quad \text{(C.7)}$$

Here, I_j is the effective ionization energy, equal to 15 eV for hydrogen and 41.5 eV for helium, and the medium is assumed to contain these two elements in a ratio 10:1, i.e., $(n_{\rm H} + 2n_{\rm H_2})/n_{\rm He} = 1/10$. Elements heavier than He contribute to the losses in less than 1%.

C.1.2.2 Synchrotron

Synchrotron losses, occurring for electrons with energies $E > mc^2$ moving in a magnetic field B, can be computed as (e.g., Ginzburg & Syrovatskii 1964, p. 145ff; Blumenthal & Gould 1970)

$$-\left(\frac{dE}{dt}\right)_{\rm Sync,e} = \frac{2}{3}c\left(\frac{e^2}{mc^2}\right)^2 B_\perp^2 \left(\frac{E}{mc^2}\right)^2 \sim 2.5\times10^{-6}\left(\frac{B}{\rm Gauss}\right)^2\left(\frac{E}{\rm GeV}\right)^2 {\rm GeV\ s^{-1}}, \tag{C.8}$$

where $B_\perp$ represents the magnetic field in a direction perpendicular to the electron velocity, and the second equality takes into account an isotropic distribution of pitch angles. In this case, particles velocities are distributed according to $p(\alpha)d\alpha = [(1/2)\sin\alpha)]d\alpha$, with α the angle between the particle's velocity and B, varying between 0 and π. Then, as $B_\perp = B\sin\alpha$, the average in Eq. (C.8) requires the integral $\int[(1/2)\sin\alpha)]\sin^2\alpha\, d\alpha = 2/3$, in order to go from $B_\perp$ to B.

C.1.2.3 Inverse Compton

The losses produced by Inverse Compton emission are given by (e.g., Blumenthal & Gould 1970)

$$-\left(\frac{dE}{dt}\right)_{\rm IC,e} = \int_0^\infty d\epsilon \int_{{E_\gamma}^{\rm min}}^{{E_\gamma}^{\rm max}} dE_\gamma\, E_\gamma c\, n_{\rm ph}(\epsilon)\, \frac{d\sigma(\epsilon, E_\gamma, E)}{dE_\gamma} \tag{C.9}$$

where $n_{\rm ph}(\epsilon)$ is the target photon distribution (usually a black or a greybody), ϵ and E_γ are the photon energies before and after the Compton collision, respectively, and $d\sigma(\epsilon, E_\gamma, E)/dE_\gamma$ is the Klein-Nishina differential cross section (Schlikeiser 2002, p. 82),

$$\frac{d\sigma(\epsilon, E_\gamma, E)}{dE_\gamma} = \frac{3\sigma_T(mc^2)^2}{4\epsilon E^2}\left[2q\ln q + (1+2q)(1-q) + \frac{(\mathcal{C}q)^2(1-q)}{2(1+\mathcal{C}q)}\right], \tag{C.10}$$

where $\sigma_T = 6.65\times10^{-25}$ cm^2 is the Thomson cross section,

$$\mathcal{C} = \frac{4\epsilon E}{(mc^2)^2} \tag{C.11}$$

is the Compton factor, and

$$q = E_\gamma \mathcal{C}(E - E_\gamma). \tag{C.12}$$

From the kinematics of the scattering process, the range of q is restricted to $(mc^2)^2/4E^2 \leq 1$, what means that, for fixed ϵ and $E > mc^2$, E_γ is restricted to $\epsilon \leq E_\gamma \leq 4E^2\epsilon/((mc^2)^2 + 4\epsilon E)$, which defines the limits of the integral in Eq. (C.9). Depending on the energy of the accelerated electron and the photon target field, there are two different regimes for the Compton losses; they are distinguished by the use of Thomson ($\mathcal{C} \ll 1$) or extreme Klein-Nishina ($\mathcal{C} \gg 1$) differential cross sections. When $\mathcal{C} \ll 1$, the Compton losses are

given by (e.g., Ginzburg & Syrovatskii 1964, p. 144ff and 382ff, Longair 1994, p. 100ff)

$$
\begin{aligned}
-\left(\frac{dE}{dt}\right)_{\mathrm{IC},e} &= \frac{4}{3} c\sigma_T U_{\mathrm{ph}} \left(\frac{E}{mc^2}\right)^2 \\
&\sim 2.67\times10^{-23} \left(\frac{U_{\mathrm{ph}}}{\mathrm{eV\,/\,cm^3}}\right) \left(\frac{E}{mc^2}\right)^2 \mathrm{GeV\ s^{-1}}, \\
&\sim 1.02\times10^{-16} \left(\frac{U_{\mathrm{ph}}}{\mathrm{eV\,/\,cm^3}}\right) \left(\frac{E}{\mathrm{GeV}}\right)^2 \mathrm{GeV\ s^{-1}}, \qquad \text{(C.13)}
\end{aligned}
$$

where U_{ph} is the photon target energy density. When, on the contrary, $\mathcal{C} \gg 1$ (e.g., in the case of a target field of $\bar{\epsilon} \sim 1$ eV and an electron of $E_e \gg 100$ GeV), the Compton loses are given by

$$
\begin{aligned}
&-\left(\frac{dE}{dt}\right)_{\mathrm{IC},e} = \frac{4}{3}\left(\frac{mc^2}{\bar{\epsilon}}\right)^2 cU_{\mathrm{ph}} \left\{\frac{3}{8}\sigma_T \ln\left(\frac{2E\bar{\epsilon}}{m^2c^4}+\frac{1}{2}\right)\right\} \\
\sim\ & 1.3\times10^{-23} \left(\frac{U_{\mathrm{ph}}}{\mathrm{eV\,/\,cm^3}}\right) \left(\frac{mc^2}{\bar{\epsilon}}\right)^2 \ln\left(\frac{2E\bar{\epsilon}}{m^2c^4}\right) \mathrm{GeV\ s^{-1}} \\
\sim\ & 2.6\times10^{-12} \left(\frac{U_{\mathrm{ph}}}{\mathrm{eV\,/\,cm^3}}\right) \left(\frac{\bar{\epsilon}}{\mathrm{eV}}\right)^{-2} \ln\left[7.6\times10^{-3}\left(\frac{E}{\mathrm{GeV}}\right)\left(\frac{\bar{\epsilon}}{\mathrm{eV}}\right)\right] \mathrm{GeV\ s^{-1}}. \qquad \text{(C.14)}
\end{aligned}
$$

Here, $\bar{\epsilon}$ is the mean energy of the photon target field. In the extreme Klein-Nishina limit, however, losses have not the same meaning as in the Thomson case. In the latter, in each Compton collision the electron losses a small fraction of its energy, whereas for $\mathcal{C} \gg 1$, the relativistic electron losses its energy in discrete amounts which are a sizeable fraction of its initial energy.

C.1.2.4 Bremsstrahlung

Additional losses are caused by the emission of bremsstrahlung γ-ray quanta in interactions between electrons and atoms of the medium. Similar to the extreme Klein-Nishina limit, the energy of the photon emitted by bremsstrahlung is of the order of the energy of the incident electron. The energy loss can be computed as (e.g., Schlickeiser 2002, p. 95ff; Ginzburg & Syrovatskii 1964, p. 143, Blumenthal & Gould 1970):

$$
-\left(\frac{dE}{dt}\right)_{\mathrm{Brem},e} = \int dE_\gamma\ E_\gamma \left(\frac{dN}{dt\,dE_\gamma}\right), \qquad \text{(C.15)}
$$

where $(dN/dt\,dE_\gamma) = c\sum_j n_j (d\sigma_j/dE_\gamma)$ represents the number of photons emitted with energy E_γ by a single electron of initial energy E in a medium with j different species of corresponding densities n_j, and where $(d\sigma_j/dE_\gamma)$ is the Bethe-Heitler differential cross section,

$$
\frac{d\sigma_j(E_\gamma,E)}{dE_\gamma} = {E_\gamma}^{-1}\frac{3}{8\pi}\alpha\sigma_T \left\{\left[1+\left(1-\frac{E_\gamma}{E}\right)^2\right]\phi_{1,j} - \frac{2}{3}\left[1-\frac{E_\gamma}{E}\right]\phi_{j,2}\right\}, \qquad \text{(C.16)}
$$

with $\alpha = 1/137.037$ being the fine structure constant, and $\phi_{1,2}$ being the scattering functions, which depend on E_γ and E. Explicit expressions for the losses can be derived in two cases. In the weak shielding regime, corresponding to low incident electron energies,

where $\phi_i \sim (Z^2 + Z_e)\phi_u$, with $\phi_u = 4(\ln(2(E/mc^2)(E - E_\gamma)/E_\gamma) - 1/2)$, and for an overall neutral plasma ($\sum Z_e = \sum Z$), the result is found to be, by integrating Eq. (C.15), equal to

$$-\left(\frac{dE}{dt}\right)_{\mathrm{Brem},e} = \frac{3\alpha c\sigma_T}{2\pi} E \sum_Z n_Z Z(Z+1)\left[\ln\left(\frac{2E}{mc^2}\right) - \frac{1}{3}\right]. \tag{C.17}$$

In the strong shielding regime, the ϕs are constants, and again integrating Eq. (C.15), the result is

$$-\left(\frac{dE}{dt}\right)_{\mathrm{Brem},e} = \frac{3\alpha c\sigma_T}{8\pi} E \sum_j n_j \left(\frac{4}{3}\phi_{1,j} - \frac{1}{3}\phi_{2,j}\right). \tag{C.18}$$

Assuming a medium composed of hydrogen and helium in proportion 10:1, that the scattering function are related by $\phi_{\mathrm{He}\,1,2}/\phi_{\mathrm{H}\,1,2} \sim 3$, and that $d\sigma_{\mathrm{H}_2}/dE_\gamma = 2d\sigma_{\mathrm{H}}/dE_\gamma$, the sum is $\sum_j n_j d\sigma(E_\gamma, E)/dE_\gamma \sim 1.3\,(n_{\mathrm{H}} + 2n_{\mathrm{H}_2})\,(d\sigma_{\mathrm{H}}(E_\gamma, E)/dE_\gamma)$. This results, taking $\phi_{1,\mathrm{H}} \sim \phi_{2,\mathrm{H}} = \phi_{\mathrm{H}} = 45$, in

$$-\left(\frac{dE}{dt}\right)_{\mathrm{Brem},e} = \frac{3.9 \times 45\,\alpha c\sigma_T}{8\pi} E(n_{\mathrm{H}} + 2n_{\mathrm{H}_2}). \tag{C.19}$$

A useful parameter (Δ) can be defined to decide which formulae is applicable to each situation. Δ is given as a function of the incident electron and the emitted photon energies, $\Delta = E_\gamma mc^2/(4\alpha E(E - E_\gamma))$. A weakly screened plasma corresponds to $\Delta \gg 1$, whereas a totally screened plasma corresponds to $\Delta \ll 1$. In intermediate cases, the fact that $\phi_1 \sim \phi_2$ can still be used, as well as that the mean energy of the emitted electron is $E_\gamma = E/2$, which corresponds to $\Delta = mc^2/(4\alpha E)$. This allow an approximate solution to be obtained (Blumenthal & Gould 1970). In the totally screened case, it is given by Eq. (C.19) but with the replacement of the factor 45 by $\phi_{1,\mathrm{H}}(\Delta)$, whose values are tabulated for different values of $\Delta \lesssim 1$ in Schlickeiser (2002), Table 4.1; the code interpolates between these values, as needed.

C.1.2.5 Triplet photo-pair production

For very high energy [$(E/mc^2)(\bar{\epsilon}/mc^2) \gg 1$] electrons, electron-positron pairs can be generated in electron-photon interactions, $e^- + \gamma \rightarrow e^- + e^+ + e^-$, and it usually referred to as triplet photo-pair production (TPP). This process, then, is important whenever the target-projectile configuration requires the use of the extreme Klein-Nishina limit to compute Compton losses. Differently to the latter, TPP provides a source of secondary electron-positron pairs that may initiate an electromagnetic cascade. However, as shown by Dermer and Schlickeiser (1991), even when the energies involved may require the application of the extreme Klein-Nishina case, in order for the TPP losses to become comparable with the latter, the Compton parameter needs to be $\mathcal{C} \sim 10^5$. For $\mathcal{C} < 10^3$, TPP losses are more than 1 order of magnitude less than those produced under the extreme Klein-Nishina process. This makes TPP losses negligible in the cases under consideration in this Thesis.

C.1.2.6 Adiabatic losses

Finally, we shall consider an adiabatic loss term of the form

$$-\left(\frac{dE}{dt}\right)_{\mathrm{Adia},e} = \frac{V}{R}\left(\frac{E}{\mathrm{GeV}}\right)\mathrm{GeV\ s^{-1}}$$
$$= 3.24\times10^{-14}\left(\frac{V}{100\,\mathrm{km\ s^{-1}}}\right)\left(\frac{100\mathrm{pc}}{R}\right)\left(\frac{E}{\mathrm{GeV}}\right)\mathrm{GeV\ s^{-1}} \quad \text{(C.20)}$$

where V is the collective wind of the region, and R the region radius (e.g. Longair 1994, p. 276). This may be relatively important for starburst regions, where R can be small in comparison with the Galactic extent and V can reach hundreds of km s^{-1}.

C.2 Secondary production processes

For the production of secondary electrons, only knock-on and pion processes are taken into account here. These processes dominate by more than one order of magnitude the production of electrons, at low and high energies respectively, when compared with neutron beta decay (see, e.g., Marscher & Brown 1978 and Morfill 1982 for discussions on this issue).

C.2.1 Electrons from knock-on (or Coulomb) interactions

Knock-on (or Coulomb) collisions are interactions in which the proton transfers an energy far in excess of the typical binding energy of atomic electrons, so producing low-energy relativistic electrons. The cross section for knock-on production was calculated by Bhaba (1938) and subsequently analyzed by Brunstein (1965) and Abraham et al. (1966), among others. The differential probability for the production of an electron of energy E_e and corresponding Lorentz factor $\Gamma_e = E_e/m_ec^2$, within an interval $(\Gamma_e - d\Gamma_e, \Gamma_e + d\Gamma_e)$, produced by the collision between a cosmic ray of particle species j, and energy factor Γ_j and a target of charge Z_i and atomic number A_i is, in units of grammage,

$$\Phi(\Gamma_e,\Gamma_j)d\Gamma_e = \left[\frac{2\pi N_0 Z_i r_e^2 Z_j^2}{A_i(1-\Gamma_j^{-2})}\left(\frac{1}{(\Gamma_e-1)^2} - \frac{s\left(\Gamma_j+\frac{s^2+1}{2s}\right)}{(\Gamma_e-1)\Gamma_j^2} + \frac{s^2}{2\Gamma_j^2}\right)\right]\times$$
$$d\Gamma_e\ \mathrm{cm^2\ g^{-1}}. \quad \text{(C.21)}$$

Here N_0 is the Avogadro's number, $r_e = e^2/mc^2 = 2.82\times10^{-13}$ cm is the classical radius of the electron, and $s = m_e/(A_im_p) \sim 1/1836$ (see below). Note that the probability for interaction is proportional to Z_i/A_i. Then, it will suffice to assume that the interstellar medium is 90% hydrogen and 10% Helium and neglect the contribution of higher atomic numbers. This approximation introduces negligible error. Contributions by various nuclei in the colliding cosmic ray population are more important, since the probability for interaction is proportional to Z_j^2. If the total contribution of all primaries with charge $Z \geq 2$ relative to that of protons is ~ 0.75, then $\sum_i\sum_j \Phi(\Gamma_e,\Gamma_j) \sim 1.75\,\Phi(\Gamma_e,\Gamma_p)$. The maximum transferable energy in this kind of collisions is (e.g., Abraham et al. 1966)

$$\Gamma_{\max} = 1 + \left(\Gamma_p^2 - 1\right)/\{s\left(\Gamma_p + [s^2 + 1/2s]\right)\}. \quad \text{(C.22)}$$

Thus, the maximum possible energy is limited only by the maximum value of Γ_p, while the minimum proton Lorentz factor that is needed to generate an electron of energy E_e is fixed by solving the inequality $\Gamma_e \leq \Gamma_{\rm max}$. The result is that $\Gamma_p \geq \Gamma_1$, with

$$\Gamma_1 = [1/2]s(\Gamma_e - 1) + \sqrt{1 + \frac{1}{2}(1+s^2)(\Gamma_e - 1) + \frac{1}{4}s^2(\Gamma_e - 1)^2}. \quad \text{(C.23)}$$

With this in mind, the source function for knock-on electrons to be considered in the diffusion-loss equation is then given by

$$Q_{\rm knock}(E_e) \sim 1.75\ m_p\ n\ 4\pi\ \int_{E_{1,p}} \Phi(E_e, E_p)\, J_p(E_p)\, dE_p\ , \quad \text{(C.24)}$$

where $E_{1,p} = \Gamma_1\, m_p$, $\Phi(E_e, E_p) = \Phi(\Gamma_e, \Gamma_p)/m_e$, i.e. energies, instead of Lorentz factors, are used to write the final integral, and J_p is the proton intensity[1]

$$J_p(E) = \frac{c\beta}{4\pi} N(E). \quad \text{(C.25)}$$

Examples of the results for the computation of the knock-on source function are given in Figure C.2. As it is shown there, and was first proposed by Abraham et al. (1966), the behavior of the knock-on source function can be well represented by a power law of the form $Q_{\rm knock}(E_e) \sim constant \times (\Gamma_e - 1)^{-\beta}$electrons cm^{-3} s^{-1} GeV^{-1}. An example of such a description can be found in the right panel of Figure C.2, where the spectrum obtained using Eq. (C.24) is superposed to the fit.

C.2.2 Electrons and positrons from charged pion decay

Positron production occurs through muon decay in the reactions $p + p \rightarrow p + \pi^+$ with the pion then decaying as $\pi^+ \rightarrow \mu^+ + \nu_e + \bar{\nu}_\mu$. Electron production occurs, similarly, through, $p + p \rightarrow p + \pi^-$ with the pion then decaying as $\pi^- \rightarrow \mu^- + \bar{\nu}_e + \nu_\mu$. Considering first the latter decays in the frame at rest with the pion, conservation of energy and momentum imply $p_\mu{}' = \left({E_\mu}^{2\prime} - {m_\mu}^2\right)^{1/2} = [{m_\pi}^2 - {m_\mu}^2]/2m_\pi$, where $m_{\mu,\pi}$ are the masses of the muon and pion, respectively, E are total energies and the prime is used to represent the pion rest frame. This implies that the energy of the pion in such frame is $\Gamma_\mu{}' = E_\mu{}'/m_\mu = [{m_\pi}^2 + {m_\mu}^2]/[2m_\pi m_\mu] \sim 1.04$. The value of $\Gamma_\mu{}'$ implies, as long as the velocity of the pion in the laboratory frame is not exceedingly small ($\Gamma_\pi > 1.04$), that the muon is practically at rest in the rest frame of the pion, and that as seen from the lab, $\Gamma_\mu \sim \Gamma_\pi$. Then, per unit Lorentz factor, the muon emissivity is equal to that of the pion

$$Q_{\pi^+}(\Gamma_{\pi^+}) = Q_{\mu^+}(\Gamma_{\mu^+})\ \ ;\ \ Q_{\pi^-}(\Gamma_{\pi^-}) = Q_{\mu^-}(\Gamma_{\mu^-}). \quad \text{(C.26)}$$

The charged pion emissivity resulting from an isotropic distribution of protons $J_p(E_p)$ interacting with –fixed target– nuclei found with number density n can be computed as

[1]Note that for the computation of secondary electrons, sometimes it is more convenient to use $Q(\Gamma)$, the emissivity as a function of the electron Lorentz factor, instead of $Q(E)$. They are related by $Q(\Gamma)d\Gamma = Q(E)dE$, then $Q(\Gamma)$-units are cm^{-2} s^{-1} sr^{-1} unit-Γ^{-1}. In order to convert electron and positron emissivities expressed as a function of Γ to those expressed as a function of energy, which are those entering into the expression of the diffusion-loss equation adopted, one has then to divide by the electron mass. Note also that the equality $J_p(\Gamma)d\Gamma = J_p(E)dE$ holds. Similarly, the relationship between $\Phi(E_e, E_p)$ and $\Phi(\Gamma_e, \Gamma_p)$ can be obtained.

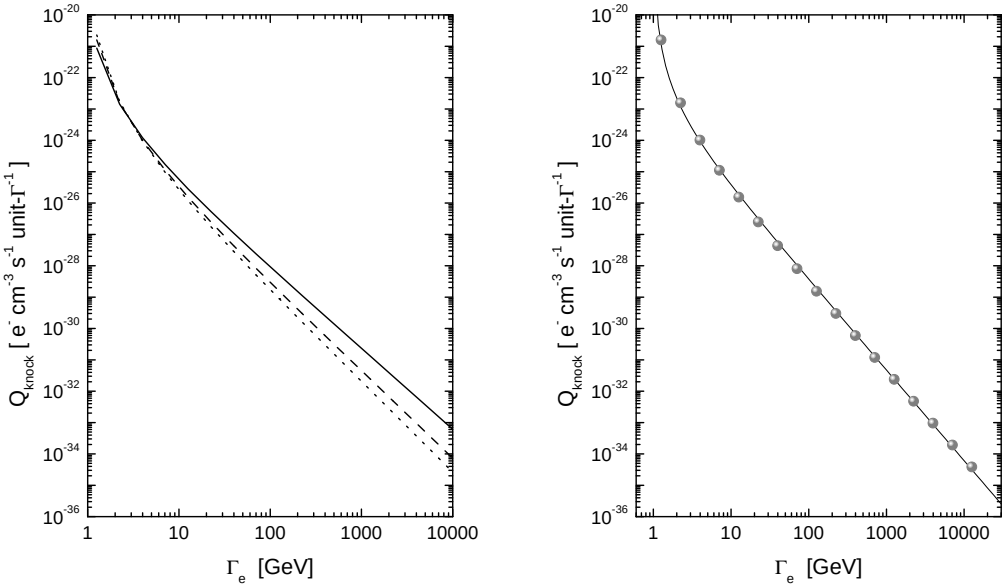

Figure C.2: Left: Knock-on source function for different cosmic ray intensity $J_p(E_p) = A(E_{\rm kin}/{\rm GeV})^{\alpha}$ protons cm^{-2} s^{-1} sr^{-1} GeV^{-1}. The source function is normalized by taking an ISM density ($n = 1$ cm^{-3}) and unit normalization of the incident proton spectrum, A=1. Curves shown are, from top to bottom, the corresponding to $\alpha = -2.1, -2.5$, and -2.7. Right: Simple power law fit of the knock-on source function for $\alpha = -2.5$. Similar fits can be plotted for all values of α. From Torres (2004).

that of the neutral pions, by just changing the spectral distribution

$$Q_{\pi^{\pm}}(\Gamma_{\pi^{\pm}}) = 4\pi n \int_{\Gamma_{th}(\Gamma_{\pi^{\pm}})} d\Gamma_p \, J_p(\Gamma_p) \frac{d\sigma(\Gamma_{\pi^{\pm}}, \Gamma_p)}{d\Gamma_{\pi^{\pm}}} \, , \tag{C.27}$$

where $\Gamma_{th}(\Gamma_{\pi^{\pm}})$ is the minimum proton Lorentz factor required to produce a pion (either positively or negatively charged) with Lorentz factor $\Gamma_{\pi^{\pm}}$. Thus, knowledge of the spectral distribution $d\sigma(\Gamma_{\pi^{\pm}}, \Gamma_p)/d\Gamma_{\pi^{\pm}}$ secures knowledge of the muon emissivity. The spectral distribution as a function of incident proton kinetic energy in the lab frame ($T_{\rm lab}$) and the lab kinetic energy of the produced pion (T_{π}) were recently parameterized by Blattnig et al. (2000). The formulae used in the code corresponds to the numerical integration of the LIDCS charged pion parameterizations due to Badhwar et al. (1977). These parameterizations are divided into two regions, corresponding to low (0.3 GeV to 2 GeV) and high (2 GeV to 50 GeV) laboratory kinetic energies ($T_{\rm lab}$). The high end of the parameterizations is defined by the energy up to which there were tested against experiments by Blattnig et al. (2000). At higher energies, neutral pion decay greatly dominates the emission of γ-rays, so that secondary electrons play a much less important role in the situations analyzed in this Thesis, and uncertainties in the cross section parameterization can be disregarded. Kamae et al. (private communication) are also to present newer parameterizations for the differential cross section of charged pion decay.

The positively charged pion spectral distribution for the range 0.3 - 2 GeV, used in

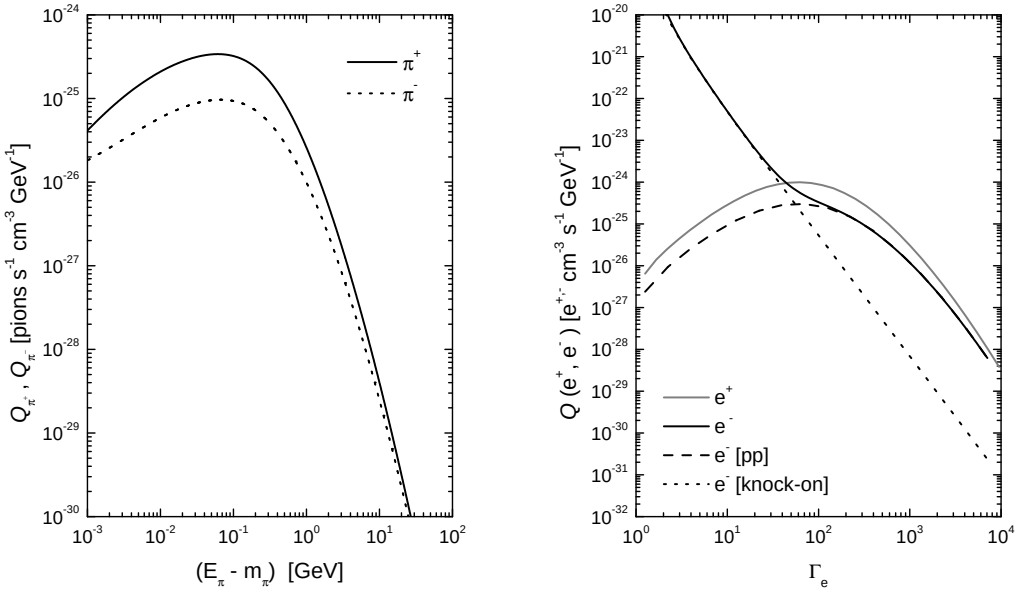

Figure C.3: Left: $\pi^{\pm}$-emissivities produced using Blattnig et al.'s parameterizations of Bhadwar et al.'s (1977) spectral distribution. Right: $e^{\pm}$-emissivities. In the case of electrons, the total emissivity adds up that produced by knock-on interactions, which dominates at low energies. In both panels, $n = 1$ cm^{-3}, and an Earth-like proton spectrum ($\propto E^{-2.75}$) are assumed. From Torres (2004).

the code, is represented by (Blattnig et al. 2000):

$$\begin{aligned} F_2 &= C_1 T_\pi^{C_2} + C_3 T_{\rm lab}^{C_4} \\ F_1 &= \exp(C_5 + \frac{C_6}{\sqrt{T}_{\rm lab}} + C_7 T_{\rm lab}^{C_8} + C_9 T_\pi^{C_{10}} + C_{11} T_\pi^{C_{12}} T_{\rm lab}^{C_{13}} + C_{14} \ln T_{\rm lab}) \\ \left(\frac{d\sigma}{dE}\right)_{\rm lab} &= C_{15} T_\pi^{C_{16}} \frac{F_1}{F_2} + C_{17} T_\pi^{C_{18}} \exp(C_{19}\sqrt{T_\pi} + C_{20}\sqrt{T_{\rm lab}}), \end{aligned} \tag{C.28}$$

whereas at higher energies is

$$\begin{aligned} F_2 &= D_1 T_\pi^{D_2} + D_3 T_{\rm lab}^{D_4} \\ F_1 &= \exp(D_5 + \frac{D_6}{\sqrt{T}_{\rm lab}} + D_7 T_\pi^{D_8} + D_9 T_\pi^{D_{10}}) \\ \left(\frac{d\sigma}{dE}\right)_{\rm lab} &= D_{11} T_\pi^{D_{12}} \frac{F_1}{F_2} + D_{13} T_\pi^{D_{14}} \exp(D_{15}\sqrt{T_\pi} + D_{16} T_{\rm lab}^{D_{17}}). \end{aligned} \tag{C.29}$$

The negatively charged pion spectral distribution for the range 0.3 - 2 GeV, used in the code, is represented by (Blattnig et al. 2000):

$$\begin{aligned} F_2 &= G_1 T_\pi^{G_2} + G_3 T_{\rm lab}^{G_4} \\ F_1 &= \exp(G_5 + \frac{G_6}{\sqrt{T}_{\rm lab}} + G_7 T_\pi^{G_8} + G_9 T_\pi^{G_{10}}) \\ \left(\frac{d\sigma}{dE}\right)_{\rm lab} &= T_\pi^{G_{11}} (G_{12} \frac{F_1}{F_2} + G_{13} \exp(G_{14}\sqrt{T}_\pi)) \end{aligned} \tag{C.30}$$

Table C.1: Constants in the parameterizations of the differential cross sections for the production of charged pions.

$C_1 = 2.2 \times 10^{-8}$	$D_1 = 4.5 \times 10^{-11}$	$G_1 = 1.06 \times 10^{-9}$	$H_1 = 2.39 \times 10^{-10}$
$C_2 = -2.7$	$D_2 = -2.98$	$G_2 = -2.8$	$H_2 = -2.8$
$C_3 = 4.22 \times 10^{-7}$	$D_3 = 1.18 \times 10^{-9}$	$G_3 = 3.7 \times 10^{-8}$	$H_3 = 1.14 \times 10^{-8}$
$C_4 = -1.88$	$D_4 = -2.55$	$G_4 = -1.89$	$H_4 = -2.3$
$C_5 = 22.3$	$D_5 = 22.3$	$G_5 = 22.3$	$H_5 = 22.3$
$C_6 = 1.98$	$D_6 = -0.765$	$G_6 = -1.5$	$H_6 = -2.23$
$C_7 = -0.28$	$D_7 = -35.3$	$G_7 = -30.5$	$H_7 = -31.3$
$C_8 = -1.75$	$D_8 = 0.0938$	$G_8 = 0.0938$	$H_8 = 0.0938$
$C_9 = -29.4$	$D_9 = -22.5$	$G_9 = -24.6$	$H_9 = -24.9$
$C_{10} = 0.0938$	$D_{10} = 0.0313$	$G_{10} = 0.0313$	$H_{10} = 0.0313$
$C_{11} = -24.4$	$D_{11} = 2.5 \times 10^6$	$G_{11} = 0.25$	$H_{11} = 2.5 \times 10^6$
$C_{12} = 0.0312$	$D_{12} = 0.25$	$G_{12} = 2.5 \times 10^6$	$H_{12} = 0.25$
$C_{13} = 0.0389$	$D_{13} = 60322$	$G_{13} = 7.96$	$H_{13} = 60322$
$C_{14} = 1.78$	$D_{14} = 1.18$	$G_{14} = -49.5$	$H_{14} = 1.1$
$C_{15} = 2.5 \times 10^6$	$D_{15} = -72.2$		$H_{15} = -65.9$
$C_{16} = 0.25$	$D_{16} = 0.941$		$H_{16} = -9.39$
$C_{17} = 976$			$H_{17} = -1.25$
$C_{18} = 2.3$			
$C_{19} = -46$			
$C_{20} = -0.989$			

whereas at higher energies is

$$\begin{aligned} F_2 &= H_1 T_\pi^{H_2} + H_3 T_{\rm lab}^{H_4} \\ F_1 &= \exp(H_5 + \frac{H_6}{\sqrt{T}_{\rm lab}} + H_7 T_\pi^{H_8} + H_9 T_\pi^{H_{10}}) \\ \left(\frac{d\sigma}{dE}\right)_{\rm lab} &= H_{11} T_\pi^{H_{12}} \frac{F_1}{F_2} + H_{13} T_\pi^{H_{14}} \exp(H_{15}\sqrt{T_\pi} + H_{16} T_{\rm lab}^{H_{17}}). \end{aligned} \quad \text{(C.31)}$$

Constants of all the parameterizations are given in Table C.1.

Figure C.3, left panel, shows an example of the π^+– and π^-–emissivity. The electron and positron emissivities are computed as a three-body decay process (see, e.g. Schlickeiser 2002, p. 115):

$$Q_{e^\pm}(\Gamma_{e^\pm}) = \int_1^{\Gamma_e{}'^{\rm max}} d\Gamma_e{}' \frac{1}{2} \frac{P(\Gamma_e{}')}{\sqrt{\Gamma_e{}'^2 - 1}} \int_{\Gamma_{\mu 1}}^{\Gamma_{\mu 2}} d\Gamma_\mu \frac{Q_{\mu^\pm}(\Gamma_{\mu^\pm})}{\sqrt{\Gamma_\mu{}^2 - 1}}. \quad \text{(C.32)}$$

Here $\Gamma_e{}'^{\rm max} = 104$, $\Gamma_{\mu 1,\mu 2} = \Gamma_{e^\pm}\Gamma_e{}' \mp \sqrt{\Gamma_e{}'^2 - 1}\sqrt{\Gamma_e{}^2 - 1}$, and the function P is $P(\Gamma_e{}') = 2\Gamma_e{}'^2 \left[3 - \frac{2\Gamma_e{}'}{\Gamma_e{}'^{\rm max}}\right] / (\Gamma_e{}'^{\rm max})^3$. Figure C.3, right panel, shows an example of the e^+– and e^-–emissivity, as implemented in the code. These results are compatible with previous computations.

Finally, in Figure C.4 we compare the inclusive cross sections for charged pions with experimental data up to about 1 TeV, which are again found in agreement with

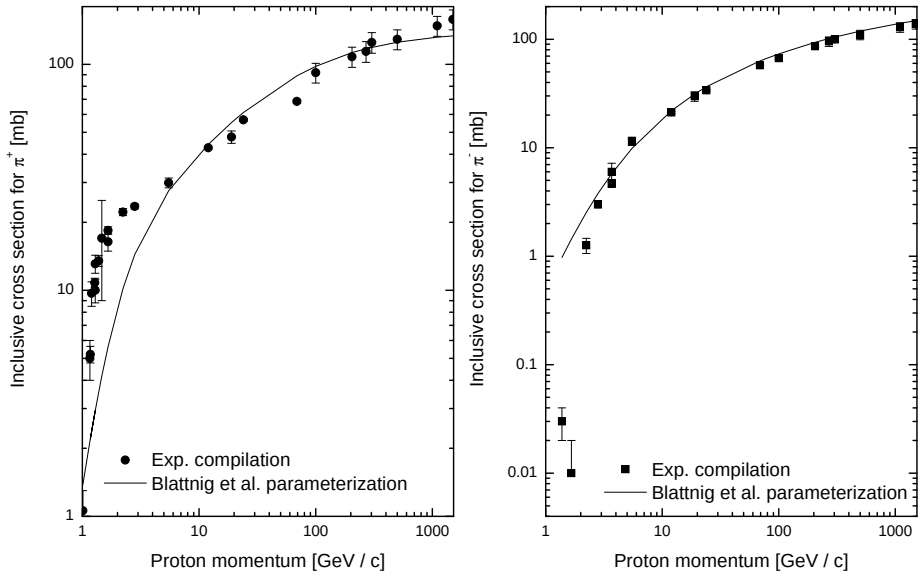

Figure C.4: Comparing inclusive cross sections for charged pions. Solid curves are obtained from Equations (30) and (31) of Blattnig et al.'s work (2000b), and experimental compilation is from Dermer (1986b).

experimental data (except for a bunch of data points at low proton energies, in the case of positive charged pions). In any case, for situations where the density of cosmic rays or of target nuclei or both are high, neutral pion decay is expected to be the dominant process above 100 MeV, so that possible uncertainties in parameterizations of charged pions cross sections are not expected to play a significant role in the prediction of fluxes.

C.3 Radiative processes

The population of relativistic cosmic ray protons and electrons, resultant from the above processes of production and energy losses, will emit photons in a wide range of wavelengths through a diversity of processes. They are described below.

C.3.1 Radio and Infrared emission

The radio spectrum is mainly conformed by the synchrotron emission of relativistic electrons under the effect of an intense magnetic field. The resultant spectrum is modulated by free-free absorption due to the presence of a plasma medium. Infrared spectrum is basically characterized by the remission of photons from the dust particles present in the medium.

C.3.1.1 Synchrotron emission

The synchrotron radiation of a population of relativistic electrons and positrons is computed starting from the energy emitted per unit time per unit frequency interval, as a function of frequency, which is given by (e.g., Kembhavi & Narlikar 1999, p. 34)

$$P(E,\nu) = \sqrt{3}(eB)\,\sin\alpha\,F(\nu/\nu_c)\,\frac{e^2}{mc^2}. \tag{C.33}$$

Here, in convenient units,

$$\nu_c = 3eB\,\sin\alpha\,\frac{E/(mc^2)^2}{4\pi mc} = 16.1\left(\frac{B\sin\alpha}{\mu\mathrm{Gauss}}\right)\left(\frac{E}{\mathrm{GeV}}\right)^2\,\mathrm{MHz} \tag{C.34}$$

is the critical frequency, and

$$F(x) = x\int_x^\infty K_{5/3}(\xi)d\xi, \tag{C.35}$$

with $K_{5/3}$ being the modified Bessel function of order 5/3. The power emitted by all electrons, units of GeV s^{-1} cm^{-3} Hz^{-1} sr^{-1}, is $\epsilon_{\rm Sync}(\nu) = (1/4\pi)\int dE\,N(E)\,P(E,\nu)$. Then, the synchrotron emissivity can be written as

$$\epsilon_{\rm Sync}(\nu) = 1.166\times10^{-20}\left(\frac{B}{\mathrm{Gauss}}\right)\int dE\,N(E)\int_0^{\pi/2}d\alpha\,\frac{\nu}{\nu_c}\sin^2\alpha\int_{\nu/\nu_c}^\infty d\xi K_{5/3}(\xi)$$
$$\mathrm{GeV\,s^{-1}\,cm^{-3}\,Hz^{-1}\,sr^{-1}}. \tag{C.36}$$

A useful result, see below, is given by the product of $\epsilon_{\rm Sync}$ and V/D^2, $f_{\rm Sync}(\nu)$. This is the synchrotron flux density (units of Jy)[2] expected from a region of volume V located at a distance D in cases in which opacities are negligible, see below. If B is measured in Gauss, and units of distance, time, and energy are as in the rest of the paper cm, s, and GeV, respectively, the synchrotron flux density in Jy is given by

$$f_{\rm Sync}(\nu) = 1.868\left(\frac{B}{\mathrm{Gauss}}\right)\left(\frac{V/D^2}{\mathrm{cm}}\right)\int dE\,N(E)\int_0^{\pi/2}d\alpha\,\frac{\nu}{\nu_c}\sin^2\alpha\int_{\nu/\nu_c}^\infty d\xi K_{5/3}(\xi)\ \mathrm{Jy}. \tag{C.37}$$

In cases where opacities are not negligible, one has to solve first for the specific intensity considering all absorption processes, compute the emissivity, and then consider the geometry through the factor $[\Omega L]_{\rm obs}$. We give details on this below.

C.3.1.2 Free-free emission and absorption

The radiation due to the deflection of a charge in a Coulomb field of another charge in a plasma is known as free-free emission or thermal bremsstrahlung, and contributes to the continuum radiation at cm-wavelengths. The emission ($\epsilon_{\rm ff}$) and absorbtion coefficients ($\kappa_{\rm ff}$) for this process are given by (e.g., Rybicki & Lightman 1979, Ch. 5, Schlickeiser 2002, Ch. 6)

$$\epsilon_{\rm ff}(\nu) = 3.37\times10^{-36}Z^2\left(n_e n_i/\mathrm{cm^{-6}}\right)(T/\mathrm{K})^{-1/2}\,(\nu/\mathrm{GHz})^{-0.1}\,e^{-h\nu/kT}\times$$
$$\mathrm{GeV\,cm^{-3}\,s^{-1}\,Hz^{-1}\,sr^{-1}} \tag{C.38}$$

$$\kappa_{\rm ff}(\nu) = 2.665\times10^{-20}Z^2\,(T/\mathrm{K})^{-1.35}\left(n_e n_i/\mathrm{cm^{-6}}\right)(\nu/\mathrm{GHz})^{-2.1}\,\mathrm{cm^{-1}}, \tag{C.39}$$

respectively. Here, the plasma is described by a temperature T, metallicity Z and thermal electron and ion densities n_e and n_i, respectively. The free-free opacity is given by $\tau_{\rm ff}\equiv\int_0^\infty dr\,\kappa_{\rm ff}\sim 8.235\times10^{-2}\,(T/\mathrm{K})^{-1.35}\,(\nu/\mathrm{GHz})^{-2.1}\left(\mathrm{EM/cm^{-6}\,pc}\right)$, where EM is the emission measure, defined as EM$=\int_0^\infty dr\,n_i n_e$. For simplicity, and in lack of other knowledge, it is assumed that the EM is constant. The turnover frequency ν_t (for

[2]This would be given in units of GeV s^{-1} Hz^{-1} cm^{-2} which can be written as Jy. The conversion is 1 Jy$=10^{-26}$ Watt m^{-2} Hz^{-1}.

frequencies less than ν_t the emission is optically thick) can also be given in terms of EM, $\nu_t = 0.3[(T/\mathrm{K})^{-1.35}\mathrm{EM}]^{1/2}$ GHz. Again, an useful quantity is $f_{\rm ff}(\nu) = \epsilon_{\rm ff}(\nu)(V/D^2)$.

Given the EM, the temperature, and the size of the emitting region, the free-free emission is completely specified. In what follows these emissivities are transformed by taking into account the absorption process, this finally yields to the predicted observed fluxes.

C.3.1.3 Dust emission

We assume that the dust photon emissivity, which dominates the luminosity at micron frequencies, is given by $q_d = q_0 \epsilon^\sigma B(\epsilon, T)$, where $\sigma \sim 1-2$ is the emissivity index, $B(\epsilon, T)$ is the Planck function of temperature T,

$$B(\epsilon, T) = \frac{2\epsilon^3}{(hc)^2(\exp(\epsilon/kT) - 1)}, \tag{C.40}$$

and ϵ is the photon energy (see, e.g., Krügel 2003, p.245). Units correspond to $[q_d] =$ photons s^{-1} cm^{-2}. Then, the flux produced by dust can be computed as

$$F = 2\pi \int_0^{\pi/2} q_d \cos\theta \sin\theta d\theta d\epsilon = \pi \int q_d d\epsilon \tag{C.41}$$

and normalized to $[L/4\pi R^2]$, with L and R being the IR luminosity and radius of the emitting region, respectively; i.e., normalized to the power per unit area through the surface of the emitting region. This fixes the dimensional constant to

$$q_0 = [L/4\pi R^2][hc]^2[2\pi]^{-1}[(kT)^{4+\sigma}\Gamma(4+\sigma)\mathcal{Z}(4+\sigma)]^{-1}, \tag{C.42}$$

where Γ and $\mathcal{Z}$ are the Gamma and Zeta functions. Units are such that $[q_0] =$ GeV$^{-1-\sigma}$ s^{-1}, and $[B(\epsilon, T)] =$ GeV cm^{-2}. The flux density of dust emission at the surface of the emitting region is obtained from the definition $F \equiv \int f_{\rm dust}(\nu) d\nu$, where units are, for consistency, $[f_{\rm dust}] =$ s^{-1} cm^{-2} Hz^{-1} GeV. At a distance D, it is then given by

$$f_{\rm dust} = h\frac{L}{4\pi R^2}\frac{1}{(kT)^{4+\sigma}\Gamma(4+\sigma)\mathcal{Z}(4+\sigma)}\frac{(h\nu)^{3+\sigma}}{\exp(h\nu/kT) - 1}\frac{R^2}{D^2}, \tag{C.43}$$

i.e., it is diluted by the last factor in the previous equation. Note that $f_{\rm dust}$ is completely specified given T, L, R, and σ. The IR photon number density per unit energy, $n(\epsilon)$, can be obtained by equating the particle flux outgoing the emission region, $\pi R^2 cn(\epsilon)\epsilon d\epsilon$, with the expression of the same quantity that make use of the emissivity law, $4\pi R^2 \pi q(\epsilon) d\epsilon$. This results in

$$n(\epsilon) = \frac{L}{\pi R^2 c}\frac{1}{(kT)^{4+\sigma}\Gamma(4+\sigma)\mathcal{Z}(4+\sigma)}\frac{\epsilon^{2+\sigma}}{\exp(\epsilon/kT) - 1} \tag{C.44}$$

When $\sigma = 0$, the photon distribution is known as a pure graybody, also known as a dilute blackbody: it has the same energy dependence than the latter but the photon number density is smaller by the dilution factor $[L/\pi R^2 c]15(\hbar c)^3/(\pi^2(kT)^4)$. The total photon density per unit energy may contain contributions of one or several graybodies (e.g. a cool and a warm component are needed to fit typical emission profiles in the IRAS band, Rodriguez-Espinosa et al. 1996) plus the undiluted CMB bath, $n(\epsilon) = (\pi^2(\hbar c)^3)^{-1}\epsilon^2/(\exp(\epsilon/kT) - 1)$. It is with this total photon density that inverse Compton processes are computed.

C.3.2 High energy emission

Hadronically-generated γ-ray emission is separately described in Appendix B. The leptonic contribution to the γ-ray spectrum is formed by bremsstrahlung and inverse Compton high energy photons, processes which are briefly described below.

C.3.2.1 Bremsstrahlung

The bremsstrahlung emissivity can be computed from the steady cosmic ray electron spectrum as the integral

$$Q_\gamma(E_\gamma)_{\rm Brem} = {E_\gamma}^{-1} \int_{E_\gamma}^{\infty} dE_e \, N_e(E_e) \, P_B(E_\gamma, E), \tag{C.45}$$

where

$$P_B(E_\gamma, E) = E_\gamma(dN/dt \, dE_\gamma) = cE_\gamma \sum_j n_j (d\sigma_j(E_\gamma, E)/dE_\gamma) \tag{C.46}$$

is the bremsstrahlung power emitted by a single electron. Assuming again a medium composed of hydrogen and helium in proportion 10:1, that the scattering function are related by $\phi_{\rm He\,1,2}/\phi_{\rm H\,1,2} \sim 3$, and that $d\sigma_{\rm H_2}/dE_\gamma = 2d\sigma_{\rm H}/dE_\gamma$, the sum is

$$\sum_j n_j d\sigma(E_\gamma, E)/dE_\gamma \sim 1.3(n_{\rm H} + 2n_{\rm H_2}) d\sigma_{\rm H}(E_\gamma, E)/dE_\gamma. \tag{C.47}$$

Finally, the integral (C.45) can be computed, within the strong shielding regime, ($\Delta \ll 1$, $E > 15\, mc^2/Z$) where $\phi_{\rm H\,1,2} \sim 45$ as

$$Q_\gamma(E_\gamma)_{\rm Brem} = n \, {E_\gamma}^{-1} \int_{E_\gamma}^{\infty} dE_e \, c \, N_e(E_e) \, \sigma_{\rm Brem}, \tag{C.48}$$

where $\sigma_{\rm Brem}$ is the bremsstrahlung cross section, equal to 3.38×10^{-26} cm^2, and $n = (n_{\rm H} + 2n_{\rm H_2})$ is the ISM atomic hydrogen density. If the spectrum of electrons is a power law of index p, the bremsstrahlung spectrum is a power law with the same index, i.e., if

$$J_e(E_e) = \frac{\beta N_e(E_e)}{4\pi} \, {\rm electrons\,GeV^{-1}\,cm^{-2}\,s^{-1}} \tag{C.49}$$

is the electron spectrum, with $N_e(E_e) = B{E_e}^{-\Gamma}$, the bremsstrahlung emission can then be analytically computed as

$$Q_\gamma(E_\gamma)_{\rm Brem} = \frac{n \, c\sigma_{\rm Brem}}{\Gamma - 1} B {E_\gamma}^{-\Gamma} {\rm GeV^{-1}\,cm^{-3}\,s^{-1}}. \tag{C.50}$$

C.3.2.2 Inverse Compton

The inverse Compton emissivity is given by (e.g. Blumenthal & Gould 1970)

$$Q_\gamma(E_\gamma)_{\rm IC} = \int_0^\infty n_{\rm ph}(\epsilon) d\epsilon \int_{E_{\rm min}}^{E_{\rm max}} \frac{d\sigma(E_\gamma, \epsilon, E_e)}{dE_\gamma} \, c \, N_e(E_e) dE_e \, . \tag{C.51}$$

The total number of photons per unit volume in the target field and their mean energy density are given by

$$n_{\rm ph} = \int n_{\rm ph}(\epsilon) d\epsilon, \tag{C.52}$$

and

$$\bar{\epsilon} = \int \epsilon \, n_{\rm ph}(\epsilon) d\epsilon / n_{\rm ph}, \tag{C.53}$$

respectively. $E_{\rm max}$ is the maximum electron energy for which the distribution $N_e(E_e)$ is valid. $E_{\rm min}$ is the minimum electron energy needed to generate a photon of energy E_γ, i.e. $E_{\rm min} = (E_\gamma/2)[1 + (1 + (mc^2)^2/\epsilon E_\gamma)^{1/2}]$.[3] When $d\sigma(E_\gamma, \epsilon, E_e)/dE_\gamma$ is given by its Thomson expression, i.e., when the Compton parameter is $\mathcal{C} \ll 1$,

$$\frac{d\sigma(E_\gamma, \epsilon, E_e)}{dE_\gamma} = \frac{\pi r_e^2 (mc^2)^4}{4\epsilon^2 E_e^3} \left\{ \frac{2E_\gamma}{E_e} - \frac{(mc^2)^2 {E_\gamma}^2}{\epsilon E_e^3} + \frac{4E_\gamma}{E_e} \ln\left(\frac{(mc^2)^2 E_\gamma}{4\epsilon E^2} \right) + \frac{8\epsilon E_e}{(mc^2)^2} \right\}, \tag{C.54}$$

the electron spectrum is a power law ($N_e(E_e) = B{E_e}^{-p}$), and the target photon distribution $n_{\rm ph}(\epsilon)$ is a blackbody, an analytical expression for $Q_\gamma(E_\gamma)_{\rm IC}$ can be obtained (see e.g. Stecker 1977, Ginzburg & Syrovatskii 1964, p. 393). The result is

$$Q_\gamma(E_\gamma)_{\rm IC} = f(\Gamma) \frac{2c\sigma_T U_{\rm ph} (mc^2)^{1-p}}{3} \left(\frac{4}{3}\bar{\epsilon} \right)^{(p-3)/2} B E_\gamma^{-(p+1)/2} \tag{C.55}$$

where $f(\Gamma)$ is a slowly-varying, analytically defined, numerical correction factor which depends only on the slope of the electron spectrum: $f(2) = 0.86$, $f(3) = 0.99$. This is not true if the photon density or the electron distribution have a more complex expression.

C.4 Opacities to γ-ray escape

γ-rays generated in an astrophysical environment, however, will not always be able to escape out of it without being partially or even completely absorbed in the dense radiation and matter fields. Two sources of opacities are considered here: pair production from the γ-rays interaction with the photon field or with the charged nucleus present in the medium. Compton scattering and attenuation in the magnetic field by one-photon pair production are negligible in comparison.

The opacity to $\gamma\gamma$ pair production with the photon field, which, at the same time, is target for inverse Compton processes, can be computed as:

$$\tau(R_c, E_\gamma)^{\gamma\gamma} = \int \int_{R_c}^{\infty} n(\epsilon) \sigma_{e^-e^+}(\epsilon, E_\gamma)^{\gamma\gamma} dr \, d\epsilon \,, \tag{C.56}$$

where ϵ is the energy of the target photons, E_γ is the energy of the γ-ray in consideration and R_c is the place where the γ-ray photon was created within the system. The cross section for $\gamma\gamma$ pair production (e.g. Cox 1999, p.214) is given by:

$$\sigma_{e^-e^+}(\epsilon, E_\gamma)^{\gamma\gamma} = \left(\frac{3\sigma_T}{16} \right) (1 - \beta^2) \left(2\beta(\beta^2 - 2) + (3 - \beta^4) \ln\left(\frac{(1+\beta)}{(1-\beta))} \right) \right) , \tag{C.57}$$

with $\beta = (1 - (mc^2)^2/(\epsilon \, E_\gamma))^{1/2}$ and σ_T being the Thomson cross section. Note that the lower limit of the integral on ϵ in the expression for the opacity is determined from the condition that the center of mass energy of the two colliding photons should be such that

[3] A fixed $E_{\rm max}$ implies that, for a given resulting upscattered photon energy, there is also a minimum energy for the photon targets in the first integral of the IC flux. Target photons with less than this energy do not contribute to the flux at the upscattered energy in question.

$\beta > 0$. The fact that the dust within the starburst reprocesses the UV star radiation to the less energetic infrared photons implies that the opacities to $\gamma\gamma$ process is significant only at the highest energies. Therefore, the maximum opacity will be determined by the maximum linear size of the emitting region in the direction to the observer, which in the case of a molecular disk of height h and inclination angle i implies:

$$\tau(R_c, E_\gamma)^{\gamma\gamma} < \tau(E_\gamma)^{\gamma\gamma}_{\rm max} \frac{h}{\cos i} \int_0^\infty n(\epsilon)\sigma_{e^-e^+}(\epsilon, E_\gamma) d\epsilon \,. \tag{C.58}$$

The opacity to pair production from the interaction of a γ-ray photon in the presence of a nucleus of charge Z needs to be considered too. Its cross section in the completely screened regime ($E_\gamma/mc^2 \gg 1/(\alpha Z)$) is independent of energy, and is given by (e.g. Cox 1999, p.213):

$$\sigma^{\gamma Z}_{e^-e^+} = \frac{3\alpha Z^2 \sigma_T}{2\pi} \left(\frac{7}{9} \ln\left(\frac{183}{Z^{1/3}} \right) - \frac{1}{54} \right) . \tag{C.59}$$

At lower energies the relevant cross section is that of the no-screening case, which is logarithmically dependent on energy:

$$\sigma^{\gamma Z}_{e^-e^+} = \frac{3\alpha Z^2 \sigma_T}{2\pi} (7/9 \ln\left(\frac{2E_\gamma}{mc^2} \right) - 109/54) \,, \tag{C.60}$$

and matches the complete screening cross section at around 0.5 GeV. Both of these expression are used to compute the opacity, depending on E_γ. Use of the fact that the cross section, in typical ISM mixtures of H and He, is ~ 1.3 times bigger than that of H with the same concentration, is also made and the opacity is accordingly increased (see, e.g., Ginzburg & Syrovatskii 1964, p. 30).

C.5 Radiation transport equation and fluxes from emissivities

The predicted total continuum emission, in any wavelength, is obtained using the equation of radiation transport. In particular, this paper analyzes the case in which emission and absorption are uniform, co-spatial, and without further background or foreground sources or sinks (see, e.g., Appendix A in Schlickeiser 2002). The solution to the radiation transport equation in these situations is

$$I_\nu = \frac{\epsilon_\nu}{\kappa_\nu}(1 - e^{-\tau_\nu}), \tag{C.61}$$

where ϵ_ν is the emission coefficient –or emissivity–, κ_ν is the absorption coefficient, and $\tau_\nu = \kappa_\nu L$ is the opacity in the far end (L) of the emission region (also referred to as the maximum opacity). In cases in which there are more than one process involved in the emission or in the absorption, a sum over processes must be performed, i.e. $\epsilon_\nu \rightarrow \sum_j \epsilon^j_\nu$, $\kappa_\nu \rightarrow \sum_j \kappa^j_\nu$, and $\tau_\nu \rightarrow \sum_j \tau^j_\nu$. Units are consistent with the rest of the paper, such that $[\epsilon_\nu]$ = GeV cm^{-3} s^{-1} sr^{-1} Hz^{-1} (in the case of γ-rays, photon emissivities are used instead, $Q/4\pi$, with units of photons cm^{-3} s^{-1} sr^{-1} GeV^{-1}), $[\kappa_\nu]$ =cm^{-1}, and $[\tau] = 1$. Additionally, I_ν is the emergent intensity ($[I_\nu]$ =GeV cm^{-2} s^{-1} sr^{-1}) after the absorption processes are considered. Consider first the case in which opacities are negligible. To compute the flux, given the knowledge of its emissivity under a particular

process, information on the solid angle -as seen from the observer- (Ω) and depth (L) along the line of sight, or volume and distance of the region of emission is needed. For instance, the integral flux of γ-rays, with no absorption, is given by

$$F_\gamma(E_\gamma > E) = \int_E^\infty Q_\gamma(E_\gamma)\frac{[\Omega L]_{\rm obs}}{4\pi}dE_\gamma = \frac{V}{4\pi D^2}\int_E^\infty Q_\gamma(E_\gamma)dE_\gamma, \tag{C.62}$$

where $Q_\gamma(E_\gamma) = Q_\gamma(E_\gamma)_{\rm Brem} + Q_\gamma(E_\gamma)_{\rm IC} + Q_\gamma(E_\gamma)_{\pi^0}$ is the total γ-ray emissivity, and $[\Omega L]_{\rm obs}/4\pi$ corrects for the fraction of the emission which is in the direction of the observer. Clearly, in this case, the differential photon flux is $F_\gamma(E_\gamma) = [V/4\pi D^2]Q_\gamma(E_\gamma)$. The second equality in the previous equation is obtained as follows. With θ representing the deviation from the line of sight to the center of the emission region, the flux is then expressed as

$$F = \int I[\cos\theta]\, d\Omega \tag{C.63}$$

$$= \int_0^{2\pi}\int_0^{\theta_{\rm max}} \epsilon\,[2R\cos\theta']\,[\cos\theta][\sin\theta]\,d\theta\,d\phi. \tag{C.64}$$

Here, $[2R\cos\theta']$ is the lineal size of the sphere at an angle θ' from its center (the size in the direction of the observer), and I is the specific intensity of the source. Using the sin theorem, $\sin\theta' = [D/R]\sin\theta$, and thus $\cos\theta' = \{1-[D/R]^2\sin^2\theta\}^{1/2}$. Integrating the previous expression yields to the result $F = 2\pi\epsilon(2R)\{-(R/D)^2(1/3)[1-D^2\sin^2\theta/R^2]^{3/2}\}$, which, evaluated between 0 and $\theta_{\rm max}$, and taking into account that $\sin\theta_{\rm max} = R/D$, reduces the flux to $F = \epsilon V/D^2$. Note that an essential point is that ϵ was assumed independent of position, and that $I = \epsilon \times linear\ size$ was used. In the case of a molecular disk, the linear size in the direction of the observer is assumed constant; i.e. for a disk with inclination from face-on equal to i, and height h, it is $h/\cos i$. Thus, if the disk has a radius R, $[\Omega L]_{\rm obs} = (h/\cos i)\times\Delta\hat{A}$, where $\Delta\hat{A} = (\pi R^2)\cos i/D^2$ is the projected area of the source, perpendicular to the line of sight. Thus the same factor is recovered to transform from emissivities to fluxes. When there are absorption processes involved, but the geometry is such that I is not depending on the position within the emitting region, i.e., when both emission and absorption coefficients are uniform and the maximum value of τ is the same for all the region[4], the flux can be computed (using Eqs. (C.61), (C.63) and the definition of τ) as

$$F_\nu = \frac{\epsilon_\nu}{\tau_\nu}(1-e^{-\tau_\nu})\frac{V}{D^2} \equiv \epsilon_\nu\frac{V}{D^2}f_1. \tag{C.65}$$

However, in the case of an sphere, for example, even when emission and absorption are uniform, the specific intensity is not. Following Eq. (C.61), one can see that, because the linear size is different at different angles θ' as measured from the center of the sphere, the opacity will also change. This change can be represented as $\tau_\nu = \kappa_\nu \times 2R\cos\theta' = \tau_{\rm max}\cos\theta'$, i.e. through the use of the maximum opacity $\tau_{\rm max}$ affecting a photon equatorially traversing the system. $\tau_{\rm max}$ is also a function of the frequency, although the subindex ν is omitted for simplicity. The flux, again given by Eq. (C.63),

[4]In the case of a uniform absorption coefficient this imposes a constraint on the geometry. For example, in the case of a molecular disk, the linear size in the direction of the observer may be considered the same, and thus τ is independent of any angle, and so is I. Thus, in this case, Eq. (C.65) applies.

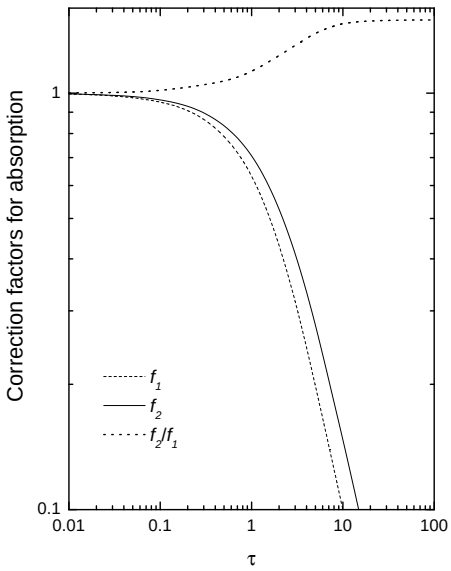

Figure C.5: Correction factors for absorption. The f_2/f_1 curve asymptotically tends to 1.5. From Torres (2004).

will be

$$\begin{aligned} F &= \int I[\cos\theta]\; d\Omega = \int \frac{\epsilon_\nu}{\kappa_\nu}(1 - e^{-\tau_\nu(\theta')})\, 2\pi\, \cos\theta\, \sin\theta\, d\theta \\ &= \frac{\epsilon_\nu}{\kappa_\nu} 2\pi \int_0^{\theta_{\max}} \left(1 - e^{\tau_{\max}\sqrt{1-(D/R)^2 \sin\theta}}\right) \cos\theta \sin\theta d\theta. \end{aligned} \tag{C.66}$$

The solution to this integral can be analytically obtained and after some algebra the result can be written as

$$F = \frac{\epsilon_\nu}{\tau_{\max}} \frac{V}{D^2} \left[\frac{3}{2} + \frac{3}{\tau_{\max}^2}\left((1+\tau_{\max})e^{-\tau_{\max}} - 1\right)\right] \equiv \epsilon_\nu \frac{V}{D^2} f_2. \tag{C.67}$$

Note that when $\tau_{\max} \ll 1$ the previous result reduces to the case of no absorption, $f_2 = 1$. Figure C.5 shows the behavior of the correction factors for absorption that appear in the different contexts analyzed in this paper, f_1 and f_2.

Appendix D

Camera subsystems controlled by PLCs

This Appendix is a brief description of the subsystems of the camera of the MAGIC Telescope that are controlled by means of autonomous Programmable Logic Controllers (PLCs). The control of the camera lids and the camera cooling system are specially described, as the author was responsible for its implementation. Finally, the current performance of the cooling system is shown.

D.1 PLCs and Modbus control

A PLC is a device that was introduced in the 60's to replace the necessary sequential relay circuits for machine control. A PLC works by looking at its inputs and depending upon their state it turns on/off its outputs. The user enters a program via software that gives the desired results. The PLC continually scans the program: first, it checks the status of each input and records this information into memory variables; secondly, it executes the program one instruction at a time taking into account the current value/status of each input and decides which should be the status of each output; finally, it updates the status of each output according to the results of the program execution.

The PLCs used to control some of the MAGIC camera subsystems are TSX Micro PLCs from Modicon Telemechanique, with a processor 37.22.101 and output relays working at 24VDC. The steering program has been written in ladder language and controls one or more digital output modules in response to the status of several digital inputs modules and the values read in the analogue input modules. The interface with the general camera control program is done through the setting and monitoring of a group of boolean and word type PLC memory variables. These variables are accessed via standard Modbus protocol functions that are incorporated in a set of C/C++ written drivers which contain all the subsystems functionality. At hardware level, the physical link between the two PLCs and the PC where the central camera control program is running is done through a Meilhaus ME-9000/4 PCI card and two RS-485 lines, which are ideal for long distance remote control applications (as is the case for MAGIC as about 200 m cable is needed to connect any element at the telescope with the PCs housed in the data taking control house) as they are differential lines.

D.2 Camera subsystems

The modularity, autonomy, and robustness of the control via a PLC has offered a way to easily introduce new elements within the global control system of the telescope. Currently, the following elements are controlled by the two existing PLCs:

- The cooling system of the camera.
- The opening and closing of the camera lids.
- The monitoring of the voltatge and current outputs of the Low Voltatge (LV) camera power supplies.
- The continuous monitoring of the temperature and relative humidity inside the box that houses the LV camera power supplies, which is attached to the camera frame and is not completely water tight. This is essential to determine if the conditions are safe enough to switch on the LV power supplies.
- The switching on/off of other telescope systems LEDs installed on the camera frame, as the Starguider, the AMC and the Camera Oscilation system LEDs.
- The supply of 220V to the calibration box.

In last four points the PLCs just offer a readout of current values of magnitudes needed to be controlled and a remote access to the switching on/off of several elements, which makes it easier to the central camera control program to take decisions and fast actuate accordingly.

The camera lids and cooling subsystems, the implementation of the control of which the author was specially responsible of, are described in more detail in the following subsections.

D.2.1 The camera lids

The camera entrance that faces the telescope mirror collector is protected from daylight with two light-and-water tight lids. As the PMTs can be damaged if they are exposed to too bright illumination, during data taking it is needed to remotely control a fast closing of the camera lids in case a sudden increase of the pixels DC current occurs (e.g. due to the accidental illumination of the reflector by a passing car). For this and any other situation that could require a fast action over the lids, the central control of the telescope can access the PLC that controls the motors and send the appropriate order to it: open, close or stop. A manual operation of the lids was also implemented to allow an easy opening/closing without using the central control program when a technical camera access is needed. The manual movement of the lids is also controlled by the PLC but the inputs, instead of being sent through the RS-485 bus, are a set of actuators operable by hand (see Figure D.1). To avoid an inconsistency of orders simultaneously received by the PLC and prevent for accidents, it is mandatory to open manually the lids if an access to the camera is done and the remote control is blocked until they have been closed again manually. Finally, the lid control subsystem allows to position the lids to "Tpoints"[1] from any previous lids state.

[1] A "Tpoint" is a special data taking run where an enough bright star is tracked and its reflected image on the camera plane is recorded by a CCD camera. For these cases the bottom lid should be closed

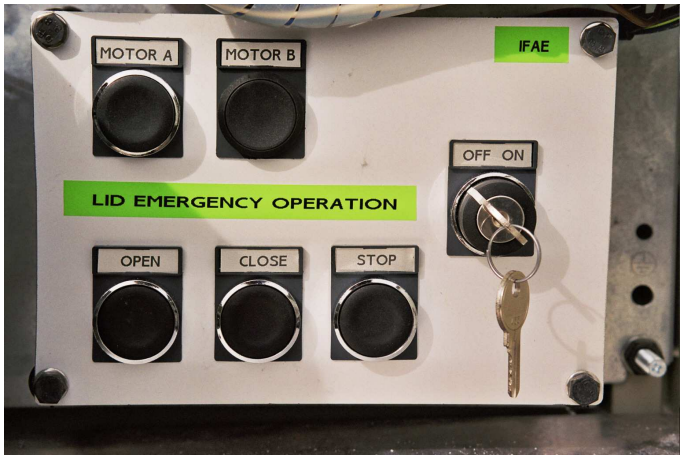

Figure D.1: Buttons installed at the base of the telescope for manual operation of the camera lids.

D.2.2 The camera cooling system

The goal of the cooling system is to regulate the temperature inside the camera with two main purposes: to ensure a stable temperature during data taking to minimize the temperature dependent fluctuations of some of the devices of the readout chain, and to control in general the temperature as to avoid extremely high temperatures which could imply the damage of camera electronic components but also too low temperature as to prevent for water condensation inside the camera.

The required specifications for the MAGIC cooling system were:

- Maintain the temperature inside the camera below 40 degrees with a power dissipation of 800 W.
- Ensure a stability of the temperature inside the camera within $\pm$ 1 degree during data taking.
- Bring the system to the same stability temperature during data taking along the whole year to get a comparable camera response independently of the season and make it as much independent as possible of the external temperature and conditions.

The choice of housing the major part of the readout electronics far from the camera, apart from the already mentioned advantages, made possible to design a simpler camera cooling system as the gross of the heat dissipation occurs outside of the camera. The chosen design which fulfilled all the requirements was a water-based cooling system. Figure D.2 shows a sketch of the system with all its elements.

At ground level there is a 200 l water tank which feeds the water pipeline that goes up to the camera. A S-shaped copper tube runs along the external lateral wall of the camera and is the heat-cool exchanger. Although all along the 12.5 mm diameter copper tube is covered by an isolator material to minimize the influence of the external temperature conditions, the circuit is filled with glycolate water to avoid freezing problems during

and the upper one opened, as there is an additional panel fixed to the bottom lid close to the plexiglas window. The Tpoints data are used to monitor the telescope focusing quality and the possible mispointing to correct for them.

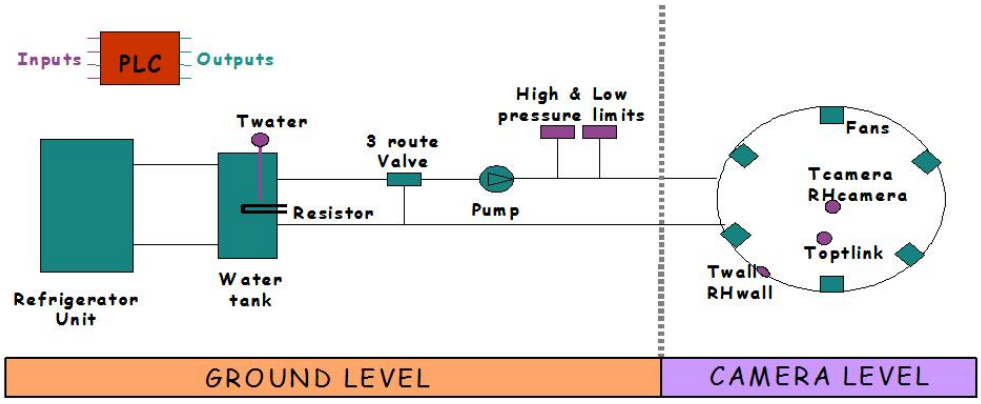

Figure D.2: Sketch of the water-based cooling system of the MAGIC camera.

winter. The water of the tank can be cooled or heated depending of the needs: if there is a risk of water condensation inside the camera, hot water is sent in order to increase the temperature and decrease the relative humidity inside the camera; if temperature grows to much, cold water is sent. A refrigerator unit is connected to the tank. Its programmable thermostat allows to select the temperature range of the water that will be sent to the camera. Currently the water in the tank is kept between 8 and 10 degrees during normal data taking. To heat the water in case it is needed, there is a 2400 W resistor inside the tank which can be switched on/off from the PLC coordinately with the refrigerator on/off switching. The temperature of the water in the tank is continuously monitored with a probe which is read by an analogue input of the PLC. A pump drives the water up to the camera exchanger circuit. A three route valve controlled by the PLC allows to choose the water to recirculate along the exchanger circuit (so its temperature gradually increases) or to renew it taking cooler (or hotter) water from the tank. Two pressure limit sensors are installed in the water circuit and are read by two digital inputs of the PLC, so if a too low (high) pressure occur, pointing to a possible leakage (obstruction) in the circuit, the pump is automatically stopped by the PLC. Finally, the cooling system is completed with a set of temperature and relative humidity (RH) sensors installed at three different positions in the camera (at the center, close to one optical link transmitter board, and close to the camera wall) and a set of fans which homogenize the temperature inside the camera and make more efficient the heat-cool exchange. Photographs of some of the described elements are shown in Figure D.3.

The PLC controls the state of all the described elements and takes actions to fulfill the temperature condition requirements. The PLC program has two modes: data taking and standby (or no data taking). While the telescope is parked or no data are taken, the cooling system is steered to keep the temperature inside the camera around 28 degrees (see Figure D.4). This prevent for possible damage of the electronics due to extremely low temperatures during the coolest days of winter and at the same time reduces the time that the system needs to bring the camera to the typical operation temperature during data taking. Currently, the hour of HV and LV camera warming up that is required before data taking for the electronics to stabilize is also enough for the temperature to reach stability. As the camera control program is launched, the PLC enters in data taking mode and steers the cooling system to regulate the temperature inside the camera around 37 degrees. Fans are switched on to homogenize the temperature and the valve is set to

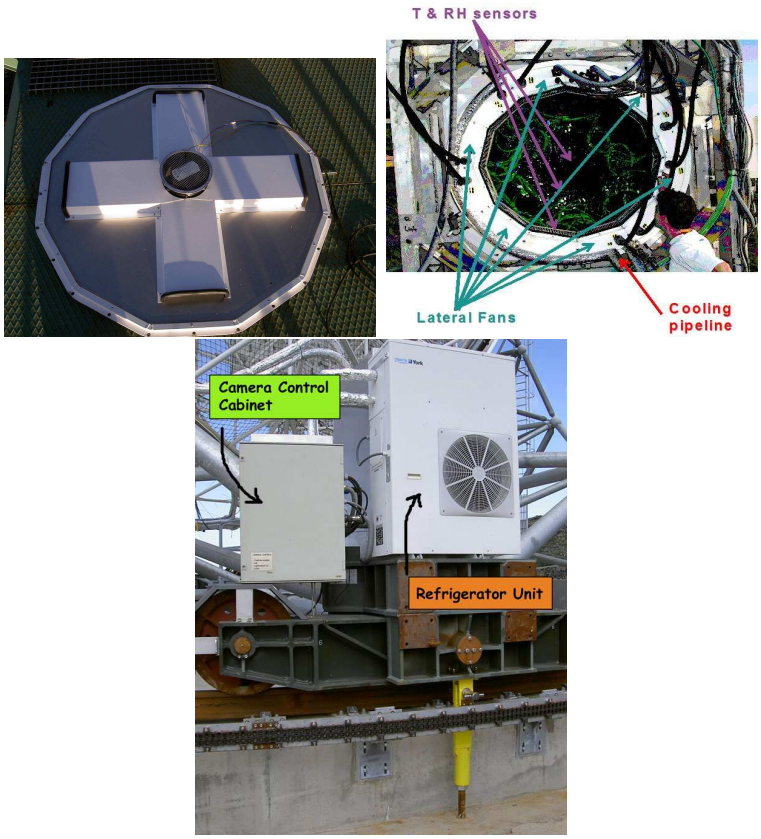

Figure D.3: Photographs of some of the elements of the cooling system of the camera of MAGIC: the central attached to the camera rear door, which provides the major temperature homogeneity inside the camera (left); rear view of the MAGIC camera with the position of the temperature and relative humidity sensors, the rest of the fans and the entrance of the water pipeline (middle); the refrigerator unit and the cabinet that houses one of the PLCs, the batteries which allow to operate the lids even if a power cut occurs, and all the electrical installation needed for the control (right).

recirculate and renew with cool water alternatively to keep the temperature well within $\pm$ 1 degree of fluctuation. Figure D.5 shows the temperature profile for a typical data taking night.

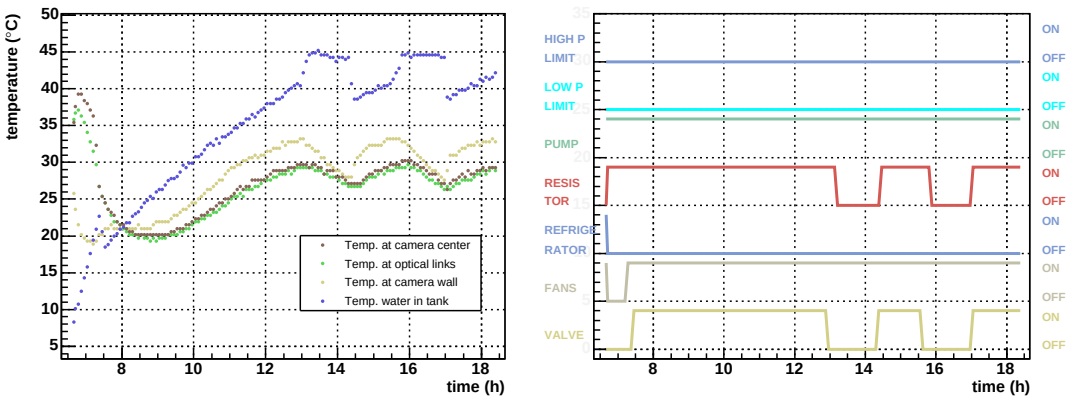

Figure D.4: During daytime, when no data taking is performed, the water of the tank (left panel blue points) is heat up to 40-45 degrees and sent to the camera. With this procedure, the camera temperature is kept around 28 degrees (green and brown points). The right panel shows the status of the different cooling system elements controlled by the PLC during the same period of temperature regulation shown in the left panel.

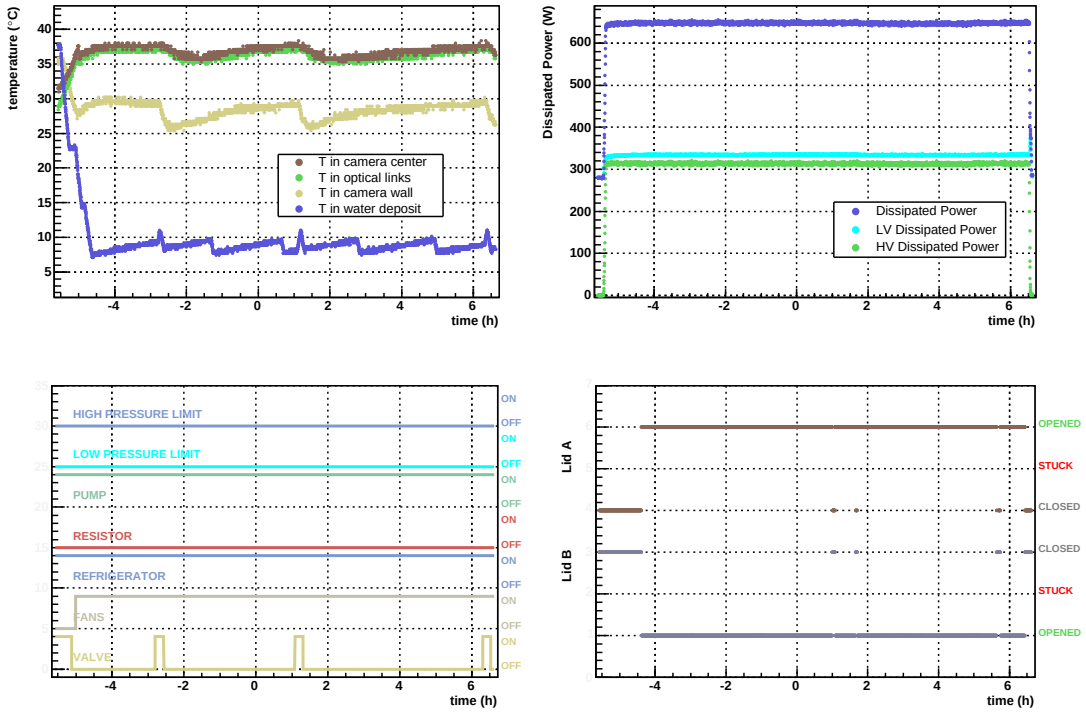

Figure D.5: The top left panel shows the evolution of the temperature inside the camera during a typical data taking night. Temperature is kept around 37 $\pm$ 1 degree homogeneously in the camera (brown and green points) while the power supplies are set to their nominal data taking value (see top right panel, the nominal power dissipation adding the HV and LV contribution is about 700 W). The bottom left panel shows the status of each of the cooling system elements, and bottom right panel shows the movement of the lids for that night, and can be observed that temperature is well stable when data taking really started (lids opened).

Appendix E

Focusing quality of the telescope

This Appendix compiles a study done to check the degradation of the quality of the telescope focusing along more than a half a year time period, during which the data analyzed in this Thesis was taken. The strongest signals available from the different data taking periods were used. The result is important for the generation of MC simulations compatible with the real data wanted to be analyzed.

E.1 Comparison of MC simulated and real γ events

A point-like source generates a distribution of photons at the focal plane of a telescope. This distribution is called Point Spread Function (PSF). Generally most of the light follows a gaussian distribution, whose σ value is an estimator of the focusing quality of the collecting mirror area. The same applies for the Čerenkov photons of an EAS, which are more or less spread once collected by the mirror dish and focused onto the camera of an IACT, depending on the quality of the telescope focusing. Disaligment of mirror panels makes the Čerenkov photons focus into a wider region of the camera, and the resulting shower images get also wider. Thus, the WIDTH of the slimmer γ-ray shower images becomes a good parameter to test the focusing quality of the telescope.

MC γ samples simulated with different values of the σ of the PSF distribution produced by the mirror dish were generated. The study consists in the comparison of the distribution of the WIDTH parameter of the different samples of MC γs with the WIDTH distribution of real γ-ray events. The main difficulty is to select an enough large sample of γ-ray images from the real data without using the traditional γ/hadron separation techniques, as they make use of an already chosen MC sample with a certain simulated PSF. Only the signal from the strongest sources can provide the required sample of real γ-ray events. The Crab Nebula has been used to check the performance of the telescope focusing for the last three data taking periods involved in the data analysis of this Thesis. However, before September the Crab Nebula is still not observable from the MAGIC site, and the data from the huge flare that the well-known Active Galactic Nucleus Mrk 501 presented on the 1st of July of 2005 has been used to determine the focusing quality of the telescope close to the epoch in which the Arp 220 data was taken.

To extract the sample of real γ-ray events from the data the following procedure has been followed (see Figures E.1, E.2 and E.3):

- Select an Off data sample as much compatible as possible with the On data sample used.

- Normalize the On and Off data samples to have the same number of events in the alpha distribution (first panel of the Figures) between 30 and 80 degrees.

- Introduce loose cuts to reject events with high probability to not be γ-induced and ease the analysis. A cut to remove the so-called "spark" events is applied. Also loose cuts in the DIST parameter, taking as a reference the MC γs distributions in different SIZE bins and taking care of keeping most of them. Finally, a very loose cut in HADRONNESS to remove hadron-like events.

- Select those events with absolute value of ALPHA below 5 degrees, and construct the distribution of the WIDTH parameter for the On data sample and for the normalized Off data sample (second panel of the Figures).

- Subtract the Off data distribution to the On one to get the WIDTH distribution of real γ events (third panel of the Figures).

Bottom panels of Figures E.1, E.2 and E.3 compare the WIDTH distribution of real γs with MC simulated γ events, produced with different values of σ of the PSF: 10, 14 and 20 mm. Figure E.1 uses as On data sample the Mrk 501 data from the flare observed on the 1st of July 2005, and Off Mrk 501 data taken during the same data taking period (P31). Figure E.2 analyzes Crab Nebula data from the beginning of October 2005 (P34), right before a technical access to refocus and repair the mirror dish of the telescope. No Off data of any galactic source was available for that data taking period, so the On data of the pulsar PSRB1957 was used as Off data sample because no signal is expected from few hours observation and for enough high energies. Figure E.3 shows the study for Crab Nebula taken at the beginning of November 2005, during period P35, right after the refocusing access. One hour of Off Crab data has been used as Off data sample.

The three analysis show a better agreement between real and MC simulated γ events for the same value of the σ of the PSF distribution that characterizes the telescope focusing: a σ of 14 mm. This result points to a no sizeable degradation of the PSF along the six months period between the two technical access for the readjustment of the mirror dish focusing, performed at the end of April, during the bright moon days between data taking periods P28 and P29, and at mid October, right after period P34. This is consistent with no improvement of the focusing quality observed in the analysis of the period P35 data, after the last telescope reflector technical access.

E.2 Comparison with muon studies

Muons travelling through the atmosphere may also emit Čerenkov radiation if they are above the emission energy threshold. As they travel with almost negligible energy losses and deflection, the profile of Čerenkov photons at ground level will essentially follow a ring distribution. As a consequence, most of the muons can be easily recognized at the camera of an IACT because of their ring-shaped images.

Based on the same idea pointed out in the previous Section, the well defined muon ring images can be used to estimate the quality of the telescope focusing. Comparing the relative ring broadening of muon ring images taken from observational data with those from MC muons simulated with different PSF widths, the PSF of the MAGIC reflector can be characterize. Figure E.4 shows the result of an extensive study over muon selected events along most of the 2005. The y-axis shows the σ value of the PSF distribution

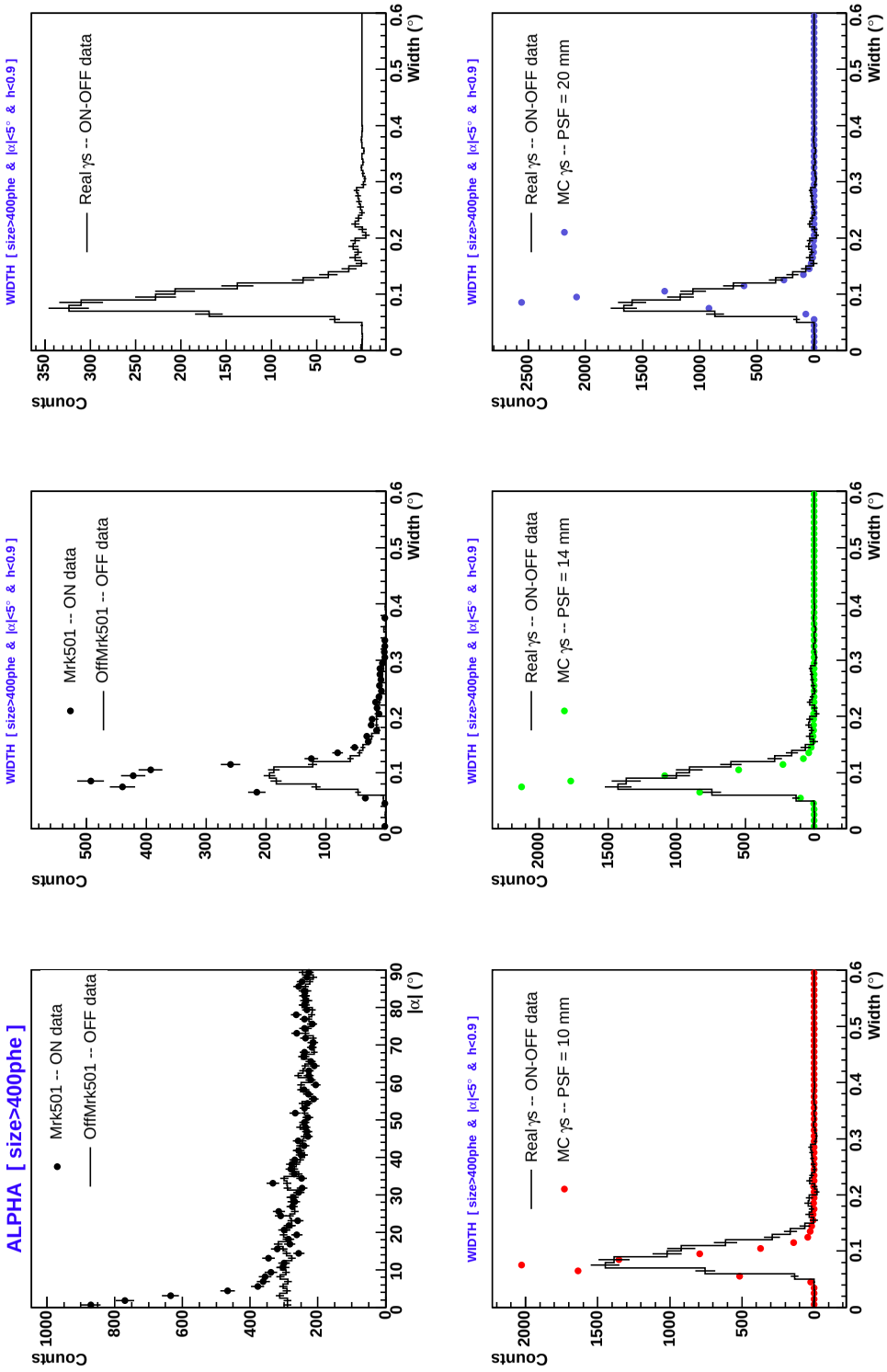

Figure E.1: Extraction of the WIDTH distribution for real γ events (top panels, see the text) from Mrk 501 On data of the 1st of July 2005 flare and Off Mrk 501 data of the same period P31. Comparison with MC γ events simulated with 10, 14 and 20 mm of σ of the PSF distribution (bottom panels).

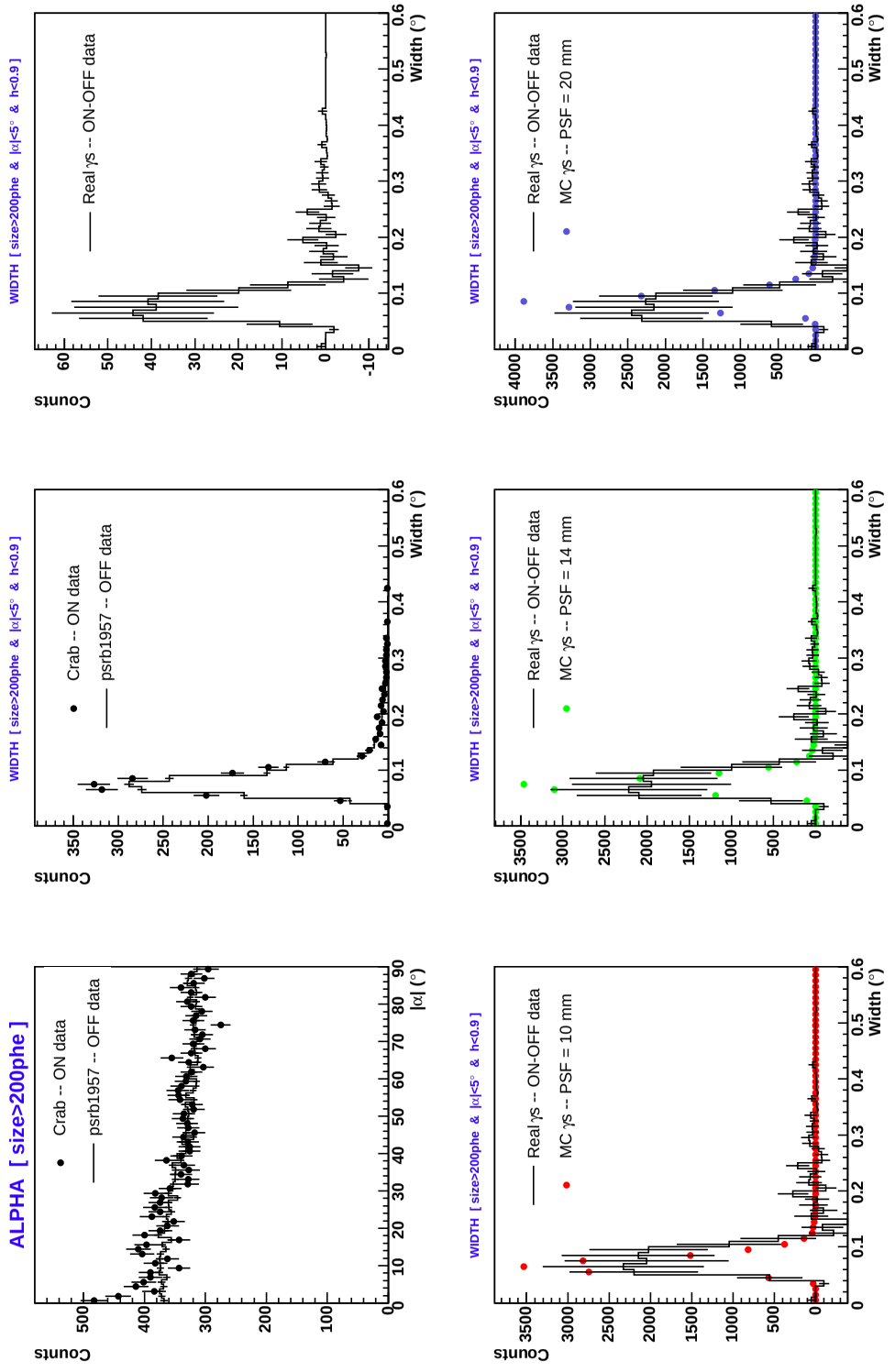

Figure E.2: Extraction of the WIDTH distribution for real γ events (top panels, see the text) from Crab Nebula On data of the end of period 34 and PSRB1957 data as Off data sample. Comparison with MC γ events simulated with 10, 14 and 20 mm of σ of the PSF distribution (bottom panels).

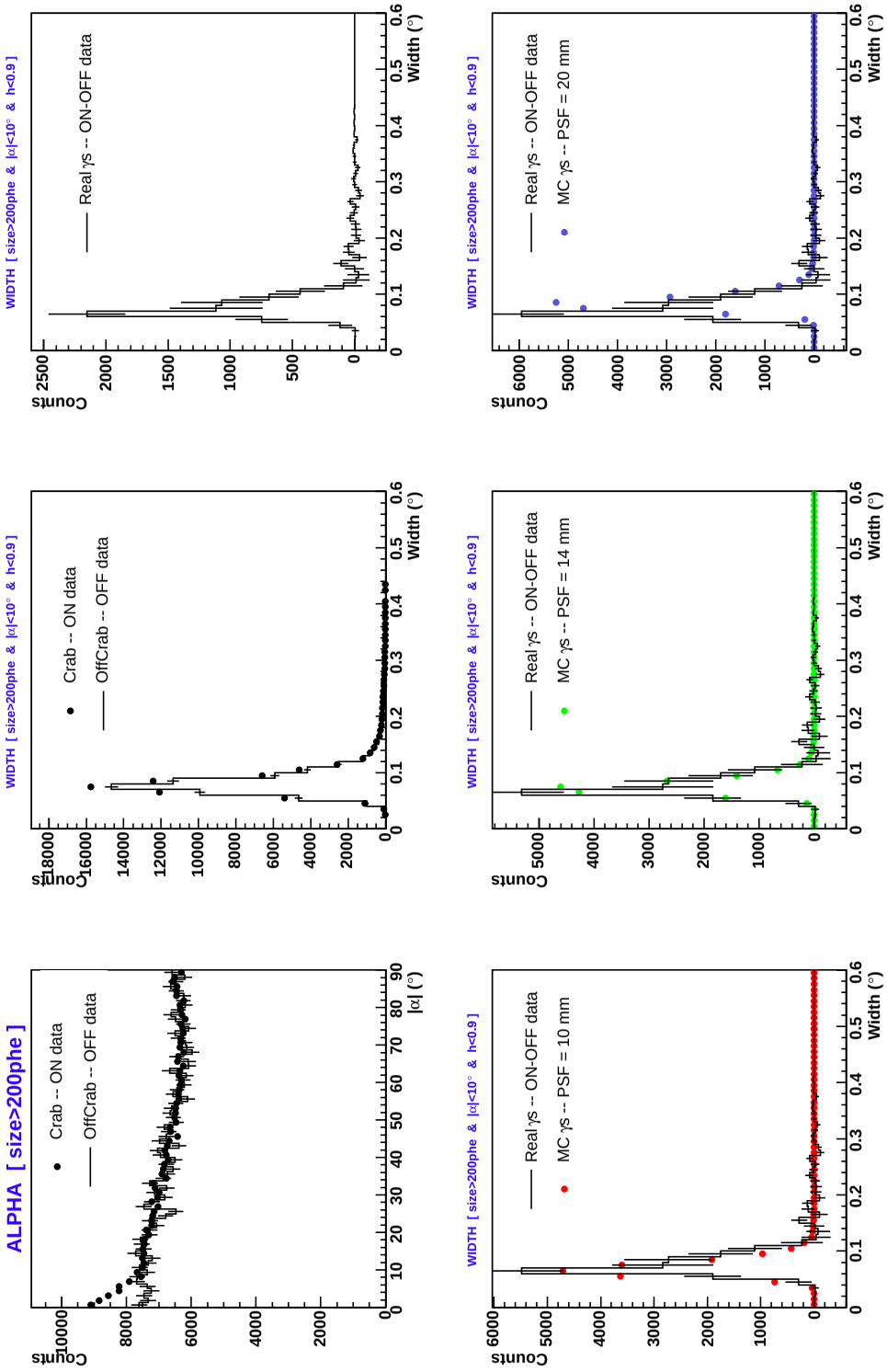

Figure E.3: Extraction of the WIDTH distribution for real γ events (top panels, see the text) from Crab Nebula On data of period 35 and Off Crab data as Off data sample. Comparison with MC γ events simulated with 10, 14 and 20 mm of σ of the PSF distribution (bottom panels).

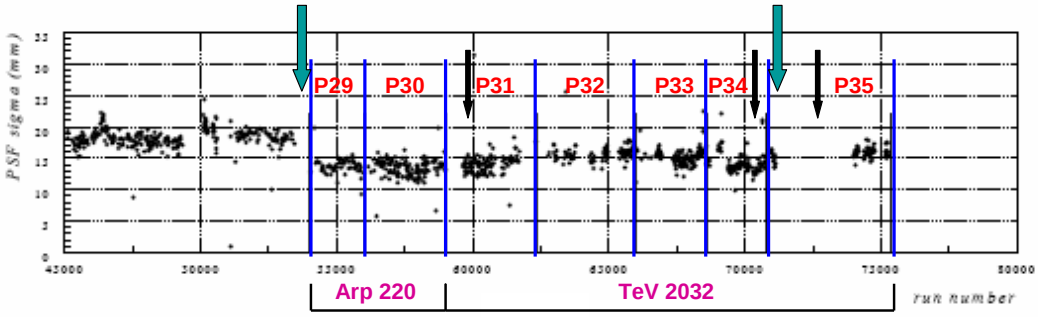

Figure E.4: Evolution of the width of the PSF distribution that characterizes the focusing of the MAGIC Telescope mirror dish, as shown by muon images analysis. The σ of the gaussian distribution ranges between 12 to 20 mm (the size of an inner pixel of the MAGIC camera is 30 mm diameter). The run number is used as time axis. The different data taking periods (from P29 to P35) from which data is analyzed in this Thesis are approximately divided by vertical blue lines. Big green arrows show the epoch in which an access to refocus and repair the mirror area was performed. Black arrows point to the epochs when the three data samples used for the analysis in the previous Section were taken. A clear improvement of the focusing quality can be observed after the refocusing access done before data taking period 29, and no evident degradation of the PSF is seen during the half a year time period before the next refocusing access.

introduced in the MC simulations that better reproduces the width of the real data muon rings for the different data taking periods.

The muon studies points to a similar conclusion as the analysis done with γ-ray real events: no important degradation of the PSF is observed during the whole data taking periods used for the analysis and the focusing quality is compatible with a gaussian σ of the PSF of around 14 mm.

E.3 Conclusion: the selected MC sample

The study of the focusing quality evolution presented in the current Appendix was motivated by the fact that a global decrease of the trigger rates was observed during the data taking periods P33 and P34. As a large amount of the data available from the TeV 2032 source was taken during that periods the aim of the study was to decide which was the more convenient MC to be used to analyze that data. The acquisition data rates recovered after the technical access done between data taking periods P34 and P35, so the abnormal lower rates pointed to a possible degradation of the focusing quality of the telescope.

In the absence of the information from direct measurements of the telescope PSF using the images of bright stars on the camera plane, but with the agreement of two independent methods, now we conclude that no important degradation of the focusing of the telescope was present during the data taking periods we are dealing with. A possible explanation for the global decrease of the rates and their afterwards recovering could be on a more or less suddenly deterioration of the mirror panels surface. A sizeable number

of mirror panels were in fact substitute during the last refocusing access, those presenting large bubble deformations caused by water entering in the sandwich support structure.

As a conclusion of this study of the evolution of the focusing quality of the telescope, the same MC sample was decided to be used for the analysis of all the data available along all the data taking periods involved, i.e., MC simulations with and added σ of the PSF of the mirror spots of 14 mm.

Bibliography

[1] Abraham P. B., Brunstein K. A. & Cline T. L. 1966, Phys. Rev. 150, 150

[2] Aharonian F. A. & Atoyan A. M. 1996, A&A 309, 91

[3] Aharonian F. A. & Atoyan A. M. 2000, A&A 362, 937

[4] Aharonian F. A. 2001, Space Science Reviews 99, 187

[5] Aharonian F. A. et al. [HEGRA collaboration] 2002, A&A 393, L37

[6] Aharonian F. A. et al. [HESS collaboration] 2004a, Nature 432, 75

[7] Aharonian F. A. et al. [HESS collaboration] 2004b, A&A 425, L13

[8] Aharonian F. A. et al. [HESS collaboration] 2004c, ApJ 614, 897

[9] Aharonian F. A. et al. [HESS collaboration] 2005a, A&A 437, 135

[10] Aharonian F. A. et al. [HESS collaboration] 2005b, A&A 432, L9

[11] Aharonian F. A. et al. [HESS collaboration] 2005c, A&A 442, 177

[12] Aharonian F. A. et al. [HEGRA collaboration] 2005d, A&A 431, 197

[13] Aharonian F. A. et al. [HESS collaboration] 2005e, Science 307, 1938

[14] Aharonian F. A. et al. [HESS collaboration] 2005f, A&A 439, 1013

[15] Albert J. et al. [MAGIC collaboration] 2005a, *The MAGIC Project: Contributions to ICRC 2005, Pune, India, Part 3: MAGIC Detector and Analysis Details*, astro-ph/0508274

[16] Albert J. et al. [MAGIC collaboration] 2005b, accepted ApJ Letters, astro-ph/0512283

[17] Anchordoqui L. A, Romero G. E. & Combi J. A. 1999, Phys. Rev. D60, 103001

[18] Anchordoqui L. A., Goldberg H. & Torres D. F. 2003, Phys. Rev. D67, 123006

[19] Anchordoqui L. A. et al. 2003b, ApJ, 589, 481

[20] Atkins R. et al. 2000, NIM A449, 478.

[21] Badhwar G. D., Stephens S. A. & Golden R. L. 1977, Phys. Rev. D15, 820

[22] Barrio J. A. et al. 1998, *The MAGIC telescope*, MPI-PhE/98-5

[23] Bartko H., Gaug M., Moralejo A. & Sidro N. for the MAGIC collaboration 2005, proceedings "Towards a Network of Atmospheric Cherenkov Detectors VII", Paris, astro-ph/0506459

[24] Bhattacharya D. et al. 1994, ApJ 437, 173

[25] Beck R. et al. 1996, ARAA, 34, 155

[26] Bell A. R. 1978, MNRAS 182, 443

[27] Benaglia P. & Koribalski B. 2004, A&A 416, 171

[28] Benaglia P., Romero G. E., Stevens I. & Torres D. F. 2001, A&A 366, 605

[29] Berezinskii V. S., Bulanov S., Dogiel V., Ginzburg V. 1990, *Astrophysics of Cosmic Rays*, North-Holland

[30] Bignami G. F. & Hermsen W. 1983, ARA&A 21, 67

[31] Blanchot G. et al. 1998, Proceedings of the IEEE Nuclear Science Symposium, Toronto.

[32] Blattnig S. R. et al. 2000, Phys. Rev. D62, 094030

[33] Blattnig S. R. et al. 2000b, published as a NASA internal document: TP-2000-210640, Langley Research Center, available online at http://techreports.larc.nasa.gov/ltrs/PDF/2000/tp/NASA2000tp210640.pdf

[34] Blom J. J., Paglione T. A. & Carramiñana A. 1999, ApJ 516, 744

[35] Bloemen J. B. G. et al. 1986, A&A 154, 25

[36] Blumenthal G. R. & Gould R. J. 1970, Rev. Mod. Phys. 42, 237

[37] Bozhokin S. V. & Bykov A. M. 1994, Astronomy Letters 20, 593

[38] Bradbury S. M. et al. 1995, Proceedings of the 24th ICRC, Rome, vol.1, 1051

[39] Bradford C. M. et al. 2003, ApJ 586, 891

[40] Brecher K. & Burbidge G. R. 1972, ApJ 174, 253

[41] Bronfman L. et al. 1988, ApJ 324, 248

[42] Brown R. L. & Marscher A. P. 1977, ApJ 212, 659

[43] Brun R. et al. "ROOT, an Object-Oriented Data Analysis Framework", http://root.cern.ch

[44] Bryant P. M. & Scoville N. Z. 1999, ApJ 117, 2632

[45] Butt Y. et al. 2003, ApJ 597, 494

[46] Bykov A. M. & Fleishman G. D. 1992a, MNRAS, 255, 269

[47] Bykov A. M. & Fleishman G. D. 1992b, Sov. Astron. Lett., 18, 95

[48] Bykov A. M. 2001, Space Sci. Rev., 99, 317

[49] Cantó J., Raga A. C. & Rodriguez L. F. 2000, ApJ 536, 896

[50] Canzian B., Mundy L. G. & Scoville N. Z. 1988, ApJ 333, 157

[51] Carilli C. L. 1996, ApJ 305, 402

[52] Castor J., McCray R. & Weaver R. 1975, ApJ L200, 107

[53] Cesarsky C. & Montmerle T. 1983, Space Sci. Rev. 36, 173

[54] Chevalier R. A. 1982, ApJ 289, 302

[55] Chevallier R. A. & Clegg A. W. 1975, Nature 317, 44

[56] Cillis A. N., Torres D. F. & Reimer O. 2005, ApJ 621, 139

[57] Clark J. S. & Negueruela I. 2002, A&A 396, L25

[58] Clark J. S. & Negueruela I. 2004, A&A 413, L15

[59] Clark J. S., Negueruela I., Crowther P. A. & Goodwin S. P. 2005, A&A 434, 934

[60] Crutcher R. M. 1988, in *Molecular Clouds, Milky-Way & External Galaxies*, R. Dickman, R. Snell & J. Young Eds., New York, Springer-Verlag, p.105

[61] Crutcher R. M. 1994, *Clouds, cores and low mass stars*, Astronomical Society of the Pacific Conference Series, volume 65; Proceedings of the 4th Haystack Observatory, edited by D. P. Clemens & R. Barvainis, p.87

[62] Crutcher R. M. 1999, ApJ 520, 706

[63] Cox A. N. 1999, *Allen's Astrophysical Quantities*, Springer Verlag, New York

[64] Cox P. & Metzger P. G. 1989, A&A Rev. 1, 49

[65] Coziol R. et al. 1998, ApJS 119, 239

[66] Della Cecca R. et al. 2002, ApJ 581, L9

[67] Dermer C. D. 1986a, A&A 157, 223

[68] Dermer C. D. 1986b, ApJ 307, 47

[69] Dermer C. D. & Schlickeiser R. 1991, A&A 252, 414

[70] Digel S. W., Moskalenko I. V., Ormes J. F. et al. 2000, *Proceedings of the workshop: New worlds in Astroparticle Physics*, astro-ph/0009271

[71] Domingo-Santamaría E. & Torres D. F. 2005a, A&A 444, 403

[72] Domingo-Santamaría E. & Torres D. F. 2005b, A&A in press, astro-ph/0510769

[73] Domingo-Santamaría E., Flix J., Rico J., Scalzotto V., Wittek W., for the MAGIC collaboration 2005, Proceedings of the 29th ICRC, Pune.

[74] Donati J.-F. et al. 2002, MNRAS 333, 55

[75] Donati J.-F. et al. 2001, MNRAS 326, 1265

[76] Dorman L. 1999, Proceedings of the 26th International Cosmic Ray Conference. August 17-25, 1999. Salt Lake City, Utah, USA. Under the auspices of the International Union of Pure and Applied Physics (IUPAP). Volume 4. Edited by D. Kieda, M. Salamon & B. Dingus, p.111

[77] Downes D. & Solomon P. M. 1998, ApJ 507, 615

[78] Downes D., Solomon P. M. & Radford S. J. E. 1993, ApJ 414, L13

[79] Drury L. O'C., Aharonian F. & Völk H. J. 1994, A&A 287, 959

[80] Dudley C. C. & Wynn-Williams C. G. 1999, MNRAS 304, 549

[81] Duric N. et al. 1995 ApJ 445, 173

[82] Elias J. H. et al. 1978 ApJ 220, 25

[83] Engelbracht C. W., Rieke M. J., Rieke G. H., Kelly D. M. & Achterman J. M. 1998, ApJ 505, 639

[84] Fichtel C. E., Ozel M. E., Stone R. G. & Sreekumar P. 1991, ApJ 374, 134

[85] Fomin V. P. et al. 1994, Astroparticle Physics 2, 137

[86] Forbes D. A. et al. 1993, ApJ 406, L11

[87] Forbes D. A., Polehampton E., Stevens I. R., Brodie J. P. & Ward M. J. 2000, MNRAS 312, 689

[88] Gaisser T. 1990, *Cosmic Rays and Particle Physics*, Cambridge University Press.

[89] Gao Y. & Solomon P. M. 2003a, ApJ Suppl. 152, 63

[90] Gao Y. & Solomon P. M. 2003b, ApJ 606, 271

[91] Ginzburg V. L. & Syrovatskii S. I. 1964, "The origin of cosmic rays", Pergamon Press, Oxford, England.

[92] GLAST Science Requirements Document, 433-SRD-0001, NASA Goddard Space Flight Center, CH-03, 2003, http://glast.gsfc.nasa.gov/project/cm/mcdl

[93] Greisen K. 1956, Prog. Cosmic Ray Physics 3, 1

[94] Greisen K. 1960, Anual Review of Nuclear Science 10, 63

[95] Hartman R. C. et al. 1999, ApJS 123, 79

[96] Hagiwara K. et al. 2002, Phys. Rev. D66, 010001. Data on the total and elastic cross sections are available at http://pdg.lbl.gov/2005/reviews/contents_sports.html#kinemaetc

[97] Hanna D. S. et al. 2002, NIM A491, 126

[98] Harris A. I., Stutzki J., Graf U. U., Russell A. P. G., Genzel R. & Hills R. E. 1991, ApJ 382, L75

[99] Harrison A., Henkel C. & Russel A. 1999, MNRAS 303, 157

[100] Heckman T. M., Armus L. & Miley G. K. 1990, ApJS 74, 833

[101] Heck D. & Knapp J. 2002, "EAS Simulation with CORSIKA: A User's Manual"

[102] Henrichs H. F., Schnerr R. S. & ten Kulve E. 2004, Conference Proceedings of the meeting: "The Nature and Evolution of Disks Around Hot Stars", Johnson City, TN

[103] Hildebrand R. H., Whitcomb S. E., Winston R., Stiening R. F., Harper D. A. & Moseley S. H. 1977, ApJ 216, 698

[104] Hillas A. 1985, proceedings 19th ICRC, La Jolla, 3, 445

[105] Hillas A. M. et al. 1998, ApJ 503, 744

[106] Hinton J. 2004, New Astron.Rev. 48, 331

[107] Holder J. et al. 2005, Proceedings of the 29th ICRC, Pune, India, astro-ph/0507451

[108] Horns D. & Aharonian F.A. 2004, Proceedings of the 5th INTEGRAL Workshop, 439, München

[109] Houghton S. et al 1997, A&A 325, 923

[110] Humphreys R. M. & Mc Elroy D. B. 1984, ApJ 284, 565

[111] Hunter S. D. et al. 1997, ApJ 481, 205

[112] Itoh C. et al. 2002, A&A 396, L1

[113] Itoh C. et al. 2003, A&A 402, 443

[114] Israel F. P. & Baas F. 2002, A&A 383, 82

[115] Jokipii J. R. & Parker, E. N. 1970, ApJ, 160, 735

[116] Jokipii J. R., Kóta J. & Merényi E. 1993, ApJ 405, 782

[117] Kamae T., Abe T. & Koi T. ApJ, 2005, ApJ 620, 244

[118] Karle A. 1997, Nuclear Instruments and Methods A387, 274-277

[119] Kawachi A. et al. 2001, Astrop. Phys. 14, 261

[120] Keto E., Hora J. L., Fazio G. G., Hoffman W. & Deutsch L. 1999, ApJ 518, 133

[121] Kembhavi A. K. & Narlikar J. V. 1999, *Quasars and active galactic nuclei*, Cambridge University Press, Cambridge

[122] Knödlseder J. 2000, A&A 360, 539

[123] Knödlseder J. 2003, in *A Massive Star Odyssey: From Main Sequence to Supernova*, Proceedings of IAU Symposium 212, held 24-28 June 2001 in Lanzarote, Canary island, Spain. Edited by Karel van der Huchtet al. San Francisco: Astronomical Society of the Pacific, 2003., p.505

[124] Kóta J. & Jokipii J. R. 1983, ApJ 265, 573

[125] Kranich D. & Stark L. S., for the HEGRA Collaboration 2003, Proceedings 28th ICRC, Tsukuba

[126] Krawczynski H. 1995, Diploma Thesis, University of Hamburg

[127] Krügel E. 2003, *The physics of interestellar dust*, IoP, Cambridge

[128] Lamers H. J. G. L. M. & Leitherer, C. 1993, AJ 412, 771

[129] Lamers H. J. G. L. M. et al. 1995, AJ 455, 269

[130] Lamers H. J. G. L. M. & Cassinelli, J. P. 1999, *Introduction to Stellar Winds*, Cambridge University Press, Cambridge

[131] Lang M. J. et. al 2004 A&A 423, 415

[132] Lebrun F. et al. 2004, Nature 428, 293

[133] Leitherer C., Robert C. & Drissen L. 1992, ApJ 401, 596

[134] Leitherer C. et al. 1999, ApJS 123, 3

[135] Leitherer C. 1999, in *Proc. of 33rd ESLAB Symp.: Star formation from the small to the large scale*, F. Favata, A. A. Kaas & A. Wilson eds., ESA SP-445, 2000

[136] Lessard R. W. et al. 2001, Astroparticle Physics 15, 1

[137] Li T.-P. & Ma Y.-Q. 1983, ApJ 272, 317

[138] Longair M. S. 1997, *High Energy Astrophysics, Vol.1: Particles, photons and their detection*, Cambridge University Press, 2nd ed. reprinted with corrections

[139] Longair M. S. 1994, *High Energy Astrophysics, Vol.2: Stars, the Galaxy and the Interstellar Medium*, Cambridge University Press, 2nd ed.

[140] Maíz-Apellániz J. & Walborn N. R. 2002, in *A Massive Star Odyssey: from Main Sequence to Supernova*, eds. K. A. van der Hucht, A. Herrero & C. Esteban, ASP Conf. Ser. 212, p. 560

[141] Manchanda R. K. et al. 1996, A&A 305, 457

[142] Mannheim K. & Schlickeiser R. 1994, A&A 286, 983

[143] Mao R. Q. et al. 2000, A&A 358, 433

[144] Marscher A. P. & Brown R. L. 1978, ApJ 221, 588

[145] Massey P., Johnson K. E. & DeGioia-Eastwood K. 1995, ApJ, 454, 151

[146] Mauersberger R., Henkel C., Wiebelinski R., Wiklind T. & Reuter H.-P. 1996, A&A 305, 421

[147] McCarthy P.J., Heckman T. & van Breugel W. 1987, AJ 92, 264

[148] Melo V. P., Perez-Garcia A. M., Acosta-Pulido J.A., Muñoz-Tuñon & Rodriguez Espinosa J. M. 2002, ApJ 574, 709

[149] Melnick J. & Mirabel I. F. 1990, A&A 231, L19

[150] Merck M. 1993, PhD. Thesis, Ludwig-Maximilians University of Müchen

[151] Mirzoyan R. & Lorenz E. 1994, Max-Planck-Institut fur Physik report MPI-PhE/94-35

[152] Moralejo A. 2000, PhD. Thesis, Universidad Complutense de Madrid

[153] Morfill G. E. 1982, ApJ 262, 749

[154] Moskalenko I. V. & Strong A. W. 1998, ApJ 493, 694

[155] Mukherjee R. et al. 2003, ApJ, 589, 487

[156] Neshpor Y. I., Kalekin O. R., Stepanian A. A. et al. 1995, Proc. 24th ICRC (Rome) 2, 1385

[157] Nishimura J. & Kamata K. 1952, Progress in Theoretical Physics 7, 185

[158] Nolan P., Tompkins W., Grenier I. & Michelson P. 2003, ApJ, 597, 615

[159] Ong R. A. 1998, Physics Reports 305, 93-202

[160] Ong R. A. 2005, Rapporteur Talk OG 1 at the 29th ICRC, Pune, India

[161] Ostankov A. et al. 2000, Nuclear Instruments and Methods A442, 117

[162] Ott J., Weiss A., Henkel, C. & Walter F. 2005, astro-ph/0505143. In *Starbursts: From 30 Doradus to Lyman Break Galaxies*, Held in Cambridge, UK, 6-10 September 2004. Edited by R. de Grijs & R.M. Gonzalez Delgado. Astrophysics & Space Science Library, Vol. 329. Dordrecht: Springer, 2005, p.P57

[163] Özel M. E. & Berkhuijsen E. M. 1987, A&A 172, 378

[164] Ozernoy L. M., Genzel R. & Usov V. 1997, MNRAS 288, 237

[165] Pagani L. et al. 1999, A&A 351, 447

[166] Paglione T. A. D., Tosaki T. & Jackson J. M. 1995, ApJ 454, L117

[167] Paglione T. A. D., Marscher A. P., Jackson J. M. & Bertsch D. L. 1996, ApJ 460, 295

[168] Paglione T. A. D., Jackson J. M. & Ishizuki S. 1997, ApJ 484, 656

[169] Paglione T. A. D., Yam O., Tosaki T. & Jackson J. M. 2004, ApJ 611, 835

[170] Paneque D. et al. 2003, Nucl. Inst. and Meth. 504, 109

[171] Paneque D. 2000, Diploma Thesis, Universitat Autònoma de Barcelona

[172] Paneque D. 2004, PhD. Thesis, Technischen Universität, München

[173] Parker E. M. 1958, Phys. Rev., 110, 1445

[174] Parizot E. et al. 2004, A&A 424, 727

[175] Pavlidou V. & Fields B. 2001, ApJ 558, 63

[176] Pence W. D. 1981, ApJ 247, 473

[177] Petry D. 2001, *in Proceedings of the I Workshop on The Nature of Galactic Unidentified Gamma-ray Sources*, O. Carramiñana, O. Reimer, D. Thomson Eds., Kluwer Academic Press, p.299

[178] Pietsch W. et al. 2001, A&A 365, L174

[179] Pittori C. et al. 2003, Chinese J. A&A 3, 517

[180] Prinja R. K. et al. 1990, AJ 361, 607

[181] Reimer A. 2003, Proceedings of the 28th International Cosmic Ray Conference, p.2505

[182] Reylonds P. T. et al. 1993, ApJ 404, 206

[183] Rice G. H. et al. 1988, ApJ 238, 24

[184] Riegel B., Bretz T., Dorner D., Wagner R. M., for the MAGIC collaboration 2005, Proceedings of the 29th ICRC, Pune.

[185] Rieke G. H., Lebofsky M. J., Thompson R. I., Low F. J. & Tokunga A. T. 1980, ApJ 238, 24

[186] Rieke G. H., Lebofsky M. J. & Walker C. E. 1988, ApJ 325, 679

[187] Rieke G. H., Harper D. A., Low F. J. & Armstrong K. R. 1973, ApJ 83, L67

[188] Risse M. 2004, Acta Phys. Polon. B35, 1787

[189] Rodriguez-Espinosa J. M., Perez-Garcia A. M., Lemke D. & Meisenheimer K. 1996, A&A 315, L129

[190] Romero G. E., Benaglia P. & Torres D. F. 1999, A&A 348, 868

[191] Romero G. E. & Torres D. F. 2003, ApJ 586, L33

[192] Rose J. et al. 2000, Nucl. Inst. and Meth. A442, 113.

[193] Rossi B. & Greisen K. 1941, Rev. Mod. Phys. 13, 240

[194] Rybicki G. B. & Lightman A. P. 1979, *Radiative processes in astrophysics*, John Wiley & Sons, New York

[195] Sanders D. B. & Mirabel I. F. 1996, ARA&A 34, 749

[196] Sanders D. B. et al. 1998, ApJ 325, 74

[197] Schlickeiser R. 2002, *Cosmic ray astrophysics*, Springer-Verlag, New York

[198] Schmidt-Kaler Th., 1982, Landolt-Börnstein Vol. 2

[199] Scoville N. Z. et al. 1991, ApJ 366, L5

[200] Smith L. F., Maeder A., 1991, A&A 241, 77

[201] Solomon P. M. & Barrett J. W. in the Proceedings of the 146th Symposium of the International Astronomical Union, held in Paris, France, June 4-9, 1990. Edited by F. Combes and Fabienne Casoli. International Astronomical Union. Symposium no. 146, Kluwer Academic Publishers, Dordrecht, 1991, p.235

[202] Solomon P. M., Downes D. & Radford S. J. E. 1992, ApJ 387, L55

[203] Solomon P. M., Radford S. J. E. & Downes D. 1990, ApJ 348, L53

[204] Solomon P. M., Rivolo A. R., Barrett J. & Yahil A. 1987, ApJ 319, 730

[205] Solomon P. M., Downes D., Radford S. J. E. & Barrett J. W. 1997, ApJ 478, 144

[206] Sorai K., Nakai N., Nishiyama K. & Hasegawa T. 2000, Publ. Astron. Soc. Japan 52, 785

[207] Sreekumar P. et al. 1992, ApJ 400, L67

[208] Sreekumar P. et al. 1993, Phys. Rev. Lett., 70, 127

[209] Stecker F. W. 1971, *Cosmic Gamma Rays*, Baltimore: Mono

[210] Stecker F. W. et al. 1975, ApJ 201, 90

[211] Stephens S. A. & Badhwar G. D. 1981, Astrophysics & Space Science 76, 213

[212] Stevens I. R. & Hartwell J. M. 2003, MNRAS 339, 280

[213] Strickland D. K., Heckman T. M., Weaver K. A. & Dahlem M 2000, AJ 120, 2965

[214] Strickland, D.K., Heckman, T.M., Weaver, K.A. et al. 2002, ApJ, 568, 689

[215] Strong A. W., Moskalenko I. V. & Reimer O. 2000, ApJ 537, 763

[216] Strong A. W. & Moskalenko I. V. 1997, Proc. Fourth Compton Symp., (eds) Dermer, C. D., Strickman, M. S. & Kurfess, J. D., p.1162; astro-ph/9709211

[217] Suchkov A., Allen R. J. & Heckman T. M. 1993, ApJ 413, 542

[218] Sugai H., Davies R. I. & Ward M. J. 2003, ApJ 584, L9

[219] Taniguchi Y. & Ohyama Y. 1998, ApJ 509, L89

[220] Telesco C. M. & Harper D. A., 1980, ApJ 235, 392

[221] Tingay S. J. 2004, ApJ 127, 10

[222] Tonello N. 2005, PhD. Thesis, Technischen Universität, München

[223] Torres D. F. 2004, ApJ 617, 966

[224] Torres D. F. 2004b, Published in *Gamma-ray Sources*, edited by K.S. Cheng & G.E. Romero, Kluwer Academic Press, 2004, The Netherlands, page 69-104. arXiv:astro-ph/0308069.

[225] Torres D. F., Romero G. E., Combi J. A., Benaglia P., Andernach H. & Punsly B. 2001, A&A 370, 468

[226] Torres D. F., Romero G. E., Dame T. M., Combi J. A. & Butt Y. M. 2003, Physics Reports 382, 303

[227] Torres D. F., Reimer O., Domingo-Santamaría E. & Digel S. 2004, ApJ 607, L99

[228] Torres D. F., Domingo-Santamaría E. & Romero G. E. 2004, ApJ 601, L75

[229] Torres D. F. & Anchordoqui L. A. 2004, Report on Progress in Physics, 67, 1663

[230] Torres D. F., Domingo-Santamaría E. 2005, Modern Physics Letters A20, 2827

[231] Turner J. L. & Ho P. T. P. 1985, ApJ 299, L77

[232] Ulvestad J. S. 2000, ApJ 120, 278

[233] Ulvestad J. S. & Antonucci R. R. J. 1997, ApJ 488, 621

[234] Vacca W. D., Garmany C. D., Schull J. M. 1996, ApJ 460, 914

[235] Van der Hucht 1986. et al. 1996, AJ 460, 91

[236] Van Buren D. & Greenhouse M. 1994, ApJ 431, 640

[237] Völk H. J. & Forman M. 1982, ApJ 253, 188

[238] Völk H., Aharonian F. A. & Breitschwerdt D. 1996, Space Science Reviews 75, 279

[239] Völk H. J., Klien U. & Wielebinski R. 1989, A&A 237, 21

[240] Wagner R. M., Lopez M., Mase K., Domingo-Santamaría E., Goebel F., Flix J., Majumdar P., Mazin D., Moralejo A., Paneque D., Rico J. & Schweizer T., for the MAGIC collaboration 2005, Proceedings 29th ICRC, Pune

[241] Ward J. S., Zmuidzinas J., Harris A. & Isaac K. 2003, ApJ 587, 171

[242] Watson A. M. et al. 1996, AJ 112, 534

[243] Weaver K. A., Heckman T. M., Strickland D. K. & Dahlem M. 2002, ApJ 576, L19

[244] Weber E. J. & Davis L. 1967, ApJ, 148, 217

[245] Weekes T. C. et al. 1989, ApJ 342, 379

[246] White R. L. 1985, ApJ 289, 698

[247] Whitmore J. 1974, Phys. Rept. 10C, 273

[248] Wild W. et al. 1992, A&A 265, 447

[249] Wild W. & Eckart A. 2000, A&A 359, 483

[250] Yao L., Seaquist E. R., Kuno N. & Dunne L. 2003, ApJ 588, 771

[251] Young J. S. & Scoville N. Z. 1991, ARA&A 29, 581

[252] Zimmermann J. 2005, "Statistical Learning in High Energy and Astrophysics", PhD. Thesis, Ludwig-Maximilians-Universität, München